Unconventional Thermoelectric Materials for Energy Harvesting and Sensing Applications

Matteo Massetti, Fei Jiao, Andrew J Ferguson, Dan Zhao, Kosala Wijeratne, Alois Würger, Jeffrey L Blackburn, Xavier Crispin, Simone Fabiano

CHEMICAL REVIEWS

pubs.acs.org/CR

Review

Unconventional Thermoelectric Materials for Energy Harvesting and Sensing Applications

Matteo Massetti, Fei Jiao, Andrew J. Ferguson, Dan Zhao, Kosala Wijeratne, Alois Würger, Jeffrey L. Blackburn,* Xavier Crispin,* and Simone Fabiano*

Cite This: https://doi.org/10.1021/acs.chemrev.1c00218

Read Online

ACCESS | Metrics & More | Article Recommendations

ABSTRACT: Heat is an abundant but often wasted source of energy. Thus, harvesting just a portion of this tremendous amount of energy holds significant promise for a more sustainable society. While traditional solid-state inorganic semiconductors have dominated the research stage on thermal-to-electrical energy conversion, carbon-based semiconductors have recently attracted a great deal of attention as potential thermoelectric materials for low-temperature energy harvesting, primarily driven by the high abundance of their atomic elements, ease of processing/manufacturing, and intrinsically low thermal conductivity. This quest for new materials has resulted in the discovery of several new kinds of thermoelectric materials and concepts capable of converting a heat flux into an electrical current by means of various types of particles transporting the electric charge: (i) electrons, (ii) ions, and (iii) redox molecules. This has contributed to expanding the applications envisaged for thermoelectric materials far beyond simple conversion of heat into electricity. This is the motivation behind this review. This work is divided in three sections. In the first section, we present the basic principle of the thermoelectric effects when the particles transporting the electric charge are *electrons*, *ions*, and *redox molecules* and describe the conceptual differences between the three thermodiffusion phenomena. In the second section, we review the efforts made on developing devices exploiting these three effects and give a thorough understanding of what limits their performance. In the third section, we review the state-of-the-art thermoelectric materials investigated so far and provide a comprehensive understanding of what limits charge and energy transport in each of these classes of materials.

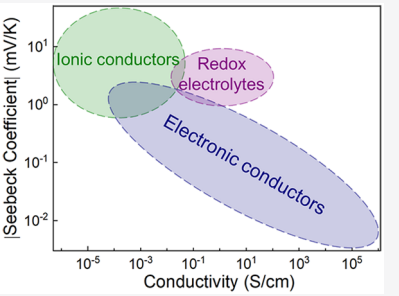

CONTENTS

Received: March 14, 2021

References BR

1. INTRODUCTION

Currently, global electricity production largely relies on fossil fuels (67%), water (16%), and nuclear energy (11%), while a small but rising fraction of electricity is produced by wind (>4%) and solar energy (>2%).[1,2] However, the conversion of primary energy sources into electricity is not always efficient (typically 35−50% for heat engines, 20% for solar thermal plants, 15−40% for solar cells), and thus a substantial amount of energy is lost as waste heat. While more than 50% of the available natural and waste heat is stored in large volumes of warm fluids (T < 250 °C), no viable technology exists to produce electricity from this low energy density heat. Efforts to adapt heat engines by replacing water steam with organic solvent steam (organic Rankine cycle) have enabled low-temperature operation.[3] However, the conversion is less efficient, reaching approximately 15−20% with heat engines that work at T_{cold} = 25 °C and T_{hot} = 150 or 250 °C.[4] Another technology that can utilize this heat resource is the thermoelectric generator (TEG). This solid-state electronic device converts the heat flow into an electric current without the need for maintenance because no moving mechanical parts or fluids are present. Like all heat engines, a thermoelectric device operates across a temperature gradient $\Delta T = T_{hot} - T_{cold}$. Today, the efficiency of the best TEGs is 15% for inorganic thin films prepared in a laboratory setting and 6.4% for industrially scalable materials based on the ball milling and sintering of bismuth telluride alloy nanoparticles (T_{cold} = 25 °C and T_{hot} = 250 °C).[5] On the basis of these materials, solar thermoelectric generators with an efficiency of 4.6% under AM1 light intensity have been fabricated.[6]

The first practical challenge for TEGs is the scaling up of material synthesis. The second limitation is the high material costs due to the scarcity of the atomic elements involved in those exotic materials.[7] Because of these challenges, it is not straightforward for TEGs to become an economically viable solution, outperforming heat engines in large-area energy harvesting applications. Without breakthroughs, it is unlikely that TEGs for low-temperature waste heat harvesting (T < 250 °C) will significantly impact the problem of CO_2 emissions.[8] Hence, research efforts in recent years have focused on thermoelectric materials composed of abundant atomic elements. In this context, widely available, although less efficient, carbon-based thermoelectric materials, i.e., carbon nanostructures[9] and conducting polymers[10] or composites of these materials,[11] have become a new subject of major interest in the scientific community. The interest in these materials is the motivation for this review.

Because one can find heat sources practically everywhere, TEGs are interesting power sources for many low-power technologies. TEGs have particular advantages over heat engines for small-scale implementations or applications, where maintenance is a major issue, such as powering autarkic sensor systems in nature or satellites in space. The miniaturization of heat engines to dimensions below 1 cm^3 leads to high-speed rotation, which wears out the cylinder piston (>10 000 rpm). Microengines also face many challenges in combustion, among which the main problem is the gap necessary between the piston and cylinder. Therefore, the efficiency drops from 40% to 0.05% when scaling down a cylinder from 10 cm^3 to 1 cm^3.[12] In contrast, the efficiency of TEGs remains constant from centimeter-scale to microthermoelectric generators.[13] In addition, the efficiencies of thermomechanical engines decreases drastically to lower power levels when scaling down,[8] such that a crossing point exists where thermoelectric devices become more efficient.

With these scaling considerations in mind, TEGs are attractive candidates for power sources or self-powered heat sensors for portable electronics and the Internet of Things (IoT) applications. For instance, in outdoor activities, TEGs are integrated with either cooking pots (PowerPot) or boots (Orange Power Wellies) to charge a mobile phone. Many low-power devices, such as radiator valves (Micropelt), sensor nodes,[14] and industrial process monitoring,[15] can be powered with TEGs. Another area of major impact is robotics and medical applications because many biosensors and medical implants[16] can be powered by exploiting body heat.[17] In these applications, the integration of TEGs on fabrics[18] and flexible substrates[19] or as electronic skin[20] might require various levels of mechanical flexibility and eventually some degree of stretchability. Unlike conventional inorganic thermoelectric materials, which are brittle and nonflexible, organic semiconductors can maintain mechanical integrity under various modes of stress and strain. Regarding the biomedical field, thermoelectric devices can also be integrated as self-powered temperature sensors for continuous monitoring, which has become exceedingly critical after the worldwide COVID-19 pandemic. These self-powered devices could directly transmit the electrical signal without any transduction, enabling easy integration of these temperature sensors in wearable electronics for real-time health monitoring.

Apart from wearable applications, TE-based devices can act as sensors in locations where solar-based energy harvesting/sensing is not a viable solution, e.g., in critical or hazardous areas inside buildings, pipelines, mines, aircraft, ships, and cars. Therefore, TE sensors may potentially impact fire detection, homeland security, and many other aspects of human life.[21,22] TE-based sensors can also be employed to monitor the environmental temperature along sections of a domestic or industrial plant for evaluating efficiency. For all of these applications, mechanical flexibility is a strict requirement, and organic semiconductors, thermoelectric fluids, and gels exploiting the thermogalvanic effect offer new opportunities in the field of stretchable and flexible electronics.[23] Finally, the exploration of the ionic Seebeck effect through the Soret effect in polymer electrolytes leads to a surprisingly high Seebeck coefficient (~10 mV K^{-1}), promoting a new research direction that uses this effect to charge supercapacitors with heat.[24]

Figure 1 summarizes the conductivity-dependent Seebeck coefficients for various classes of thermoelectric materials. In contrast to conductivity (σ), which is directly proportional to the charge carrier concentration (n) in the material, the Seebeck coefficient (S) typically decreases with increasing charge carrier concentration. Therefore, Seebeck coefficients equal to or higher than 1 mV K^{-1} are likely to be found in insulator materials having electronic structures with large energy gaps.[25] However, the low electrical conductivity of insulators (below 10^{-12} S cm^{-1}) makes reliable thermovoltage measurements very challenging. For heat-to-electricity conversion, the thermoelectric power factor ($S^2\sigma$) is the most critical parameter, which typically shows a maximum in the intermediate charge concentration region corresponding to semiconducting materials (10^{-5} S cm^{-1} < σ < 10^4 S cm^{-1} and 500 μV K^{-1} > S > 50 μV K^{-1}). This is because the thermal conductivity (k) of these materials is usually below unity, mainly due to the absence of long-range crystalline order. Thus, the phonon component is

https://doi.org/10.1021/acs.chemrev.1c00218
Chem. Rev. XXXX, XXX, XXX−XXX

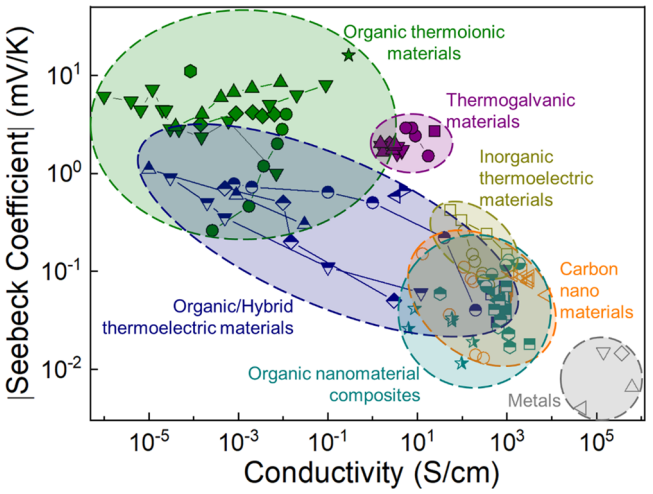

Figure 1. Seebeck coefficient as a function of the conductivity for organic/hybrid thermoelectric materials (see relative section 4.1), carbon nanomaterials (see relative section 4.2), organic nanomaterial composites (see relative section 4.2.5), organic thermoionic materials (see relative section 4.3), thermogalvanic materials (see relative section 4.4), inorganic thermoelectric materials (green open symbols), and metals (gray open symbols). For the conductivity of redox electrolytes, only the transport of ions is considered.

effectively reduced. Indeed, this behavior represents one of the greatest advantages of organic semiconductors over inorganic semiconductors, where most of the current research is focused on decreasing thermal conductivity. Hence, research and technology development on organic thermoelectric materials has mainly focused on semiconductors and semimetals. As shown in Figure 1, nonredox electrolytes (green symbols) and redox electrolytes (thermogalvanics, purple symbols) can generate larger Seebeck coefficients than electronic organic (blue symbols) or inorganic (yellow symbols) semiconductors, which makes them potentially suitable for thermoelectric applications despite their low conductivity.

In this article, we review three major classes of thermoelectric materials and devices working in the low-temperature range (T < 250 °C) and based on highly abundant elements: (i) thermoelectric generators based on conducting polymers, carbon nanostructures, and their composites, (ii) thermogalvanic cells, and (iii) ionic thermoelectric supercapacitors/batteries. In the first section, we present the basics of thermoelectric phenomena. The second section reviews the working principle behind the devices exploiting the different thermodiffusion phenomena, highlighting the key parameters necessary to improve their performances. Finally, in the third section, we provide an overview of the key materials investigated so far by the research community, and summarize the recent efforts to produce devices employing such materials.

2. THERMOELECTRIC EFFECTS IN A NUTSHELL

When mobile (uncharged) particles are subject to a temperature gradient, they undergo a steady drift toward the hot or cold side. Typically, mobile particles at the hot end move faster than those at the cold end. Thus, as shown in Figure 2a, the hot particles have a larger mean free path and diffuse further than the cold particles, leading to a high net particle density at the cold end. This effect, observed in gaseous, liquid, and even solid systems, is called thermophoresis (also thermodiffusion, or the Soret effect) and has been known for a long time.[26] Thermophoretic forces

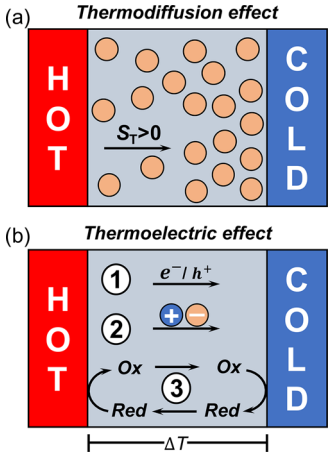

Figure 2. Illustration of (a) the thermodiffusion (S_T > 0) of particles and (b) three different concepts of thermoelectric effects: (1) electronic conductors, (2) nonredox electrolytes, (3) redox electrolytes.

have been used, for example, in the manufacturing of optical fibers in vacuum deposition processes[27] or to separate different polymer particles in field-flow fractionation.[28] Furthermore, thermophoresis has been demonstrated as a versatile technique for manipulating single biological macromolecules, such as DNA, in micro- and nanochannels by means of light-induced local heating.[29]

When a colloidal suspension is placed in a temperature gradient ∇T, the particle motion can no longer be described by Brownian motion. In the absence of an external force, particles then tend to accumulate at the cold or hot boundary. This is phenomenologically described by writing the particle current density (j) as:

$$j = -D\nabla c - D_T c\nabla T \quad (1)$$

where c is the particle concentration, D the diffusion coefficient of a colloidal suspension under Brownian motion, and D_T the thermodiffusion coefficient. The two components of eq 1 represent the motion of particles under a concentration gradient (∇c, kinetic diffusion) and a thermal gradient (∇T, thermal diffusion).

The dispersed particles display a thermodiffusive drift velocity $\vec{v}$, which depends linearly on ∇T with a proportionality constant equal to D_T:

$$\vec{v} = -D_T\nabla T, \quad (2)$$

Depending on the sign of D_T, the particles will accumulate either at the cold or the hot side. In a closed system, the steady state implies zero current ($j = 0$), $cv + D\nabla c = 0$, leading to a stationary concentration gradient:

$$\nabla c = -cS_T\nabla T \quad (3)$$

where the Soret coefficient $S_T = D_T/D$ is provided by the ratio of D_T and the ordinary diffusion coefficient D. These transport coefficients, D_T and D, describe nonequilibrium properties.

Gaseous systems can be dealt with exactly in the framework of kinetic theory. In the 1910s, Enskog and Chapman found that in a gas mixture, heavier and larger atoms accumulate at the cold side.[30] These mass and size effects were confirmed experimentally with ammonium isotopes $N_{14}H_3/N_{15}H_3$ and dimer molecules H_2, D_2, N_2, and O_2.

A more complex problem is encountered in liquids because the transport properties are strongly influenced by molecular

https://doi.org/10.1021/acs.chemrev.1c00218
Chem. Rev. XXXX, XXX, XXX−XXX

interactions, such as electrostatic and dispersion forces, and the hydrodynamic flows induced by moving particles. In many instances, even the sign of the thermodiffusion coefficient D_T cannot be determined from simple arguments.[31] Moreover, the Soret coefficient shows an intricate size dependence. For very small molecules, the coefficients D_T and D carry the same hydrodynamic factor, and the Soret coefficient $S_T = -H/k_BT^2$ is provided by the molecular solvation enthalpy H, which is a purely thermodynamic quantity. However, for colloidal particles and polymers, D_T is independent of the size or molecular weight, and instead, D decreases with the hydrodynamic radius. As a consequence, the Soret coefficient S_T increases with the particle size, and large particles and high polymers accumulate exponentially at the boundary.

If the particles subject to the thermal gradient are charged (Figure 2b), the accumulation of particles at the cold end will also produce a repulsive electrostatic force and therefore electric potential, which pushes the charges back to the hot end. The electric potential difference (ΔV) produced by the temperature difference (ΔT) is known as the Seebeck effect, and the proportionality constant is called the Seebeck coefficient (S):

$$\Delta V = -S\Delta T \tag{4}$$

This Seebeck coefficient, or thermopower, is related to the entropy of charge carriers within a material with a temperature gradient. Carriers move from the hot side of the material (high entropy) to the cold side of the material (low entropy), establishing a steady-state voltage.

2.1. Electron Conductors

In electronic thermoelectric materials, charges are carried by free electrons and holes. At the hot end of the thermoelectric material, the number of free charge carriers is high, and accordingly, the entropy is larger than at the cold end. As a consequence, there is a steady flow of electrons and holes toward the cold end, where they recombine. From a thermodynamic point of view, the corresponding entropy flow from hot to cold drives the thermoelectric effect. In the first approximation, these electrons and holes behave like a gas of charged particles. Hence, their dynamics are described by kinetic theory, for example, in a quasi-classical approximation that keeps quantum statistics but relies on a classical equation of motion for the carriers.[32] In a closed geometry, the Seebeck coefficient is readily obtained from the condition that thermodiffusion and thermoelectric currents cancel each other, $J = \sigma\Delta V - \sigma_T\Delta T = 0$, where the electronic transport is described by the conductivity σ and the thermodiffusion coefficient σ_T. Analogous to the Soret effect discussed above, the Seebeck coefficient is defined as $S = \sigma_T/\sigma$. Whereas σ is always positive, the sign of σ_T depends on whether electrons or holes dominate thermodiffusion. For a more extensive discussion and explanation of the thermodynamic and kinetic models underlying the Seebeck effect, we refer the reader to the following review by Goupil et al.[33]

In a p-doped semiconductor, holes are the majority mobile charge carriers; thus, a positive charge builds up at the cold end, generating a positive potential. Similarly, when electrons are the majority free carriers (n-type material), they will produce a negative potential at the cold end (see Figure 2b, example 1). By convention, the sign of the electronic Seebeck coefficient (S_e) is provided by the potential at the cold side with respect to the hot side, thus indicating the type of majority charge carriers, i.e., electrons or holes, with $S_e > 0$ for p-type semiconductors and $S_e < 0$ for n-type semiconductors.

In a metal, electronic transport properties are intimately related to the electronic band structure and to the density of states at the Fermi level E_F. To determine whether electrons or holes are the majority carriers in an electrical conductor, one needs to look at the density of states $N(E)$ in an energy window k_BT centered at the Fermi level E_F. If $N(E)$ is constant in this range, the electron contribution to the thermodiffusion current cancels that of the holes, $J_e + J_h = 0$, as shown schematically in Figure 3a together with the Fermi−Dirac distribution $f(E) = 1/[e^{(E-E_F)/k_BT} + 1]$. If, on the other hand, the density of states increases with energy, $dN(E)/dE > 0$, there are more carriers with $E > E_F$ than "holes", resulting in a net charge current J. In a closed geometry, this results in a polarization field and a thermoelectric potential with a negative Seebeck coefficient, $S_e < 0$ (Figure 3b). By the same token, if the density of states decreases with energy as in Figure 3c, there are more "hole" carriers below the Fermi level, resulting in a positive Seebeck coefficient $S_e > 0$.

These qualitative considerations can be made rigorous in terms of a Sommerfeld expansion,[32] which results in the Mott formula[34,35]

$$\begin{aligned} S_e(E_F) &= \frac{\pi^2}{3}\frac{k_B}{e}(k_BT)\left[\frac{\partial \ln \sigma}{\partial E}\right]_{E=E_F} \\ &= \frac{\pi^2}{3}\frac{k_B}{e}(k_BT)\left\{\frac{\partial[n(E)]}{n\partial E} + \frac{\partial[\mu(E)]}{\mu\partial E}\right\}_{E=E_F} \end{aligned} \tag{5}$$

This simple expression rationalizes two important features of the thermoelectric effect. First, noting that the last factor is of the order of the inverse Fermi level, one finds $S_e(E_F) \sim (k_B/e)(k_BT/E_F)$, which is smaller, by a factor of k_BT/E_F, than the result from classical Drude theory. Second, the Seebeck coefficient may be observed to have a negative sign, e.g., for bismuth, nickel, and alkali metals, whereas classical theory always predicts $S_e > 0$. These features highlight the quantum nature of the thermoelectric effect.

Organic semiconductors are generally crystalline or amorphous materials with weak intermolecular interactions. This weak coupling leads to narrow electronic bandwidths. Unlike nearly perfect crystals where the electronic states are delocalized, charge carriers in organic semiconductors are usually localized over spatially and energetically distributed transport sites. The widely accepted transport mechanism is that the charge carriers hop from one localized state to another within a lattice of molecular sites. In general, the Seebeck coefficient of conducting polymers varies broadly, ranging from <10 $\mu V\ K^{-1}$ for highly doped polymers up to 1000 $\mu V\ K^{-1}$ for lightly doped polymers. The dramatic reduction of S_e at high doping levels arises from E_F moving into the conduction band where the number of electronic states above and below E_F are equivalent.[36]

2.2. Nonredox-active Electrolyte

Similar to electrons, when ions in an electrolyte are subject to a thermal gradient ∇T (Figure 2b, example 2), they thermodiffuse from the hot side to the cold side, inducing a concentration gradient $\nabla c/c = -S_T\nabla T$ (Soret effect) and an internal electric field $E = -S_i\nabla T$ (Seebeck effect).

These effects result in entropy flow through a nonequilibrium system,[26] and the underlying thermodynamic forces on small ions are provided by gradients of the Massieu−Planck entropy potentials $-\mu_\pm/T$. Because the chemical potentials $\mu_\pm(T,c_\pm)$ depend on both temperature $T(\mathbf{r})$ and concentration $c_\pm(\mathbf{r})$, the thermodynamic forces comprise gradients of both quantities, $f_\pm$

https://doi.org/10.1021/acs.chemrev.1c00218
Chem. Rev. XXXX, XXX, XXX−XXX

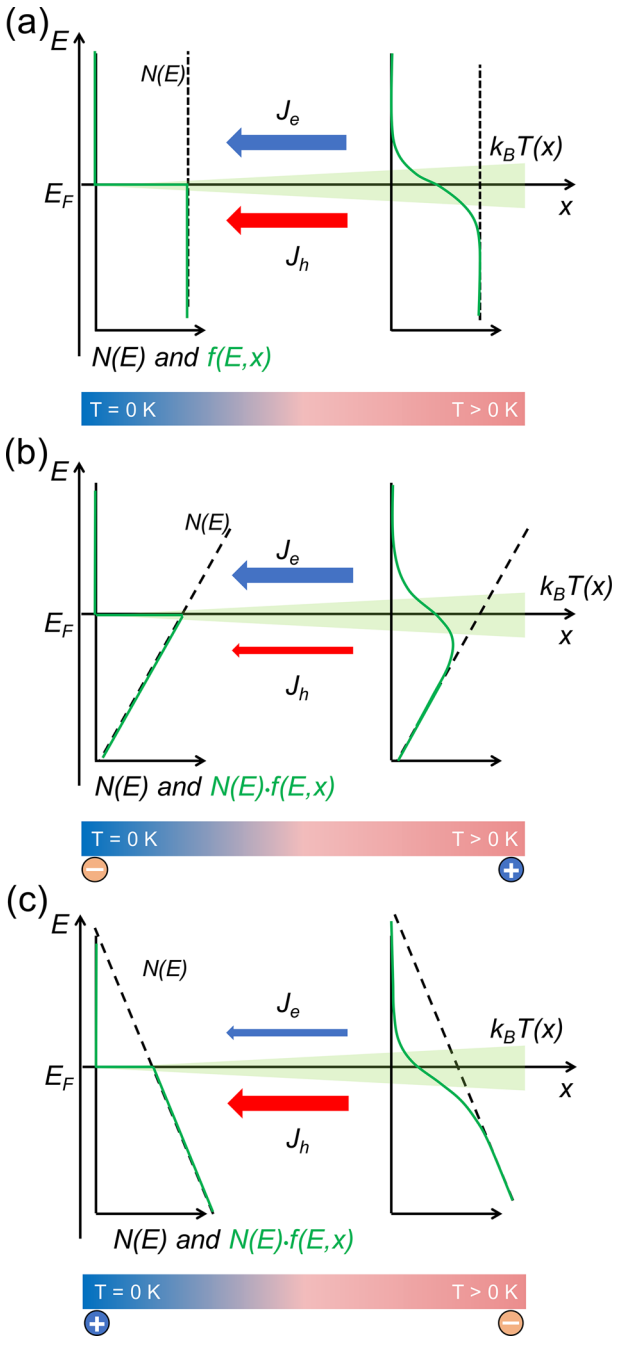

Figure 3. (a) Case of a constant density of states $N(E)$. The left and right sides correspond to the cold and hot ends of the material. The Fermi distribution (green curves) is plotted for the two temperatures ($T = 0$ K and $T > 0$ K). (b) Case of a linearly increasing $N(E)$ with a net electron current and a negative thermopower. (c) Case of a linearly decreasing $N(E)$ that is specific to conductors with a positive Seebeck coefficient.

$= H_\pm \nabla T/T - k_B T \nabla c_\pm/c_\pm$, where the first term drives thermodiffusion with the solvation enthalpy $H_\pm$ and the second term drives the usual gradient diffusion. Imposing zero ion currents and Gauss' law, one readily obtains the steady-state Soret coefficient of the salt solution,[37]

$$S_T = -\frac{H_+ + H_-}{k_B T^2} \tag{6}$$

and the electrolyte Seebeck coefficient,

$$S_i = \frac{H_+ - H_-}{2eT}. \tag{7}$$

Measured ionic enthalpies are generally negative and on the order of k_BT,[38] such that the Soret coefficient is positive. The Seebeck coefficient may take either sign with absolute values on the order of $k_B/e \sim 100\ \mu V\ K^{-1}$. The thermoelectric field often dominates thermophoresis in colloidal suspensions. Because of the different ion enthalpies, the Seebeck field is expected to change its sign upon varying the composition x of mixed electrolytes, such as $NaCl_xOH_{1-x}$.[39] This effect has been confirmed for suspensions of nanomicelles[40] and micrometer-scale colloidal particles,[41] which is in quantitative agreement with the measured enthalpies.[38] As a caveat, note that eq 6 applies to small ions only, the size of which is small compared to the Debye screening length. In regard to ions larger than the Debye length, such as polyelectrolytes, the Seebeck coefficient takes a more intricate form.[42]

Ionic enthalpies arise from complex water−ion interactions that are comprised of electrostatic, dispersion, and hydration forces. To date, there is no satisfactory theoretical framework for calculating enthalpies from first principles. More recently, nonequilibrium molecular dynamics simulations were used to study the Soret coefficient of alkali halide solutions and showed that the ordering of water around alkali cations impacts the Soret coefficient of the salts[43] and that the thermal polarization of free water affects the thermoelectric behavior of the solution.[44]

Experimentally, the S_i of a nonredox-active electrolyte sandwiched between two electrodes is defined as the ratio between the open-circuit potential (ΔV) and the ΔT between the hot and cold sides (compared to the ionic Seebeck coefficient, the Seebeck coefficient of the metal electrodes is small ($<10\ \mu V\ K^{-1}$) and can be neglected). A survey of nonredox-active electrolytes of interest for ionic thermoelectric applications is presented in section 4.

2.3. Redox-active Electrolyte

When the electrolyte subjected to the thermal gradient is also redox active, it undergoes an electrochemical reaction at the hot and cold electrodes (Figure 2b, example 3):

$$Ox + e^- \rightleftharpoons Red \tag{8}$$

Upon electron transfer, the reaction releases or requires free energy (ΔG) expressed as entropic (ΔS) and enthalpic (ΔH) contributions:

$$\Delta G = \Delta H - T\Delta S \tag{9}$$

As a consequence, the concentrations satisfy the mass action law:

$$n_{ox} = e^{-\Delta G/k_BT} n_{red} = \varphi^{-1} n_{red} \tag{10}$$

The temperature difference at the electrodes results in a spatial variation of the fugacity φ, which in turn imposes gradients of oxidant and reductant,

$$\nabla n_{ox} = \varphi^{-1}\nabla n_{red} + \varphi^{-1} n_{red} \frac{\Delta H}{k_B T} \frac{\nabla T}{T} \tag{11}$$

In addition to eq 10, the stationary state satisfies the condition of zero current of each ion species $J_i = 0$, and Gauss's law. Proceeding as in ref 45, one finds a potential difference between hot and cold electrodes, $\Delta V_{redox} = -S_{redox}\Delta T$, where the Seebeck coefficient is given by the reaction enthalpy:

https://doi.org/10.1021/acs.chemrev.1c00218
Chem. Rev. XXXX, XXX, XXX−XXX

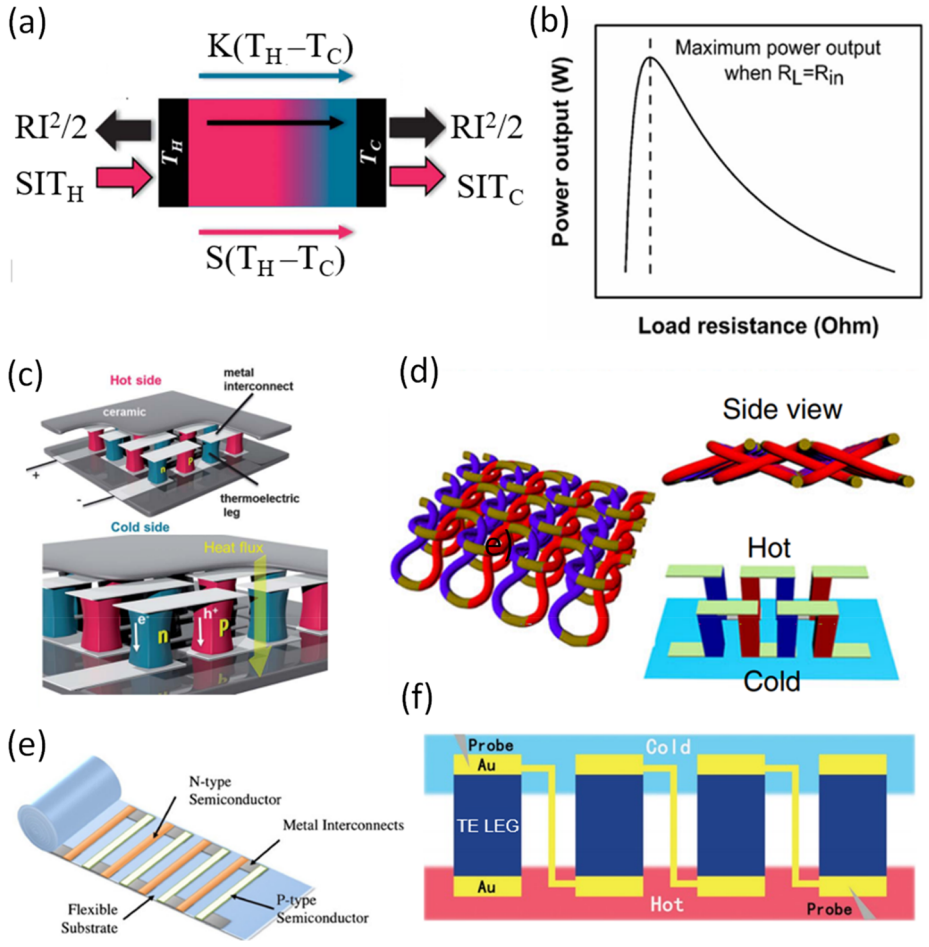

Figure 4. (a) Sketch of the different thermal energy fluxes passing through a thermoelectric leg subjected to a temperature gradient. Adapted with permission from ref 49. Copyright 2012 Royal Society of Chemistry. (b) Representation of a standard power output vs load resistance for TEG. (c) Classical thermoelectric modules, based on n- and p-legs, interconnects, and ceramic plates. Reproduced with permission from ref 49. Copyright 2012 Royal Society of Chemistry. (d) Woven-yarn structure to integrate TEG into textile for fibers. Reproduced with permission from ref 50. Copyright 2020 Nature. (e) Sketch of a planar thermoelectric module on a flexible substrate. Reproduced with permission from ref 51. Copyright 2011 IOP. (f) Unipolar thermoelectric generator, with a planar structure. Reproduced with permission from ref 47. Copyright 2017 Royal Society of Chemistry.

$$S_{redox} = \frac{\Delta H}{eT} \tag{12}$$

Taking the sum of the thermodiffusion and redox contribution, we have:

$$S = S_i + S_{redox} \tag{13}$$

As a caveat, we note that the two terms are not additive in general.

3. THERMOELECTRIC DEVICE CONCEPT

3.1. Thermoelectric Generators (TEGs)

The fundamental element of a TEG is a thermocouple consisting of p-type and n-type TE material that are connected electrically in series and thermally in parallel, having an internal electrical resistance ($R_{pn} = R_p + R_n$, without considering the metallic electrical interconnections) and subjected to a temperature gradient $\Delta T = T_H - T_C$. Assuming that heat propagates from the hot to the cold side only through the thermocouple, then the losses through the metal contacts, due to their high thermal conductivity, can be neglected. This configuration is exploited to maximize the electrical output by creating a unidirectional charge flow inside the device by summing the thermovoltage contributions from the two materials ($S = S_p - S_n$). The thermal energy flow consists of three contributions (Figure 4a): (i) the rate of Peltier heat absorbed from the hot side due to the thermogenerated current I ($Q_{Peltier} = ST_HI$), (ii) the Joule heating emanating at the hot side due to the thermogenerated current I ($Q_{Joule} = {}^1/_2I^2R$), and (iii) the heat flux crossing the leg ($K\Delta T$) in the absence of an electrical current (K is the thermal conductance of the thermocouple). At the hot junction, the thermal input power can be expressed as:

$$Q_H = ST_HI - \frac{1}{2}RI^2 + K(T_H - T_C) \tag{14}$$

The electrical power output of the TEG when the current passes across a load resistance (R_L) is:

$$P = VI \tag{15}$$

with an open-circuit voltage:

$$V = S\Delta T \tag{16}$$

and a current:

$$I = S\Delta T/(R + R_L) \tag{17}$$

The efficiency Φ of the TEG is the ratio between the electrical power output P and the thermal power input Q_H:

https://doi.org/10.1021/acs.chemrev.1c00218
Chem. Rev. XXXX, XXX, XXX−XXX

$$\Phi = \frac{S\Delta TI}{(ST_H I - \frac{1}{2}RI^2 + K\Delta T)} \tag{18}$$

By adjusting the dimensions of the thermocouple elements, it is possible to match the internal resistance R_{pn} and the load resistance R_L. Thus, the maximum efficiency Φ_{max} can be written as[46]

$$\Phi_{max} = \frac{\Delta T}{T_H} \frac{\sqrt{1+ZT} - 1}{\sqrt{1+ZT} + T_C/T_H} \tag{19}$$

$$Z = \frac{S^2}{K_{pn}R_{pn}} \tag{20}$$

where ZT is the dimensionless figure-of-merit for the thermocouple and expresses the conversion efficiency of the thermocouple. From this parameter, another parameter (zT) has been derived, which is based on the thermoelectric properties of a single material (S, k, σ):

$$zT = \frac{\sigma S^2}{k} T \tag{21}$$

The regimes of operation at maximum efficiency and maximum power output differ. At maximum power, the external load resistance equals the internal resistance of the device $R_L = R_{pn}$ (Figure 4b). The output voltage is half of the open-circuit voltage $V = V_{oc}/2$, so that the maximum power generated is:

$$P_{max} = \frac{V_{oc}^2}{4R} = \frac{S^2(T_H - T_C)^2}{4R} \tag{22}$$

The Seebeck voltage produced by a single thermocouple is too small ($S \sim 200\ \mu V\ K^{-1}$) to power any application; therefore, to reach suitable power outputs, the strategy is to connect multiple thermocouples electrically in series and thermally in parallel in a high-density configuration to maximize the power extraction per unit area. Finally, the thermoelectric module is sandwiched between ceramic plates to ensure good thermal exchange with the surroundings and to avoid short circuits between the metal contacts. The design of OTEGs varies in shape and size. In addition to the typical vertical geometry, which includes bulky pellets of active materials, OTEGs can also be manufactured as flat plates for thin films or woven-yarn textiles for fibers (Figure 4d,e). Using only one thermoelement, unipolar OTEG can sometimes be fabricated (Figure 4f).[47,48] Moreover, OTEG can be manufactured by low-cost, low-temperature, and large-area techniques such as printing and drop casting.

3.2. Thermogalvanic Cells (TGCs)

A thermogalvanic cell consists of two electrodes at different temperatures in contact with an electrolyte containing a redox couple. The redox electrolyte contains the reductant (red) and the oxidant (ox) of one electrochemical half-reaction. Importantly, the electron transfer of this half reaction at the electrode must be reversible. As illustrated in Figure 5, the thermogalvanic cell is an electrochemical thermoelectric generator that produces a difference in electric potential when a temperature gradient is set across the two electrodes. Because the redox electrolyte will transport an electric current through molecular shuttles by convection, diffusion, and migration between the two electrodes, a constant power can be extracted by connecting two electrodes to an external R_L.[52]

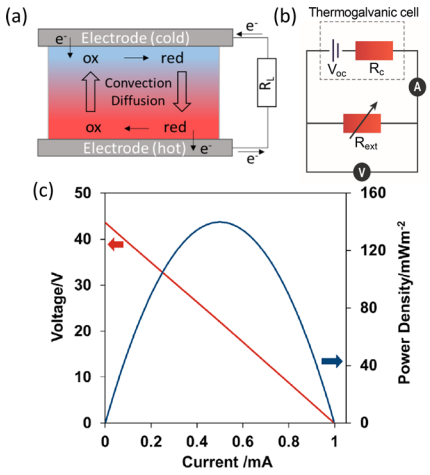

Figure 5. (a) Schematic diagram and (b) equivalent circuit of a typical thermogalvanic cell. (c) $I-V$ and $P-V$ curves of a thermogalvanic cell. Reproduced with permission from ref 52. Copyright 2018 Linköping University Press.

The equivalent electrical circuit of a TGC (Figure 5b) is a generator composed of an ideal potential source (Seebeck voltage) in series with an internal resistance R. The current–voltage characteristics follow that of a Thevenin generator:

$$V = V_{oc} - RI \tag{23}$$

$$V_{oc} = -S_{redox}\Delta T \tag{24}$$

The internal resistance is provided by the slope of the $I-V$ characteristic, while the intercept with the V-axis is the open-circuit voltage V_{OC}, and the intercept on the I-axis is the short-circuit current I_{SC} (Figure 5c). The power varies quadratically with the thermogenerated current (Figure 5c):

$$P = VI = V_{oc}I - RI^2 \tag{25}$$

The conditions for maximum power are found on the $I-V$ characteristics as the largest area under a rectangle determined by the point $(I_{SC}/2, V_{OC}/2)$:

$$P_{max} = \frac{V_{oc}I_{sc}}{4} \tag{26}$$

The maximum power corresponds to a choice of load resistance that is equal to the internal resistance (eq 24 and eq 16). Three types of resistive phenomena contribute to the internal resistance: (i) mass transfer resistance, (ii) ohmic resistance, and (iii) charge transfer resistance.[53−55] The ohmic resistance originates from the resistance due to the electrical connections to the external circuit, the bulk electrolyte resistance, and the electrode resistance. Often, the dominant phenomenon is the ionic resistance of the electrolyte (R_I):

$$R_I = \frac{L}{A\sigma} \tag{27}$$

where A is the cross-sectional area defined by the geometry of the two electrodes, and L is the separation distance of the two electrodes. For noninteracting ions, the ionic conductivity σ is approximated by:

$$\sigma = \frac{F^2}{RT} \sum_i D_i c_i z_i^2 \tag{28}$$

https://doi.org/10.1021/acs.chemrev.1c00218
Chem. Rev. XXXX, XXX, XXX−XXX

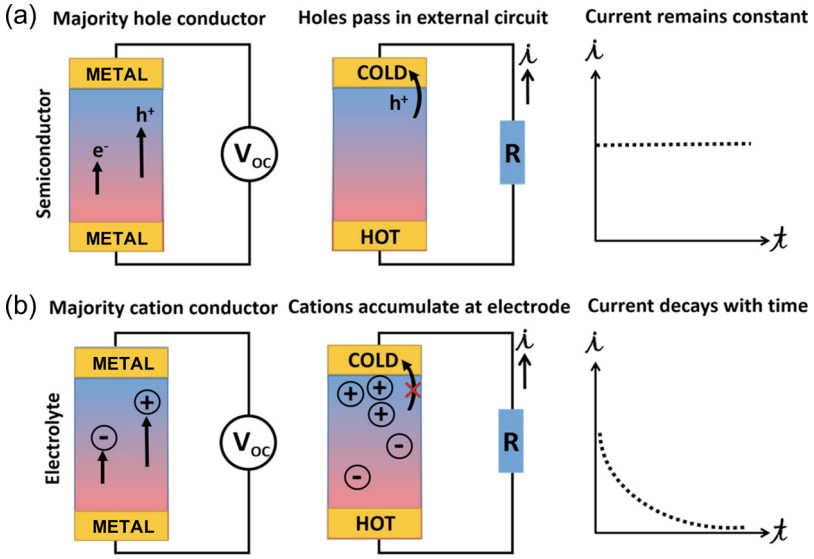

Figure 6. Thermoelectric effects with (a) electronic charge carriers (electrons or holes) in a semiconductor and (b) ionic charge carriers in an electrolyte. Reproduced with permission from ref 64. Copyright 2017 Wiley-VCH.

where D_i is the diffusion coefficient of ion i, c_i is the ionic concentration, and z_i is its charge.

Hence, reducing the internal resistance is possible by increasing the concentration of the redox electrolyte and increasing the diffusion coefficient. In the Stokes−Einstein model, the ionic diffusion coefficient is a function of the viscosity γ of the solvent and the hydrodynamic radius r_H of the ions:

$$D = \frac{k_B T}{6\pi\gamma r_H} \tag{29}$$

where k_B is the Boltzmann constant and T is the absolute temperature. Hence, small, solvated ions in a low viscosity solvent are two factors minimizing the internal resistance of the TGCs.

The rate of the electron transfer reaction at the electrode/electrolyte interface is related to the exchange current, I_0, which is characterized by the charge transfer resistance R_{CT}:

$$R_{CT} = \frac{RT}{AnF|I_0|} \tag{30}$$

where A is the area of the electrode and R is the gas constant. The exchange current is provided by the Butler−Volmer expression of the electrochemical current (Tafel equation):

$$\ln(I) = \ln(I_o) - \frac{\alpha n F \eta}{RT} \tag{31}$$

where η is the overpotential and α is the charge transfer coefficient. R_{CT} can be as small as 1 Ω in a good TGC, e.g., the electron transfer at the platinum electrode for a ferric/ferrocyanide redox couple in salted water.[56]

The mass transport resistance, i.e., the transport of reactants from the solution to the electrode is governed by three main processes (migration, diffusion, and convection) that limit the current I_{lim}:[55]

$$R_{mt} = \frac{RT}{nF|I_{lim}|} \tag{32}$$

If the steady-state current $|I_{lim}|$ is limited by the diffusion of reactants, it can be written as:

$$I_{lim} = \frac{nFADc}{\delta} \tag{33}$$

where D is the diffusion coefficient of the electroactive species, A is the active electrode area, c is the concentration of the redox species, and δ is the thickness of the diffusion layer at the electrode, which theoretically is the maximum of the interelectrode distance. In practice, δ is smaller than the interelectrode distance because of convection.[55]

The thermoelectric figure-of-merit ZT (eq 19) cannot provide a simple expression for thermogalvanic cells because several resistive contributions might limit the thermogenerated current. Because those contributions can be seen in series, depending on the geometry of the cell and its constituents (electrolyte, redox species, electrode), one resistive contribution can be dominant, and a simplified expression can be extracted. In many cases, the R_{mt} is larger than (i) R_I with high salt and redox couple concentrations and (ii) R_{CT} using conventional metal electrodes. In that case, Abraham et al. proposed the following expression:[55]

$$ZT^* = \left(\frac{z^2F^2}{R}\right) S_{redox}^2 \frac{D_{lim} c}{\kappa} \tag{34}$$

where z is the charge of the ion, F is the Faraday constant, D_{lim} is the limiting diffusion coefficient, c is the concentration of the redox couple, κ is the thermal conductivity, and R is the gas constant. The power conversion efficiency is the ratio between the output electric power and the input thermal power in the thermogalvanic cell:

$$\Phi = \frac{\text{electrical power}}{\text{thermal power}} \tag{35}$$

The input thermal power depends on the geometry of the cell defining the thermal conductance but also the thermal contact between the various materials and the thermal conductivity of each material (ceramic, metal, electrolyte, separator). By neglecting the small thermal contributions, the rate of heat flow from the hot electrode to the cold electrode is dominated by the heat transport through the electrolyte and the rate of heat transfer induced by the electrochemical current.[57]

https://doi.org/10.1021/acs.chemrev.1c00218
Chem. Rev. XXXX, XXX, XXX−XXX

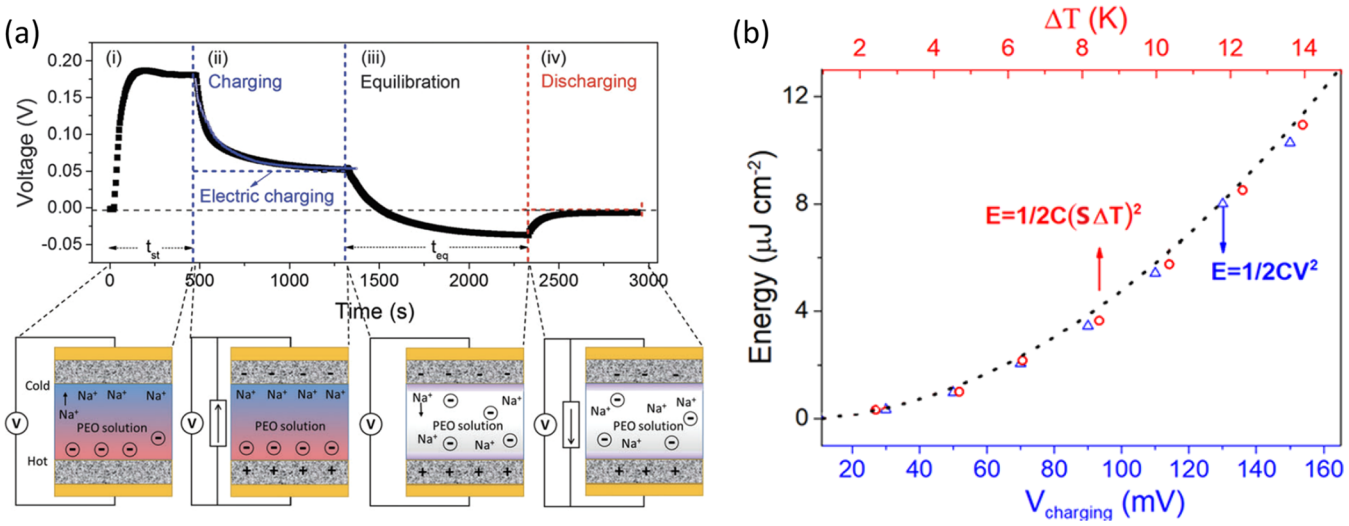

Figure 7. (a) Full charge and discharge cycle of the ionic thermoelectric supercapacitor (ITESC). (i) Establishing an ionic thermovoltage while a ΔT is applied to the device, (ii) thermoelectric charging of the supercapacitor, (iii) cooling to reach equilibrium at $\Delta T = 0$, and (iv) discharging. (b) Electrical energy stored in a supercapacitor upon either electrical charging with an external applied $V_{charging}$ or thermoelectric charging (temperature gradient) through the electrolyte of the supercapacitor. Reproduced with permission from ref 24. Copyright 2016 The Royal Society of Chemistry.

$$\frac{dQ}{dT} = kA\frac{\Delta T}{d} + \frac{IT\Delta S}{nF} \tag{36}$$

where k is the thermal conductivity of the electrolyte, A is the electrode cross-sectional area, ΔT is the temperature gradient between the two electrodes separated by a distance d, I is the cell current, and ΔS is the entropy of the cell reaction. In practice, the second term can be neglected because it is only a few percent of the total expression. Within these approximations, the total efficiency at maximum power is written as:[54,58]

$$\Phi = \frac{V_{oc}I_{SC}}{4KA\frac{\Delta T}{d}} \tag{37}$$

where I_{SC} is the short-circuit current limited by the most resistive phenomena (R_{ET}, R_I, or R_{mt}). To compare the efficiency Φ of different devices working at different temperatures (T_H is the hot electrode temperature), the relative conversion efficiency Φ_r is determined as the ratio of the total efficiency to the Carnot efficiency Φ_C.

$$\Phi_r = \frac{\Phi}{\Phi_C} \tag{38}$$

$$\Phi_c = \frac{\Delta T}{T_H} \tag{39}$$

For the redox couple ferric/ferrocyanide and a flat platinum electrode, Φ_r is approximately 0.50%.[59,60] Increasing the surface area of the electrodes is a strategy to increase efficiency. Indeed, multiwalled carbon nanotube electrodes[61] achieve Φ_r = 1.4%, while electrodes made of composites of single-walled carbon nanotubes and reduced graphene oxide electrodes reach Φ_r = 2.6%;[62] finally, platinum nanoparticle-decorated carbon aerogel electrodes reach a record high efficiency of 4.0%.[63]

3.3. Ionic Thermoelectric Supercapacitors

While ions can diffuse along the temperature gradient as electronic charge carriers, they cannot pass through a metal electrode to generate an external current (as illustrated in Figure 6). Instead, ions will accumulate at the interface between the metal electrodes and the electrolyte acting as an electric double layer (EDL), which induces a transient current; additionally, the charge stored in EDL capacitors can be represented by integrating the current.[64,65] Therefore, the ionic thermoelectric effect is not suitable for typical thermoelectric generators under continuous operation. Alternatively, when using high capacitance electrode materials, such as carbon nanotubes and conductive polymers, the amount of accumulated charge can be greatly enhanced, and electrical energy can be harvested by charging supercapacitors (the so-called ionic thermoelectric supercapacitor ITESC)[24,66,67] or batteries. In this way, thermal energy is converted into stored electrical energy through the ionic thermoelectric effect and can be consumed upon discharging.

The basic operational protocol of an ITESC is illustrated in Figure 7a.[24] (i) First, a ΔT is established between the two electrodes separated by an electrolyte, and after a certain stabilization time (t_{st}), a thermovoltage reaches $V_{thermo} = S_i\Delta T$. (ii) The two electrodes are connected through a load resistance and V_{thermo} charges the supercapacitor. The charge Q_{ch} stored at the electrodes of the ITESC can be obtained by integrating the current during charging. (iii) When the device is fully charged, the external load resistance is disconnected (open circuit), and the heat source is turned off. The thermovoltage decays to zero without ΔT, and the open-circuit potential is mainly dependent on the stored charge at the electrode/electrolyte interface. (iv) Finally, the device is discharged by connecting the two electrodes through an external circuit. The amount of charge Q_{dis} equals the integration of the discharge current. Ideally, the maximum stored electrical energy is described as:

$$E_{ch} = \frac{1}{2}CV_{thermo}^2 = \frac{1}{2}C(\Delta TS_i)^2 \tag{40}$$

which quadratically increases with the Seebeck coefficient of the material. Figure 7b displays the electrical energy stored in a supercapacitor versus both voltage in the case of electrical charging and temperature in the case of thermoelectric charging. An ITESC is suitable for harvesting energy from intermittent heat sources, namely, the sun. During the daytime, ITESCs can be charged by being heated by the sun, and during the night, the stored electrical charge can be utilized by discharging the device.

https://doi.org/10.1021/acs.chemrev.1c00218
Chem. Rev. XXXX, XXX, XXX−XXX

Recently, Kim et al. developed an ITESC with a polystyrene sulfonic acid (PSSH) electrolyte and observed almost no leakage current, showing that the stored electric energy could be maintained for more than 24 h.[66] As the temperature changes, the equilibrium condition at the solid−liquid interface is disrupted, and the ion density varies, affecting the interfacial potential. The role of the electrode material work function[68] was systematically studied: by changing the temperature, the charge motion creates a varying potential difference across the double layer at the electrode−electrolyte interface such that a direct relationship between temperature sensitivity and work function of electrode potential could be shown. In addition, other studies were conducted to investigate the role of ion concentration[69] and ion size:[70] the results showed that the ions size is the main factor affecting the voltage generation (the bigger the ion, the lower the voltage generated for the same ΔT), while the ion concentration seemed to play a secondary role.

The efficiency of the heating−cooling cycle in ITESCs could be derived from the ratio of the produced electrical energy and the thermal energy passing through the device.[64] The maximum charging efficiency ($\Phi_{\Delta T\mathrm{ch}}$) of an ITESC can then be expressed as:

$$\Phi_{\Delta T\mathrm{ch}} = \frac{\Delta T}{2T_\mathrm{H} + \frac{10\kappa}{\sigma_i S_i^2} - \frac{1}{2}\Delta T} \tag{41}$$

The maximum charging efficiency is closely related to the key material parameters, i.e., σ_i, S_i, and k, which are gathered to define the ionic thermoelectric figure-of-merit of an electrolyte zT_i:

$$zT_i = \frac{\sigma_i S_i^2}{k} T \tag{42}$$

Similar to classic electronic materials, the efficiency will increase for electrolytes with high ionic conductivity and Seebeck coefficient and low thermal conductivity. They also directly derived Φ_ch based on ZT_i:

$$\Phi_\mathrm{ch} = \frac{\Delta T}{T_\mathrm{H}} \frac{ZT_i}{2ZT_i + \frac{10T}{T_\mathrm{H}} - \frac{1}{2}ZT_i\frac{\Delta T}{T_\mathrm{H}}} \tag{43}$$

Compared with electronic thermoelectric materials, electrolytes have a higher Seebeck coefficient and lower thermal conductivity. However, because of their relatively low ionic conductivity, the zT_i values and efficiencies are lower than those of good electronic thermoelectric materials (Figure 8a). Note that the efficiency evaluation here only considers the charging process and neglects the heat used to warm up the materials, which is proportional to the mass and heat capacitance of the electrodes and electrolyte. In a first approximation, this contribution to thermal energy is assumed to be similar for an ITESC and for a supercapacitor that is charged by a TEG. Importantly, the comparison of zT between an electronic conductor and an ionic conductor has meaning only if the electronic conductor is considered for a TEG coupled in series with a supercapacitor. Indeed, this circuit is an equivalent circuit of an ITESC. Despite the relatively low efficiency of ITESC, it shows one key advantage compared to a TEG coupled with a supercapacitor. At comparable temperature differences, electronic thermoelectric materials having good performances (e.g., Bi_2Te_3 alloys) possess a lower Seebeck coefficient (~200 μV K^{-1}) than ionic thermoelectrics (up to 10000 μV K^{-1}). As a result, the stored energy in the same supercapacitor (C = 1 mF)

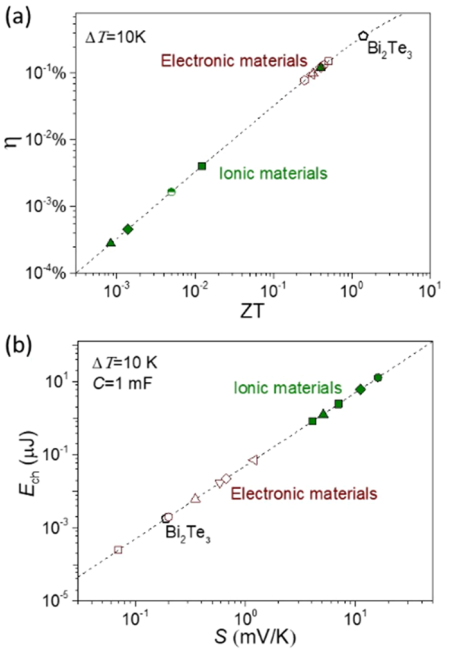

Figure 8. (a) Efficiency vs zT of typical electronic and ionic thermoelectric materials (ΔT = 10 K). (b) Stored energy in a supercapacitor with a capacitance of 1 mF as a function of the Seebeck coefficient of different thermoelectric materials at ΔT = 10 K. Adapted with permission from ref 64. Copyright 2017 Wiley-VCH.

charged by ionic thermoelectric materials is many orders of magnitude larger than that charged with an electronic material, as illustrated in Figure 8b.

4. STATE-OF-THE-ART MATERIALS

4.1. Organic TE Materials

The versatile chemical synthesis, low-cost solution processability, and exclusive mechanical robustness endow organic conductors with broad appeal in thermoelectric applications. However, the limited solubility of organic conductive materials is typically a drawback with regard to building vertical legs (thickness of 10−100 μm) in the traditional architecture of a thermoelectric module. One must also consider the anisotropy of charge transport in organic materials, especially in the electrical conductivity where the difference between the in-plane/cross-plane σ can reach very high values (10^5 S cm^{-1} in PEDOT:PSS).[71] Processing powder into the shape of pellets, such as typically employed for inorganics, is of course a possible alternative.

Despite their low solubility, solution-processable organic conductors can form thin films, which provide new opportunities by enabling the design of OTEGs in various shapes and sizes, e.g., flat plates for thin films or woven-yarn textiles for fibers.[72] Ultimately, OTEGs can be manufactured by low-cost, low-temperature, and large-area techniques, such as printing and drop casting. Although the power density is relatively low, OTEGs provide the possibility for a variety of novel low-power applications.[73] Because the main effort in OTEGs is to optimize the thermoelectric properties of materials, we review the milestones with regard to material development and understanding.

The molecular structures of some typical organic electronic (semi)conductors explored for thermoelectric applications are shown in Figure 9. The performance of materials with a zT value

https://doi.org/10.1021/acs.chemrev.1c00218
Chem. Rev. XXXX, XXX, XXX−XXX

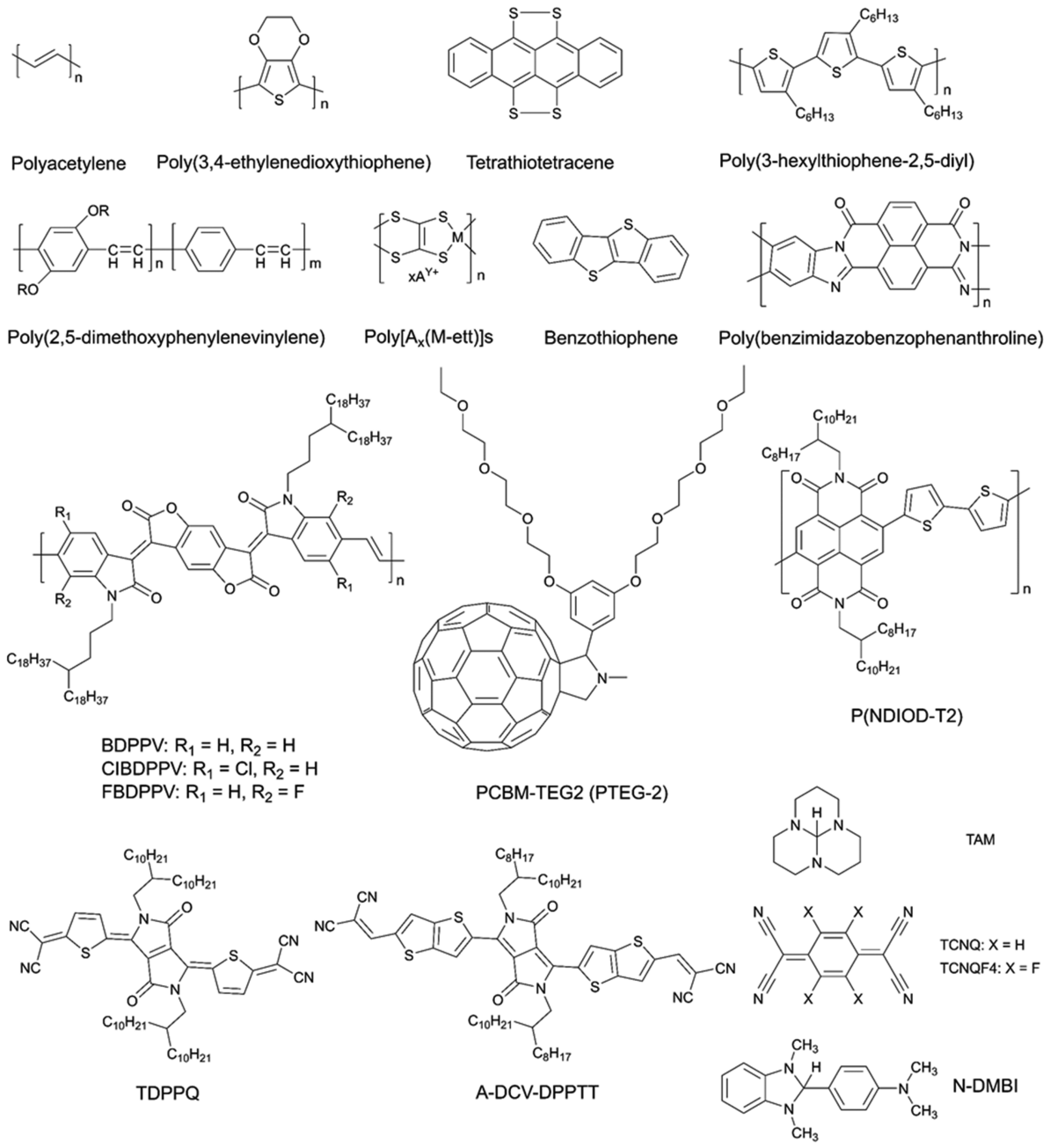

Figure 9. Chemical structures of the typical conductors and dopant molecules used in OTEGs.

larger than 0.1 or a *PF* larger than 100 μW m^{-1} K^{-2} are summarized in Table 1.

4.1.1. p-Type TE Polymers. Since high conductivity was discovered in I_2-doped polyacetylene (PA), many different conducting polymers, such as polypyrrole (PPy), polythiophene (PTh), polyaniline (PANi), and poly(3,4-ethylenedioxythiophene) (PEDOT), have been designed and synthesized, spurring the development of organic electronics.[100−111] Typically, conducting polymers have relatively low thermal conductivity (0.1−0.7 W m^{-1} K^{-1}). Thus, they are expected to be good candidates for organic thermoelectric applications if their Seebeck coefficient can be improved in their highly conducting state. Because conducting polymers are typically formed as thin films (<1 μm in thickness), it is experimentally challenging to accurately measure their out-of-plane thermal conductivity. For that reason, not all polymers are fully characterized. However, the numerator of *zT*, which is the power factor (*PF*), enables the first comparison of the thermoelectric performance of various polymers:

$$PF = \sigma S^2 \tag{44}$$

The conductivity, Seebeck coefficient, and thermal conductivity of a conductive polymer are interrelated and each exhibit a different dependence on carrier density. Hence, the maximum *zT* is usually found for a specific carrier density. Other parameters also affect the transport properties, such as the regioregularity of the polymer chains[112] and the distribution of molecular weight,[113] which depend on the chemical synthesis, molecular disorder, nanomorphology obtained upon film formation, and fabrication methods.[88]

4.1.1.1. Doping/Dedoping. The use of chemical doping for the optimization of OTE materials dates back to as early as 1980,

https://doi.org/10.1021/acs.chemrev.1c00218
Chem. Rev. XXXX, XXX, XXX−XXX

Table 1. Summary of Reported Organic Thermoelectric Materials with *PF* Values above 50 μW m^{-1} K^{-2} or *zT* Values above 0.1.

materials	doping/treatment	S (μV K^{-1})	σ (S cm^{-1})	PF (μW m^{-1} K^{-2})	k (W m^{-1} K^{-1})	zT[a]	ref
		P-type					
PA	I_2	28.4	11110	900			74
PA	$FeCl_3$	15.3	7530	180			74
PEDOT:Tos	TDAE	200	80	324	0.34	0.25	10
PEDOT:Tos	DMF	55	1500	454			75
PEDOT-Tos-PP		117	923	1270			76
PEDOT	BTFMSI	~37	~1070	147	0.19	0.22	77
PEDOS-C6		103	335	354.7			78
PEDOT:PSS	EG	62	900	350	0.37	0.28	79
PEDOT:PSS	EG/DMSO	73	880	469	0.33	0.42	79
PEDOT:PSS	TSA/DMSO N_2H_4/DMSO	49.3	1310	318.4	0.3	0.31	80
PEDOT:PSS/Te nanorod (NR)		163	19.3	70.9	0.22−0.30	0.1	81
PEDOT:PSS	HNO_3/PEIE	32	2700	168			82
PEDOT/Bi_2Te_3		~165	~500	1350	0.7	0.58	83
P3HT	TCB	~50	320	62.4	0.23	~0.1 (365 K)	84
P3HT		56	509	160			85
P(EtOPV-*co*-PV)	$Mo(tfdCOCF_3)_3$	47	349	78			86
$(BTBT)_2AsF_6$		15	4100	88			87
PBTTT	F_4TCNQ	42	670	120			88
PBTTT	$FeCl_3$	9.4	2 10^5	~2000			89
PANi/Te NR		102	102	105	0.21	0.156	90
PDPP-$g_32T_{0.3}$	$FeCl_3$	56	360	110			91
		N-Type					
poly[K_x(Ni-ett)]		−151.7	64	147	0.31	0.20 (440 K)	92
poly[K_x(Ni-ett)]	electrochemical	~-150	~310	~670	0.84	0.32 (400 K)	93
Ni NR/PVDF		−27	3000	220	0.55	0.15 (380 K)	94
PTEG-2	N-DMBI	~-250	~13	~80	<0.1	0.3 (393 K)	95
UFBDPPV	TAM	−198	22.5	80			96
FBDPPV	TAM	−32	21	51			97
TDPPQ	Bi	−585	3.3	113		0.23 (333 K)	98
A-DCV-DPPTT	N-DMBI	−666	4.9	217	0.34	0.23 (373 K)	99

[a]The temperature for the summarized *PF* or *zT* values is room temperature unless otherwise stated.

when the Seebeck coefficient of undoped trans-PA was measured (equal to 900 ± 50 μV K^{-1}). Indeed, the possibility of reaching electrical conductivities exceeding 45000 S cm^{-1} in heavily doped PA films represents an interesting opportunity for the development of a new family of thermoelectric materials.[114,115] The reported maximum *PF* of PA is as high as 900 μW m^{-1} K^{-2} when doped with iodine and 180 μW m^{-1} K^{-2} when doped with $FeCl_3$.[74,116] However, the application of PA as a thermoelectric material has been limited by its insolubility and poor stability in air and even in an inert atmosphere.

A major breakthrough in organic thermoelectrics was made in 2011 by Crispin et al.,[10] in which PEDOT-Tos was chemically polymerized by using iron(III) tris-*p*-toluenesulfonate as the oxidant; the resulting film had a conductivity as high as 300 S cm^{-1} and a moderate Seebeck coefficient (40 μV K^{-1}) at room temperature. The oxidation state of the polymer was altered through reduction with strong amines such as tetrakis-(dimethylamino)ethylene (TDAE) in an inert atmosphere, yielding *PF* values that ranged from 38 μW m^{-1} K^{-2} for the pristine doped polymer to 324 μW m^{-1} K^{-2} at an optimum oxidation level of 22% (Figure 10a). With a lateral thermal conductivity of 0.37 ± 0.07 W m^{-1} K^{-1} measured through the 3ω technique, the *zT* value of PEDOT-Tos reached 0.25 (Figure 10b). Furthermore, the PEDOT-Tos films were stable in air at the optimum oxidation level. A vertically structured prototype of a completely organic TEG with 55 legs was made, in which the n-legs were composed of a blend of TTF-TCNQ in PVC, and the p-legs were vapor-polymerized PEDOT-Tos. At a ΔT of 10 K, the extrapolated power density was 0.128 μW cm^{-2}. Recently, Villalva et al. investigated poly(ethyleneimine)-ethoxylate (PEIE) as work function modification agent for nitric acid (HNO_3) doped PEDOT:PSS as well as an encapsulation agent, preventing HNO_3 evaporation from the PEDOT:PSS film:[82] indeed the presence of PEIE contributed to avoid the drop of electrical conductivity after air exposure by forming a barrier preventing the escape of nitric acid from the PEDOT film. In addition, PEIE ethoxy groups enhance charge carrier extraction through the modification of PEDOT work function, which, together with the lower ordering in the PEIE-coated films, might be responsible for the increase in *S*: the result is an increase in *PF* from 72 to 168 μW m^{-1} K^{-2}. Other examples of doping/dedoping processes, especially regarding PEDOT:PSS, to optimize both *S* and σ can be found in literature achieving high *PF* (>100 μW m^{-1} K^{-2}), showing that the tuning of the doping level is a crucial strategy to maximize the TE properties of organic semiconductors.[76−80]

In addition to chemical doping, the oxidation level of conducting polymers can be easily tuned by electrochemical doping/dedoping processes.[117] This fine-tuning of the electronic properties of a polymer allows theoretical studies to be carried out to obtain a better understanding of the doping effects from a molecular level, which can guide the future development of OTE materials.[118] We send the reader to other reviews covering all of this progress in detail.[119−123]

https://doi.org/10.1021/acs.chemrev.1c00218
Chem. Rev. XXXX, XXX, XXX−XXX

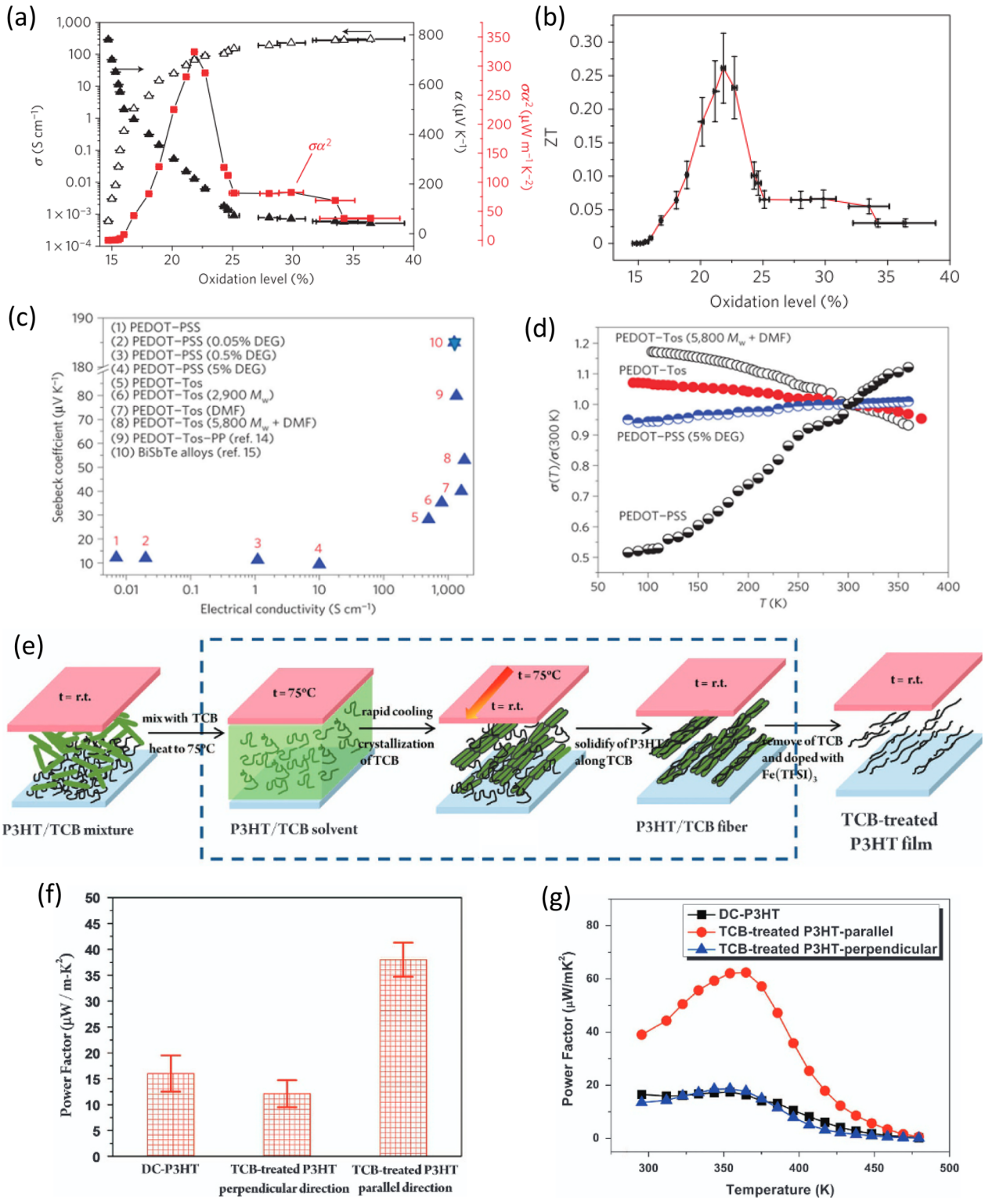

Figure 10. (a) Electrical conductivity, Seebeck coefficient, and *PF* and (b) *zT* of PEDOT:PSS at different oxidation levels after TDAE treatment. (a–b) Reproduced with permission from ref 10. Copyright 2011 Nature. (c) Seebeck coefficient vs electrical conductivity of different PEDOT derivatives and (d) Temperature dependence of electrical conductivity (normalized to 300 K) for the different PEDOT-Tos and PEDOT-PSS samples. (c–d) Reproduced with permission from ref 75. Copyright 2014 Nature. (e) Scheme of the morphology of TCB-treated P3HT films, and *PF* of TCB-treated P3HT films vs (f) the measurement direction and (g) temperature. (e–g) Reproduced with permission from ref 10, 75, and 84. Copyright 2016 Nature.

4.1.1.2. Morphology Control. Upon solvent evaporation and film formation, conducting polymers do not form single crystal structures, but instead form amorphous, paracrystalline, or semicrystalline structures. Charge carrier transport, dominated by interchain coupling, is therefore dramatically affected by the morphology of the film. Moreover, chemical defects, including twisted and kinked chains, are responsible for decreasing intrachain charge carrier mobility. Hence, the higher purity

https://doi.org/10.1021/acs.chemrev.1c00218
Chem. Rev. XXXX, XXX, XXX–XXX

and crystallinity are expected to improve the TE properties. Regarding PEDOT:PSS, for example, treatment with high boiling point solvents, such as dimethyl sulfoxide (DMSO) and ethylene glycol (EG), results in greatly improved electrical conductivities and $zT > 0.1$, with record values of zT estimated to be 0.42 at room temperature (note: thermal conductivity was measured in the out-of-plane direction, while σ and S were measured in the in-plane direction).[79] The use of these solvents, in a process that is typically referred to as secondary doping, enhances the conductivity of the PEDOT:PSS film by removing the excess PSS and assisting the formation of an interconnected three-dimensional PEDOT network.

This morphology optimization of PEDOT-based conductors leads to the observation that the highly doped conducting polymer shows semimetallic character.[75] As shown in Figure 10c, different PEDOT samples with conductivities ranging from 10^{-2} to 10^{3} S cm^{-1} and their corresponding Seebeck coefficients were investigated. While keeping the oxidation/doping level constant, the morphology is tuned from amorphous to semicrystalline, thus simultaneously enhancing the Seebeck coefficient and electrical conductivity. The PEDOT-Tos sample obtained by vapor-phase polymerization using a triblock copolymer of poly(ethylene glycol-propylene glycol-ethylene glycol) (PEG-PPG-PEG, 58000 Mw + DMF) as a template shows both the highest conductivity and Seebeck coefficient. The explanation for the improvement in both the Seebeck coefficient and conductivity is proposed as a transition from a Fermi glass to a semimetal; this theory is supported by the temperature dependence of conductivity (Figure 10d). The semimetallic character that originates from the formation of a network of bipolarons results in an empty bipolaron band that slightly overlaps with the valence band.

Morphology control has been used to enhance the thermoelectric properties of other doped conjugated polymers. In 2016, Chen et al. reported highly ordered poly(3-hexylthiophene-2,5-diyl) (P3HT) films prepared by the epitaxial growth method, in which the solvent, 1,3,5-trichlorobenzene (TCB), was used as the template.[84] The molecules in the quasi-one-dimensional (1D) P3HT film were highly oriented parallel to the fiber axis direction (as shown in the scheme in Figure 10e) with a decreased number of defects and enhanced carrier mobility; thus, the conductivity (parallel to the fiber axis) was markedly improved, reaching a maximum value of 320 S cm^{-1}. With this enhancement in electrical conductivity, maximum PF and zT values of 62.4 μW m^{-1} K^{-2} and 0.1, respectively, were reached at 365 K in the direction parallel to the fiber axis (Figure 10f,g). This result is one of the highest values reported for pure P3HT materials. The same strategy of P3HT fiber alignment was also applied by Untilova et al. in 2020 by using high temperature rubbing,[124] a technique enabling the preparation of highly aligned polymer films with a thickness of a few tens of nanometers:[85] the alignment of the fibers, coupled with the molybdenum dithiolene complex Mo(tfdCOCF$_3$)$_3$ as doping specie, allowed reaching an impressive PF of 160 μW m^{-1} K^{-2}.

The effect of morphology control on P3HT has been systematically studied by Lim et al. in 2019:[125] by vapor doping with F_4TCNQ, they were able to control the morphologies of the doped P3HT films. They observed that crystalline regions have higher doping efficiency compared to amorphous ones, which, coupled with higher charge mobility, leads to higher values of σ. On the other hand, S appeared to be less affected by the morphology while instead being strongly influenced by structural ordering, in agreement with other research group results,[126,127] while also extending what Patel et al. previously observed with poly(2,5-bis(3-tetradecylthiophen-2-yl)thieno-[3,2-b]thiophene) (PBTTT) vapor-doped with F_nTCQ, where a PF as high as 120 μW m^{-1} K^{-2} was achieved.[128]

Highly ordered PANi chains have also been reported recently, with enhancements in electrical conductivity as well as the Seebeck coefficient by a factor of 3.3 and 1.2, respectively.[129] The use of a self-assembled supramolecule (SAS) like (3,6-dioctyl-decyloxy-1,4-benzenedicarboxylic acid) as a template has proven to be an effective way to obtain highly ordered PANi-SAS films, reaching a maximum PF of 31 μW m^{-1} K^{-2}.[129] The importance of structural ordering has also been shown by Brinkmann et al., who recently reported a method to obtain highly oriented PBTTT films with high persistence length, capable of reaching exceptional electrical conductivities larger than 10^5 S cm^{-1} and corresponding PF of 2 mW m^{-1}K^{-2}.[89]

Thin-film nanostructuring has emerged as an alternative way to further enhance the thermoelectric properties of conducting polymers. For example, Sun et al. demonstrated a three-in-one improvement in the PF of PANi when the material is organized as nanotubes.[133] The power factor of the as-synthesized β-naphthalene sulfonic acid-doped polyaniline nanotubes was 2 orders of magnitude higher than that of pristine bulk PANi films. The reason for this improvement was ascribed to a sharper DOS, which leads to an increase in S by a factor of 7, an increase in charge mobility alongside the nanotube axis (i.e., increase in σ) and higher phonon scattering (i.e., lower lattice component of the thermal conductivity). Subsequent studies on PPy nanotube films and the nanostructures of other conducting polymers have also been reported.[134] Conducting multilayered polymer structures with enhanced thermoelectric performance was published by Jo et al.[135] A 5-layer PEDOT:PSS/PANI−CSA film with a thickness of 20 nm was prepared through layer-by-layer deposition. The PF of the multilayer film reached 49 μW m^{-1} K^{-2}, 2 times higher than that of the single PEDOT:PSS layer.

Another interesting strategy to control the morphology and mechanical properties of TE conducting polymer materials consists of realizing composites of conducting polymers and insulators, which can contribute to improving the material processability. For example, Yang et al. investigated the thermoelectric properties of poly(3-butylthiophene-2,5-diyl) (P3BT) nanowire interpenetrating networks in an insulating polystyrene (PS) matrix.[136] Because of the quasi-1D charge transport in this bulk interpenetrated network, the P3BT/PS blend (40−60% P3BT) showed a higher electrical conductivity (1 mS cm^{-1}) and lower thermal conductivity (0.2 W m^{-1}K^{-1}) than neat P3BT (0.1 mS cm^{-1}, 0.3 W m^{-1}K^{-1}, respectively), without sacrificing the Seebeck coefficient (600 μV K^{-1}). The PF of the blend was approximately 1 order of magnitude higher than that of the neat P3BT. Although the overall performance was not a record, it demonstrated the possibility of improving thermoelectric properties by blending conducting polymers with insulating matrices.

The use of an insulating polymer as a matrix is also a possible solution to improve the stability of the TE properties of organic semiconductors under mechanical stress. In 2019, Baran and co-workers demonstrated in two different works the possibility of achieving self-healing and stretchable PEDOT:PSS based composites with the addition of a polymeric surfactant (Triton X-100) and ionic liquids (1-ethyl-3-methylimidazolium cations with 4,5-dicyanoimidazolate and dicyanamide containing nitrogen anions), respectively.[130,131] The presence of Triton X-100

https://doi.org/10.1021/acs.chemrev.1c00218
Chem. Rev. XXXX, XXX, XXX−XXX

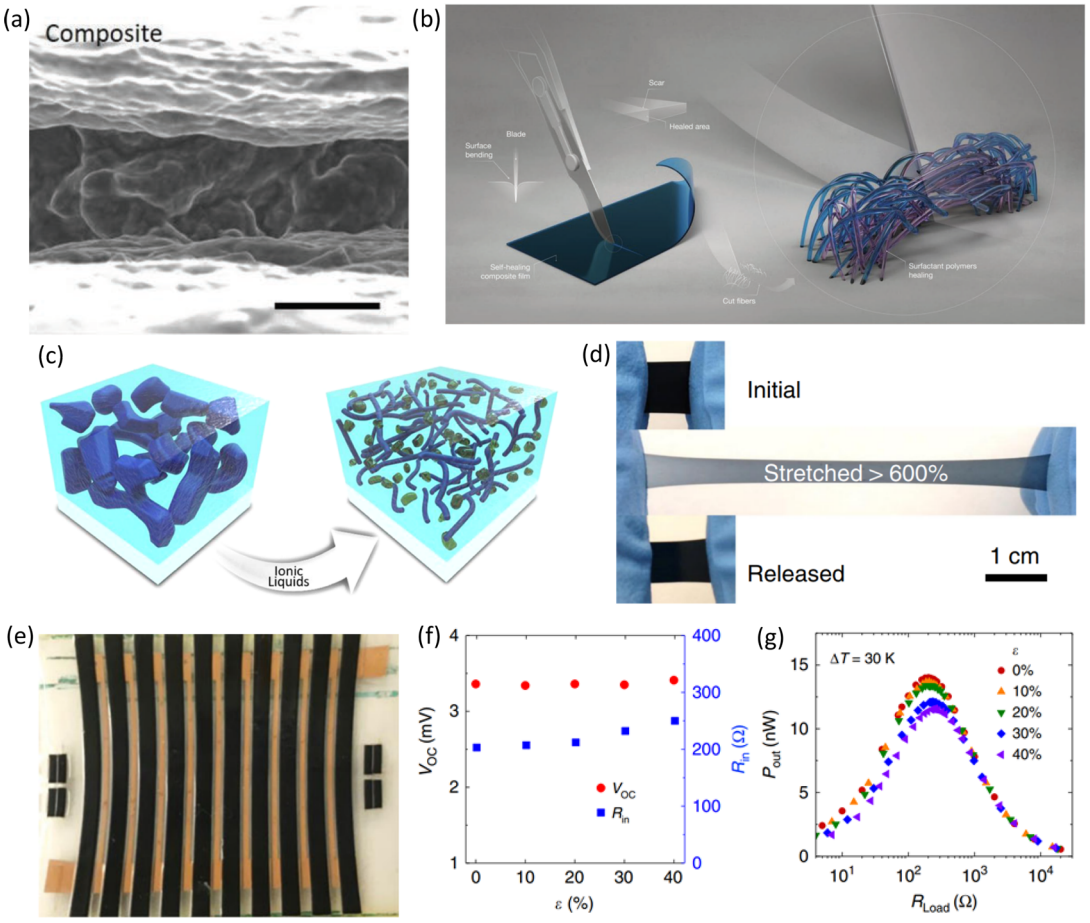

Figure 11. (a) SEM image of the cut on the PEDOT:PSS/Triton X-100 composite film and (b) Schematic illustration for the mechanical and thermoelectrical self-healing process of the composite film. (a–b) Reproduced with permission from ref 130. Copyright 2019 Wiley. (c) Schematic of the IL-induced morphological transition of PEDOT:PSS from the amorphous structure into crystalline nanofibrils inserted in IL-assisted soft domains. Reproduced with permission from ref 131. Copyright 2019 American Chemical Society. (d) Schematic of the stretchability of the PEDOT:PSS-polyurethane-IL composite. (e) Photograph of a stretchable TE module composed of 10 legs. (f) V_{OC} and R_{in} vs tensile strain (ε) applied to a module at ΔT = 30 K. (g) P_{out} vs R_{load} under different strains at ΔT = 30 K. (d–g) Reproduced with permission from ref 132. Copyright 2020 Nature.

creates a viscoelastic composite in which the PEDOT:PSS is dispersed in the surfactant matrix which acts as a viscous fluid and thus after a cut, it can freely flow from both sides of the separated regions and form a physical contact, effectively mending the "wound" (Figure 11a,b), thus allowing the composite to recover its thermoelectric and electrical properties. On the other hand, the use of the ionic liquids (IL) allowed increasing at the same time both S and σ of PEDOT:PSS, by modifying the doping level and nanostructure of PEDOT:PSS via an ion-exchange process. In addition, the presence of the IL resulted in the formation of PEDOT:PSS nanofibrils embedded in a soft matrix, improving its mechanical stretchability (Figure 11c).

Recently, Kim et al. combined the two previously discussed strategies by reporting an aqueous-processed poly(3,4-ethylenedioxythiophene)-polyurethane-ionic liquid composite, having both high conductivity (>140 S cm^{-1}) and stretchability (>600%),[132] as shown in Figure 11d. The addition of water-borne polyurethane and of an ionic liquid (tricyanomethanide) not only increases tremendously the elasticity of the composite but also helps maintaining high values of electrical conductivity. The high conductivity of the composite is due to a smoother morphology of the film, possessing a roughness of around 42 nm because of the counterion exchange between the conducting polymer and IL, which causes a morphological change in the PEDOT:PSS toward a crystalline nanofibrillar structure, which is beneficial not only to charge transport along the polymer chains but also for the formation of a percolating network within the polyurethane matrix. Finally, they realized a TEG composed of 10 thermocouples (Figure 11e), showing a constant open circuit voltage under different strain levels while keeping the variation in electrical resistance below 50%, even under high mechanical stresses (Figure 11f,g).

Apart from blending organic semiconductors with polymeric electrolytes/matrices or IL, other methods to obtain flexible organic thermoelectric have been reported: Kim et al. reported the wet-spinning into sulfuric acid of PEDOT:PSS, possessing a Young's modules of 1.9 GPa and a σ > 800 S cm^{-1}, that can be integrated into textiles.[137] Indeed, in a following work, they show the possibility of integrating a TEG with a vertical architecture into the sewing thread of a wool fabric, demonstrating the possibility of achieving a power of 1.2 μW with a ΔT = 65 K.[138]

4.1.1.3. Hybrid Composites. Organic–inorganic composites present a unique way to optimize the zT value of thermoelectric materials through proper molecular and interfacial designs. In 2010, a high-performance water-processable polymer–inorganic hybrid TE material with a room temperature zT value of

https://doi.org/10.1021/acs.chemrev.1c00218
Chem. Rev. XXXX, XXX, XXX–XXX

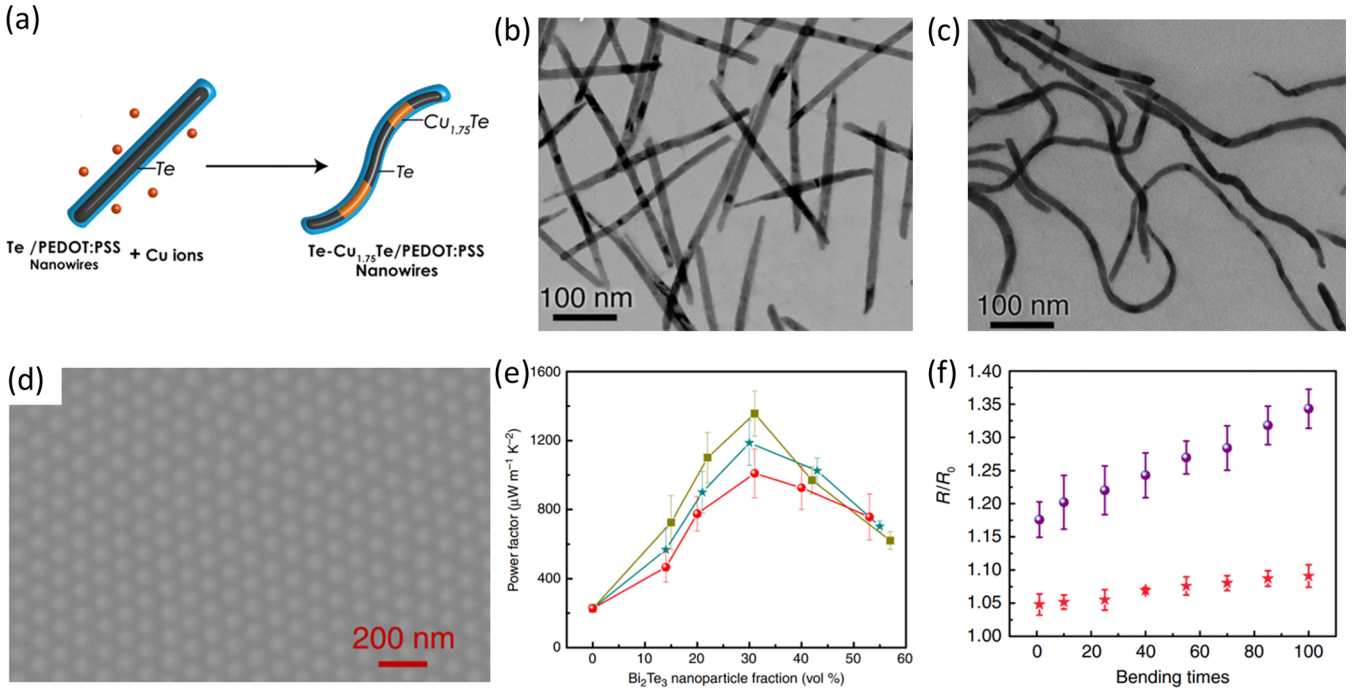

Figure 12. (a) Cartoon depiction of Cu incorporation and the nucleation of Cu-Te alloy phases within PEDOT:PSS-Te NWs, and TEM images of (b) PEDOT:PSS-Te and (c) PEDOT:PSS-Te(Cux) NWs showing a transition from straight to bent wires. (a–c) Reproduced with permission from ref 140. Copyright 2016 American Chemical Society. (d) Scanning electron microscopy (SEM) image of a PEDOT/Bi_2Te_3(100) hybrid film. (e) Power factor of the PEDOT:PSS-Bi_2Te_3 composite as function of nanoparticle fraction, and (f) Change in the electrical resistance of the PEDOT:PSS-Bi_2Te_3 composite as a function of the number of bending cycles. (d–f) Reproduced with permission from ref 83. Copyright 2018 Nature.

approximately 0.1 was reported.[81] A smooth PEDOT:PSS/Te nanorod composite film, prepared by solution casting, had both high electrical conductivity and a high Seebeck coefficient at room temperature. The in-plane thermal conductivity of the composite film, characterized by means of the 3-ω method, ranged from 0.22 to 0.30 W m^{-1} K^{-1}. This combination yielded excellent *PF* (~70 μW m^{-1} K^{-2}) and *zT* (~0.1) values at room temperature, demonstrating a record for organic composites. The same authors investigated the origin of the high performance of these hybrid materials.[139] By varying the nanowire:polymer ratio, a maximum conductivity (11 S cm^{-1}) was found at an intermediate content of Te nanowires (0.86 weight fraction). They also developed a series-connected model to explain the behavior of the composite, which emphasized the importance of understanding and controlling the interfacial volume in this organic–inorganic system to enhance carrier transport in hybrid materials and devices.

In 2016, Zaia et al. developed a method to control the growth of heterostructures within hybrid organic/inorganic nanocomposites.[140] Nanoscale domains of a $Cu_{1.75}Te$ alloy at different doping concentrations were grown by adding different amounts of copper(II) nitrate hemipentahydrate to a dispersion of PEDOT:PSS-Te NWs (Figure 12a). A 22% enhancement in *PF* was achieved in the low-doping regime, with *PF* values reaching up to 84 μW m^{-1} K^{-2} (Figure 12c). This approach could be adapted to other systems for the rational design of solution-processable TE materials. Combining transport measurements with theoretical simulations, Kumar et al. further studied the thermoelectric properties of the PEDOT:PSS-Te(Cu_x) nanowire hybrid material system.[88] They proposed that the thermoelectric properties were dominated by the polymer matrix and that the positive effect of the inorganic NWs was due to the templating effect of the PEDOT:PSS morphology at the interface with the Te(Cu_x) NWs as well as the charge redistribution between the two conductors.

Very impressive results have also been obtained by combining the two most iconic organic/inorganic thermoelectric materials: PEDOT:PSS and bismuth telluride. In 2018, flexible PEDOT/Bi_2Te_3 hybrid films with monodispersed and periodic Bi_2Te_3 nanophases (Figure 12d) were fabricated by Wang et al.[83] Periodic Bi_2Te_3 nanofillers could significantly scatter phonons, resulting in an ultralow in-plane thermal conductivity of ~0.7 W m^{-1} K^{-1}, while the continuous PEDOT phase provided favored electronic transport with an ultrahigh power factor of ~1350 μW m^{-1} K^{-2} (Figure 12e). Consequently, a high *zT* value of 0.58 was obtained at room temperature. In addition, the as-fabricated hybrids showed superior mechanical flexibility, and their thermoelectric properties showed negligible changes after 100 bending cycles (Figure 12f). Katz et al. reported another PEDOT:PSS- Bi_2Te_3 composite with an enhanced *PF*.[141] Both n- and p-type Bi_2Te_3 particles were ball-milled, dispersed in alcohol, and drop cast on a glass slide to form a thin layer. This step was followed by drop casting PEDOT:PSS on top of the Bi_2Te_3 particle layer. By controlling the load of PEDOT:PSS, maximum *PF*s of 70 and 40 μW m^{-1} K^{-2} were achieved for p- and n-type composite materials, respectively. This method facilitated the development of polymer–inorganic composite materials, and it overcame the organic–inorganic miscibility issues typical of these hybrid materials.

Similarly, P3HT–inorganic composites have also been studied as promising TE materials.[142] Bi_2Te_3 was added to a solution of $FeCl_3$-doped P3HT and mixed via ultrasonication. A 15 μm thick composite film was then obtained by drop casting and vacuum drying the films at room temperature. The authors suggested an energy-filtering effect at the organic–inorganic semiconductor interface to explain why the P3HT-Bi_2Te_3

https://doi.org/10.1021/acs.chemrev.1c00218
Chem. Rev. XXXX, XXX, XXX–XXX

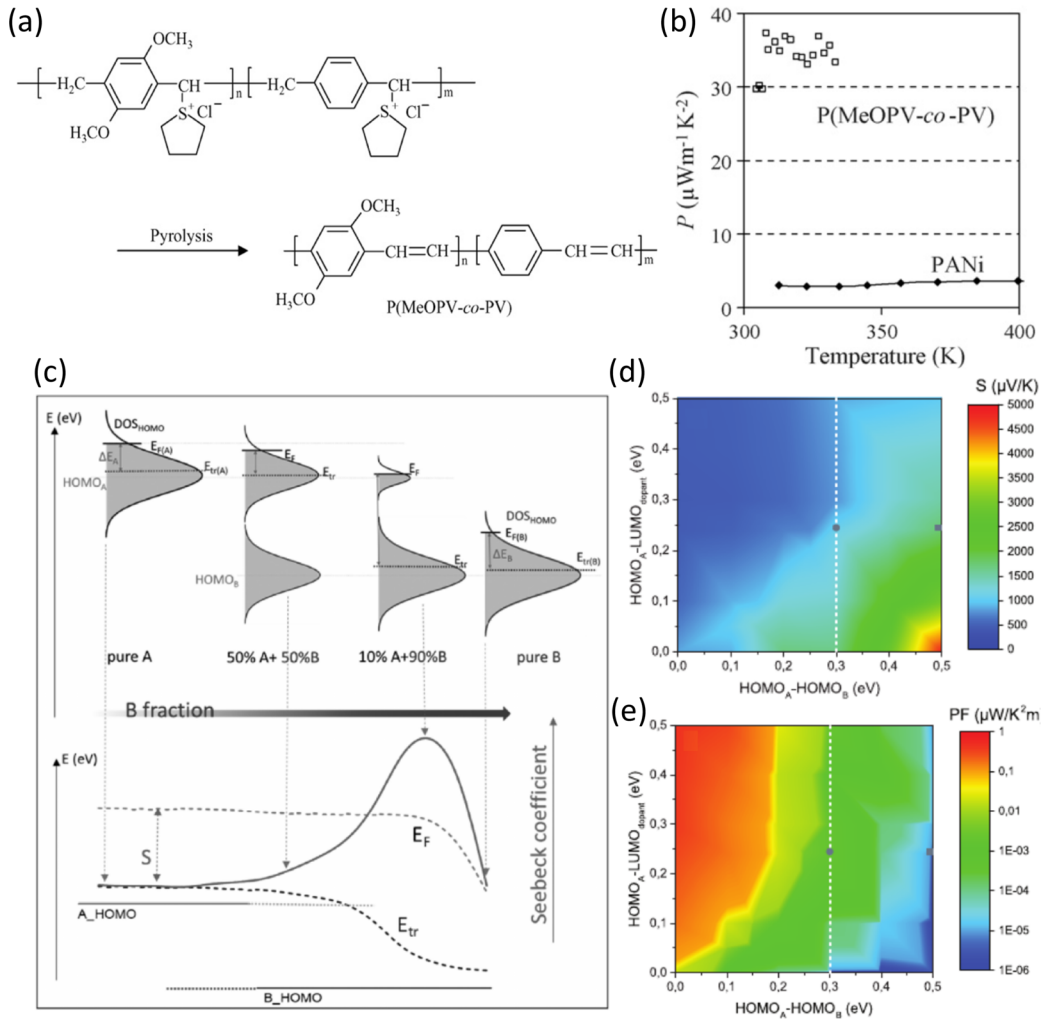

Figure 13. (a) Synthetic route for the synthesis of P(MeOPV-*co*-PV) and (b) Temperature dependence of the *PF* of camphorsulfonic acid-doped polyaniline (PANi) and iodine-doped P(MeOPV-*co*-PV) at a stretching ratio of 4.4. (a–b) Reproduced with permission from ref 146. Copyright 2006 Elsevier Ltd. (c) Illustration of DOS engineering to achieve a high Seebeck coefficient. Dependence of the (d) Seebeck coefficient and (e) *PF* on the HOMO-HOMO offset between the two polymer components and the offset between the HOMO of polymer A and the LUMO of the dopant. Closed symbols correspond to the P3HT:PTB7 (circles) and P3HT:TQ1 blends (squares). (c–e) Reproduced with permission from ref 149. Copyright 2018 Wiley.

nanocomposite exhibited a *PF* (13.6 μW m^{-1} K^{-2}) more than 3 times higher than that of pure P3HT (3.9 μW m^{-1} K^{-2}). The authors suggested that this effect was due to lower energy carriers scattering at the interface between P3HT/Bi_2Te_3, contributing to increase *S* without significantly affecting σ.

4.1.1.4. Chemical Structure Design. In addition to the aforementioned strategies, modification of the chemical structures of the conducting polymer backbone or side chains can also affect the TE properties of organic semiconductors. For example, Leclerc et al. reported the thermoelectric properties of a series of polycarbazole derivatives.[143] By varying the side chains both on the carbazole cycle and on the nitrogen atom of the backbone unit, two poly(diindolocarbazole)s comprised of thiophene units were synthesized, showing the best combination of the Seebeck coefficient (71 μV K^{-1}) and conductivity (0.29 S cm^{-1}) but with a modest *PF* of only 0.15 μW m^{-1} K^{-2}. Later, in 2009, three different carbazole-based copolymers, namely, poly[*N*-9′-heptadecanyl-2,7-carbazole-alt-5,5-(2,2′-bithiophene)] (PCDT), poly[*N*-9′-heptadecanyl-2,7-carbazole-*alt*-5,5′-(2,2′-(1,4-phenylene)dithiophene)] (PCDTB), and poly-[*N*-9′-heptadecanyl-2,7-carbazole-*alt*-5,5′-(4′,7′-di-2-thienyl-2′,1′,3′-benzothiadiazole] (PCDTBT), were synthesized through Suzuki coupling polymerization.[144] After optimization, the $FeCl_3$-doped PCDTBT films showed a relatively high electrical conductivity (160 S cm^{-1}) and Seebeck coefficient (34 μV K^{-1}), which resulted in a *PF* of 19 μW m^{-1} K^{-2}.

Another interesting candidate for TE application is alkoxy-substituted poly(*p*-phenylene vinylene) (PPV), showing high conductivity values >200 S cm^{-1} when doped with I_2.[145] In 2006, Hiroshige et al. first evaluated the thermoelectric properties of poly(2,5-dimethoxyphenylenevinylene) and its derivatives.[146] Stretched copolymers consisting of both 2,5-dimethoxy-substituted phenylenevinylene units and unsubstituted units (P(MeOPV-co-PV)) exhibited an electrical conductivity of 184 S cm^{-1} and a Seebeck coefficient of 44 μV K^{-1} at 313 K upon I_2 doping, resulting in a *PF* larger than 30 μW m^{-1} K^{-2}, as shown in Figure 13b. The same authors also investigated the effect of different alkoxy substituents and stretching treatments on the TE properties of copolymers consisting of both 2,5-dialkoxy-substituted PPV units and unsubstituted units (P(ROPV-co-PV)) (RO = MeO, EtO, and BuO).[86] Among all the copolymers, I_2-doped P(EtOPV-*co*-PV)

https://doi.org/10.1021/acs.chemrev.1c00218
Chem. Rev. XXXX, XXX, XXX−XXX

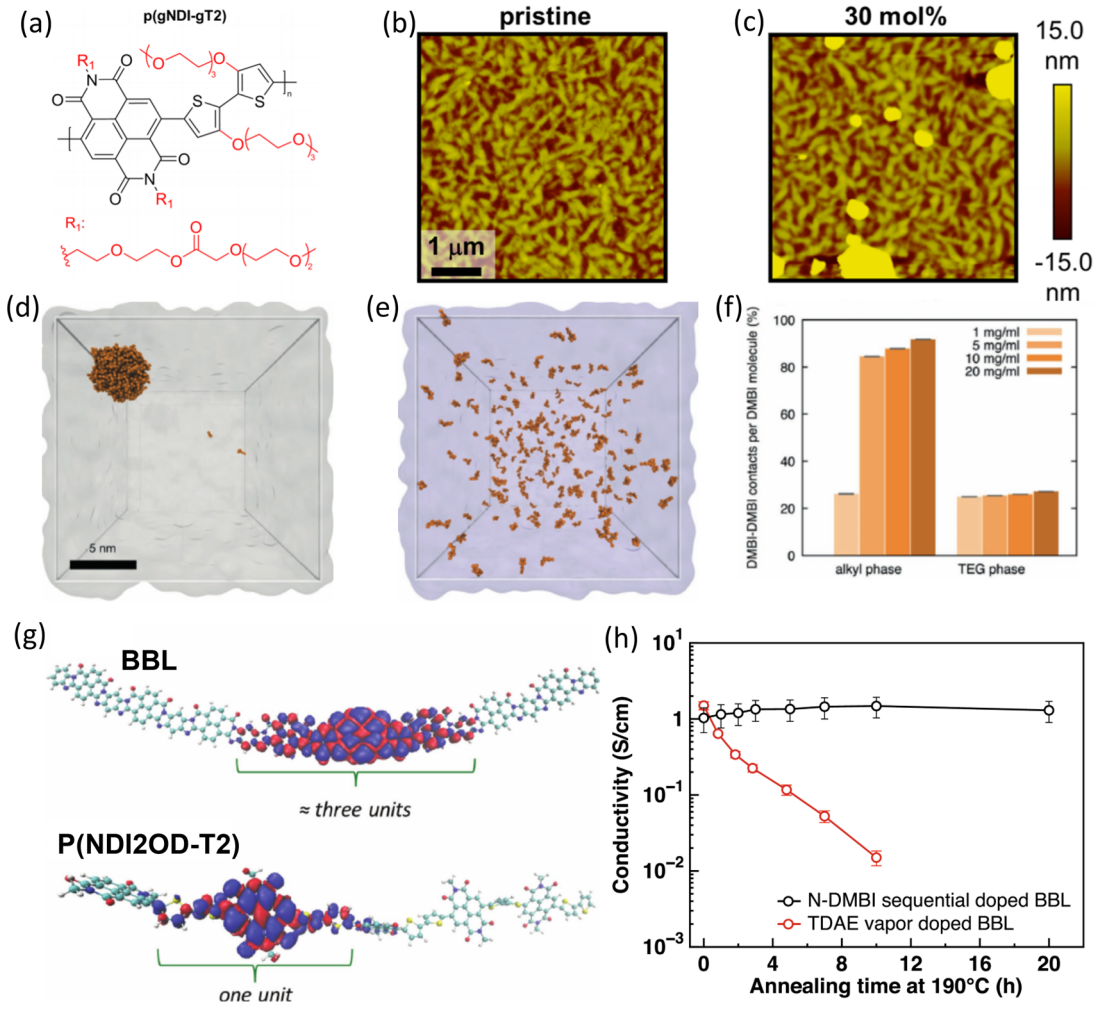

Figure 14. (a) Molecular structures of P(gNDI-gT2) and AFM images of (b) pristine and (c) 30% doped σ p(gNDI-gT2). (a–c) Reproduced with permission from ref 158. Copyright 2018 American Chemical Society. Representation of coarse-grained molecular dynamics simulations of n-DMBI molecules dissolved in (d) pure N2200 side chain phase and (e) pure TEG-N2200 side chain phase. (f) Normalized number of contacts between dopant molecules in N2200 and TEG-N2200 at different concentrations. (d–f) Reproduced with permission from ref 159. Copyright 2018 Wiley. (g) Calculated spin density distribution for BBL and P(NDI2OD-T2). Reproduced with permission from ref 160. Copyright 2016 Wiley. (h) Effect of the annealing temperature on the secondary doping of BBL using N-DMBI. Reproduced with permission from ref 161. Copyright 2020 American Chemical Society.

exhibited the best overall performance at a stretching ratio of 3.1, with a conductivity of 349.2 S cm^{-1}, Seebeck coefficient of 47.3 $\mu V\ K^{-1}$ and thermal conductivity of 0.25 W $m^{-1}\ K^{-1}$ at 313 K. The corresponding *PF* of 78.1 $\mu W\ m^{-1}\ K^{-2}$ and high zT value near 0.1 were records at the time for conducting polymers.

An interesting category for thermoelectric application is represented by random copolymers: they can be considered as irregular polymers with structural disorder along the backbone. This disordered structure can be favorable to adjust the energy level and the electrical properties to potentially enhance TE behaviors.[147,148] Therefore, Li et al. designed and synthesized a series of new random copolymers by copolymerizing D−A type and D−D type building blocks along polymer chains with the aim of improving the TE and electrical properties:[91] the tuning of the energy levels resulted in an increased doping level while strong D−A interchain interactions allowed obtaining a high degree of crystallinity for efficient charge transport. The result is an impressive *PF* of 110 $\mu W\ m^{-1}\ K^{-2}$, due to an impressive charge mobility 1 $cm^2\ V^{-1}\ s^{-1}$ which leads to a $\sigma > 300$ S cm^{-1} without affecting the *S*.

4.1.1.5. DOS Engineering. In Mahan and Sofo's pioneering work, a Δ-shaped transport distribution above the Fermi level was demonstrated to maximize the thermoelectric properties.[150] On the basis of this idea, Sun et al. used F4TCNQ as a p-type dopant in a mixture of P3HT and different fractions of poly(3-hexylthiophene-thiophene) (P3HTT). It was found that the Seebeck coefficient of P3HT mixed with 2% P3HTT increased from ≈580 $\mu V\ K^{-1}$ for pristine P3HT to 700 $\mu V\ K^{-1}$, while its conductivity remained at approximately 1.5×10^{-4} S cm^{-1}.[151] Li et al.[152] expanded on these results by offering a method to properly select the polymer blend composition to maximize *PF*. On the basis of these results, Kemerink et at.[149] reported a universal method to engineer the charge carrier DOS to maximize thermoelectric performance (explained in Figure 13d). A few conjugated polymers, namely, P3HT, poly({4,8-bis[(2-ethylhexyl) oxy] benzo[1,2-b:4,5-b′] dithiophene-2,6-diyl}{3-fluoro-2-[(2-ethylhexyl) carbonyl]thieno[3,4-b] thiophenediyl}) (PTB7), and poly[2,3-bis(3-octyloxyphenyl)- 5,8-quinoxalinediyl]-2,5-thiophenediyl] (TQ1), were selected because they had different HOMO energy levels. P3HT was mixed with varying fractions of PTB7 and TQ1 and then doped

https://doi.org/10.1021/acs.chemrev.1c00218
Chem. Rev. XXXX, XXX, XXX−XXX

with F4TCNQ. They found that at the optimized mixing ratio, the Seebeck coefficient of the mixture largely exceeded that of any of the pure materials (1100 μV K^{-1} at P3HT$_{0.1}$:PTB7$_{0.90}$ and 2000 μV K^{-1} at P3HT$_{0.05}$:TQ1$_{0.95}$ vs 142 μV K^{-1}, 469 μV K^{-1}, and 1560 μV K^{-1} for pure P3HT, PTB7, and TQ1, respectively), as shown in Figure 13d,e. These observed trends in the Seebeck coefficient were in good agreement with kinetic Monte Carlo simulations with parameters based on experimental data. In a following work, Kemerink et al.[153] reviewed the thermoelectric properties of conjugated blends, trying to review all the results obtained offering guidelines to design organic thermoelectric materials.

4.1.2. n-Type TE Polymers and Composites. Regarding the fabrication of practical thermoelectric devices, both electron and hole conducting materials with large *PF* values are needed. Compared to their p-type counterparts, n-type conducting polymers have shown inferior thermoelectric properties, mainly due to their less effective and stable doping mechanisms. Conventional conducting polymers such as PA and PANi can behave as both p-type and n-type conductors when doped appropriately.[154,155] However, because they are typically unstable in the n-type state under ambient conditions, their TE performance is insufficient. Although increasing examples of n-type conducting polymers with improved TE properties have been reported, more effort is needed to better understand the relationship between the chemical structure and doping of n-type TE materials to develop efficient and stable TE devices. In the following, we provide a few examples of state-of-the-art n-type TE materials.

In 2014, Chabinyc et al. reported the TE properties of the n-type polymer poly-*N*,*N*-bis(2-octyl-dodecyl)-1,4,5,8-napthalenedicarboximide-2,6-diyl]-alt-5,5-(2,2-bithiophene) (P(NDI2OD-T2)[156] doped in solution with an air-stable dopant (4-(1,3-dimethyl-2,3-dihydro-1*H*-benzoimidazol-2-yl)phenyl) (N-DMBI) before film formation.[157] The electrical conductivity of the P(NDI2OD-T2) films could be varied over several orders of magnitude by tuning the N-DMBI molar concentration. The electrical conductivity, however, reached an unsatisfactory maximum value of only 5 10^{-3} S cm^{-1}, which was attributed to the limited solubility/miscibility of the dopant in the polymeric matrix. The authors suggested that only ∼1% of the DMBI molecules introduced in solution were active and contributed free carriers to the film, implying that only 1 in 1000 P(NDI2OD-T2) repeat units were doped.

This extrinsic limitation could be overcome by proper engineering of the polymer backbone and/or alkyl side chains. In two parallel studies, Müller et al.[158] and Koster et al.[159] showed that functionalizing the NDI-based polymer with polar side chains (Figure 14a), such as oligoethylene glycol-based side chains, led to a high electrical conductivity of more than 10^{-1} S cm^{-1} for an N-DMBI due to a low segregation of the dopant molecules (Figure 14b−f). Overall, the n-type polymers resulted in a larger thermoelectric *PF* of up to 0.4 μW m^{-1} K^{-2} compared to other NDI-based polymers functionalized with alkyl side chains. Caironi et al. reported that, compared to nonthionated P(NDI2OD-T2), the thionated P(NDI2OD-T2) gave rise to higher electrical conductivity and stable operation in air due to a deeper LUMO level, lying below the threshold for air stability at −4 eV.[162,163] Nevertheless, the thionated polymer showed a relatively low *PF* (0.04 μW m^{-1} K^{-2}). The same authors reported that the incorporation of "kinked" comonomers in NDI-based polymers enhanced dopant/polymer miscibility, allowing for a ∼20-fold increase in doping efficiency.[164]

Fabiano et al. argued that the low electron conductivity typically observed for n-type P(NDI2OD-T2) might be ascribed to the strong charge carrier intrachain localization,[160] which is a common characteristic of donor−acceptor polymers.[165] After replacing the donor bithiophene (T2) unit in P(NDI2OD-T2) with the more electron-deficient bithiazole (Tz2) unit (i.e., P(NDI2OD-Tz2)), they observed that the polymer donor−acceptor character decreased and its electron affinity increased, which resulted in an improved polymer doping efficiency. Moreover, because of the far lower intrachain steric demand of Tz2 than T2, the polymer backbone became more planar, thus enhancing the intermolecular $\pi-\pi$ stacking interactions, which led to a higher electron conductivity (up to ∼0.1 S cm^{-1}) and increased the thermoelectric response (*PF* up to 1.5 μW m^{-1} K^{-2}) compared to P(NDI2OD-T2).

Pei et al. synthesized a series of benzodifurandione-based PPV (BDPPV) samples with high electron affinities (LUMO levels deeper than −4.0 eV) and investigated their electrical conductivity, Seebeck coefficient, and *PF* values.[166] The LUMO levels of Cl-substituted BDPPV (ClBDPPV) and F-substituted BDPPV (FBDPPV) were 0.29 and 0.16 eV farther from vacuum than that of BDPPV, reaching values of −4.30 and −4.17 eV, respectively. The electrical conductivity of the N-DMBI-doped films increased dramatically with dopant concentrations lower than 10 wt %, reaching values as high as 14 S cm^{-1}. The electrical conductivity then decreased as the N-DMBI content increased above 10% in the blend. The Seebeck coefficient remained negative for all three N-DMBI doped polymers, but the absolute value of the thermopower continuously decreased with increasing dopant concentration. Overall, FBDPPV showed the highest *PF* (28 μW m^{-1} K^{-2}) at the optimal doping concentration of 5 wt % at room temperature. Later, Zhao et al. demonstrated that low-cost, air-stable, and solution-processable tetrabutylammonium fluoride (TBAF) could be used as an effective n-dopant for ClBDPPV to boost the electrical conductivity of this polymer up to 0.62 S cm^{-1}.[167] This n-doping mechanism relied on electron transfer from the F$^-$ anions to the electron-deficient polymer ClBDPPV via an anion−π electronic interaction. A *PF* of 0.63 μW m^{-1} K^{-2} was obtained at a content of 25 mol % TBAF. This work provides an alternative air-stable dopant for high-performance solution-processable n-type thermoelectric materials. Recently, in 2021, they expanded their results by doping donor−acceptor (D−A) polymers, with dichloro substitutions, using N-DMBI: the Cl-substituted D−A due to the low lying LUMO level (<−4 eV) and to the dense packing of the hydrophobic groups, blocking O_2 and H_2O interactions, allowed to maintain 31% of the original σ after 222 days of air exposure.[168]

In 2016, Fabiano et al. showed that solution-processable ladder-type conducting polymers, such as polybenzimidazobenzophenanthroline (BBL), were promising n-type materials for TE applications.[160] After exposure to tetrakis(dimethylamino)-ethylene (TDAE) vapors, the electrical conductivity of spin-coated BBL films could be dramatically increased, reaching values as high as 2.4 S cm^{-1}, while the Seebeck coefficient reached a value of −60 μV K^{-1}. Thus, by optimizing the TDAE exposure time, the *PF* of the doped BBL film could be optimized to a value of 0.43 μW m^{-1} K^{-2}. Although the TE performance of BBL was not extraordinary, its high electrical conductivity, originating from its highly rigid and planar backbone (Figure 14g), provided a molecular-design guideline for new TE polymers. Recently, sequential doping has proven useful to

https://doi.org/10.1021/acs.chemrev.1c00218
Chem. Rev. XXXX, XXX, XXX−XXX

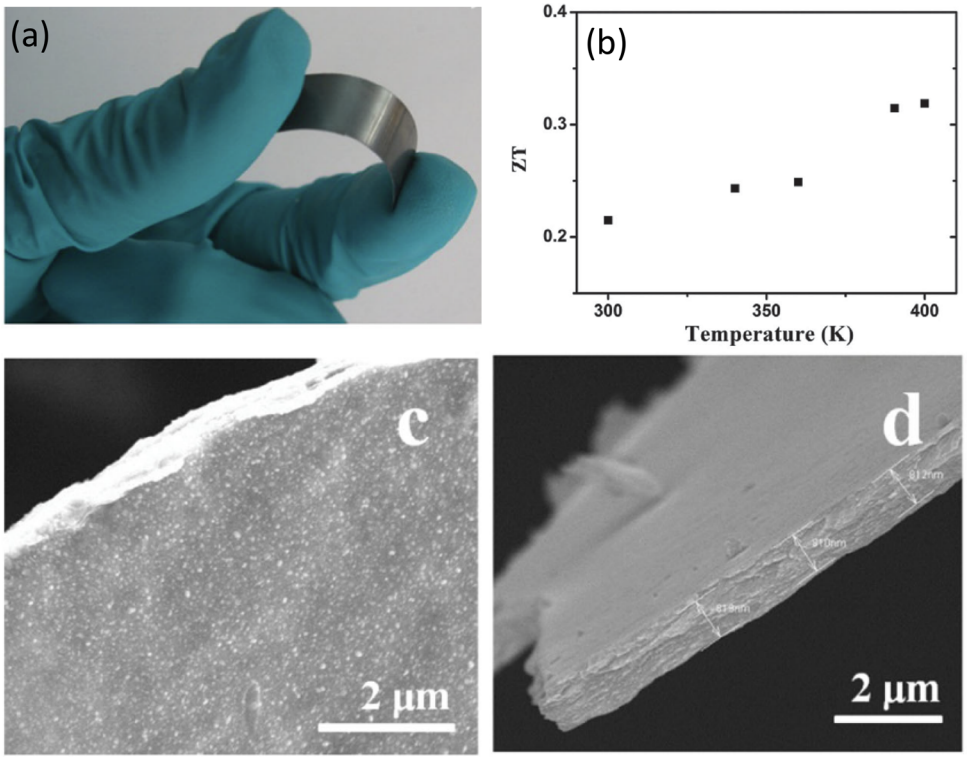

Figure 15. (a) Image of the poly[K_x(Ni-ett)]/PVDF composite on PET substrate. (b) *ZT* value versus temperature. (c) Top-view and (d) cross-section SEM images of poly[K_x(Ni-ett)]/PVDF films. Reproduced with permission from ref 93. Copyright 2016 Wiley.

improve the TE properties of BBL. First, the BBL film was spin-coated on a glass substrate and then annealed; subsequently, N-DMBI, dissolved in an orthogonal solvent (chloroform), was spin-coated on top of the polymer film. They reported a maximum *PF* of 1.5 μW m^{-1}K^{-2} with an electrical conductivity of approximately 1 S cm^{-1} (Figure 14h) and a Seebeck coefficient of −110 μV K^{-1}, showing an improvement by nearly a factor of 4 compared to the BBL/TDAE blend.[161] The same authors recently reported an n-type all-polymeric ink based on a BBL:poly(ethyleneimine) (PEI) blend, having an electrical conductivity as high as 8 S cm^{-1}, and demonstrated high thermoelectric power output (56 nW per thermocouple with a temperature difference below 50K) when a BBL:PEI-based n-leg was coupled to a PEDOT:PSS-based p-leg.[169]

Another growing interest in the field of organic thermoelectricity has been stimulated by metal−organic compounds. In 2012, Zhu et al. reported the n-type TE properties of the metal coordination polymer poly[K_x(Ni-ett)] (ett = ethylenetetrathiolate) with a high *zT* value of 0.20 at 440 K.[92] The authors synthesized a series of poly[A_x(Ni-ett)]s samples with different counterions (i.e., K^+, Na^+, and Bu_4N^+). By air oxidation, poly[A_x(Ni-ett)] could be obtained as a precipitate. Among the different samples, poly[K_x(Ni-ett)] had the best thermoelectric performance, with an electrical conductivity of 64 S cm^{-1}, a Seebeck coefficient as high as −151.7 μV K^{-1}, and a thermal conductivity of only 0.31 W m^{-1} K^{-1} at 440 K. When the metal ligand was changed to Cu, the resulting metal-coordinated polymer showed p-type TE performance, allowing for the fabrication of modules composed of 35 p−n couples. The resulting TE module had an open-circuit voltage of 0.26 V at a temperature difference of 80 K, and its power output was estimated to be 2.8 μW cm^{-2} at a temperature difference of 30 K.

Although these metal coordination polymers showed remarkably high thermoelectric performance, their insoluble and infusible characteristics hindered their processability and practical application in flexible thermoelectrics. To overcome this problem, the same authors used polymeric matrices to prepare solution processable composites.[170] The wet ball-milling method was employed to prepare thermoelectric composites of poly(M-ett). By optimizing the use of different polymer matrices, solvents, ball-milling times, weight ratios, and drying temperatures, maximum *PF* values of 0.43 μW m^{-1} K^{-2} and 0.86 μW m^{-1} K^{-2} were reached at 300 K for poly[K_x(Ni-ett)]/PVDF/NMP (n-type) and poly[Cu_x(Cu-ett)]/PVDF/DMSO (p-type), respectively. To demonstrate their practical application in solution-processable thermoelectrics, a flexible device made of six inkjet-printed thermocouples was fabricated on a PET substrate.

In 2016, the same authors reported flexible, high-performance poly[K_x(Ni-ett)] films prepared by electrochemical deposition.[93] Thin-film samples, prepared by applying a potential of 0.6 V (vs Ag/AgCl), showed better performance than the aforementioned pellets. The Seebeck coefficient of the poly-[K_x(Ni-ett)] films was similar to that of the pellets, but its electrical conductivity (>300 S cm^{-1}) was several times higher. Therefore, even though the thermal conductivity was slightly higher than that of the pellets (0.84 W m^{-1} K^{-1} at 400 K for thin films vs 0.28 W m^{-1} K^{-1} at 400 K for pellets), the *zT* value of poly[K_x(Ni-ett)] films at 400 K could reach 0.32, a new record for n-type organic thermoelectric materials (Figure 15b). Later, Yee et al. systematically studied the reaction conditions of poly[K_x(Ni-ett)], such as the counterion, nickel equivalency, and oxidation extent, to reliably and reproducibly synthesize poly[K_x(Ni-ett)]/PVDF in large quantities of up to 15 g. After optimization, the *PF* of the poly[K_x(Ni-ett)]/PVDF composite

https://doi.org/10.1021/acs.chemrev.1c00218
Chem. Rev. XXXX, XXX, XXX−XXX

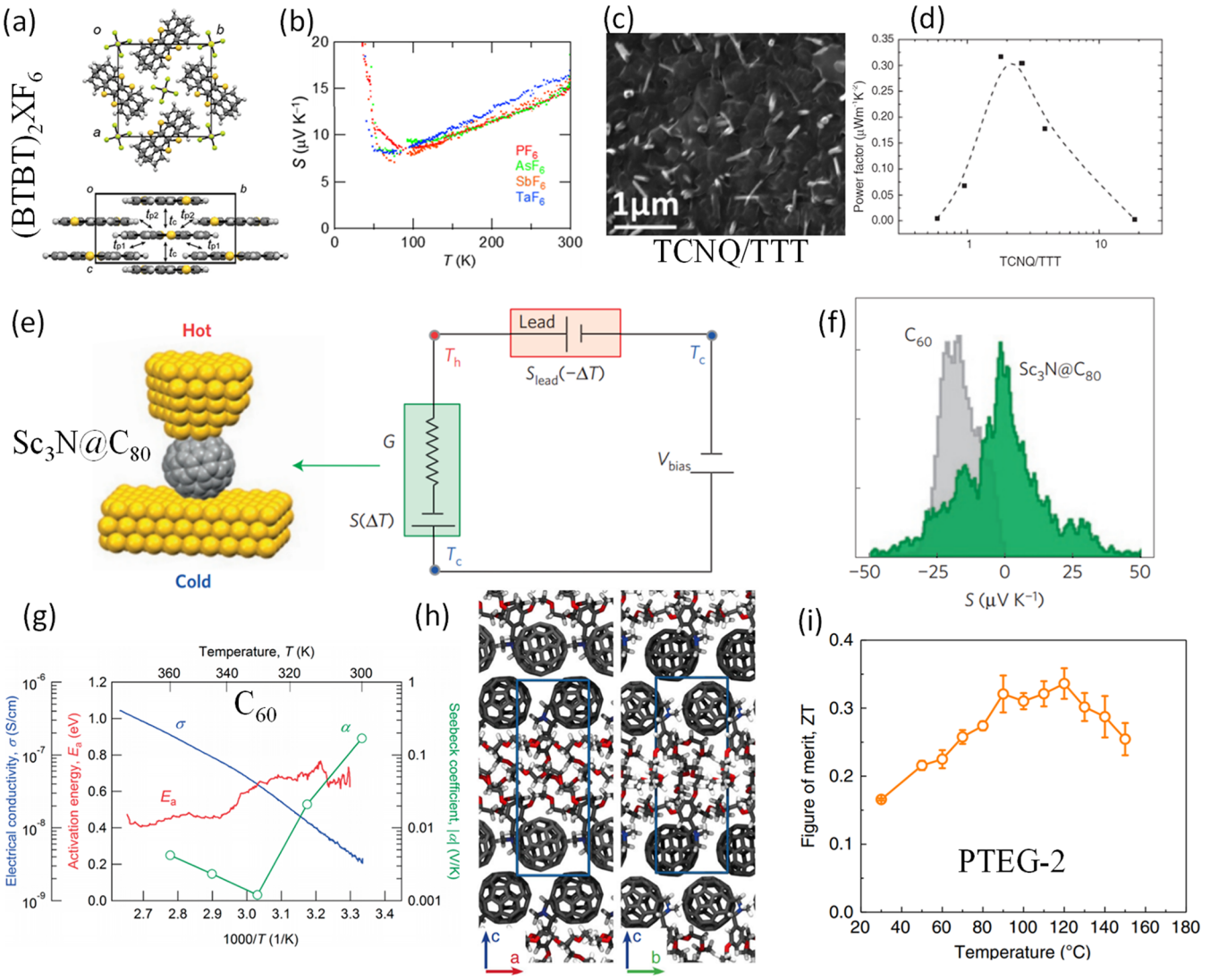

Figure 16. (a) Schematic of the crystal structure $(BTBT)_2XF_6$ and (b) Seebeck coefficient of $(BTBT)_2XF_6$ as a function of temperature. (a–b) Reproduced with permission from ref 87. Copyright 2016 American Chemical Society. (c) SEM image of TCNQ:TTT thin films with TCNQ:TTT molar ratio of 18.6 and (d) *PF* dependence TCNQ/TTT molar ratio. (c–d) Reproduced with permission from ref 180. Copyright 2017 Wiley. (e) Schematic of the measurement setup for the simultaneous measurements of *S* and σ of individual $Sc_3N@C_{80}$ molecules and (f) Histograms of S (green) at first contact for Sc3N@C80 compared to the values for C60 (in gray). (e–f) Reproduced with permission from ref 182. Copyright 2016 Nature. (g) σ, activation energy of conductivity (E_a), and *S* (α) of a C_{60} thin film as a function of temperature. The sign of all plotted *S* values is negative. Reproduced with permission from ref 183. Copyright 2015 Japan Society of Applied Physics. (h) Schematic representation of PTEG-2 molecular packing, as atomistically resolved by molecular dynamics simulations, with the unit cell highlighted in blue. (i) zT of PTEG-2 as a function of temperature, showing the record for an n-type solution processable organic semiconductor. Reproduced with permission from ref 95. Copyright 2020 Nature.

film improved to 23 μW m^{-1} K^{-2}.[171] Furthermore, thermal annealing was also investigated as an effective posttreatment process to simultaneously enhance the conductivity and thermopower of poly[K_x(Ni-ett)]/PVDF composite films.[172]

Organic/inorganic composites have also been investigated for use as n-type thermoelectric materials, where the organic insulating polymers act as the polymeric matrices to effectively decrease the thermal conductivity and the inorganic semiconductors/metals function as the active thermoelectric material. For example, very recently, n-type composite thermoelectric materials with remarkable TE properties have been prepared by simply blending an insulating polymer together with metallic nanowires.[94]

Drop-cast Ni-NW/PVDF films, manufactured with the Ni-NW content in the composites varying from 20 to 80 wt %, show electrical conductivity and Seebeck coefficient increasing with the Ni-NW content and reaching maxima of 4701 S cm^{-1} and −20.6 μV K^{-1} at 80 wt % Ni, respectively. The temperature dependence of the conductivity of the Ni (80 wt%)/PVDF nanocomposite film showed typical metallic behavior, i.e., decreasing with increasing temperature, while the absolute value of the Seebeck coefficient showed the opposite trend. As a result, the *PF* of the composite film increased with temperature, from 200 μW m^{-1} K^{-2} at room temperature to 220 μW m^{-1} K^{-2} at 380 K. Combined with the low and nearly constant thermal conductivity of 0.55 W m^{-1} K^{-1} over the whole temperature range, a high zT value of 0.15 was achieved for the Ni (80 wt %)/PVDF composite film at 380 K.

A final mention must be made regarding the development of new dopant molecules to increase the efficiency of the doping

https://doi.org/10.1021/acs.chemrev.1c00218
Chem. Rev. XXXX, XXX, XXX−XXX

process in n-type organic semiconductors. Saglio et al. synthesized benzimidazoles with different linear and branched alkyl substituents and observed a clear dependence of the nature of the alkyl substituent on dopant intercalation into the semicrystalline morphology.[173] It was found out that increasing the length or the steric hindrance of the alkyl substituents, the miscibility between dopant and copolymer is enhanced, leading to an increase by a factor of ≈7 in the electrical conductivity. Following this idea of optimizing the dopant specie, Yang et al. recently reported a DTF calculation-based method which led to the synthesis of a triaminomethane-type dopant (TAM), exhibiting high stability and strong hydride donating property due to its thermally activated doping mechanism. Thanks to this approach, they were able to efficiently dope fluorinated benzodifurandione-based poly(pphenylene vinylene) (FBDPPV), enabling it to reach an impressive value of n-type conductivity for an organic semiconductor (21 S cm^{-1}) and a *PF* of 51 $\mu W\ m^{-1}\ K^{-2}$ even in films with thickness above 10 μm.[97] Finally, they reported one of the first examples of all-polymer TEG, with a power output of 77 nW at $\Delta T \approx 50$ K. On the basis of these impressive results, Lu et al. tried to investigate the role of molecular dopant cations on carrier transport by comparing two n-dopants, TAM and N-DMBI-H.[96] The weak π-backbone affinity of TAM cations, coupled with the spatial screening of the Coulomb potential thanks to its side chains, allows negligible perturbation of the polymer backbone conformation and microstructural ordering, thus resulting in a $\sigma \approx 22$ S cm^{-1} and a *PF* of 80 $\mu W\ m^{-1}\ K^{-2}$. Apart from the impressive results, this work provided a successful strategy, applicable to other polymers, to increase the efficiency of the n-type doping process.

4.1.3. Small Molecules. In addition to conducting polymers, the thermoelectric properties of small molecules such as pentacene, fullerene, and phthalocyanine (*Pc*) have also been investigated. Theoretical studies have shown, for example, that *Pc* crystals can be excellent thermoelectric materials when n-doped, with the highest thermoelectric zT value of 2.5 in NiPc.[174] Compared to conducting polymers, small molecules can be easily purified and crystallized, yielding well-defined structures that allow the establishment of structure−property relationships. In the following, we will examine some of the recent progress in small-molecule thermoelectrics.

4.1.3.1. Charge Transfer Salts. TTF-TCNQ is a well-known charge-transfer salt with a room temperature conductivity as high as 500 S cm^{-1} in a single crystal. Its Seebeck coefficient and thermal conductivity have been reported to be −28 $\mu V\ K^{-1}$ and 1 $W\ m^{-1}\ K^{-1}$, respectively. Although the calculated zT value of TTF-TCNQ is only on the order of 10^{-2}, it was used for the fabrication of prototype thermoelectric devices early on, mainly due to the lack of high-performance n-type materials at that time.[10] Polycrystalline films of TTF-TCNQ show a much lower electrical conductivity (5−30 S cm^{-1}) than single crystals.[175−177] Using *N*,*N*-dimethylacetamide (DMA) as the solvent, a drop-cast TTF-TCNQ polycrystalline film can be prepared with a high density of TTF-TCNQ nanofibers. The obtained film shows an improved electrical conductivity of up to 58 S cm^{-1}, while its Seebeck coefficient is 32.3 $\mu V\ K^{-1}$, similar to the reported values for typical TTF-TCNQ polycrystalline films. Thus, a maximum *PF* of 6.05 $\mu W\ m^{-1}\ K^{-2}$ at room temperature is achieved.[178] In addition to TTF-TCNQ, the TE properties of other similar charge transfer complexes have also been evaluated. Evaporated films of TMTTF-TCNQ and HMTTF-TCNQ (TMTTF, tetramethyl-TTF; HMTTF, hexamethylene-TTF) and solution-processed nanoparticle films of (TTF)[Ni(dmit)$_2$]$_2$ (dmit: 1,3-dithiole-2-thione-4,5-dithiolato) were systematically investigated by Mori et al., with the (TTF)[Ni(dmit)$_2$]$_2$ single crystals showing the highest *PF* of 29 $\mu W\ m^{-1}\ K^{-2}$ at room temperature.[179] In 2016, Mori et al. reported the thermoelectric properties of another system, benzothienobenzothiophene (BTBT)-based molecular conductors.[87] Different charge transfer complexes of $(BTBT)_2XF_6$ (X = P, As, Sb, and Ta, structure in Figure 16a) were prepared, and their thermoelectric performances were characterized at room temperature. All the charge transfer complexes showed a similar Seebeck coefficient of approximately 15 $\mu V\ K^{-1}$, while $(BTBT)_2AsF_6$ possessed the highest electrical conductivity of 4100 S cm^{-1}. Thus, a *PF* as high as 88 $\mu W\ m^{-1}\ K^{-2}$ was achieved for $(BTBT)_2AsF_6$, while all the other complexes had similar values (<50 $\mu W\ m^{-1}\ K^{-2}$) (Figure 16b).

Both p-doped and n-doped tetrathiotetracene (TTT) thin films were reported by Pudzs et al.[180] p-Type TTT_2I_3 thin films were obtained by vacuum deposition or the postdeposition of iodine (I_2), yielding an electrical conductivity of 1.3 S cm^{-1}, a Seebeck coefficient of 63 $\mu V\ K^{-1}$, and a *PF* of 0.52 $\mu W\ m^{-1}\ K^{-2}$. For vacuum codeposited n-type TTT-TCNQ films, an electrical conductivity of 0.57 S cm^{-1}, a Seebeck coefficient of −75 $\mu V\ K^{-1}$, and a power factor of 0.33 $\mu W\ m^{-1}\ K^{-2}$ were obtained at an optimized ratio of 1:2 (Figure 16d). A prototype thin-film TE generator based on both n- and p-type TTT complexes was also built as a proof of concept. Efforts have also been made on the development of metal−organic complexes such as *Pc*−metal complexes (CoPc, NiPc, CuPc, ZnPc, etc.), porphyrin-metal complexes (such as Co(tbp)I, tbp = tetrabenzoporphyrinato), and CuTCNQ, with improved thermoelectric performance. We will not go into the details of the TE properties of these metal−organic complexes, but we refer to recently published reviews.[181]

4.1.3.2. Small Molecule Semiconductors. The thermoelectric properties of Na-, K-, and bidoped fullerenes were reported long ago.[184,185] In 2013, Barbot et al. reported n-doped fullerene with cesium carbonate (Cs_2CO_3) via a cosublimation process.[186] The conductivity of the C_{60}:Cs_2CO_3 thin film sharply increased to 6.6 S cm^{-1} at a molar ratio of 35.8% Cs_2CO_3, compared to undoped films with a conductivity of only 3.8×10^{-8} S cm^{-1}. The absolute value of the Seebeck coefficient decreased gradually with the dopant concentration, from 1715 $\mu V\ K^{-1}$ to less than 200 $\mu V\ K^{-1}$. After optimization, a high *PF* of 28.8 $\mu W\ m^{-1}\ K^{-2}$ was achieved at a molar ratio of 15.2% Cs_2CO_3.

By using a modified scanning tunneling microscope to study the single-molecule junctions of an endohedral fullerene [a fullerene cage (C_{80}-Ih) encapsulating three scandium atoms joined to one nitrogen $Sc_3N@C_{80}$], Agrait et al. demonstrated that the sign and magnitude of the thermopower could be tuned by changing the orientation and pressure (Figure 16f).[182] The origin of this bithermoelectric effect was also elucidated by means of density functional theory calculations, highlighting the importance of transport resonances at the molecular junctions. Later, Lambert et al. measured a positive Seebeck coefficient in exohedrally decorated $C_{50}Cl_{10}$ fullerene molecules and found that *S* could be increased by placing more $C_{50}Cl_{10}$ molecules in series.[187] Compared to a single $C_{50}Cl_{10}$, the Seebeck coefficient of the dimer increased from 8 $\mu V\ K^{-1}$ to 30 $\mu V\ K^{-1}$, while the *PF* increased from 5 $\mu W\ m^{-1}\ K^{-2}$ to 60 $\mu W\ m^{-1}\ K^{-2}$.

Recently, very large Seebeck coefficients of more than 150 mV K^{-1} have been reported for pure C_{60} thin films by in situ measurements under ultrahigh vacuum (Figure 16g).[183] Because of their high resistance, it is difficult to accurately

https://doi.org/10.1021/acs.chemrev.1c00218
Chem. Rev. XXXX, XXX, XXX−XXX

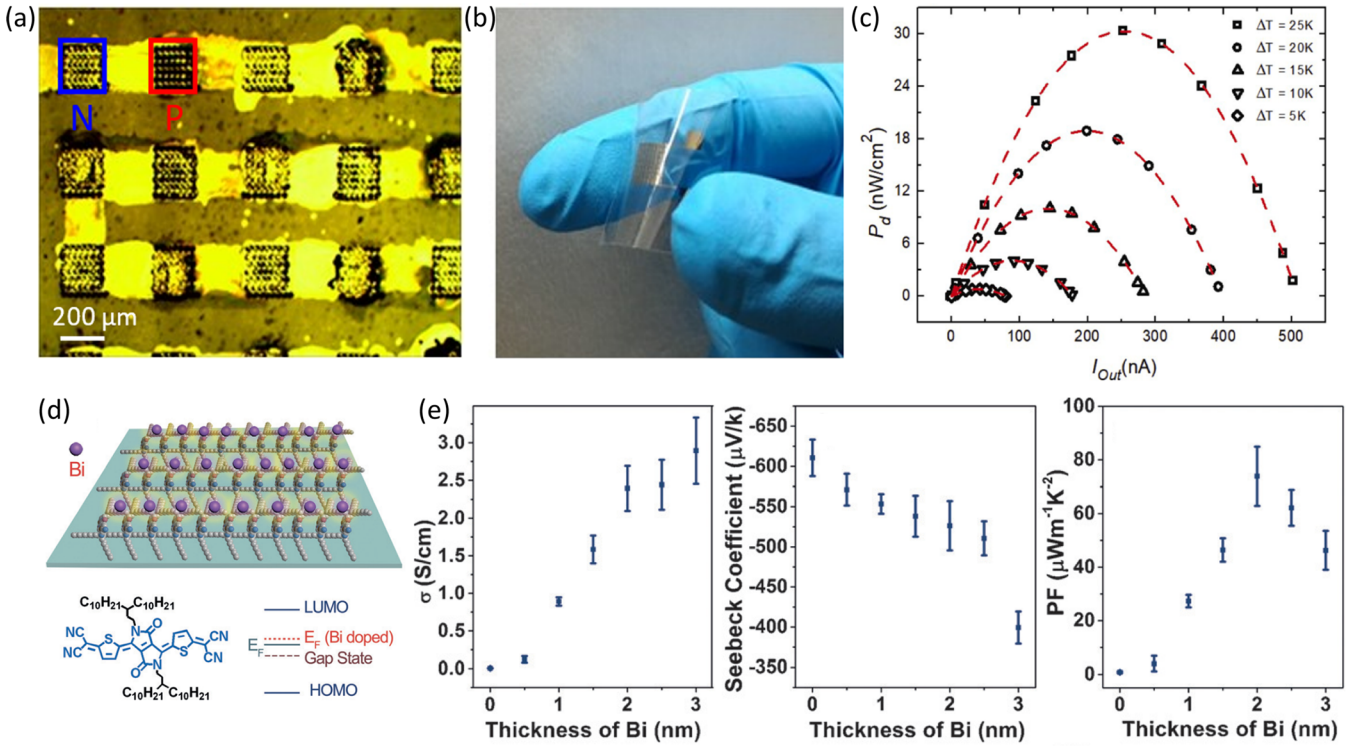

Figure 17. (a) Optical microscopy images of the fully printed vertical OTEG and (b) Photograph of the entire flexible monolithic OTEG. (c) Power density (P_d) vs output current (I_{out}). (a–c) Reproduced with permission from ref 190. Copyright 2020 Elsevier Ltd. (d) Mechanism of Bi interfacial doping of TDPPQ and molecular structure of TDPPQ. (e) Thermoelectric properties of TDPPQ doped with different thicknesses of Bi. (d–e) Reproduced with permission from ref 98. Copyright 2016 Wiley.

measure the Seebeck coefficient of pure (undoped) C_{60} films. However, Nakamura et al. developed a thermopower measurement system that solves this problem by using a custom high-input impedance differential amplifier. Although the electrical conductivity of undoped semiconductor films is relatively low ($<10^{-9}$ S cm^{-1}), thermoelectric materials with such high Seebeck coefficients could also be used for sensing, as they are able to react to small variations in temperature. Thus, the thermopower measurement system developed by Nakamura et al. will be useful for the future screening of high-impedance thermoelectric materials.

Improved thermoelectric properties of doped pentacene films were reported in 2011.[188] It was found that the electrical conductivity of an I_2-doped pentacene film decreased with increasing film thickness, and the obtained *PF* of 115 nm thick films was as high as 13 μW m^{-1} K^{-2} at room temperature. The stability of the I_2-doped pentacene film was also improved by encapsulating the doped films with a polyimide protective layer.

In addition to the development of n-type polymer thermoelectrics, very promising n-type thermoelectric performances have been reported in organic small molecules through the proper selection of dopants as well as an appropriate design of the molecular structure. Regarding molecular structure engineering and appropriate dopant selection, Koster et al. tailored the polarity of fullerene derivatives to enhance the miscibility between the host and dopant molecules.[189] They showed that functionalizing the fullerene with a hydrophilic triethylene glycol-type side chain led to a greatly improved doping efficiency of 18%, compared to <1% for the nonpolar side chain-functionalized reference fullerene using the same dopant concentration. The improved doping efficiency increased electrical conductivity, which reached a maximum of 2.05 S cm^{-1} and enabled a *PF* of 16.7 μW m^{-1} K^{-2}. They further improved their results by using as side chain a double ethylene glycol (PTEG-2) doped with 8 wt % N-DMBI, recording a high value of $zT > 0.3$ at 120 °C.[95] The obtained films showed an impressive *PF* of 80 μW m^{-1} K^{-2} coupled with an ultralow and constant thermal conductivity ($k < 0.1$ W m^{-1} K^{-1}) over the studied temperature range, exhibiting one of the highest *PF* values ever reported for a small-molecule semiconductor (Figure 16i).

Previously, Massetti et al. employed fullerene modified with a single ethylene glycol chain together with an inkjet printable formulation of PEDOT:PSS; this work was the first example of a monolithic and integrated μ-OTEG (Figure 17a), achieving a power density of 30 nW cm^{-2} at an external temperature difference of 25 K (Figure 17b,c).[190] The 128 thermocouples were defined inside plastic and flexible PEN film, thus limiting the thermal losses that are generally linked to the use of plastic substrates by using a combination of laser micromachining and inkjet printing; this method provided the first example of a complete printed and integrated OTEG.

Zhu et al. demonstrated that Bi, an excellent dopant that has been widely used in inorganic TE materials, allows for the interfacial doping of small molecules (sketch in Figure 17e), resulting in high n-type performance.[98] The electrical conductivity of thiophene-diketo-pyrrolopyrrole based quinoidal (TDPPQ) films in contact with a 2 nm thick Bi layer dramatically increased from <0.01 S cm^{-1} (undoped film) to 2.4 S cm^{-1}, while the Seebeck coefficient was only slightly affected. With a thicker Bi film, the electrical conductivity became saturated, while the Seebeck coefficient began to drop. A maximum *PF* of 62 μW m^{-1} K^{-2} was reached at 20 °C for an

https://doi.org/10.1021/acs.chemrev.1c00218
Chem. Rev. XXXX, XXX, XXX−XXX

optimized Bi thickness of 2 nm (Figure 17f), and these values increased to 113 μW m^{-1} K^{-2} at a higher temperature (60 °C).

In contrast to the extrinsic doping approach, a solution-processable and self-doped small-molecule perylene diimide (PDI) was reported by Russ et al.[191] Quaternary amine substituents containing different spacer groups were used to functionalize the PDI molecule. The electrical conductivity increased 100-fold when the alkyl spacer groups between quaternary amine substituents and the PDI core increased from two (PDI-1) to six (PDI-3) methylene units, reaching values as high as 0.5 S cm^{-1}. All three PDIs had an n-type Seebeck coefficient of ~ -200 μV K^{-1}, regardless of the alkyl spacer length. Thus, a *PF* as high as 1.4 μW m^{-1} K^{-2} was obtained for the PDI-3 film.

Zhu et al. demonstrated that small changes in the conjugated molecular structure dramatically affected the thermoelectric performance of small molecules. For example, by going from a quinoid to an aromatic structure, a 50 times higher *PF* with values up to 236 μW m^{-1} K^{-2} was achieved for chemically doped dihydropyrrolo[3,4-*c*]pyrrole-1,4-diylidene)bis(thieno[3,2-*b*]-thiophene) derivatives.[99] Experimental analysis and theoretical calculations revealed that the aromatic structure provided the molecule high electron mobility and appropriate energy levels for a more efficient doping reaction with N-DMBI. Because of the low in-plane thermal conductivity of 0.34 W m^{-1} K^{-1}, a high *zT* value of 0.23 was measured at 373 K, which was the highest value reported to date for small-molecule organics. Kemerink et al. investigated the n-type thermoelectric properties of [6,6]-phenyl-C61-butyric acid methyl ester (PCBM) for different solution-based doping methods.[192] The authors presented a novel inverse-sequential doping method where PCBM was deposited on a previously cast N-DMBI dopant film, achieving a *PF* as high as 35 μW m^{-1} K^{-2} with a conductivity of 0.40 S cm^{-1}. The authors also showed that adding a small fraction of higher electron affinity material (i.e., core-cyanated naphthalene diimide) into PCBM could lead to a higher *S*. This addition creates a second "trap" in the DOS, leading to a sharp increase in the Seebeck coefficient while at the same time decreasing the electrical conductivity. In addition, they presented a simple analytical model to unify the thermopower and conductivity of both p- and n-type TE materials and found good consistency between the experimental and calculated data. Remarkably, they found that most of the p-type data were described well by the model using a hop frequency of approximately $0.5-5 \times 10^{11}$ s^{-1}, whereas a higher frequency of about $0.5-5 \times 10^{13}$ s^{-1} was required for n-type data, implying that n-type organic semiconductors seemed to have more potential to eventually achieve higher *zT* than p-type materials.

4.1.4. Thermal Transport in Organic Semiconductors.

So far, we mainly focused on showing different ways to enhance the *PF* of organic thermoelectric materials, trying to match the values of bismuth-telluride alloys. However, to achieve higher *zT*, thermal conductivity is another critical parameter that must be optimized. The thermal conductivity (k) of organic (semi-)conductors is generally considered to be lower than 1 W m^{-1} K^{-1}.[193] However, similarly to the electrical conductivity, thermal conductivity in organic semiconductors is also an anisotropic property, as heat transport is generally more efficient along the chain direction than between chains. This is due to the weak nature of the van der Waals interactions between adjacent chains and/or the formation of lamella separated by the side chains, which limit the phonon and electron transport, thus reducing the lattice and the electronic components of the thermal conductivity. Therefore, in many organic semiconductors, such as P3HT or PBTTT-C_{14}, it is possible to observe a significant anisotropy factor from the in-plane to the out-of-plane direction, showing larger phonon propagation distances along the π-conjugated backbone.[194] Stretch-aligning semi-crystalline or amorphous polymer films/fibers also drastically increases the phonon propagation, with k values along the stretching direction being more than 1 order of magnitude higher than those perpendicular to the stretching direction.[195−197] For example, k = 40 W m^{-1}K^{-1} was recorded along the polyethylene axis in crystalline films, while the transverse value of k was around 100 times lower (around 0.3−0.4 W m^{-1}K^{-1}).[195] In addition, molecular dynamic (MD) simulations have shown a correlation between high thermal conductivities and rigidity of the polymer backbone due to the suppressed segmental rotations, leading to long-distance phonon propagation (that is, higher persistence length).[198] The increase of the persistence length is also linked to higher charge carrier mobility, which is also a critical parameter for σ and *S*, and thus further complicating independent optimization of the material parameters that determine *zT*. Therefore, to maximize the thermoelectric properties, the effect of polymer backbone rigidity on the lattice component of the thermal conductivity needs to be considered when designing new conducting polymers.

Furthermore, the process of doping organic semiconductors not only increases the electrical conductivity but also leads to a rise of the electronic component of k under the Wiedemann−Franz law ($k \propto L\sigma$, where L is the Lorenz number).[199] While noticeable for conductivities above 10 S cm^{-1}, this effect becomes predominant for σ exceeding 500 S cm^{-1}, as shown for PEDOT:PSS.[199,200] To further understand the impact of charge carriers on thermal conductivity, Kemerink et al.[201] analyzed the effect of energetic disorder and correlation length on the relationship between σ and k. Monte Carlo (MC) simulations showed that lowering the energetic disorder is a key strategy to reduce L (up to 5 times lower than the Sommerfield value). This decreases the contribution of charge carriers to the thermal conductivity and improves the thermoelectric figure of merit.

Finally, Campoy-Quilles et al. showed how, counterintuitively, the doping process (at least for low dopant concentrations) might be beneficial to reduce the thermal conductivity.[202] For the system PBTTT doped with F_4TCNQ, they observed that both annealing temperature (acting on the size of the polymeric crystalline domains) and doping process (at doping concentrations < 1 mol %) can be used to tune the thermal conductivity of PBTTT. In particular, they observed a 2-fold reduction in the value of k without significantly affecting the crystalline quality of the film. This process resembles the effect of phonon scattering observed in inorganic alloys.

Overall, while several theoretical studies have enhanced our understanding of thermal transport in organic semiconductors, more research needs to be done to enable a proper control of σ, *S*, and k. Here, we want to stress the critical role of anisotropy on the thermoelectric properties of organic semiconductors and the importance of measuring and correlating all thermoelectric parameters in the same direction. For a more detailed theoretical description of the physics behind heat transport in organic semiconductors, we refer the reader to the following seminal works.[203−206]

https://doi.org/10.1021/acs.chemrev.1c00218
Chem. Rev. XXXX, XXX, XXX−XXX

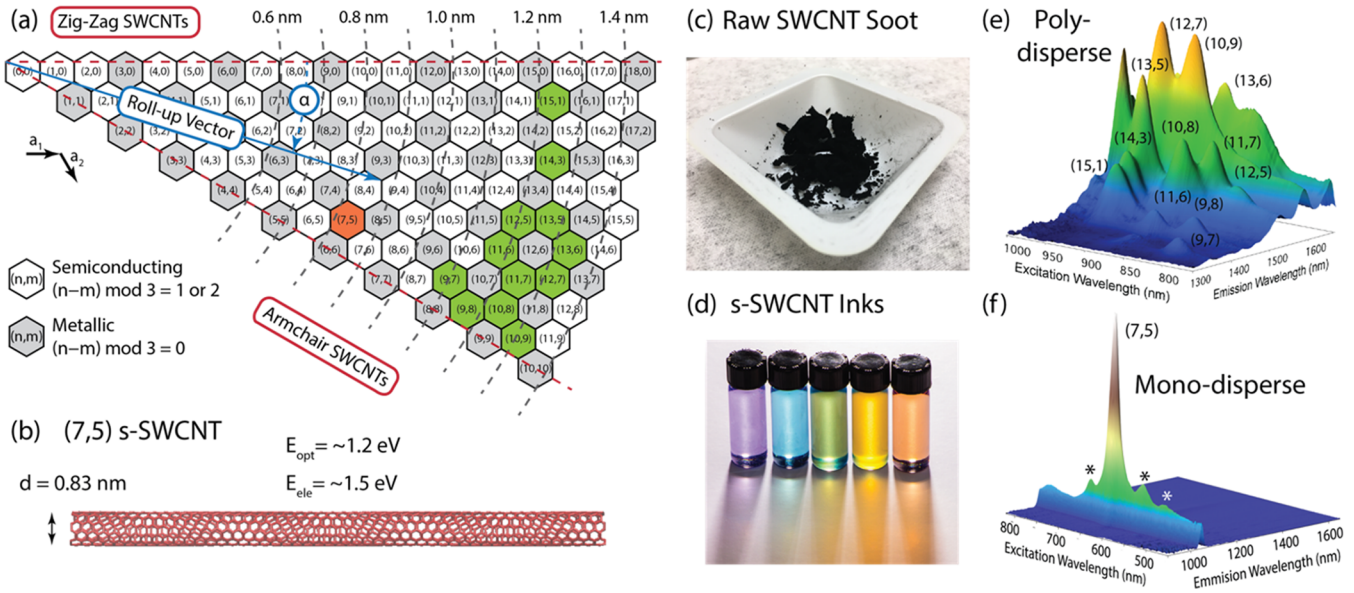

Figure 18. (a) Schematic of a section of a graphene sheet, showing the chiral indices (n,m) of SWCNTs formed by rolling the sheet from (0,0) to (n,m) along a roll-up vector (blue line). White hexagons correspond to (n,m) indices of semiconducting SWCNTs, while gray hexagons correspond to metallic SWCNTs. The green hexagons and orange hexagon correspond to the s-SWCNT species present in the polydisperse and monodisperse samples for which PL are displayed in (e) and (f). (b) Chemical structure of the (7,5) s-SWCNT, illustrating the nanotube diameter as well as the optical and electronic bandgap energies. (c) Photograph of raw SWCNT soot produced by the laser vaporization (LV) method. (d) Photograph of semiconducting SWCNT inks prepared by selective extraction with polyfluorene polymers. The color of each ink is determined by the diameter distribution of dispersed s-SWCNTs. (e) Photoluminescence excitation (PLE) map of polydisperse SWCNT sample with many s-SWCNTs present (green hexagons, a), each s-SWCNT peak labeled by its (n,m) indices. (f) The PLE map of a monodisperse sample is dominated by a single species, in this case the (7,5) s-SWCNT (orange hexagon, a). Phonon sidebands of the (7,5) excitation spectrum are labeled with asterisks.

4.2. Carbon Nanomaterials

Carbon nanomaterials (CNMs) such as carbon nanotubes (CNTs) and graphene have received a great deal of attention over the past decades for energy conversion, storage devices, catalysts, and biosensors. Both CNTs and graphene are composed of an extended hexagonal lattice of sp^2-bonded carbon atoms, which renders exceptional electrical, optical, thermal, chemical, and mechanical properties. CNTs and graphene high electrical conductivities, resulting from nearly identical and small effective masses for electrons and holes,[207] make them interesting candidates for thermoelectric applications. At the level of an individual CNT or an isolated graphene sheet, this high electrical conductivity is offset by the strongly disadvantageous property of high intrinsic thermal conductivity for both materials.[207] Additionally, the Seebeck coefficient is relatively low for both semimetallic graphene, multiwalled carbon nanotubes (which statistically are mostly metallic) and the ca. 33% of as-produced single-walled carbon nanotube (SWCNT) samples that have metallic electronic structure.[208] Thick CNTs layers, often composed of unaligned "bundles and mats" can have much lower electrical and thermal conductivities than individual CNTs due to electrical and thermal contact resistances between bundles. Composites of CNTs/graphene with polymers (or inorganic materials) can potentially decouple electrical and thermal conductivity by introducing interfaces that provide more facile paths for electron transfer than phonon transfer. Additionally, the introduction of interfaces provides an opportunity to realize carrier energy filtering to decouple the thermopower and electrical conductivity. Molecular dopants offer a means to tune the dark carrier density and may also introduce sites that effectively scatter phonons. The complex interrelationship between the thermopower, electrical conductivity, and thermal conductivity in nanocarbon materials and composites should remain an active area of fundamental research. Furthermore, recent strategies for separating SWCNTs by electronic structure and systematic tuning of the Fermi level by doping have enabled the realization of high thermoelectric power factors for both semiconducting and metallic SWCNT networks. Some of these results have been recently reviewed.[208] Here we take specific remarkable examples of those achievements while also focusing on a number of new achievements that have emerged in this fast-moving field over the past few years since that review.

4.2.1. Synthesis, Processing, and Basic Properties of SWCNTs. Single wall carbon nanotubes (SWCNT), discovered in 1991, can be thought of as a graphene sheet that has been wrapped up into a seamless cylinder (Figure 18a).[209] Early studies utilizing scanning tunneling microscopy and spectroscopy found that both metallic and semiconducting carbon nanotubes existed, depending sensitively on the wrapping angle.[210] SWCNTs can be produced by a number of different methods and the resulting material properties can depend quite sensitively on the production method. Synthesis methods include chemical vapor deposition (fixed bed, fluid bed, floating catalyst, and plasma enhanced), laser vaporization, and arc discharge.[211]

Most synthetic routes to produce SWCNTs produce the statistically expected ratio between those two forms with 1/3 of metallic tubes (m-SWCNT) and 2/3 of semiconducting tubes (s-SWCNT). As such, most syntheses tend to produce raw SWCNT soot that is black (Figure 18b) because it contains a polydisperse mixture of many SWCNTs (Figure 18e) that absorb with different wavelengths. However, a number of effective strategies have been perfected over the past decade to separate s-SWCNTs and m-SWCNTs by electronic structure (Figure 18d,f).[212] The optical bandgap of s-SWCNTs is

https://doi.org/10.1021/acs.chemrev.1c00218
Chem. Rev. XXXX, XXX, XXX−XXX

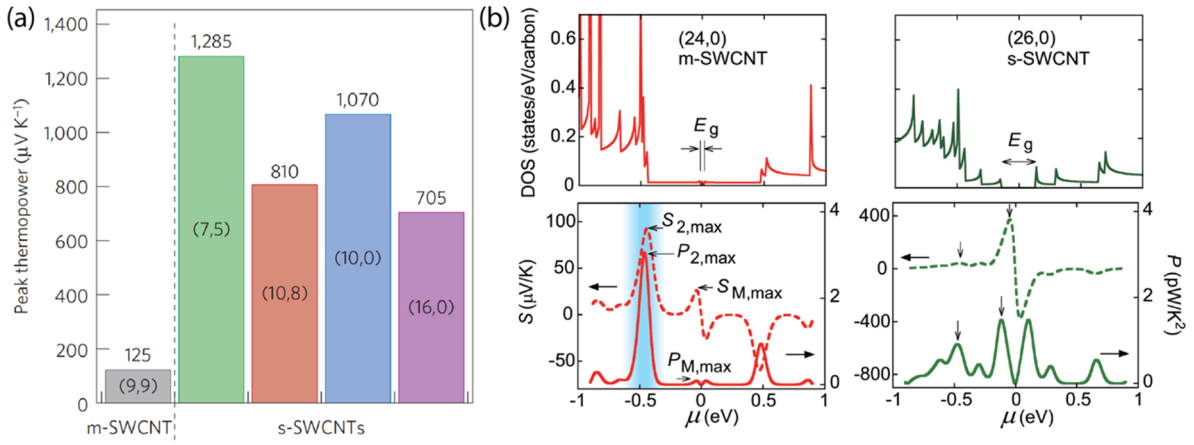

Figure 19. (a) Thermopower for five s-SWCNT species and one m-SWCNT species, calculated by density functional theory (DFT). Reproduced with permission from ref 9. Copyright 2016 Springer Nature. (b) Typical calculated results for (top panels) the electronic density of states and (bottom panels) Seebeck coefficient (dashed lines) and power function (solid lines) for (24,0) m-SWCNT and (26,0) s-SWCNT as a function of chemical potential (μ). Reproduced with permission from ref 233. Copyright 2016 IOP.

inversely dependent on diameter and varies from ca. 0.5 to 1.4 eV for a corresponding diameter range of 2.6−0.6 nm that is typical of most commonly used synthesis routes.[213] Given the relatively large diameter-dependent exciton binding energy,[214] this translates to an electronic bandgap (the relevant metric for thermoelectrics) of ca. 0.6−1.8 eV.

As-produced SWCNT samples typically consist of long (>1 μm) SWCNTs that are present in large bundles, consisting of, e.g., 10 or more SWCNTs, due to van der Waals attractions between nanotubes. A general strategy for incorporating SWCNTs into solid-state films required for applications such as thermoelectrics involves dispersing the SWCNTs into a solvent by ultrasonic processing. Coupled with a broad variety of surfactants, dispersing polymers, and solvents with varying Hansen solubility parameters, such processing routes can be used to produce a wide range of SWCNT dispersions in aqueous or organic solvents with or without a dispersing agent.[215−218] These dispersions can then be deposited into films and structures of varying form factor by a number of different deposition methods, including vacuum filtration, spin-coating, ultrasonic, or pressure-driven spray deposition, ink-jet printing, blade coating, Gravure printing, and others.[219] Aqueous and organic solvent-based dispersions are also the starting points for most separations of SWCNTs by electronic structure, diameter, and chirality. The most relevant separation/enrichment strategy for TE applications is the separation of as-prepared SWCNT soot into populations of pure semiconducting, pure metallic, or tunable populations with controlled metal/semi ratios. Many separation techniques are applicable to aqueous SWCNT dispersions, including density gradient ultracentrifugation,[216,220] column chromatography separation,[221] and aqueous two-phase extraction.[222,223] A predominant strategy for selective enrichment of semiconducting SWCNTs in organic solvents involves the use of polymers that preferentially wrap and disperse s-SWCNTs, leaving m-SWCNTs undispersed.[224,225] These polymer-wrapped s-SWCNT inks tend to have vibrant tunable colors, due to the selection of a relatively narrow subset of s-SWCNTs (Figure 18d).

The cavitation energy in ultrasonic dispersion processes is used to debundle the SWCNTs, with an unavoidable side-effect being the progressive cutting and shortening of the SWCNTs with increasing sonication time. Because electrical conductivity in an electronically coupled SWCNT network scales with increasing length of the individual nanotubes, the thermoelectric properties of such ultrasonic-processed SWCNTs is generally degraded as the sonication time is increased.[226] Because of the ultrasonic-induced shortening of SWCNTs, new routes are being explored for less severe processing of SWCNTs for opto-electronic applications. Recent studies have demonstrated shear-force mixing as an attractive alternative to ultrasonic processing.[227] Shear-force mixing does not feature any cavitation forces and has been shown to enable the dispersion of very long SWCNTs with retained electrical and optical properties. Another strategy that has emerged involves using as-produced SWCNTs that are never subjected to any ultrasonic or shear-force solution-phase processing.[228−231] Such samples tend to be highly fibrous interwoven SWCNT mats produced by floating catalyst chemical vapor deposition (FCCVD). Such mats can be gently processed by simple densification steps or spinning steps to produce high-density mats or fibers, respectively, that can be used directly in thermoelectric applications. We discuss these advances in section 4.2.3.

4.2.2. Tunable Thermoelectric Performance of "Neat SWCNTs". Before discussing the role(s) of CNTs for enhancing thermoelectric composites, we first consider the thermoelectric properties and performance of SWCNTs on their own. The understanding of this important model system is derived from the extensive research devoted to the control of the electronic structure with the goal to fine-tune the Seebeck coefficient and the electrical conductivity. The tuning of these properties has been achieved by controlling the ratio of semiconducting vs metallic, the presence of multiwalls possessing specific electronic properties, the doping by replacement of atoms in the tubes, or by redox reaction with another external chemical species. Here, we summarize some of the key advances and strategies employed for tuning, optimizing, and mechanistically understanding the thermoelectric performance of "neat" SWCNT samples. Several years ago, important computational work demonstrated that the Seebeck coefficient can be (1) particularly large in pure s-SWCNTs (Figure 19a) and (2) modulated with high sensitivity through doping (Figure 19b).[9,232,233] Specifically, around 2015, a number of groups predicted exceptionally large peak thermopowers for s-SWCNTs that could exceed 1 mV K^{-1} and that depended sensitively on Fermi energy.[9,232,233] Other

https://doi.org/10.1021/acs.chemrev.1c00218
Chem. Rev. XXXX, XXX, XXX−XXX

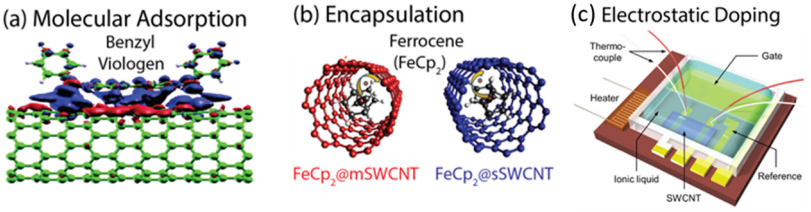

Figure 20. (a) Example of molecular doping of SWCNTs, in this case, n-type doping by adsorption of benzyl viologen to the SWCNT surface. Reproduced with permission from ref 234. Copyright 2009 American Chemical Society. (b) Example of m-SWCNT (left) and s-SWCNT (right) doped n-type by encapsulation of ferrocene molecules. Reproduced with permission from ref 240. Copyright 2014 IOP Science. (c) Schematic of electrolyte gating experimental setup for measuring thermoelectric properties of carbon nanotube films. Reproduced with permission from ref 248. Copyright 2019 American Chemical Society.

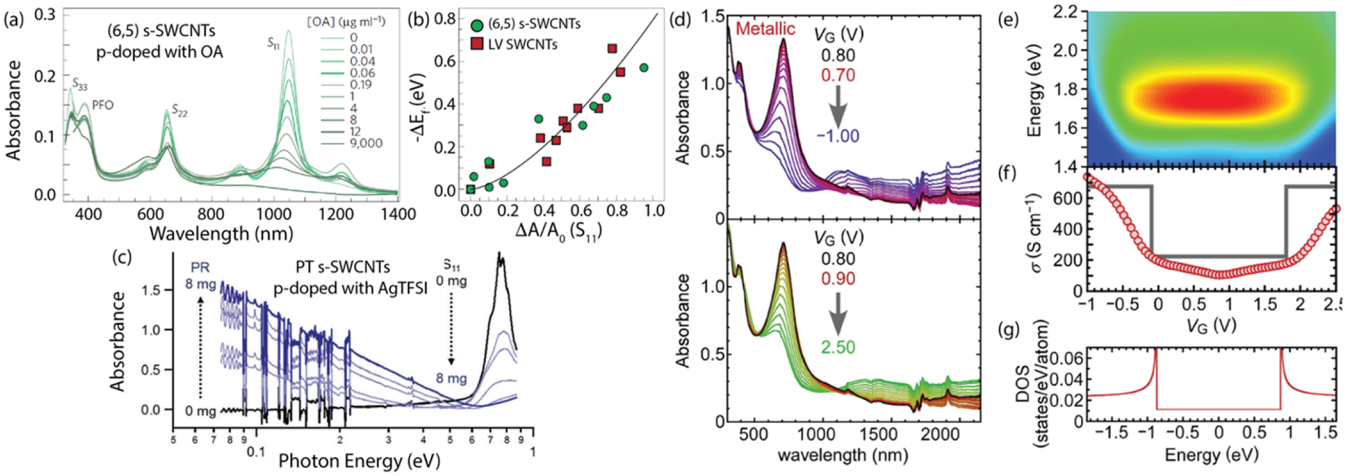

Figure 21. (a) Evolution of (6,5) s-SWCNT network optical absorption as a function of p-type dopant (OA) concentration that the film is soaked in, showing S_{11} transition quenching. (b) Change in Fermi level (ΔE_f) for (6,5) or LV SWCNTs as a function of the degree of S_{11} quenching for progressively p-doped networks. (a,b) Reproduced with permission from ref 9. Copyright 2016 Springer Nature. (c) Plasma-torch s-SWCNTs progressively doped with AgTFSI, showing that the plasma resonance (PR) grows in as the S_{11} is quenched. Reproduced with permission from ref 254. Copyright 2018 Taylor & Francis. (d) Evolution of absorption spectrum for arc-discharge m-SWCNTs with gate voltage (V_g). (e) Contour map of absorbance for same m-SWCNT sample as a function of absorbed photon energy and gate voltage. (f) Conductivity of the same m-SWCNT sample versus gate voltage. (g) Schematic diagram of density of state for the (15,6) s-SWCNT, chosen as representative of the arc-discharge SWCNTs. (d–g) Reproduced with permission from ref 243. Copyright 2014 Wiley.

predictions also suggested multiple maxima in the Seebeck and power function due to the sharp van Hove singularities (vHS) of SWCNTs, especially in cases where the Fermi energy overlapped with a region of energy comprising multiple closely spaced vHS (e.g., Figure 19b, left).[233]

Even though CNTs had been studied in TE composites for many years by that point, these exciting predictions and associated experiments jump-started a renewed interest in the ultimate potential of neat SWCNT-based TE materials. By neat, we mean SWCNT thin films and samples where the SWCNTs can be considered the primary or sole transport medium, as opposed to SWCNT-based composites, where transport within both the SWCNT and matrix material(s) must be considered in concert. This is not to say that such films are comprised solely of SWCNTs; for example, many of these SWCNT networks contain residual "wrapping" polymer that was used to disperse the SWCNTs and most optimized networks include dopant molecules used to tune the Fermi energy and carrier density (in direct analogy to semiconducting polymer thermoelectrics). The important distinction employed in the following conversation is that the dominant charge transport pathways in "neat" SWCNT samples are the nanotubes and bundles themselves and not these secondary phases.

We break this section into subsections based on critical considerations for employing neat SWCNTs as thermoelectric materials. First, we discuss the noncovalent and covalent functionalization and doping strategies used to tune the thermoelectric properties of neat SWCNT networks. These can generally be applied to either mixed (semi/metal) samples or samples of highly pure s-SWCNTs or m-SWCNTs. Next, we discuss solution-processed SWCNTs that have been separated by electronic structure to explore the dependence of TE performance on the proportion of s-SWCNTs, m-SWCNTs, and the doping-controlled carrier density. Finally, we discuss the anisotropy of the TE transport properties within highly aligned SWCNT samples.

4.2.2.1. Noncovalent Functionalization and Doping. Because of the strong dependence of conductivity and thermopower on Fermi energy, a dominant route used to optimize the TE performance of CNTs involves tuning the electronic structure, carrier density, and Fermi level via noncovalent doping. The most typical strategy for noncovalent doping of SWCNTs is molecular redox doping, which involves exposing CNTs to organic molecules with strong electron donor or acceptor character to promote spontaneous electron transfer to/from the SWCNTs. Molecules can be adsorbed onto the surfaces of SWCNTs (Figure 20a)[9,234−237] and/or may be

https://doi.org/10.1021/acs.chemrev.1c00218
Chem. Rev. XXXX, XXX, XXX−XXX

encapsulated within the endohedral volume of the SWCNTs (Figure 20b).[238−242] Donor molecules with HOMO values closer to vacuum than the first SWCNT conduction level (c_1) values serve as reductants, injecting electrons into the SWCNTs that can contribute to electrical conductance in a coupled SWCNT network. In contrast, acceptor molecules with LUMO values farther from vacuum then the first SWCNT valence level (v_1) serve as oxidants, removing electrons from SWCNTs to produce mobile holes in SWCNT networks. Another noncovalent method for doping SWCNT networks involves electrostatic gating in an electrochemical transistor-based (FET) geometry (Figure 20c). This method is particularly useful for systematically tuning the Fermi level with relatively fine control in both the p- and n-type regimes.[243] Several studies have used this strategy to perform simultaneous measurements of conductivity and thermopower to probe the p- and n-type *PF* of a variety of SWCNT samples.[243−248]

Quantitative correlation of TE properties with carrier density and Fermi level is a difficult task with disordered organic semiconductors such as semiconducting polymers and SWCNTs. A significant amount of research is still devoted to understanding the appropriate analyses needed to make these correlations in SWCNTs, and we point the reader to a couple of recent book chapters[249,250] and another recent study.[251] Briefly, optical and infrared spectroscopies are particularly useful for tracking the doping-induced modifications to the carrier density of SWCNTs. The strong excitonic optical transitions for s-SWCNTs in the visible and near-infrared are particularly sensitive to the carrier density, due to impact of phase space filling by charge carriers on the oscillator strength of excitonic transitions (Figure 21a,b). Because a direct estimation of areal or volumetric carrier density in SWCNTs can be quite challenging, the relative strengths of these optical transitions are routinely tracked as a function of doping as a proxy for the carrier density in a s-SWCNT network. X-ray photoelectron spectroscopy can also be used to probe the change in Fermi level, as a function of systematic changes in doping level because the kinetic energy of photoelectrons are referenced to the Fermi level (Figure 21b).[9,235,252,253]

Nonoguchi et al. demonstrated that the plasmon resonance of free charge carriers in the infrared can also be used to systematically track relative carrier density in s-SWCNTs (Figure 21c).[254] While most molecular doping strategies do not modify the Fermi level strongly enough to quench the relatively high-energy excitonic transitions of m-SWCNTs,[255] the plasmon resonance intensity can report on systematic changes to the carrier density in m-SWCNTs.[256] However, electrostatic gating has been shown to be effective in modulating the Fermi level to a large enough degree to quench m-SWCNT excitonic transitions (Figure 21d,e), and the doping-induced tuning of the Fermi level increases the conductivity for both s- and m-SWCNTs, as shown in Figure 21f,g for electrostatic doping of m-SWCNTs.[243]

A wide variety of redox molecules can p/n-dope SWCNTs. Early doping work centered around aggressive acids and bases, many of which were known from decades of research to intercalate graphite. Bronsted acids such as nitric, sulfuric, and chlorosulfonic acids are widely known to produce p-type SWCNTs,[257] as are halide gases with large electronegativities such as bromine and iodine.[258] Alkali metals such as sodium, lithium, and cesium were shown in early SWCNT research to produce n-type SWCNTs.[259] A wide variety of Lewis acids and bases has been explored for doping SWCNTs and other types of CNTs.[260] Some basic trends are as follows. Aromatic dopants functionalized with highly electron-withdrawing groups (e.g., F, CF_3, CN) tend to serve as good oxidants for producing p-type SWCNTs. Some examples include tetracyanoquinodimethane (TCNQ), tetracyanobenzene (TCNB), and many of their derivatives (e.g., F_4-TCNQ, etc.). Transition metal chlorides such as $FeCl_3$,[230,231,261,262] $AuCl_3$,[228] and AgCl[242] also tend to be good p-type dopants for SWCNTs. The reactivity of very strong chloride-based oxidizing agents such as $SbCl_5$ can be difficult to control, leading to both oxidation and chlorination of aromatic species.[263] As such, these acids can be "masked" with alkyloxonium cations (e.g., as triethyloxonium hexachloroantimonate [$Et_3O^+SbCl_6^-$]) to produce strong oxidants that exclusively form aromatic radical cations due to electronic doping (i.e., electron extraction from the HOMO of the aromatic system) without concomitant side-wall chlorination or alkylation.[264] Triethyloxonium hexachloroantimonate (abbreviated here as OA) has been used to produce p-type SWCNTs with conductivity that is both highly tunable[9,208,252,253,265] and relatively stable in ambient conditions.[266]

Bis(cyclopentadienyl)M(II) compounds with the formula $M(C_5H_5)_2$, where M is a transition metal (e.g., cobaltacene,[238] ferrocene,[239] nickelocene), tend to have small ionization potentials and serve as good reductants. Several studies have shown that these n-type dopants can actually be encapsulated within SWCNTs during the doping process,[238,241] which provides a unique strategy for improving the stability of n-type doping (vide infra). A number of amine-, imine-, and phosphine-based molecules also have ample reducing strength to produce n-type SWCNTs, as demonstrated by a few survey studies of such molecules.[235,236] These include molecules such as hydrazine, ethylenediamine, methylamine, diethylamine, oleylamine, diphenylphosphine, triphenylphosphine, and associated derivatives, as well as polymers such as polyethylenimine (PEI).[50,235,236] PEI has been especially popular for *n*-type doping of SWCNTs in TE applications,[228,230,267−270] in large part for the relative stability imparted by the viscous polymer that tends to coat SWCNTs well and be somewhat impermeable to atmospheric ingress.[235,236] Reduced viologens are also highly reductive and have been used widely to produce *n*-type SWCNTs.[231,234,252,262]

Because of rapid compensation of electrons by oxygen and/or water molecules, n-type dopants tend to be significantly less stable than their p-type counterparts, so a significant amount of research has been devoted to developing means by which to improve n-type doping stability for TE applications of CNTs. Fukumaru et al. succeeded in intercalating cobaltocene ($CoCp_2$) inside the tubes to transform a p-type into a n-type SWCNT (Seebeck coefficient = −41.8 μV K^{-1}), with a superior air stability due to the molecular shielding effect.[241] Electron transfer from encapsulated $CoCp_2$ increased the carrier density in the s-SWCNTs and the electrical conductivity of the CoCp2@SWCNT film reached 432 S cm^{-1}, compared to 44.5 S cm^{-1} for empty SWCNTs. The power factor of the CoCp2@SWCNT film was 75.4 μW m^{-1} K^{-2}, and combined with a low thermal conductivity of 0.15 W m^{-1} K^{-1}, a zT value of 0.157 was achieved at 320 K (zT = 0.025 without $CoCp_2$ doping).[241]

Nonoguchi et al. demonstrated air stability for mixed SWCNTs n-type doped with a variety of phosphine-, amine-, and imine-containing aromatic dopants[236] and also demonstrated a strategy for combining ordinary salts such as sodium chloride (NaCl), sodium hydroxide (NaOH), and potassium hydroxide (KOH) with crown ethers for the production of

https://doi.org/10.1021/acs.chemrev.1c00218
Chem. Rev. XXXX, XXX, XXX−XXX

stable n-type SWCNTs (Figure 22a).[237] The stable complexes formed between crown ethers and metal-ions enhances the

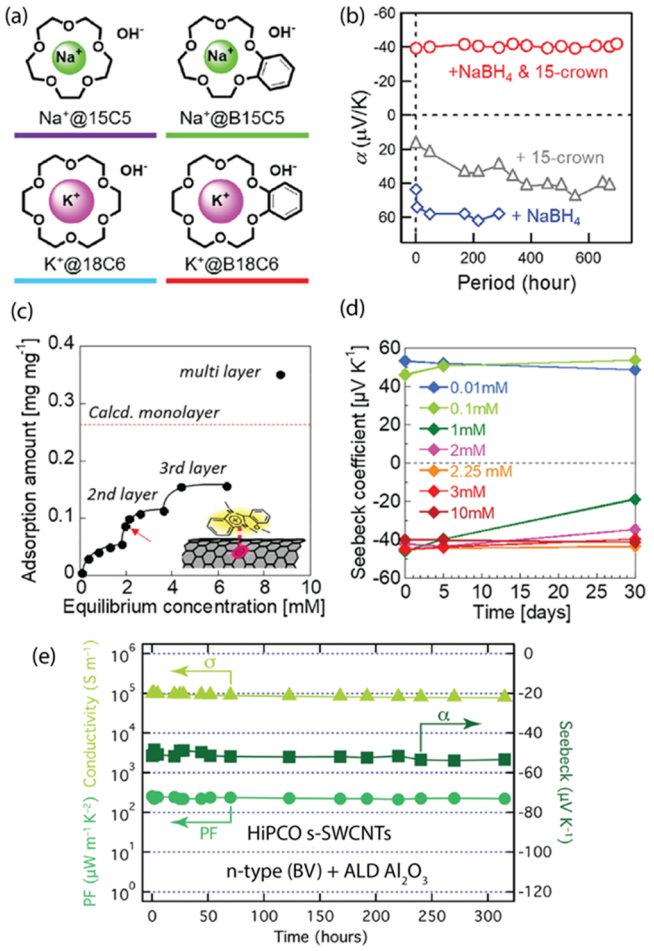

Figure 22. (a) Benzo-crown ether-stabilized alkali metal n-type doping strategy developed by Nonoguchi et al. (b) Only the crown ether-stabilized metal salt succeeds in doping the SWCNTs n-type, whereas the isolated crown ether and sodium borohydride do not. (a,b) Reproduced with permission from ref 237. Copyright 2016 Wiley. (c) Adsorption isotherms of o-MeO-DMBI on SWCNT networks showing formation of multiple layers on the SWCNT surface. (d) n-Type stability is achieved only after the formation of the second layer of dopants. (c,d) Reproduced with permission from ref 271. Copyright 2019 American Chemical Society. (e) s-SWCNT networks doped n-type by potassium crown ether and BV are stable after encapsulation with 50 nm of Al_2O_3 via atomic-layer deposition. Reproduced with permission from ref 252. Copyright 2017 Royal Society of Chemistry.

reducing power of the "naked" counteranions, which enhances the electron donating ability of anions that would not typically reduce SWCNTs, such as OH^- or Cl^-, to enable n-type doping of SWCNTs (Figure 22b). A recent study from Nakashima et al. tracked adsorption isotherms of the n-type dopant 2-(2-methoxyphenyl)-1,3-dimethyl-2,3-dihydro-1*H*-benzo[*d*]-imidazole (o-MeO-DMBI) and found that the formation of multilayers was critical to achieving long-term stability of the n-type thermopower and *PF* (Figure 22c,d).[271]

We note here that while several of these doping strategies have provided relatively air-stable mixed SWCNTs (containing both s- and m-SWCNTs), their success has been more limited in highly pure s-SWCNT samples. This has motivated other strategies, such as physical encapsulation, for retaining n-type TE properties. As an example, MacLeod et al. encapsulated benzyl viologen-doped s-SWCNTs with Al_2O_3, deposited by atomic-layer deposition, to produce highly stable n-type s-SWCNTs (n-type *PF* > 400 μW m^{-1} K^{-2}, Figure 17e).[252] In contrast, identically prepared unencapsulated s-SWCNT networks swiftly transitioned to intrinsic networks with low *PF* values.[252] It remains a challenge to the field to explore the roles of electronic structure, diameter, dopant redox potential, temperature dependence, and encapsulation strategy on the stability of n-type SWCNT networks for durable TE applications.

4.2.2.2. Separated Semiconducting and Metallic SWCNTs. Semiconductors remain the predominant materials explored for thermoelectrics due to the Seebeck coefficient being particularly small for metals. As such, a natural progression for the field of SWCNT thermoelectrics involves understanding the role of SWCNT electronic structure, and several studies over the past several years have explored SWCNT samples with finely tunable populations of s- and m-SWCNTs. Nakai et al. (Figure 23)

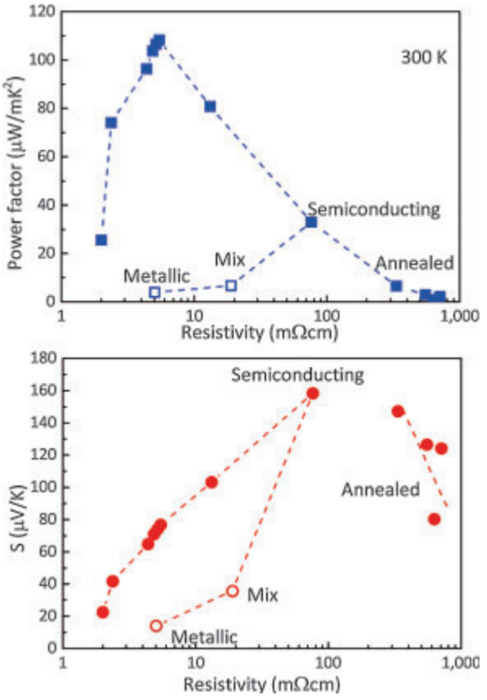

Figure 23. Power factor (top) and Seebeck coefficient (bottom) as a function of resistivity for s-SWCNT networks (filled symbols) and mixed or metallic SWCNT networks (open symbols). High resistivity data points for s-SWCNTs correspond to thermally annealed samples, while low-resistivity data points correspond to acid-doped p-type samples. Reproduced with permission from ref 272. Copyright 2014 IOP Science.

produced an early study on SWCNTs separated by density gradient ultracentrifugation (DGU), demonstrating an inherently low Seebeck coefficient for m-SWCNTs (10−20 μV K^{-1}) and high Seebeck coefficients for s-SWCNTs (80−160 μV K^{-1}).[272] Theoretical calculations that followed closely thereafter captured the high Seebeck coefficient in s-SWCNTs (up to ca. 2000 μV K^{-1}) and also found that a decrease in the diameter (increase in the band gap) of the s-SWCNT leads to higher Seebeck coefficients.[9,232]

These early studies suggested that one of the general issues leading to limited *PF* in films of doped-SWCNTs is the presence

https://doi.org/10.1021/acs.chemrev.1c00218
Chem. Rev. XXXX, XXX, XXX−XXX

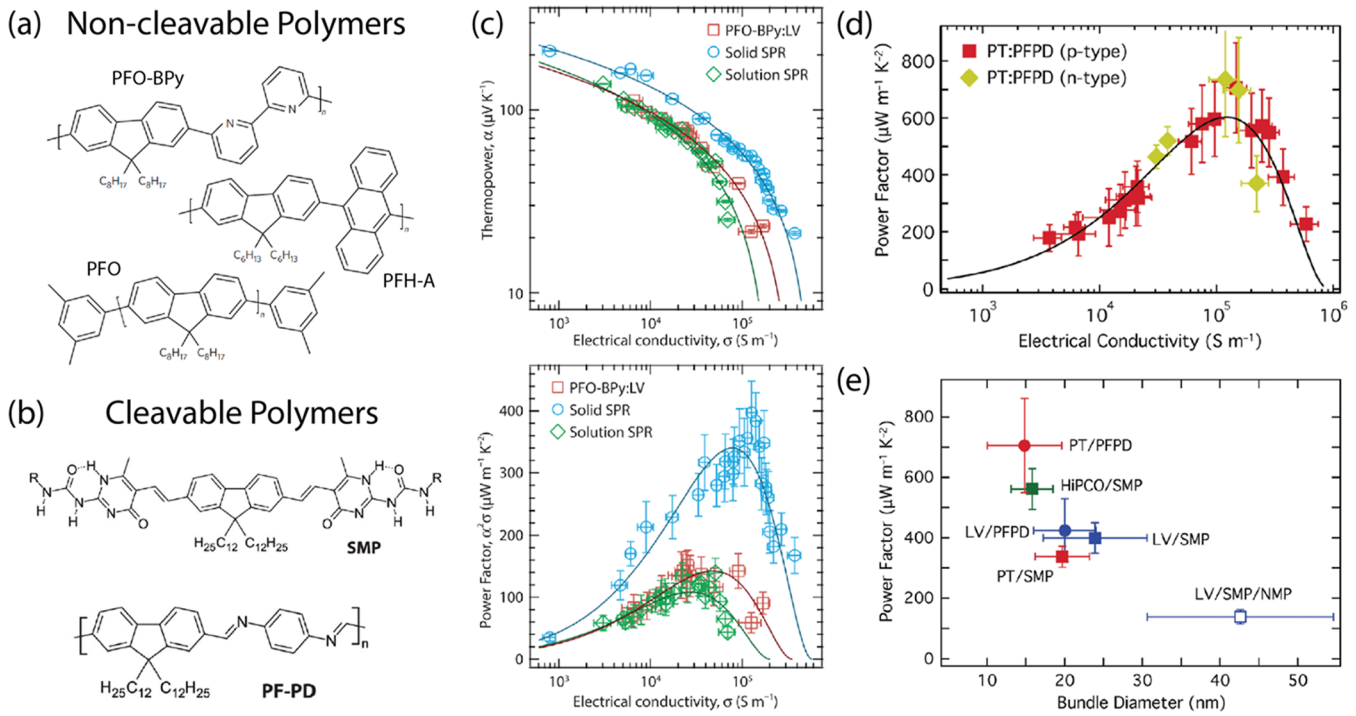

Figure 24. (a) Three noncleavable and (b) two cleavable polymers used to selectively disperse semiconducting SWCNTs from raw soot. (c) Dependence of thermopower (top) and power factor (bottom) on conductivity for controllably doped laser vaporization (LV) s-SWCNT films prepared from either noncleavable PFO-BPy polymer (red squares) or SMP cleavable polymer (green diamonds and blue circles). Green diamonds represent removal of the SMP polymer in solution before spray-depositing s-SWCNT network. Blue circles represent removal of the SMP polymer in the solid-state after spray deposition of the s-SWCNT network. (d) Dependence of power factor on conductivity for controllably doped plasma torch s-SWCNT network prepared with cleavable PFPD polymer, where the polymer was removed in the solid state. Red squares show p-type *PF* resulting from doping with triethyloxonium hexachloroantimonate and gold diamonds show n-type *PF* resulting from doping with benzyl viologen. (e) Dependence of power factor on average bundle diameter (analyzed via AFM) in various s-SWCNT networks. (c) Reproduced with permission from ref 265. Copyright 2016 American Chemical Society. (d,e) Reproduced with permission from ref 252. Copyright 2016 Royal Society of Chemistry.

of metallic m-SWCNT in quantities large enough to create percolation paths dominating the electronic transport and providing low Seebeck coefficient. Research at the National Renewable Energy Lab has attempted to address this issue through studies utilizing selective polymer-based enrichment of s-SWCNTs,[225] in conjunction with fine-tuning the Fermi level with molecular doping.[9,252,253,265] With these strategies, Avery et al. reached a p-type $PF = 340\ \mu W\ m^{-1}\ K^{-2}$ at the optimal doping level for s-SWCNT networks composed of ca. 1.0 nm average diameter s-SWCNTs.[9] The s-SWCNT networks produced in this study had some polyfluorene-based polymer remaining on s-SWCNT surfaces because typical "non-cleavable" wrapping polymers cannot be fully removed from the resulting s-SWCNT network (Figure 24a).

Follow-on work demonstrated that a polyfluorene wrapping polymer with easily cleavable hydrogen bonds between monomers (Figure 24b) enabled the improvement of the *PF* for a given SWCNT source material.[252,265] The first study demonstrated that the p-type *PF* of s-SWCNT networks prepared from enriched laser vaporization SWCNTs could be improved from ca. 150 $\mu W\ m^{-1}\ K^{-2}$ (noncleavable polymer) to 400 $\mu W\ m^{-1}\ K^{-2}$ by complete removal of the cleavable polymer (Figure 24c).[265] This result unambiguously confirms that the doped s-SWCNTs themselves are the sole source of the high TE performance in these networks. MacLeod et al. then expanded this approach by utilizing another cleavable polymer based on imine linkages between monomers.[252] The champion p-type *PF* of 700 $\mu W\ m^{-1}\ K^{-2}$ in this study belonged to polymer-free s-SWCNT networks prepared from plasma torch synthesized SWCNTs enriched by the imine-based cleavable polymer (Figure 24d). This study also demonstrated that, due to the equivalent electron and hole effective masses in SWCNTs, n-type s-SWCNT thin films with equally large *PF* could be produced by utilizing an amine-based n-type dopant (Figure 24d). The peak *PF* correlated inversely with the average diameter of s-SWCNT bundles in the network (Figure 24e). Huang et al. also demonstrated a flavin-based s-SWCNT extraction method, whereby the TE performance metrics were improved by 2 orders of magnitude when the flavin was fully removed from the s-SWCNT network.[273]

The thermal conductivity of mixed SWCNTs and enriched s-SWCNTs has also received significant attention recently, with several intriguing questions remaining to be answered. Avery et al. found that the thermal conductivity of undoped s-SWCNT networks was relatively high (k = 16.5 W m^{-1} K^{-1}) and dominated by phonons because the network was not electrically conductive (Figure 25a).[9] This value matches quite well with the values reported by Huang et al., ≈ 10 W m^{-1} K^{-1} for undoped electronically sorted SWCNT networks and ≈16 W m^{-1} K^{-1} for an undoped and unsorted SWCNT network (Figure 25b).[274] Avery et al. found that doping the network dramatically lowered the thermal conductivity to k = 2 − 4.5 W m^{-1} K^{-1}.[9] For optimally doped polymer-free s-SWCNT networks, this relatively low thermal conductivity has led to the realization of zT values in the range of ca. zT = 0.01−0.12.[9,252] This study and the subsequent follow-up demonstrated that there is a small, but real, electronic contribution to the thermal conductivity because k increases weakly with carrier density but in a fashion that is

https://doi.org/10.1021/acs.chemrev.1c00218
Chem. Rev. XXXX, XXX, XXX−XXX

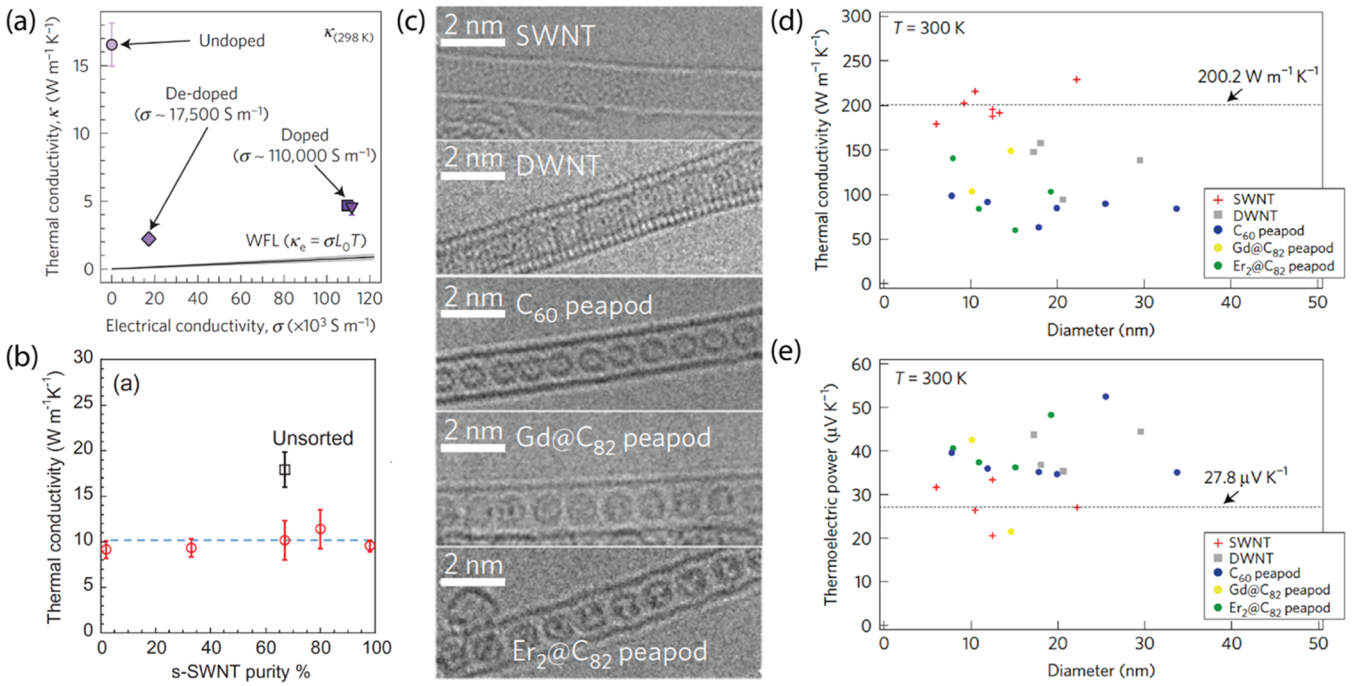

Figure 25. (a) Dependence of thermal conductivity on electrical conductivity for redox-doped s-SWCNTs at T = 298K. The trend line in the lower portion of the plot shows the dependence expected for the electrical component of thermal conductivity (κ_e) by the Wiedemann–Franz law. Reproduced with permission from ref 9. Copyright 2017 Springer Nature. (b) Dependence of thermal conductivity for SWCNT networks on the ratio of semiconducting and metallic SWCNTs (red circles). Also shown is the value measured for an unsorted network (black square). Reproduced with permission from ref 274. Copyright 2019 Taylor & Francis. (c) TEM images of unfilled SWCNTs and DWCNTs, along with CNTs filled with fullerenes. (d) Thermal conductivity (κ) and (e) thermopower (S) of fullerene-encapsulated CNT bundles measured at T = 300 K as a function of the CNT bundle diameter. The dashed lines show the average κ and S values of SWCNTs measured between different samples. (c–e) Reproduced with permission from ref 276. Copyright 2017 Springer Nature.

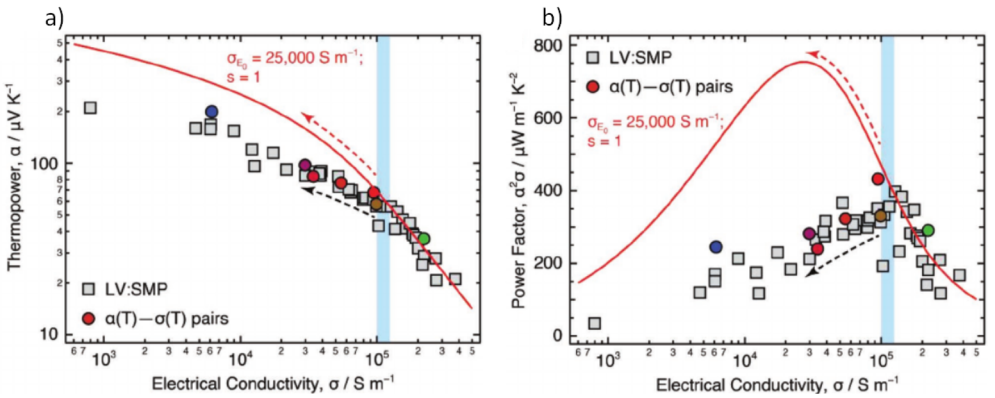

Figure 26. Room temperature thermopower (a) and power factor (b) for polymer-free ~1.3 nm diameter laser vaporization (LV) s-SWCNT networks, as a function of room-temperature electrical conductivity. SWCNTs were originally dispersed with the cleavable SMP polymer, which was then removed in the spray-deposited film. Gray squares show data points for progressive doping of a single s-SWCNT network, while colored circles show data taken for samples that were measured with temperature-dependent thermopower and conductivity measurements. The blue shaded region shows the range where the Fermi level crosses into the first valence level (v_1) and the sample transitions from nondegenerate to degenerate. The red solid line shows the transport model used to simulate the Seebeck and PF vs σ. Reproduced with permission from ref 253. Copyright 2019 Wiley.

generally consistent with the Weidemann–Franz law (Figure 25a).[9,252]

Several other studies have explored the impact of molecular dopants, adsorbates, and encapsulants on the thermal conductivity of CNTs, and the effects seem to be mixed and may be complex.[275,276] For example, doping was observed to reduce k for acid-doped highly aligned SWCNT fibers, although iodine doping did not change k.[275] Komada et al. found that fullerene encapsulation into SWCNTs and DWCNTs reduced k by around 35%, while increasing S by 40% (Figure 25c,e).[276]

Most recently, an interesting region was observed in the temperature-dependent thermal conductivity that suggests that the phonon contribution to k (k_{ph}) can be completely eliminated within a narrow temperature range.[277] Specifically, k_{ph} reaches a minimum near 0 at T = 200 K for ~1.0 nm diameter HiPCO s-SWCNTs, whereas k_{ph} steadily rises for larger diameter (~1.35 nm) plasma torch (PT) between 100 and 350 K. The source of this suppression of k_{ph} is currently unclear but is likely due to a T-dependent phonon scattering mechanism. Such phonon scattering could arise from tube–tube interactions or

https://doi.org/10.1021/acs.chemrev.1c00218
Chem. Rev. XXXX, XXX, XXX–XXX

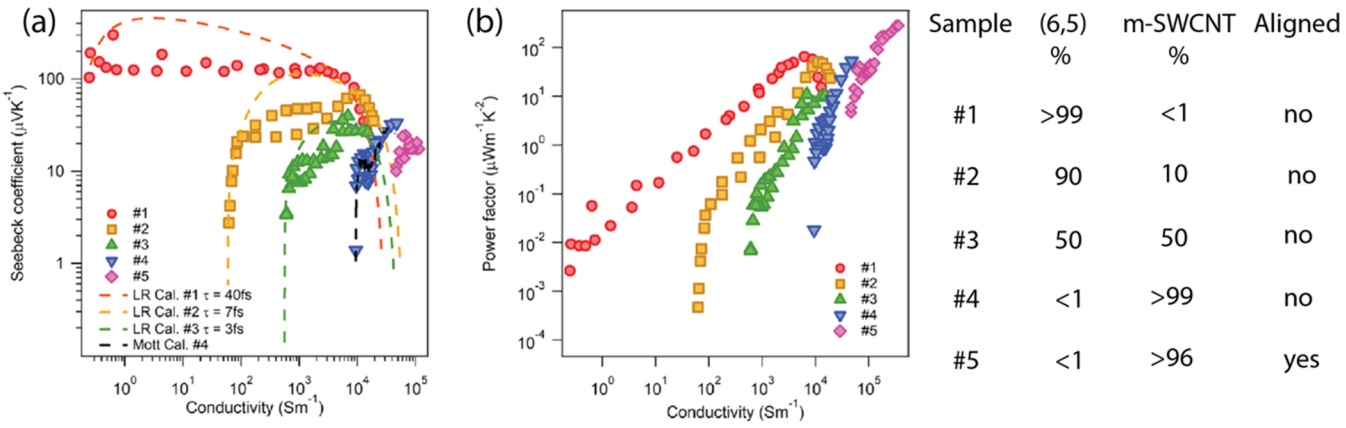

Figure 27. (a) Relationship between Seebeck coefficient and (b) power factor and conductivity of five samples with different semiconductor−metal ratios (table on right). The dashed lines in (a) are theoretical simulations. Mott's formula was used for sample 4 (Mott Cal.), whereas the linear response theory combined with the thermal Green's function method within the constant relaxation time approximation was used for samples 1−3 (LR Cal.). See reference for fitting details. Reproduced with permission from ref 248. Copyright 2019 American Chemical Society.

interactions between the s-SWCNTs and exohedral or endohedral dopants and/or solvent molecules. Elucidation of this mechanism in future studies could lead to significant improvements in zT.

Mechanistically, the studies discussed above suggest a few ways forward for improving the performance of highly enriched s-SWCNT thermoelectrics. First, the morphology of the s-SWCNT appears to play a crucial role in transport. Removal of the insulating dispersion polymer improves carrier mobility, conductivity, power factor, and zT,[252,265] and larger s-SWCNT bundles appear to reduce TE performance.[252] Molecules adsorbed on either exterior or interior surfaces of the SWCNTs dramatically impact conductivity and thermopower via doping and may modulate the thermal conductivity. Understanding the impacts on thermal conductivity may prove to be particularly fruitful, as it appears that the dominant phonon contribution can be dramatically reduced in some situations.

All of these observations point to a TE transport mechanism that depends heavily on the transport barriers present at the junctions between bundles, a conclusion that is in agreement with recent studies on polymer-free s-SWCNT networks[253] that adapted the transport model originally used by Kang et al. to describe TE transport in semiconducting polymers.[278] Specifically, the red lines in Figure 26 show the $s = 1$ relationship determined by this model that is expected for "intrinsic" transport properties of crystalline semiconductors with near-parabolic band dispersion near the band edge, where transport is limited by deformation potential scattering via acoustic phonons. This transport mode appears to describe the data on s-SWCNT networks well when the carrier density is high and the network is degenerately doped. The deviation from the "intrinsic" $s = 1$ behavior at low carrier density suggests that extrinsic factors limit transport and the ultimate PF achievable in the doped networks in this regime. It is quite possible that these "extrinsic" factors correspond to some of the morphological factors mentioned above that limit carrier transport from bundle-to-bundle in disordered s-SWCNT networks. Figure 26 demonstrates that identifying these extrinsic factors and mitigating them may provide a pathway toward the realization of substantially higher PF values in doped nanotube networks.

Second, it is critical to tune and optimize the doping level in s-SWCNTs to optimize the TE performance. This conclusion is reinforced by the recent study of Huang et al., who found a relatively small difference between the TE performance of as-produced mixed metal/semi SWCNT thin films and highly enriched thin films *in the absence of doping*,[274] reinforcing the need for carrier density control. Effective doping primarily requires finding dopants with the right balance between redox potential and environmental stability, but recent studies suggest morphology may play a role as well. Nonoguchi et al. found that the effectiveness of doping s-SWCNT networks depended on the SWCNT thickness and the dispersing polymer, and obtained a peak PF of 412 μW m^{-1} K^{-2} for ca. 200 nm thick films.[254] Doping also appears to lower the thermal conductivity,[9,252] although further studies are needed to determine the precise mechanism at play. With respect to stability, s-SWCNT networks tend to be less stable to environmental degradation of n-type conductivity than their mixed and metallic counterparts. This sensitivity to ambient conditions appears to be an issue for both chemically doped s-SWCNTs[252] and s-SWCNTs doped via atomic substitution (e.g., N).[279] Looking forward, it will be critical to further explore the mechanism(s) for this sensitivity and strategies for mitigating it. Encapsulation is certainly one strategy,[252] but it is possible that dopants with better inherent stability can also be developed.

While a number of research reports have now explored the potential TE benefits of enriched s-SWCNTs, very recent research suggests that the exploration of highly enriched m-SWCNTs may also prove fruitful. Ichinose et al. recently compared the carrier density-dependent TE power factor of SWCNT networks as a function of diameter, alignment, and metal/semi enrichment (Figure 27).[248] They found that the typical behavior found for s-SWCNT networks, where S decreases continuously with increasing σ, does not hold for m-SWCNT networks. Instead, S *increases* continuously with increasing σ due to the increasing curvature in the DOS as E_F is swept toward the first vHS via electrostatic doping (Figure 27a). The authors study samples with relatively small average diameter (ca. 0.7 nm) and large diameter (ca. 1.4 nm), in either unaligned or aligned films, and find the largest PF of ca. 300 μW m^{-1} K^{-2} for aligned networks of large diameter m-SWCNTs (Figure 27b).

It is encouraging to see that m-SWCNTs are not universally detrimental to TE performance and that enriched m-SWCNT networks can enable large TE PFs, exciting and somewhat unexpected findings that warrant more detailed fundamental

https://doi.org/10.1021/acs.chemrev.1c00218
Chem. Rev. XXXX, XXX, XXX−XXX

studies. Because alignment enhances the *PF* (measured in the alignment direction) by a factor of 4−5 compared to randomly aligned SWCNTs,[246] the m-SWCNT sample is prepared from aligned, large-diameter arc discharge SWCNTs that were enriched by density gradient ultracentrifugation (DGU).[248] Therefore, it is illuminating to compare aligned networks of enriched m-SWCNT and s-SWCNT prepared from similar large-diameter source material as a function of carefully controlled carrier density. Detailed comparisons of the thermal conductivity of m- and s-SWCNT networks will also be critical because little research exists for the former. It is also interesting to note that neither highly enriched m- or s-SWCNTs have been studied extensively within SWCNT-based TE composites. These studies should provide much-needed insight into the ultimate potential of highly enriched SWCNTs in organic thermoelectric devices and applications.

4.2.2.3. Covalent Functionalization and Doping. Beyond the noncovalent doping strategies discussed in section 4.2.2.1, a number of groups are also exploring covalent routes toward functionalizing and doping CNT networks to improve their TE performance. These strategies can be separated into two primary categories: (1) CNT sidewall functionalization with covalent defects and/or functional groups to modify carrier/phonon transport, and (2) substitutional doping of electron-deficient or electron-rich atoms into the CNT lattice to tune carrier density. In an early study belonging to the first category, Zhao et al. performed an Ar-plasma treatment to induce covalent defects within a free-standing bulky CNT paper.[280] The authors reported that an optimized Ar-plasma treatment led to a significant enhancement of the Seebeck coefficient up to ∼350 μV K^{-1} and a reduction of the thermal conductivity to as low as 0.3 W m^{-1} K^{-1}, leading to a zT value about 0.4 at 670 K (60 times higher than the pristine CNT paper).[280] Recently, Nonoguchi et al. examined the effect of UV/ozone oxidation on the TE performance of s-SWCNT networks (Figure 28).[281] The authors suggest that the oxidative treatment introduced epoxy and carbonyl groups onto the s-SWCNT sidewall, which in turn increased the carrier concentration (Figure 28a). The enhanced Seebeck coefficient of the defective s-SWCNTs (Figure 28b) improved the power factor relative to similarly prepared s-SWCNT networks that were chemically doped with AgTFSI (Figure 28c).[281]

A number of groups have also recently explored the potential of substitutional atomic doping for tuning the carrier density and providing more stable TE properties relative to those of chemically doped SWCNT networks. This strategy is analogous to the aliovalent doping strategies typically used in bulk covalent semiconductors such as silicon, where the incorporation of electron-deficient (e.g., boron) or electron-rich (e.g., phosphorus) leads to p- and n-type doping, respectively. There is a huge body of literature devoted to studying atomic substitutional doping in SWCNTs,[282−284] but only recently has this approach been applied extensively to the TE properties of CNT networks. Liu et al. utilized an ammonia plasma to dope s-SWCNTs with nitrogen atoms and realize n-type TE transport.[279] Before doping the s-SWCNT networks had a thermopower of 125 μV K^{-1} and a power factor of 95 μW m^{-1} K^{-2}. N-doped films showed a thermopower of −80 μV K^{-1} in air at 110 °C, although they still behaved as p-type semiconductors under ambient conditions at room temperature.[279] Dorling et al. use acetonitrile to introduce N atoms into a MWCNT synthesis to produce N-doped MWCNTs.[285] The authors find n-type transport (negative thermopower) in the neat N-doped

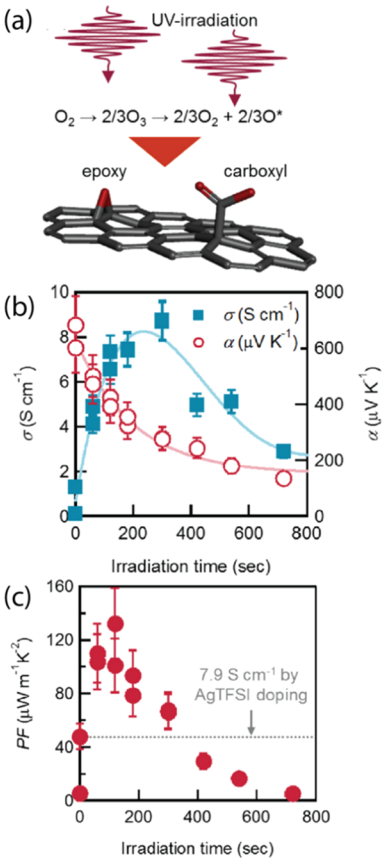

Figure 28. (a) Schematic of UV/ozone treatment to induce oxygenic functional groups on sidewalls of s-SWCNTs. (b) Conductivity and Seebeck coefficient and (c) power factor of s-SWCNTs as a function of UV irradiation time. The dashed line in (c) references a chemically doped s-SWCNT network. Reproduced with permission from ref 281. Copyright 2019 AIP.

MWCNTs, although composite films with P3HT have positive thermopower for MWCNT contents less than 40%. Interestingly, some p-type P3HT composites with low N-MWCNT content (e.g., 30%) can be converted to n-type by UV irradiation, an effect attributed to modification of the polymer microstructure and concomitant interactions with MWCNTs.[286] The same group doped SWCNTs with N atoms via ammonolysis, but oxygenic functional groups induced by acid-based purification prevented the realization of a negative thermopower.[285]

Chiang et al. developed a wet chemistry-based strategy to produce boron-doped (mixed electronic structure) SWCNTs with boron content in the range of 0−3 atomic % (Figure 29).[287] The authors found that boron doping improved both the conductivity and thermopower of the SWCNT networks, ultimately leading to a 6-fold improvement of the power factor up to ca. 60 μW m^{-1} K^{-2} at boron concentrations in the range of 2−3 atomic% (Figure 29f). Chemical doping of the B-doped SWCNTs led to an additional improvement in power factor up to ca. 100 μW m^{-1} K^{-2} (Figure 29g).[287]

4.2.2.4. Transport Anisotropy in TE Properties. SWCNTs are prototypical one-dimensional semiconductors with ultrahigh aspect ratios because a typical as-prepared individual nanotube has a diameter in the range of 0.6−2.0 nm and a length of >1 μm. As such, the structural, electronic, and optical properties of nanotubes are highly anisotropic. Recent studies have delved

https://doi.org/10.1021/acs.chemrev.1c00218
Chem. Rev. XXXX, XXX, XXX−XXX

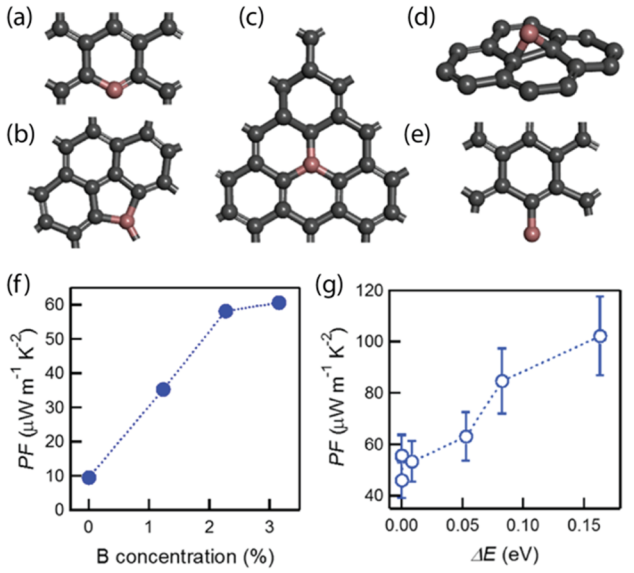

Figure 29. (a–e) Possible boron configurations in a boron-doped SWCNT. (a) Borabenzene. (b) Borole. (c) Substituted boron. (d) C-BH-C. (e) C-BH_2. (f) Maximum power factors measured in the range of 37–200 °C, as a function of boron concentration. (g) Power factor of chemically doped B-SWCNTs (3.15 atomic % B) as a function of Fermi level shift (ΔE) at room temperature. Reproduced with permission from ref 287. Copyright 2019 American Chemical Society.

into the implications of this anisotropy on TE properties at the macroscopic level for highly aligned thin films of SWCNTs.[246,247,288] Fukuhara et al. used slow vacuum filtration of unsorted arc discharge SWCNT dispersions to produce highly aligned SWCNT thin films and used electrolyte gating to tune the Fermi level in both the p- and n-type doping regimes (Figure 30).[246] They found that the conductivity along the alignment direction was several times larger than conductivity in the direction perpendicular to alignment (Figure 30b). In contrast, the Seebeck coefficient was isotropic, with a peak magnitude of ca. 50 μV K^{-1} for appropriately doped p- and n-type SWCNTs for either parallel or perpendicular transport (Figure 30c). The conductivity anisotropy led to a parallel *PF* (ca. 160 μW m^{-1} K^{-2}), roughly four times that of the perpendicular *PF* (ca. 40 μW m^{-1} K^{-2}) (Figure 30d). Consistently, as discussed above, Ichonese et al. found that the TE power factor of highly aligned arc discharge m-SWCNT (>96% m-SWCNT purity) thin films was ca. five times higher than that of randomly aligned m-SWCNT (>99% m-SWCNT) thin films.[248]

Yamaguchi et al. studied the thermal conductivity of unsorted arc discharge SWCNT thin films that were prepared via vacuum filtration to be either highly aligned, poorly aligned, or completely random.[288] The thermal conductivity of the poorly aligned film was 28 ± 1.2 W m^{-1} K^{-1}, while that of the randomly aligned film was 14 ± 2.8 W m^{-1} K^{-1}, in a similar range to that found by a number of other groups for undoped randomly aligned SWCNT networks.[9,274] For the highly aligned film, they found a parallel thermal conductivity, $k_{\parallel}$, of 43 ± 2.2 W m^{-1} K^{-1} and a perpendicular thermal conductivity, $k_{\perp}$, of 0.085 ± 0.017 W m^{-1} K^{-1}, for a thermal conductivity anisotropy of ca. 500. The large differences in thermal conductivity were explained by the different mechanisms controlling phonon transport (the dominant source of thermal conductance) in the different films. Specifically, the authors' analysis suggests that $k_{\perp}$ in the highly aligned film is dominated by the intertube thermal resistance, whereas $k_{\parallel}$ is dominated by the internal thermal conductance of a SWCNT in the axial direction. In poorly aligned and random films, the thermal conductance is weighted by the contributions of both internal thermal conductance and intertube thermal resistance.

Nonoguchi compared the in-plane and through-plane TE performance of mixed SWCNTs doped with crown ether-stabilized alkali metal salts.[237] The KOH/18-crown-6-ether doped CNT film had an enhanced in-plane *PF* of 220 μW m^{-1} K^{-2} and through-plane *PF* of 27 μW m^{-1} K^{-2}, but because of the suppressed through-plane thermal conductivity (0.12 W m^{-1} K^{-1} compared to 39 W m^{-1} K^{-1}), the through-plane zT (0.07) value was more than 3 times higher than in-plane zT (0.02) at 310 K.

4.2.3. TE Generators from CNT-based Fibers and Fabrics. The inherently threadlike nature of CNTs is an important advantage for thermoelectric energy harvesting, especially from the standpoint of wearable, flexible, and lightweight TE generators. As such, CNTs can be easily fabricated by a variety of means into fabric-like form factors. A particularly attractive aspect of these strategies arises from the relatively gentle processing methods that can be applied to as-grown CNT samples. Because these processing routes do not typically involve ultrasonication to produce surfactant- or polymer-based dispersions, they naturally leave the CNTs as long as possible, which dramatically improves network conductivity. These fabrics also often (but do not always) tend also to have well-aligned CNTs, improving the conductivity as discussed in section 4.2.2.4. Yarns and fibers can be directly spun from as-produced CNT "webs" or "socks", often straight from the reactor in a continuous process and typically via pulling

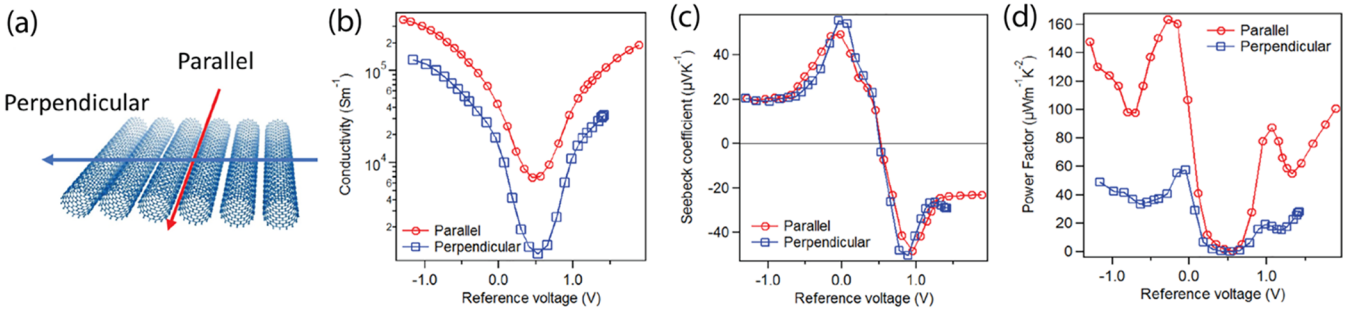

Figure 30. (a) Schematic of highly aligned SWCNT film. (b–d) Comparison of electrical conductivity (b), Seebeck coefficient (c), and TE power factor (d) measured for electrostatically doped SWCNT samples in the direction parallel or perpendicular to SWCNT alignment. Reproduced with permission from ref 246. Copyright 2018 AIP.

https://doi.org/10.1021/acs.chemrev.1c00218
Chem. Rev. XXXX, XXX, XXX–XXX

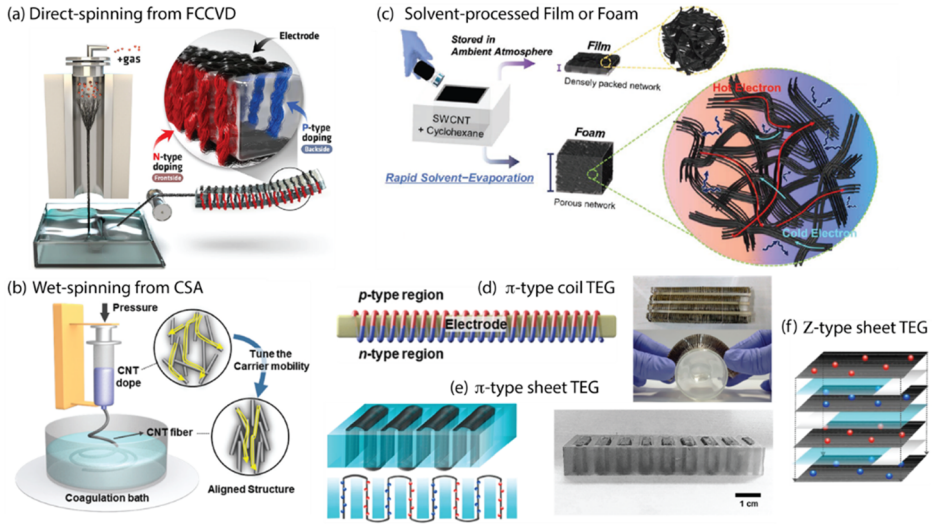

Figure 31. (a) Schematic of the fabrication of DWCNT yarn via direct spinning from FCCVD reactor onto a PDMS support. $FeCl_3$ and PEI were used to dope the frontside p-type and backside n-type, respectively. Reproduced with permission from ref 230. Copyright 2017 American Chemical Society. (b) Schematic of wet-spinning process from chlorosulfonic acid for fabrication of highly aligned CNT fibers. (c) Schematic of solvent-based process for forming either densified SWCNT films or low-density SWCNT foams. Reproduced with permission from ref 262. Copyright 2019 Wiley. (d) Schematic (left) and photograph (right) of π-type coil TEG formed by wrapping CNT yarn around PET spacer and brush-doping p- and n-type dopants. Reproduced with permission from ref 292. Copyright 2019 Royal Society of Chemistry. (e) Schematic (left) and photograph (right) of π-type sheet TEG formed by selective-area brush-doping of dopants onto continuous CNT sheet that is snaked through a PDMS support. Red and blue dots represent n-type and p-type dopants. (f) Schematic of out-of-plane Z-type sheet TEG, where each sheet is separated by a PDMS spacer (light blue) and junctions are formed by deposition of silver paste. Red and blue dots represent n-type and p-type dopants. (e–f) Reproduced with permission from ref 269. Copyright 2020 American Chemical Society.

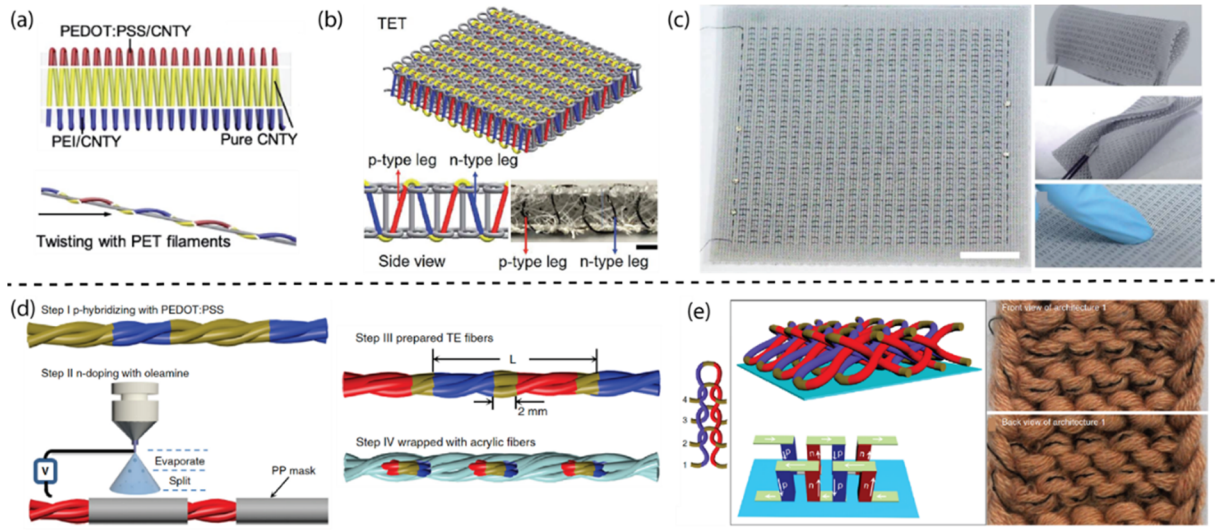

Figure 32. (a) Schematic of p/n CNT yarn (CNTY) doped p-type with PEDOT:PSS and n-type with PEI, after which it is twisted around PET filaments. (b) Schematic of out-of-plane thermoelectric textile (TET) fabricated by knitting CNT-twisted PET filaments (π-type knit). (c) Photographs of the flexible knitted TET. (a–c) Reproduced with permission from ref 270. Copyright Royal Society of Chemistry. (d) Schematic of fabrication process for CNT fibers doped alternately p- and n-type with PEDOT:PSS and oleamine, respectively, after which the CNT fibers are wrapped with acrylic fibers. (e) Schematic (left) and photographs (right) of out-of-plane knitted TET prepared from CNT/acrylic fibers (π-type knit). (d–e) Reproduced with permission from ref 50. Copyright 2020 Royal Society of Chemistry.

through a liquid densification bath and rolling onto a roller (Figure 31a).[230] Vertically aligned CNT arrays can also be dry-spun into fibers.[289] Mild liquid-phase processing can be achieved by producing slurries in solvents (with no surfactants and no sonication) or by producing true solutions in strong acids such as chlorosulfonic acid.[247,275] The latter technique can be paired with a coagulation-bath-assisted spinning process to produce highly aligned CNT fibers with exceptional alignment, strength, and conductivity (Figure 31b).[290] As-produced web-like material can also be densified into disordered or aligned fabric-like sheets that can be stacked, cut, and shaped by a variety of means and into a variety of form factors. Alternatively, web-like material can be expanded into flexible and moldable foams with very low density (Figure 31c).[262]

CNT fibers, yarns, and sheets can be fabricated into TE generators with a variety of shapes and form factors, but there are two predominant styles that have been explored for CNT TEGs. The "Z-type" or "accordion-style" TEGs place flat p- and n-type

https://doi.org/10.1021/acs.chemrev.1c00218
Chem. Rev. XXXX, XXX, XXX−XXX

Table 2. Summary of Fabrication Methods and Dopants for π-Type CNT-based TEGs

CNT synthesis and (type)	fabric style	TEG style	p-type dopant	p-type dopant	peak p-type *PF* (μW m^{-1} K^{-2})	peak n-type *PF* (μW m^{-1} K^{-2})	key module metric(s)
FCCVD (FWCNTs)	aligned sheet	π-type (sheet)	$FeCl_3$	PEI	250	255	23 mV 8 μW
FCCVD	aligned sheet	Z-type	$FeCl_3$	BV	2500	1100	0.66 μW cm^{-2} (5.3 μW)
FCCVD	disordered sheet	Z-type		PEI	1800	1500	2.5 μW
FCCVD	yarn	π-type (knit)	PEDOT:PSS	PEI	513	668	500 V m^{-2} 50 mW m^{-2} (383 μW)
DWCNT	wet-spun fibers	π-type (coil)	H-carbazole	Dpp	432	323	15.4 μW g^{-1} (0.12 μW) 259 μW g^{-1} (2.02 μW)
FCCVD	twisted fibers	π-type (knit)	PEDOT:PSS	oleamine	330	320	70 mW m^{-2} (4.5 μW)
TUBALL (SWCNT)	solvent-prepped sheet	π-type (coil)		PEI	411	90	4.6 μW cm^{-2} (10.3 μW) 2.0 μW cm^{-2} (4.4 μW) 0.5 μW cm^{-2} (1.1 μW)
FCCVD (DWCNT)	yarn	π-type (coil)	$FeCl_3$	PEI	2387	2456	1.2 V g^{-1} (22.5 mV) 700 μW g^{-1} (1.3 μW) 45 mV 4.2 μW
FCCVD	disordered sheet	π-type (in-plane)	Au/PANI	PEI	2454	1707	0.4 μW cm^{-2} 550 μW g^{-1} (1.7 μW)
eDIPS (SWCNT)	porous foam	π-type (foam)	$FeCl_3$	BV	1.1	1.0	0.5 μW cm^{-2} 82 μW g^{-1} (1.5 μW)
MWCNTs	coated PET yarn	π-type (in-plane)	PEDOT:PSS (separate leg)	PEI			143 mV 7.1 nW

CNT sheets in series with a flat insulating spacer in between each sheet (Figure 31f).[269,291] Conducting metal pastes may be used to "glue" isolated p-type and n-type sheets together and establish good contact at each p/n junction, or alternatively a continuous sheet may be alternately doped with different chemical dopants. The conductive nature of the CNTs allows for the fabrication of metal-free TEGs. When expanded, such TEGs resemble an accordion. Once collapsed, a thermal gradient can be established in the out-of-plane direction (with respect to the planes of individual p/n sheets and the planes of hot- or cold-side temperature sinks) to produce voltage and power via transport of carriers.

Another broad category of TEG commonly fabricated from CNTs is the π-type TEG, where p−n legs are arranged in such a fashion as to have their primary transport plane in the same direction as the thermal gradient (Figure 31d,e).[269,292] In most cases, the SWCNT fiber/sheet transport plane is perpendicular to the planes of substrate or fabric into which it is integrated (out-of-plane geometry). This geometry of TEG is commonly used for "conventional" TEGs based on bulk inorganic semiconductors. However, in some cases, the SWCNT fiber/sheet transport plane lies along the plane of a substrate or fabric into which it is integrated (in-plane geometry). The out-of-plane geometry tends to maximize the areal density of p/n legs for enhanced power density (i.e., W cm^{-2}). Recent examples of π-type SWCNT-based TEGs based solely on doped SWCNTs utilize a continuous sheet geometry (π-type sheet, Figure 31e),[269] a coiled geometry in which yarns or sheets are coiled around an insulating spacer (π-type coil, Figure 31d),[230,268,292] in-plane substrate- or fabric-mounted geometries (π-type in-plane),[231,293] and a TEG based on PDMS-separated SWCNT foam blocks (π-type foam).[262] SWCNT fibers or yarns can also

https://doi.org/10.1021/acs.chemrev.1c00218
Chem. Rev. XXXX, XXX, XXX−XXX

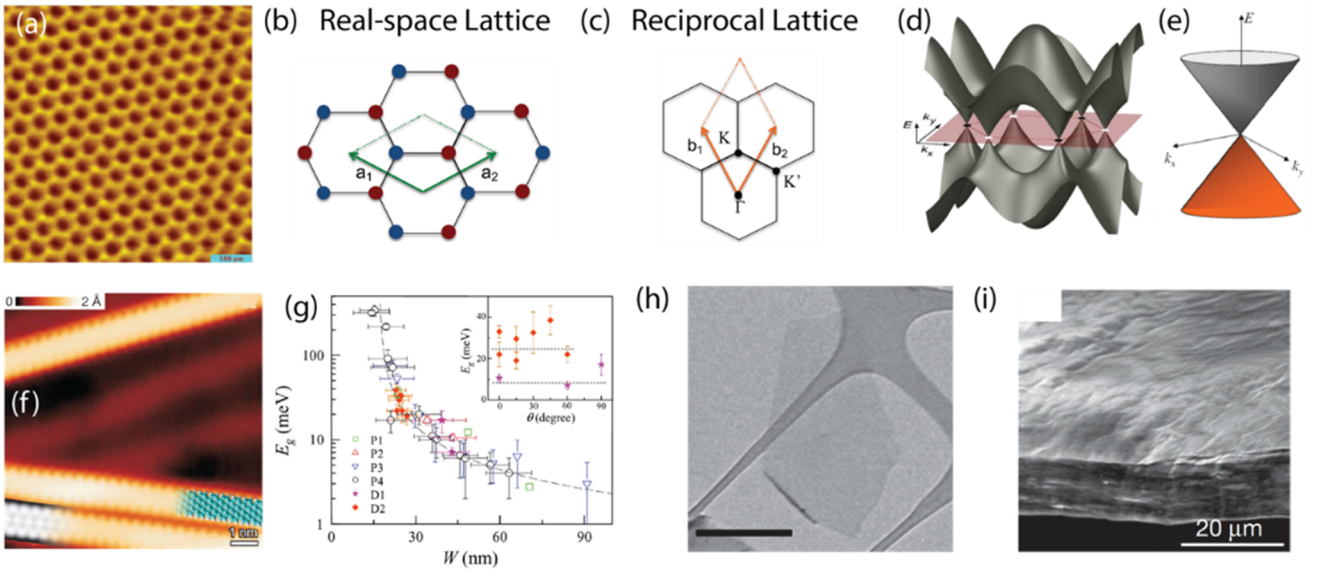

Figure 33. (a) Scanning tunneling microscopy (STM) image of monolayer graphene sheet. Reproduced with permission from ref 297. Copyright 2012 IOP Publishing. (b) Real-space lattice, (c) Reciprocal-space lattice, and (d) Energy band structure of graphene showing Dirac cones meeting at K and K′ points (white and black circles). (e) Zoom of K-point where linear electronic bands cross at the Dirac point. (d,e) Reproduced with permission from ref 297. Copyright 2012 IOP Publishing. (f) STM image of chemically grown graphene nanoribbons (GNRs). Blue and white overlays show cartoons of atomic structure for the GNRs. Reproduced with permission from ref 298. Copyright 2010 Springer Nature. (g) Experimental bandgaps for GNRs as a function of width. Reproduced with permission from ref 299. Copyright 2007 American Physical Society. (h) TEM image of monolayer graphene flake, exfoliated in NMP solvent. Scale bar is 500 nm. Reproduced with permission from ref 300. Copyright 2008 Springer Nature. (i) Cross-sectional SEM image of restacked reduced graphene oxide (rGO) thin film. Reproduced with permission from ref 301. Copyright 2007 Springer Nature.

be combined with other conventional fibers (e.g., acrylics, PET, etc.) into integrated energy-harvesting textiles (π-type knit, Figure 32).[50,270] The p- and n-type doping in these π-type TEGs is typically achieved by soaking, spraying, or brushing chemical dopants onto targeted areas to form periodic repetitions of p−n junctions.

Table 2 summarizes the fabrication methodology and dopants used to fabricate a variety of Z-type and π-type CNT-based TEGs, along with the optimized performance metrics. Where reported, performance metrics such as peak open circuit voltage and peak power are provided as densities normalized to either area or mass of the TEG. Mass-normalized voltage and power density is one metric where CNTs compare especially well to their inorganic counterparts because carbon is typically substantially lighter than the elements used in compound semiconductors.

4.2.4. Graphene. Graphene is a Dirac semimetal with linear bands for electrons and holes that cross at the Dirac point (Figure 33). As such, it serves as a fascinating model system for studying the thermoelectric properties of massless Dirac fermions that result from linear band dispersion. The Fermi level or chemical potential of graphene can be modulated in a similar fashion to CNTs, by employing molecular doping, substitutional doping, and electrostatic doping. The reports of experimentally measured zT values for graphene are still rare, but many theoretical studies have been carried out to explore its thermoelectric properties and several recent experimental studies have begun publishing PF and zT values. A few recent review articles have been published on graphene-based thermoelectrics,[294−296] so here we highlight many of the salient advances in the past decade.

It is important to point out that the term "graphene" is used to refer to a broad family of materials. At the purest level, monolayer graphene is a single sheet of hexagonally bonded sp^2-hybridized carbon atoms (Figure 33a). Monolayer graphene can be exfoliated from graphite or grown on copper foil by chemical vapor deposition (CVD). Monolayer graphene can be further nanostructured, most typically by the growth or cutting of a graphene sheet into nanoribbons (Figure 33f), where the narrow width of the graphene sheet confines charge carriers and opens up a band gap (Figure 33g). Graphene can also be exfoliated from graphite into solution as small flakes while retaining its identity as graphene (Figure 33h). Another distinct method of exfoliation involves the production of graphene oxide (GO) or reduced graphene oxide (rGO) by first oxidizing graphite, then exfoliating the GO, and finally reducing the oxide functional groups to produced rGO. Solution-exfoliated flakes of graphene, GO, or rGO can be restacked to form thick films (Figure 33i) that can be used directly in TE devices. Here we divide our discussion of graphene TE properties by focusing on these unique classifications accordingly.

4.2.4.1. Monolayer Graphene. Early work related to thermoelectric properties of monolayer graphene focused on thermal conductivity, which in theory should be exceptionally large.[302,303] Balandin et al. introduced a scanning Raman technique (Figure 34a) that utilizes the temperature coefficient of the graphene G band to estimate a thermal conductivity of 4840−5300 W m^{-1} K^{-1}.[302] Because phonons contribute significantly to this large thermal conductivity, subsequent studies demonstrated a dramatic reduction in k for isotopically engineered monolayer graphene sheets (Figure 34b).[304]

The dependence of conductivity and thermopower on Fermi level or chemical potential in graphene has been treated theoretically with a number of different approaches. Figure 35a displays an early study applying Mott's formula to this question.[305] Conductivity increases linearly away from the charge-neutrality point (CNP), as expected for a Dirac semimetal. The Seebeck coefficient is zero at the CNP and has

https://doi.org/10.1021/acs.chemrev.1c00218
Chem. Rev. XXXX, XXX, XXX−XXX

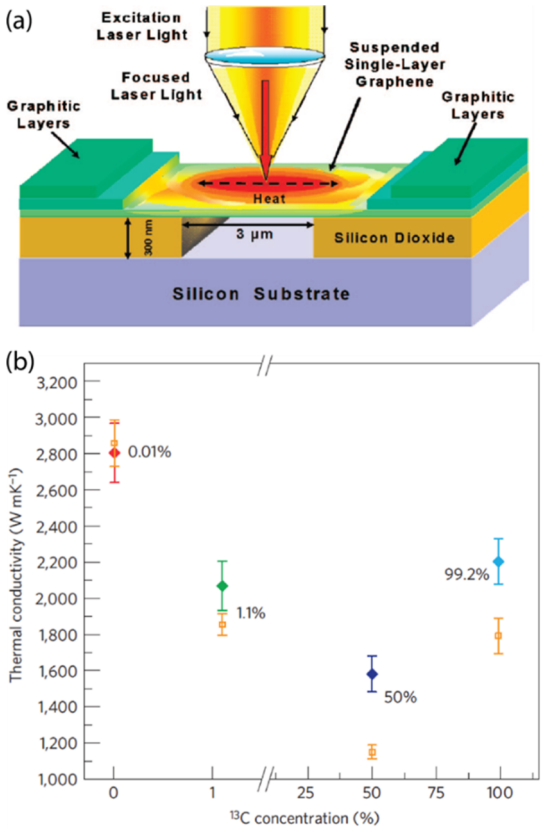

Figure 34. (a) Schematic of Raman microscopy measurement introduced by Balandin et al. to measure thermal conductivity of monolayer graphene suspended over a trench. Reproduced with permission from ref 302. Copyright 2008 American Chemical Society. (b) Thermal conductivity of isotopically engineered monolayer graphene measured by similar technique by Chen et al. (closed diamonds) as a function of ^{13}C concentration. Open orange squares show molecular dynamics simulations for comparison. Reproduced with permission from ref 304. Copyright 2012 Springer Nature.

maxima for both p- and n-type graphene for small shifts of the chemical potential away from the CNP (Figure 35b).[305] Zuev et al. probed the carrier density dependence of σ (Figure 35c) and S (Figure 35d) for exfoliated mesoscopic graphene samples where the chemical potential was swept in positive and negative directions via electrostatic gating.[306] The Seebeck coefficient was carrier-density dependent (Figure 35d) and scaled linearly with temperature (inset), with a peak value of $\sim -80\ \mu V\ K^{-1}$ at room temperature.[306] Both this study[306] and subsequent studies[307] find divergent/anomalous behavior for thermopower near the Dirac point at low temperatures based on the characteristic behavior of massless Dirac quasiparticles. Later, a similar Seebeck coefficient value was reported together with a thermal conductivity of $\sim 600\ W\ m^{-1}\ K^{-1}$ at room temperature for monolayer graphene.[308]

Kanahashi et al. used a similar electrostatic gating approach to realize exceptionally large *PF*s in CVD-grown monolayer graphene (Figure 35e,f).[309] The Seebeck coefficient scaled inversely with conductivity as $S \propto \sigma^{-1}$, as expected by the Mott equation, and the *PF*s reached as high as 6930 $\mu W\ m^{-1}\ K^{-2}$ (p-type) and 3290 $\mu W\ m^{-1}\ K^{-2}$ (n-type) at 300 K.

4.2.4.2. Graphene Nanoribbons and Nanostructured Graphene. Different groups have used the nonequilibrium Green's function formalism to calculate the thermoelectric properties of GNRs. GNRs with a width of 1.8 nm and a band gap of $E_g = 667$ meV were predicted to have Seebeck coefficients ca. 500 times larger than monolayer graphene, reaching peak values of $\pm 4000\ \mu V\ K^{-1}$ (Figure 36a).[310] Defects and edge imperfections served to increase the GNR thermopower and decrease thermal conductivity, but zT decreased for defective GNRs because these changes were outweighed by a large decrease in electrical conductivity.[310] This reduction in zT contrasts with the behavior calculated by Sevencli et al. for edge-disordered zigzag graphene nanoribbons (ZGNRs).[311] In this case, the authors found a large reduction in thermal conductivity, whereas the electrical conductivity decreased to a much smaller degree at chemical potentials within the bandgap of the ZGNR and a very sharp derivative of electrical conductance at the onset of the ZGNR conduction and valence bands produced large S. As a result, a zT value of as high as 4 at room temperature was predicted (Figure 36b).[311] Chen et al. predicted that periodic lattices of GNRs could improve zT due to the beneficial effect of interfaces between GNR sections with different widths.[312]

Nanopatterning of graphene into nanoribbon sections are also predicted as a route to improving thermoelectric performance. Kim and Grossman used classical and quantum mechanical calculations to study the effect of H and C5 functionalization on the TE properties of patterned graphene "nanoroads", where functionalization introduced peaks in the density of states at the band edge (Figure 36c,d).[313] Unlike conventional 3D TE materials, the increase of *PF* and the reduction of thermal conductivity was achieved simultaneously, resulting in a high theoretical zT value of ~3 at room temperature (Figure 36d).

Recent experimental evidence provides support for the predicted enhancement of TE performance for GNRs and nanostructured graphene, relative to unstructured graphene. Graphene nanomeshes with GNR features having widths less than 10 nm were shown to have thermal conductivity reduced to as low as $\sim 78\ W\ m^{-1}\ K^{-1}$ and S as high as $-520\ \mu V\ K^{-1}$, although the electrical conductivity was reduced as a result of the nanostructuring.[314] Recent studies on CVD-grown and suspended GNRs (Figure 37a) with 250 nm length and 40 nm width[315] demonstrated several-fold enhancement of S relative to unstructured graphene and a large improvement of the ratio of electrical to thermal conductivity (σ/k) relative to prior work.[308,314,316] These enhancements ultimately resulted in a zT value of 0.12 at $120 < T < 220$ K (Figure 37b).[315]

4.2.4.3. Exfoliated Graphene Flakes and Reduced Graphene Oxide. Graphene can also be solution-processed when exfoliated into small flakes in solvent. A wide variety of methods can be used, but sonication and centrifugation remains the most popular.[317] The primary advantages of these solution-dispersed graphene flakes is that the dispersions can be deposited by any number of solution deposition techniques to produce thick films of electrically percolated graphene flakes, and the dispersions allow for easy integration into composites with other organic or inorganic species. These thicker films and composites are more representative of the form factors needed for TE devices because it would be challenging to incorporate monolayer graphene and graphene NRs into macroscopic devices that can generate appreciable power densities. In the dispersion process, graphene is often oxidized in a modified Hummer's method to produced graphene oxide (GO), which is typically p-type because of the oxygenic groups. GO is typically chemically reduced (e.g., with hydrazine) to produce reduced graphene oxide (rGO), but the oxygenic functional groups are difficult to fully remove and the resulting rGO is still typically weakly p-type.[318−320] The oxygen

https://doi.org/10.1021/acs.chemrev.1c00218
Chem. Rev. XXXX, XXX, XXX−XXX

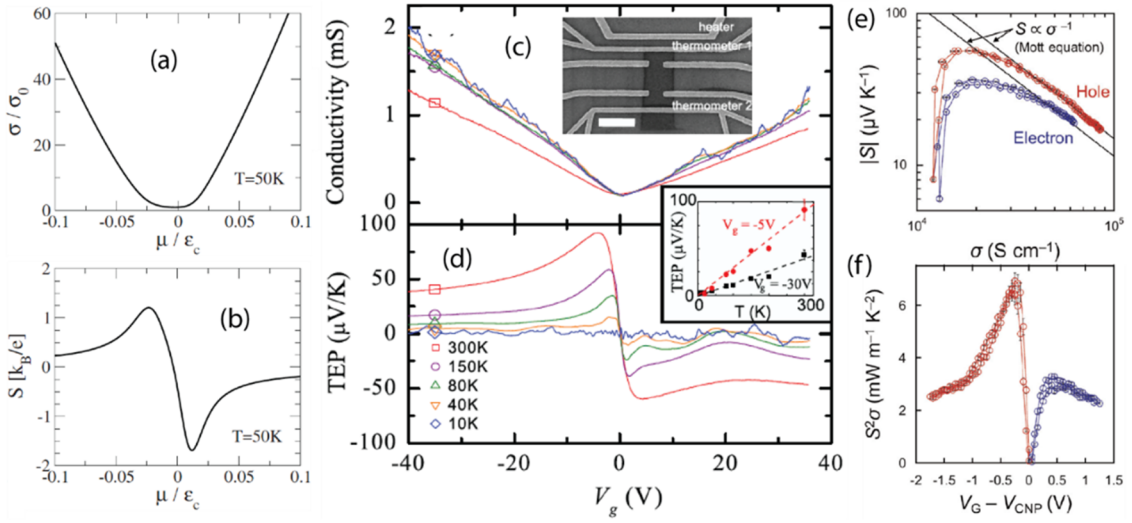

Figure 35. (a,b) Theoretical calculation of the low temperature (50 K) electrical conductivity (a) and Seebeck coefficient (b) of monolayer graphene as a function of chemical potential (μ), where the chemical potential is set to zero at the CNP of graphene. Reproduced with permission from ref 305. Copyright 2007 American Physical Society. (c,d) Experimental measurement of temperature-dependent electrical conductivity (c) and Seebeck coefficient (d) of monolayer graphene as a function of applied gate voltage (V_g), where V_g electrostatically modulates the chemical potential. Inset in (c) shows an SEM image of a typical device (2 μm scale bar), and inset in (d) shows temperature-dependent Seebeck coefficients taken at $V_g = -30$ V (square) and -5 V (circle). Dashed lines are linear fits to data. Reproduced with permission from ref 306. Copyright 2007 American Physical Society. (e) Seebeck coefficient as a function of electron and hole conductivities for large-area electrostatically doped monolayer graphene. Black trend lines show the σ^{-1} dependence for S expected from the Mott equation. (f) *PF* for electrostatically doped monolayer graphene. (e,f) Reproduced with permission from ref 309. Copyright 2019 Springer Nature.

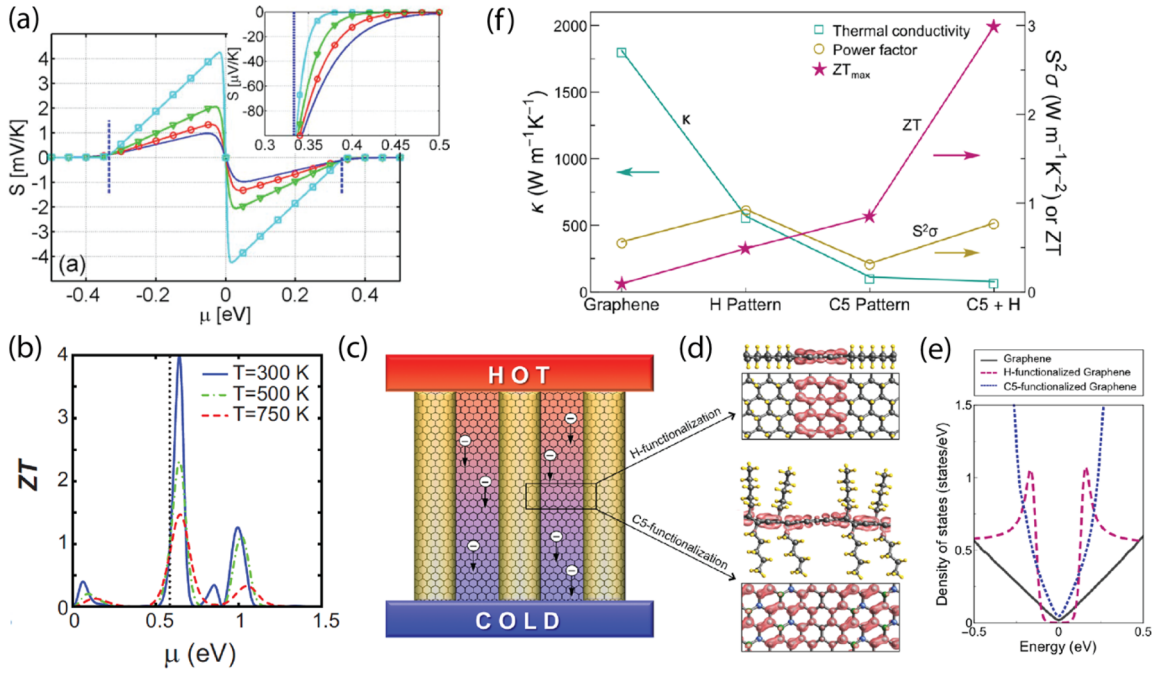

Figure 36. (a) Calculated thermopower of a perfect $n = 15$ armchair GNR as a function of chemical potential (μ) at different temperatures: $T = 75$ K (light-blue squares), $T = 150$ K (green triangles), $T = 225$ K (red circles), $T = 300$ K (dark-blue line). The dashed-blue lines indicate the first conduction (E_c) and valence (E_v) sub-band edges. Inset shows a zoom for $\mu > E_c$. Reproduced with permission from ref 310. Copyright 2009 American Institute of Physics. (b) Calculated zT versus chemical potential (μ) at different temperatures for zigzag GNR with length of 4 μm. Zero μ is the charge-neutrality point, and the dotted vertical line represents the first conduction sub-band edge. Reproduced with permission from ref 311. Copyright 2010 American Physical Society. (c) Schematic of TE generator based on patterned graphene nanostructures with armchair boundary. Yellow shaded area indicates the patterned region. (d) H-functionalized graphene with a 6 Å pattern width (top) and C5-functionalized graphene (bottom). C and H atoms represented by gray and yellow spheres, respectively. Pink contour represents charge density of the conduction band. Green and blue spheres indicate C sites, where C5 chains are attached on the top and bottom surfaces of graphene, respectively. (e) Density of states per unit cell of H- and C5-functionalized graphene. (f) Calculated thermal conductivity (green), *PF* (orange), and zT (red) of H- and C5-patterned graphene nanostructures at room temperature. Values are calculated along the pattern direction for $N_c = 8$ pattern width. (c–f) Reproduced with permission from ref 313. Copyright 2015 American Chemical Society.

https://doi.org/10.1021/acs.chemrev.1c00218
Chem. Rev. XXXX, XXX, XXX−XXX

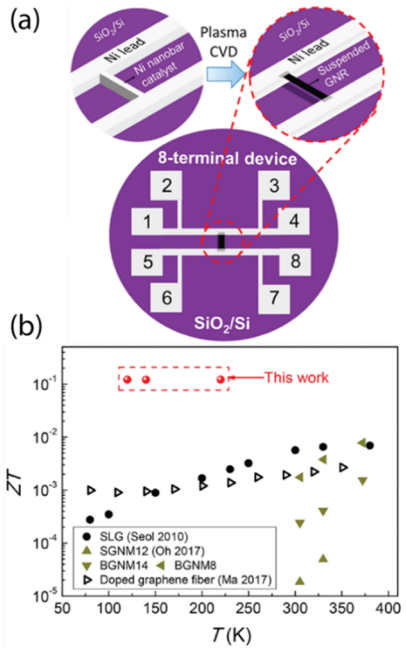

Figure 37. (a) Rapid-heating plasma-CVD method for synthesizing suspended GNRs along with 8-terminal Ni films. The 8-terminal test structure allows measurements of electrical and thermal conductivities and the Seebeck coefficient of GNRs on the same device. (b) Temperature-dependent zT of the GNRs produced by this rapid-heating plasma-CVD synthesis route (red spheres), as compared to other reports[308,314,316] in the literature. Reproduced with permission from ref 315. Copyright 2019 American Chemical Society.

functional groups also break up the sp^2 bonds and delocalized π electron density that is a highly desirable characteristic of graphene and typically limits the conductivity of rGO to ca. 10 S cm^{-1}.[320] Li et al. demonstrated that dramatically increasing the reduction temperature to 3300 K substantially improves the conductivity and TE performance of restacked rGO thin films.[321] These so-called high-temperature rGO (HT-rGO) thin films reached electrical conductivities in the range of 1500−4000 S cm^{-1} ($300 < T < 3000$ K) and peak Seebeck coefficient of ca. 150 $\mu V\ K^{-1}$ around 1200 K, with a peak PF of 54.5 $\mu W\ cm^{-1}\ K^{-2}$ (5450 $\mu W\ m^{-1}\ K^{-2}$) at 3000 K, making them attractive for high-temperature TE applications.[321]

Novak et al. introduced a graphite-intercalation compound (GiC) strategy (Figure 38a) for producing nonoxidized graphene flakes (NOGF).[323] The resulting restacked NOGF thin films were n-type, with Seebeck coefficient of $-45.3\ \mu V\ K^{-1}$, electrical conductivity of 3280 S cm^{-1}, and PF of 673 $\mu W\ m^{-1}\ K^{-2}$. Flexible devices were robust with respect to bending and produced 2.2 mV using body heat.[323] Complementary n-type and p-type films could be prepared by changing the surfactant utilized in the intercalation-exfoliation process, with polyvinylpyrrolidone (PVP) producing n-type NOGF and pyrenebutyric acid (PBA) producing p-type NOGF (Figure 38b).[322] Both types of NOGF films showed similar magnitudes of thermopower, conductivity, and PF (>600 $\mu W\ m^{-1}\ K^{-2}$), enabling an all-graphene TE device that produced 5.0 nW peak power at $\Delta T = 50$ K (Figure 38c).[322]

4.2.5. Nanocarbon Composites. Nanocarbons (i.e., carbon nanotubes, graphene, carbon quantum dots, etc.) have long been used as inclusions or "fillers" to improve the mechanical and electrical properties of composite materials.[324,325] About a decade ago, attention turned to the exploitation of these unique nanoscale carbon systems in TE composites,[326−329] where the primary focus has been on exploiting their impressive intrinsic carrier transport to enhance TE composites where the electrical conductivity of the host limits the overall TE performance (i.e., polymer-based hosts).

One of the primary motivations for the inclusion of nanoscale materials in TE composites is their potential to enhance the TE performance due to quantum effects that arise because of their size/shape and the nanoscale interfaces that are introduced with

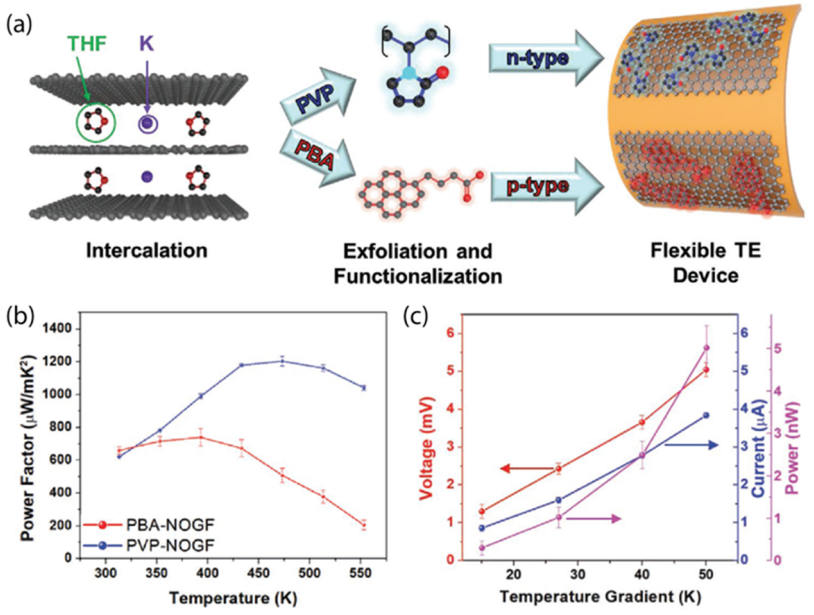

Figure 38. (a) Schematic for intercalation/exfoliation procedure to produced nonoxidized graphene flakes (NOGF), where changing the surfactant modifies the majority carrier type. (b) Power factors achieved for restacked NOGF films comprised of p-type PBA-NOGF and n-type PVP-NOGF. (c) Voltage, current, and power for a device prepared from the n-type and p-type NOGF thin films. Reproduced with permission from ref 322. Copyright 2020 Wiley.

https://doi.org/10.1021/acs.chemrev.1c00218
Chem. Rev. XXXX, XXX, XXX−XXX

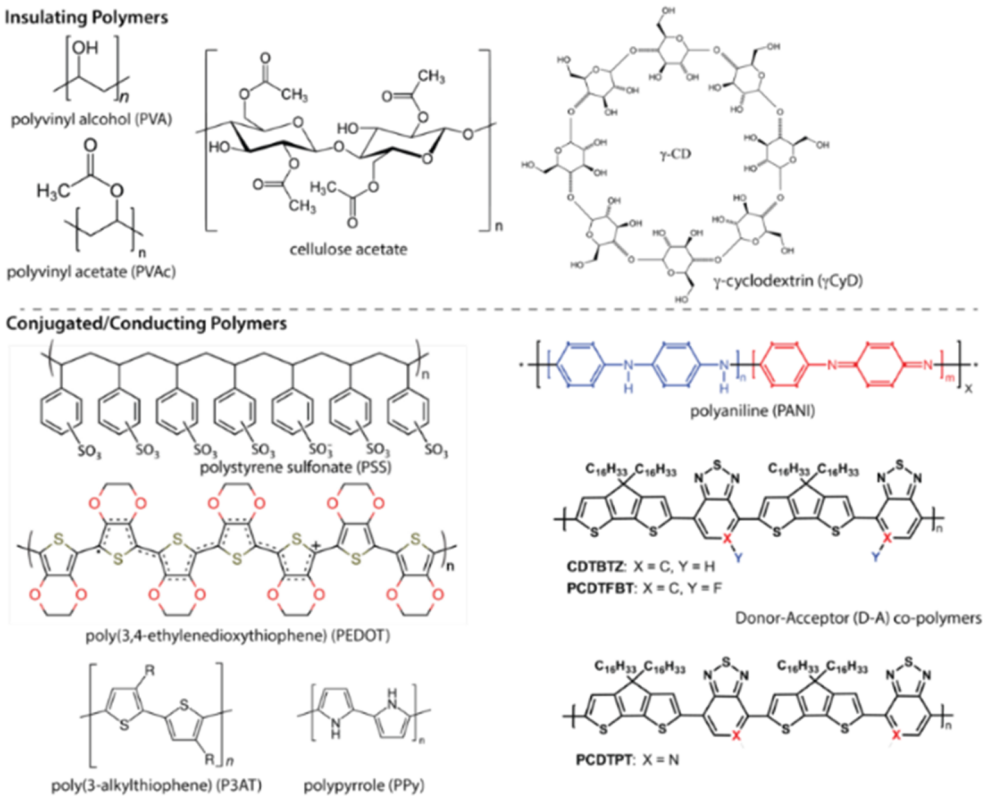

Figure 39. Commonly employed insulating (top) and conjugated/conducting (bottom) polymers, used in blended polymer−CNT TE composites.

the other components.[330−332] A challenge in nanocomposites is exerting control over the energy barrier(s) that limit charge transport between the two phases or between conductive segments of the primary transport material. These barriers can be large and force the charge carriers to pass only through the percolation transport network of the most conductive component. However, these energy barriers may also provide a means to exploit quantum effects for carrier filtering to enhance the Seebeck coefficient.[333−337]

Several combinations of materials, with varying levels of complexity for the final composite, have been proposed and explored. Such composites have produced interesting results and some high TE metrics, but charge carrier transport within such systems is still poorly understood. More recent work has also begun exploring the use of CNTs or graphene to enhance the TE properties of composites with inorganic materials.

Several open questions remain in the context of nanocarbon composites. These include whether the composite system can be considered as (i) a single conductive material with hybrid electronic states and conductive paths determined by both components or (ii) as a "simple" mixture whose properties can be described using typical "composite models". Additionally, as outlined in Lin et al., it is yet to be determined conclusively whether the phenomenon of carrier energy filtering by electronic barriers at interfaces is a viable approach to decouple the thermopower and electrical conductivity in nanocarbon composites.[338] While the answers to these questions likely depend on the precise nature of the composite system, fundamental studies focused on addressing these topics may enable further improvements in the thermoelectric performance of nanocomposite materials and devices. Within this review, we note the studies that ascribed the observed improvements in thermoelectric performance to carrier energy filtering, but we encourage the reader to evaluate these conclusions within the context of the analyses outlined by Lin et al.[338]

4.2.5.1. Blended Polymer−Carbon Nanotube Nanocomposites. The unique electronic and mechanical properties of CNTs described earlier has motivated significant effort toward the fabrication and characterization of TE composites with CNT inclusions. Much of the effort has focused on blended TE composites with CNT conductive fillers incorporated into either insulating or conducting polymeric host matrices (Figure 39),[339−358] although there have been some recent efforts toward the use of molecular host materials.[359−366] Over the past decade, TE composites with CNT conductive fillers have regularly achieved room-temperature TE power factors exceeding 100 μW m^{-1} K^{-2}.[339−355,357,358,361−364,366] For a thorough review of polymer-based blended TE composites with carbon nanotube fillers, we direct the reader to recent reviews by Blackburn et al.[208] and Nandihalli et al.[367] Here we will focus on key advances in blended TE composites comprising organic host matrices and CNT inclusions.

Despite their possible detrimental influence on charge-carrier transport, there continues to be some effort related to the inclusion of insulating polymers into CNT-based composites.[350,354,358] As described below, several insulating polymers (e.g., arabic gum, polyvinyl acetate, etc.) have been employed as a stabilizing binder to improve the morphology and charge transport in blended composites of CNTs and conducting polymers.[327,339,341] However, there have been some impressive results recently where the composite is comprised of an interconnected CNT network stabilized by an insulating polymer binder. Mo et al. prepared ca. 30 μm thick cellulose acetate/SWCNT composites by bar-coating from an acetone paste, which exhibited a TE power factor of ca. 140 μW m^{-1} K^{-2} for *p*-type transport and could be easily doped n-type via

https://doi.org/10.1021/acs.chemrev.1c00218
Chem. Rev. XXXX, XXX, XXX−XXX

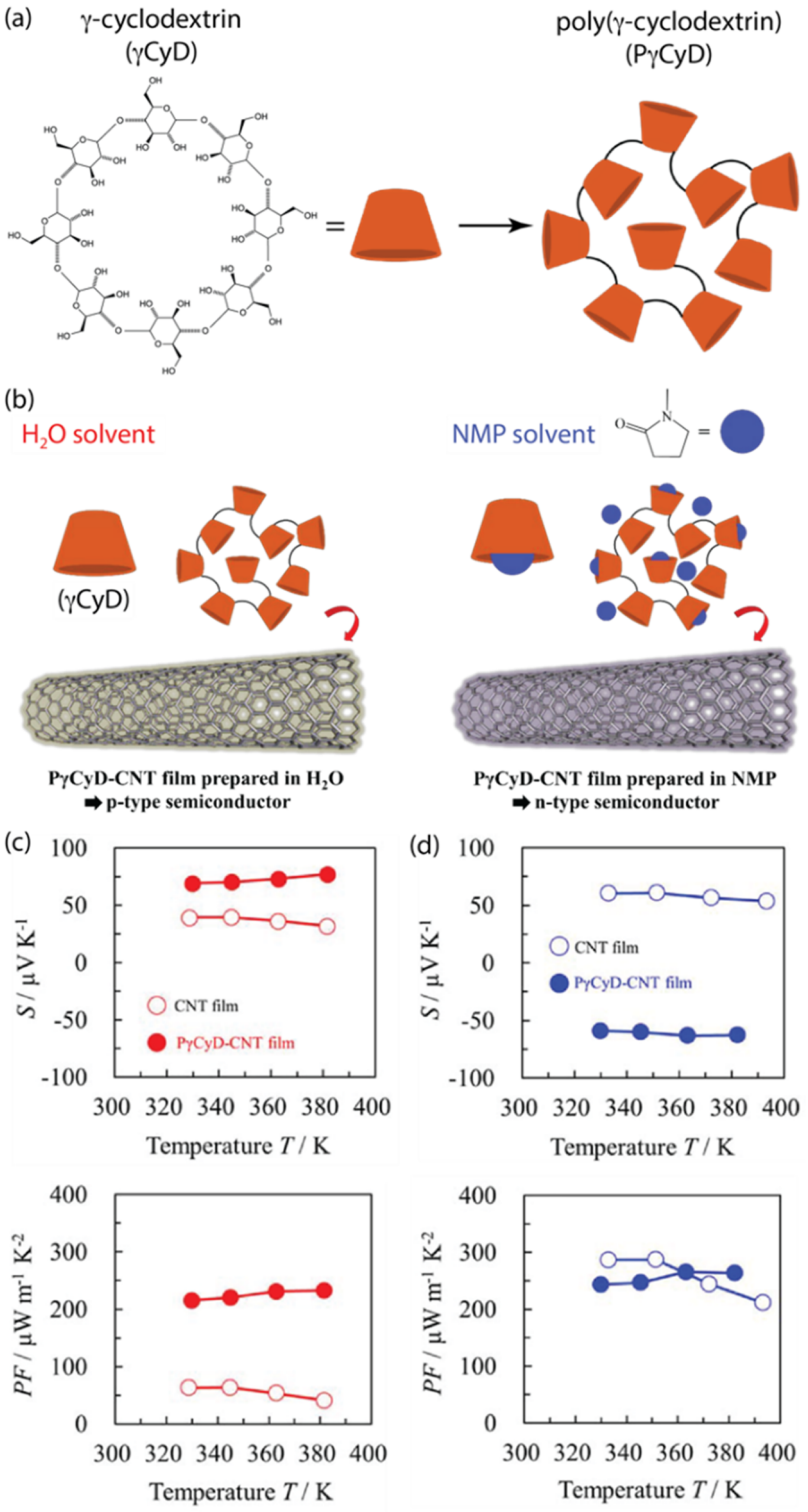

Figure 40. Thermoelectric performance of blended composites of poly(γ-cyclodextrin) (PγCyD) with CNT inclusions. Cartoons illustrating (a) the PγCyD structure, showing "pockets" in the γ-cyclodextrin macrocycles, and (b) the different PγCyD-solvent interactions with either H_2O or NMP that result in the observed (c) p-type or (d) n-type TE transport behavior. Adapted with permission from ref 354. Copyright 2020 The Japan Society of Applied Physics.

painting the freestanding films with a solution of 6 wt % polyethylenimine (PEI) in ethanol.[358] The authors attributed the impressive performance to the presence of "secondary" aggregates (i.e., bundles of bundles) and a corresponding reduction in the interbundle resistance, in addition to possible carrier energy filtering enhancement of the Seebeck coefficient at the CNT−cellulose acetate junction. More recently, Hata et al. demonstrated composites of CNTs embedded in a γ-cyclodextrin polymer cross-linked with epichlorohydrin (PγCyD) that exhibit TE power factors >200 $\mu W\ m^{-1}\ K^{-2}$ for both p-type and n-type transport (Figure 40).[354] The difference in the majority carrier type was attributed to different

https://doi.org/10.1021/acs.chemrev.1c00218
Chem. Rev. XXXX, XXX, XXX−XXX

interactions between the processing solvent, either H_2O or *N*-methyl-2-pyrrolidone (NMP), where the "pocket" in the γCyD macrocycle is capable of hosting the NMP molecule (Figure 40b), leading to enhanced n-type behavior than for an equivalent composite prepared from polyvinylpyrrolidone (PVP).

In recognition that the presence of the insulating polymer can introduce detrimental energetic barriers to charge carrier transport, Ha et al. performed an esterification of polyvinyl alcohol (PVA), and a subsequent condensation reaction between the resulting PVA-COOH and amine-functionalized SWCNTs, to produce PVA-grafted nanotubes that exhibited peak TE power factor of ca. 85 $\mu W\ m^{-1}\ K^{-2}$ for the composite with ca. 30 wt % SWCNTs.[350] With the addition of a small amount (3 wt %) of the commercial nonionic surfactant Triton X-100 during the condensation step, the Seebeck coefficient of the composite was more than doubled (to ca. 85 $\mu V\ K^{-1}$) with only a small decrease in the electrical conductivity, resulting in an enhancement of the TE power factor to >200 $\mu W\ m^{-1}\ K^{-2}$.

The majority of recent research on CNT-based TE composites has focused on several prototypical conjugated/conducting polymers, including PANI,[355] PEDOT,[349,351,352,356] and P3HT.[357] PANI, primarily in the emeraldine form, has been one of the most widely studied polymer host matrices for TE composites with CNT inclusions, partly because of its amenability to tuning of the polymer redox and electrical transport properties through protonation of the imine nitrogen atoms. Early work by Meng et al. demonstrated a rather low TE power factor (ca. 5 $\mu W\ m^{-1}\ K^{-2}$) for composites where the PANI was polymerized after formation of a MWCNT network.[328] This peak TE power factor was observed for composites with ca. 15 wt % PANI, corresponding to a thin coating of the PANI on the MWCNT bundle surface. The Seebeck coefficient more than doubled compared to the PANI-free MWCNT network, with only a small decrease in the electrical conductivity. Replacement of the MWCNTs with SWCNTs saw an improvement in both the Seebeck coefficient (ca. 40 $\mu V\ K^{-1}$) and electrical conductivity (<12 500 $S\ m^{-1}$) for the PANI/SWCNT composite, resulting in a 4-fold increase of the TE power factor to ca. 20 $\mu W\ m^{-1}\ K^{-2}$.[329] The authors attributed these observations to strong interactions between the conjugated π-orbitals of the CNTs and PANI, which induced ordering in the polymer chains on the nanotube surface, resulting in enhancement of the electrical conductivity and Seebeck coefficient. An increase in polymer ordering is expected to reduce the bandgap. Both this reduced bandgap and the measured increase of the carrier density would be expected to reduce the Seebeck coefficient. Therefore, the observation of a simultaneous increase in both the electrical conductivity and Seebeck coefficient suggests that either (i) the thermoelectric properties of the composite are dominated by conduction pathways restricted to the SWCNTs or (ii) the strong interactions between the polymer chains and nanotubes may result in a hybrid material with enhanced electronic properties relative to the individual components.

The choice of solvent is known to influence the PANI polymer chain conformation in solution, with *m*-cresol yielding expanded polymer coils that favor π-polaron delocalization along the polymer chain.[368] This favorable solvent−polymer interaction was exploited by Wang et al. to in situ polymerize PANI in a SWCNT dispersion in *m*-cresol, resulting in a more uniform PANI coating on the nanotube surface and exceptional electrical conductivities exceeding 140 000 $S\ m^{-1}$ and peak TE power factors of ca. 220 $\mu W\ m^{-1}\ K^{-2}$.[347] Perhaps the most impressive TE performance was recently achieved for composites where PANI was polymerized in dispersions containing amine-functionalized single- and double-walled CNTs, where careful control of the charge-carrier density by camphor sulfonic acid (CSA) resulted in thin-film composite TE power factors of ca. 400 $\mu W\ m^{-1}\ K^{-2}$ (Figure 41).[355] The enhanced performance relative to unfunctionalized CNTs was attributed to better dispersion of the amine-functionalized CNTs in solution and a resulting improved coating by, and interaction with, the PANI chains (Figure 41).

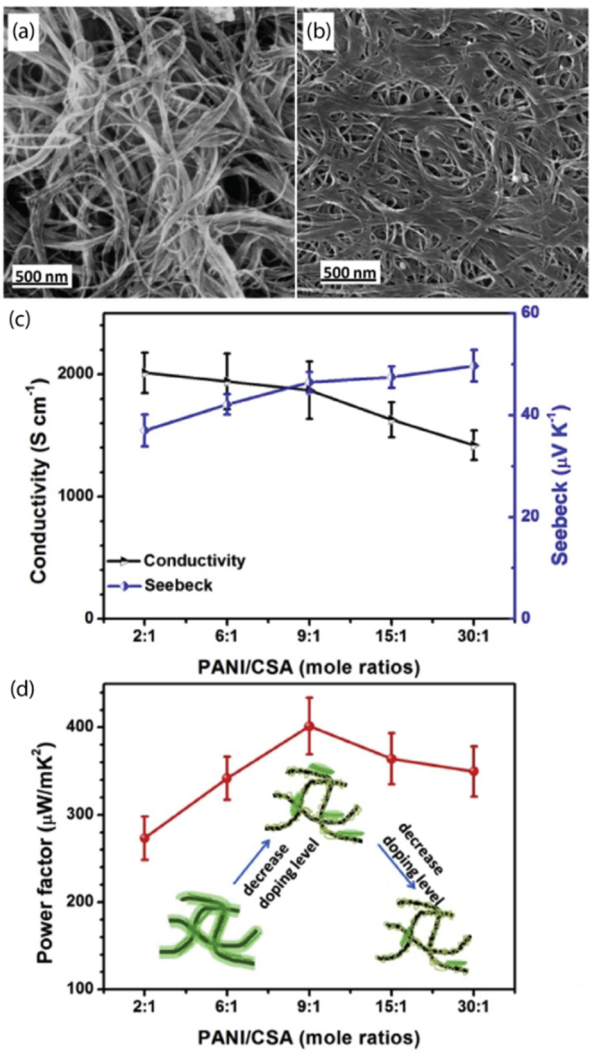

Figure 41. Thermoelectric composites of polyaniline (PANI) and amine-functionalized carbon nanotubes (a-CNTs). SEM images of (a) a-CNT and (b) 94 wt % a-CNT/PANI films, illustrating that the PANI serves to coat the a-CNT bundles and generate a more densely packed network. (c) Electrical conductivity and Seebeck and (d) corresponding TE power factor of 94 wt % a-CNT/PANI composites with varying mole ratios of PANI/CSA. Adapted with permission from ref 355. Copyright 2018 Elsevier Ltd.

For prepolymerized PANI, Yao et al. exploited the favorable solvent interaction with *m*-cresol, in addition to the susceptibility of PANI to doping with CSA, to prepare composites with significantly enhanced electrical conductivity and TE performance (*PF* ca. 175 $\mu W\ m^{-1}\ K^{-2}$).[342] Despite the rather large SWCNT content (64 wt %), the thermal conductivity was still as low as 0.43 $W\ m^{-1}\ K^{-1}$, more than an order of magnitude lower

https://doi.org/10.1021/acs.chemrev.1c00218
Chem. Rev. XXXX, XXX, XXX−XXX

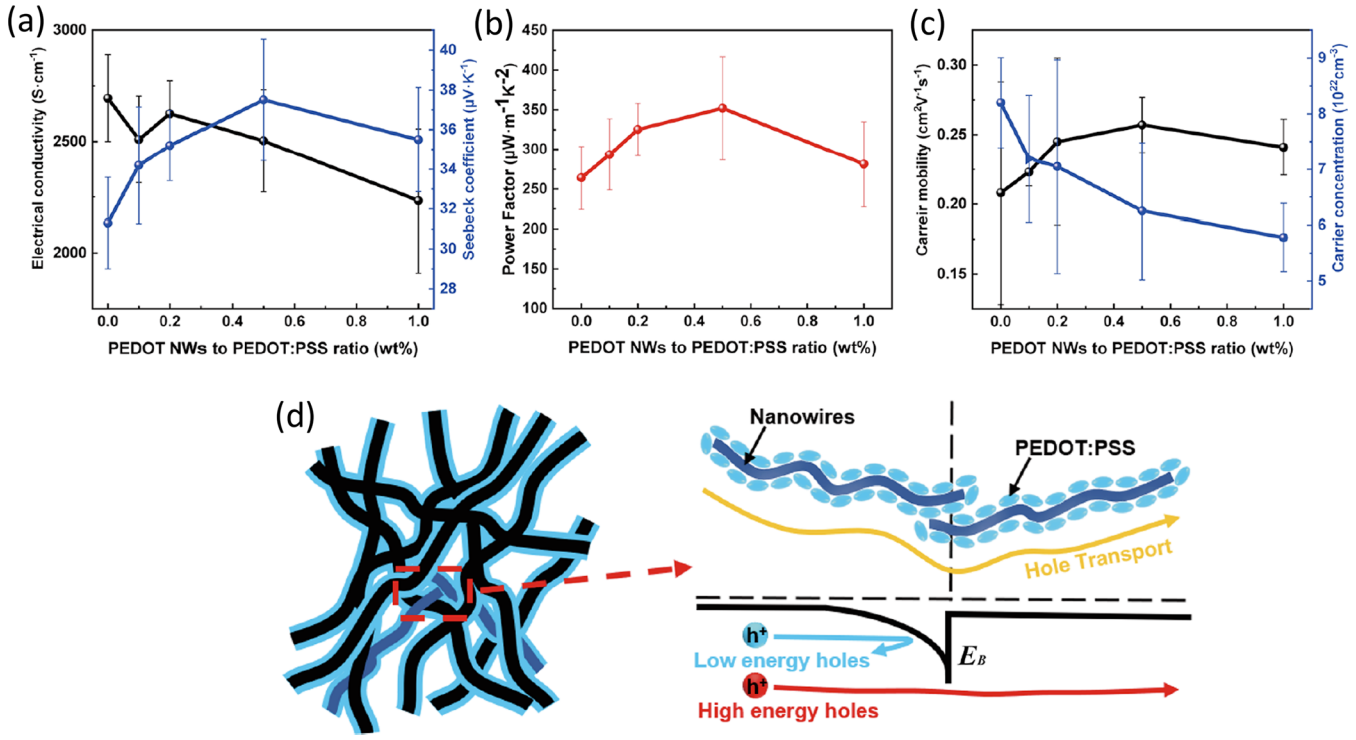

Figure 42. Impact of the loading of PEDOT NWs (PEDOT NW to PEDOT:PSS weight ratio) on the thermoelectric properties of ternary composite films of SWCNT/PEDOT:PSS/PEDOT NW: (a) electrical conductivity and Seebeck coefficient, (b) thermoelectric power factor, and (c) carrier mobility and concentration from Hall effect measurements. (d) Schematic illustration of carrier energy filtering effect proposed at NW and PEDOT:PSS interfaces. Reproduced with permission from ref 352. Copyright 2019 American Chemical Society.

than expected from simple mixing of the two components. A subsequent study by Weng et al. found that replacing the SWCNTs with DWCNTs and preparation of the dispersions using a probe-tip sonicator, resulted in peak TE power factors exceeding 200 μW m^{-1} K^{-2} for composite prepared with CSA-doped PANI.[344] A recent study of the effect of polymer molecular weight and nanotube content in CSA-doped PANI/SWCNT composites found that extremely high electrical conductivities (>400 000 S m^{-1}) could be achieved, albeit at the expense of severely reduced Seebeck coefficient and TE power factors <100 μW m^{-1} K^{-2}.[369]

Early work by the groups of Yu and Grunlan on PEDOT:PSS/CNT composites focused on the use of either polymeric[339] or dual polymeric-molecular[341] CNT stabilizers aimed at improving the solid-state microstructure and carrier transport in the composites. These efforts achieved electrical conductivities around or exceeding 100 000 S m^{-1}, resulting in power factors of ca. 160 μW m^{-1} K^{-2} for PEDOT:PSS/SWCNT composites stabilized by polyvinyl acetate (PVAc) and ca. 500 μW m^{-1} K^{-2} for PEDOT:PSS/DWCNT composites stabilized by both PVAc and tetrakis(4-carboxyphenyl)porphyrin (TCPP). Inspired by the observation that solvent treatments (e.g., ethylene glycol, EG) can remove excess insulating PSS from the PEDOT:PSS matrix to enhance both the electrical conductivity and Seebeck coefficient,[79] Lee et al. used EG to remove excess PSS from PEDOT:PSS/DWCNT composites and enhance the electrical conductivity for all DWCNT loadings, culminating in a peak power factor of ca. 150 μW m^{-1} K^{-2}.[346]

An alternative strategy to eliminate the insulating PSS is the formation of composites of CNTs with PEDOT, where the ethylenedioxythiophene (EDOT) monomer is polymerized immediately prior to composite formation. A recent approach, where the EDOT monomer is chemically polymerized in situ in a preprepared aqueous SWCNT suspension resulted in a composite with strong interactions between the PEDOT chains and the SWCNT sidewall and an interconnected 3D network of PEDOT-wrapped SWCNT bundles, leading to a TE power factor of ca. 150 μW m^{-1} K^{-2}.[351] The factor of 4 improvement over previous attempts at in situ chemical polymerization enhancement was attributed to the improved formation of a thin, uniform PEDOT coating on the carbon nanotubes. An even larger enhancement in the TE performance was obtained for the samples prepared from EDOT monomers electropolymerized in a 3-phase process that were subsequently mixed with acid-doped, amine-functionalized nanotubes (a-SWCNTs).[349] In this case, the acid doping of the a-SWCNTs resulted in a large increase of the electrical conductivity within the composite and TE power factors approaching 350 μW m^{-1} K^{-2}. The precise balance between the electrical conductivity and Seebeck coefficient in the blended PEDOT/a-SWCNTs was found to depend on the chemical identity of the counterion employed in the 3-phase interfacial EDOT electropolymerization procedure. The perchlorate (ClO_4^-) anion afforded the largest electrical conductivity, at the expense of a reduction in the Seebeck coefficient, but the hexafluorophosphate (PF_6^-) anion gave the highest TE power factor.[349]

Templated chemical polymerization of EDOT in a solution of sodium dodecyl sulfate (SDS) and iron (III) chloride ($FeCl_3$) has also been used to prepare PEDOT nanowires that were dispersed with SWCNTs and subsequently combined with a PEDOT:PSS suspension.[352] The resulting blended ternary PEDOT NW/SWCNT/PEDOT:PSS composite with 0.5% by weight PEDOT NW to PEDOT:PSS yielded a TE power factor of ca. 350 μW m^{-1} K^{-2} (Figure 42a,b), which the authors

https://doi.org/10.1021/acs.chemrev.1c00218
Chem. Rev. XXXX, XXX, XXX−XXX

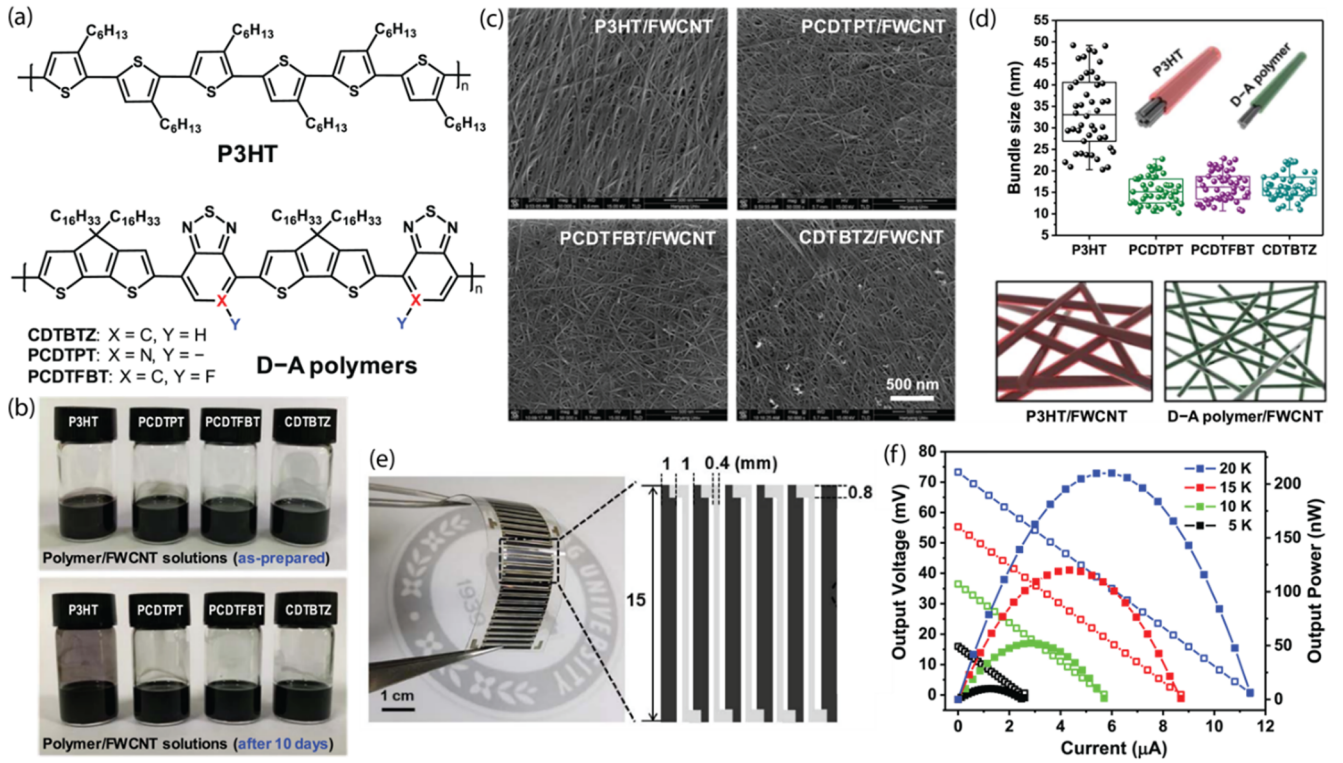

Figure 43. Thermoelectric composites prepared using donor−acceptor (D−A) conjugated polymers. (a) Chemical structures of P3HT and three D−A polymers used in the study. (b) Photographs showing vials containing polymer/FWCNT composite solutions: (upper panel) as-prepared and (lower panel) after 10 days of storage. The vials were vigorously shaken just before being photographed. (c) SEM images of drop-cast polymer/FWCNT composite films prepared using different conjugated polymers. All images have the same scale bar. (d, top) Bundle size distributions estimated from SEM images in (c) for the various polymer/FWCNT composite films. The inset image shows schematic illustrations of probable FWCNT bundles in P3HT/FWCNT and D−A polymer/FWCNT composites. (d, bottom) Schematic comparisons of FWCNT bundle structures and their interconnections in drop-cast films of P3HT/FWCNT and D−A polymer/FWCNT composites. (e, left) Photograph showing PCDTPT/FWCNT composite-based flexible p-type TEG device and (e, right) magnified schematic illustration showing specific configuration of several legs and electrodes in the TEG device. (f) Plots of output power and voltage vs current of the flexible TEG device at various temperature gradients (ΔT = 5, 10, 15, and 20 K). Adapted with permission from ref 353. Copyright 2019 American Chemical Society.

attributed to an enhanced Seebeck coefficient due to carrier energy filtering at the PEDOT NW/PEDOT:PSS interface (Figure 42d).[352]

In contrast to these observations for PEDOT, initial attempts at in situ chemical polymerization of 3-hexylthiophene in a dispersion of MWCNTs in chloroform yielded P3HT/MWCNT composites with very low electrical conductivities (<15 S m^{-1}) and Seebeck coefficients (<12 μV K^{-1}).[370] The ability of poly(3-hexylthiophene), in combination with ultrasonic agitation, to exfoliate and solubilize carbon nanotubes in organic solvents,[371−373] was subsequently exploited by Bounioux et al. to prepare TE composites of P3HT with both SWCNTs and MWCNTs.[374] The undoped composites exhibited quite low electrical conductivities, with the peak TE power factor for the P3HT:SWCNT composite of ca. 18 μW m^{-1} K^{-2}, about 2 orders of magnitude larger than that of the P3HT:MWCNT composite. To enhance the TE performance, the authors employed anhydrous iron (III) chloride ($FeCl_3$) in nitromethane as a p-type dopant. The increased carrier density gave an order of magnitude increase in the peak electrical conductivity to ca. 150 000 S m^{-1} for the P3HT/SWCNT composite at lower SWCNT content than for the undoped samples, resulting in a peak TE power factor of ca. 95 μW m^{-1} K^{-2} despite a drop in the Seebeck coefficient to ca. 25 μV K^{-1}.[374]

Subsequently, Lee et al. were able to achieve slightly higher TE power factors for undoped P3HT/SWCNT composite samples prepared via wire-bar coating,[375] due primarily to an increase in the Seebeck coefficient (ca. 38 μV K^{-1}) but also an enhanced electrical conductivity (ca. 50 000 S m^{-1}) over drop-cast films. This improvement was attributed to an improved composite morphology, with the formation an interconnected network of fairly small SWCNT bundles (6−23 nm in diameter), which is known to enhance the TE performance.[252] This performance was improved through a spin-casting doping process, using $FeCl_3$ in nitromethane, primarily due to a factor of 5 increase in the electrical conductivity (>275 000 S m^{-1}) that overcame a small decrease (<20%) in the Seebeck coefficient to yield a TE power factor of ca. 270 μW m^{-1} K^{-2}.[345] Here, the $FeCl_3$ doping of P3HT/SWCNT composite results in significant charge-carrier injection into P3HT, suggesting that the increased electrical conductivity likely arises from improved carrier transport through both the polymer matrix and interconnected SWCNT network. Hong et al. demonstrated a further increase in the TE power factor to ca. 325 μW m^{-1} K^{-2} via spray deposition of the P3HT/CNT composite, this time containing inclusions of few-walled carbon nanotubes (FWCNTs).[376] Despite a significant reduction of the electrical conductivity (<35 000 S m^{-1}), these spray-coated films exhibited Seebeck coefficients approaching 100 μV K^{-1}, even with the inevitable presence of metallic species in the FWCNTs. More recently, Jung et al. demonstrated that drop-cast P3HT/FWCNT composites can achieve TE power factors of ca. 230

https://doi.org/10.1021/acs.chemrev.1c00218
Chem. Rev. XXXX, XXX, XXX−XXX

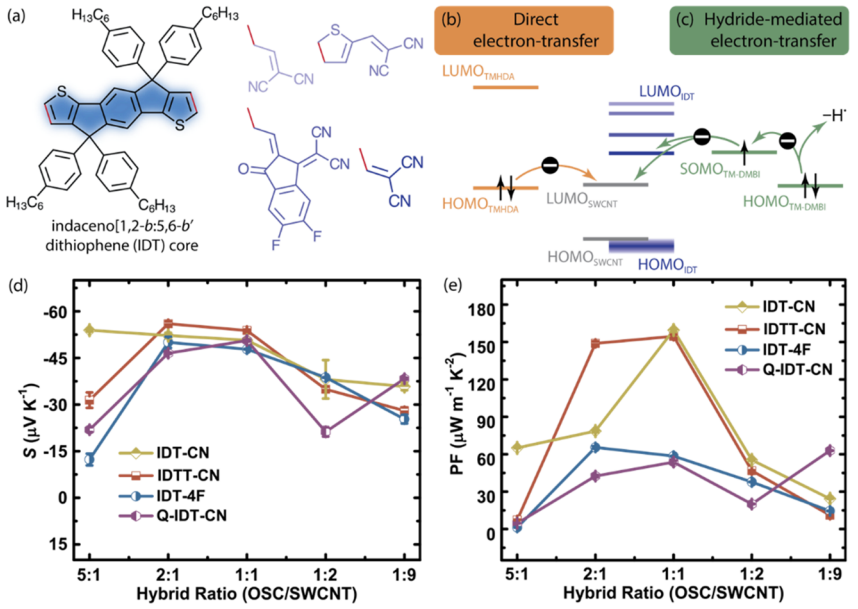

Figure 44. Controlling n-type doping in composites of molecular organic semiconductors (mOSCs) and CNTs. (a) Chemical structures of the 4,9-dihydro-*s*-indaceno[1,2-*b*:5,6-*b*′]dithiophene (IDT) core (left) and the terminal groups (right). Cartoons illustrating (b) direct electron transfer and (c) hydride abstraction-mediated electron transfer from two different n-type dopants. The composites doped with an alkyl diamine derivative exhibit (d) n-type Seebeck coefficients and (e) large TE power factors. Adapted with permission from ref 366. Copyright 2019 Elsevier BV.

μW m^{-1} K^{-2}, despite rather large bundle sizes of ca. 33 nm in diameter.[353]

Poly(alkylthiophenes) are well-known to exhibit optical and electronic properties that strongly depend on the regioregularity of the side chains attached to the polythiophene backbone, which subsequently determines the extent of ordering within the solid-state microstructure. Tonga et al. demonstrated that the impact of this regioregularity extends to the TE performance of composites with SWCNT inclusions, with iodine-doped regioregular-P3HT/SWCNT composites displaying a superior electrical conductivity and Seebeck coefficient to their regiorandom counterparts, resulting in a factor of 50 increase in the TE power factor to ca. 150 μW m^{-1} K^{-2}.[357] These observations suggest that the conformation of the polymer, and the impact that this might have on the resulting microstructure of the composite, should be considered when choosing the host in polymer-based CNT composites.

In 2019, Jung et al. demonstrated that "donor−acceptor" polymers with alternating electron-rich and electron-poor conjugated moieties (Figure 43a), similar to those employed in high-performance organic photovoltaics, were capable of dispersing FWCNTs more effectively than P3HT (Figure 43b), resulting in about a factor of 2 reduction in the size of the bundles in the resulting network (Figure 43c,d).[353] The improved electrical transport in these networks (σ > 70 000 S m^{-1}) resulted in peak TE power factors exceeding 300 μW m^{-1} K^{-2}, with the best performance demonstrated by the PCDTPT/FWCNT networks (ca. 460 μW m^{-1} K^{-2}), despite a slight reduction in the Seebeck coefficient compared to the P3HT composite. The authors were able to fabricate an all p-type TEG (Figure 43e) using the PCDTPT/FWCNT networks that was capable of generating >200 nW for a temperature difference of 20 K (Figure 43f).[353]

4.2.5.2. Blended Molecule−Carbon Nanotube Nanocomposites. In contrast to their polymer counterparts, molecular organic semiconductors (mOSCs) have received far less attention as a component in CNT-based TE composites. The recent emergence of high-performance molecular electron acceptors for organic photovoltaics provides an excellent example of the rich chemical diversity available for small molecule-based TE materials. The precise chemical structure, chemical tunability, and potential for unrivaled purity, coupled to the recent demonstration of exceptionally large Seebeck coefficients,[191,377−379] suggests mOSCs as high-performance TE composite materials with a huge potential for carefully designed structure−function studies. It is important to note here that the distinction between a composite, which we define as having a significant volume fraction loading of multiple components that are mixed together prior to network formation, and small molecule-doping of a preformed porous CNT network becomes a little blurred. The following discussion focuses on the former, where we expect the molecular species to play additional roles beyond being a simple surface-adsorbed redox (charge-transfer) dopant. Even here this definition can be open to interpretation, and any omission on the part of the authors is unintentional.

Motivated by the potential advantages of mOSCs, Wu et al. investigated composites of amino-substituted rylene diimides, previously explored as self-doped TE molecular crystals,[191] and SWCNTs prepared via vacuum filtration of an ultrasonically prepared dispersion of the two components.[359] The amino-substituted rylene diimides appear to be effective n-type dopants for the SWCNT network, resulting in an n-type Seebeck coefficient comparable to the best-performing n-type dopants explored to date. In this context, the SWCNT inclusions enable far superior electrical conductivities (>40 000 S m^{-1}) to thin films of the substituted rylene diimides. The composites prepared from both derivatives achieve peak TE power factors exceeding 100 μW m^{-1} K^{-2}, with the optimum SWCNT to rylene diimide weight ratio lying between 2:1 and 1:1.[359] While the TE performance of the composites appears to be dominated by the SWCNT network, there is a clear influence from the electronic properties of the rylene diimide. The composite containing the naphthalene diimide derivative slightly outperforms the perylene diimide derivative, primarily due to a slightly

https://doi.org/10.1021/acs.chemrev.1c00218
Chem. Rev. XXXX, XXX, XXX−XXX

larger Seebeck coefficient that might arise from the wider bandgap of the naphthalene diimide. This observation points to a potential modulation of the carbon nanotube density of states by the rylene diimide, which would require more detailed investigations of the electronic structure of the composites. However, the morphology in the two composites varies dramatically, suggesting that significant changes in the charge carrier transport (mobility) could play a dominant role in the observed changes in the Seebeck coefficient.

Shortly thereafter, and inspired by the substitutional chemistry of the rylene diimides described above, Gao et al. explored a series of acridone derivatives with different terminal tertiary amine groups (ADTA) as n-type components in SWCNT-based TE composites.[361] Irrespective of the chemical nature of the terminal tertiary amine group, the samples all exhibited n-type behavior at elevated temperature, although the room-temperature behavior appeared to be rather complex and suggestive of incomplete n-type doping. For instance, both the piperidine- and 4-hydroxypiperidine-terminated acridones exhibited p-type TE power factors of >150 μW m^{-1} K^{-2} at room temperature, whereas the diethyl amine-terminated acridone exhibited a n-type TE power factor of ca. 125 μW m^{-1} K^{-2} at room temperature.[361] The same group explored a similar series of compounds, this time based on acridine derivatives where the nature of the terminal tertiary amine group, the length of the connecting alkyl chain, and the anion chemistry were systematically varied.[363] Once again, the TE transport behavior was rather complex, with small changes in the chemical structure of the acridine derivative resulting in dramatic switches between p-type and n-type behavior.

Diphenylamine and carbazole moieties are common in hole (p-type) transport materials for organic electronic and optoelectronic applications.[380,381] Inspired by their potential for effective p-type transport, Yin et al. prepared a series of compounds to compare the impact of both the central core and the peripheral moieties on the TE performance of the corresponding SWCNT composites.[362] When the diphenylamine units were connected to a biphenyl core the composite exhibited the largest Seebeck coefficient, consistent with the larger bandgap of the mOSC and lowest electrical conductivity. Replacing the biphenyl core with pyrene resulted in a reduction of the Seebeck coefficient but a slight increase in the electrical conductivity. However, the highest TE performance was exhibited by the mOSC with carbazole moieties attached to a pyrene core, primarily due to the improved electrical conductivity (ca. 190 000 S m^{-1}) that enabled a peak TE power factor of ca. 110 μW m^{-1} K^{-2}.[362]

Recently, Yin et al. explored the TE performance of composites for a series of mOSCs based on the 4,9-dihydro-*s*-indaceno[1,2-*b*:5,6-*b*′]dithiophene (IDT) core (Figure 44a),[366] which is similar to one of the highest performing nonfullerene electron acceptors in organic photovoltaics. To control the charge-carrier density and improve the electrical transport, the authors also investigated n-type doping using two dopants that function via different electron-transfer mechanisms (Figure 44b,c). For all combinations of the SWCNTs with the four ITD molecules and two dopants, the composites exhibited n-type transport and TE power factors exceeding 50 μW m^{-1} K^{-2} (Figure 44d,e). For the 1,3-dimethyl-2-(2,4,6-trimethoxyphenyl)-2,3-dihydro-1*H*-benzo[*d*]imidazole (TM-DMBI) dopant, the electron injection is mediated by hydride transfer, apparently resulting in more effective charge transfer (cf., lower Seebeck coefficients and larger electrical conductivities) that may push the carrier density of the composite beyond the peak TE performance. In contrast, the highest performance was observed for direct electron transfer from the alkyl diamine-based electron dopant to the composites possessing the two largest bandgap IDT derivatives (*PF* > 150 μW m^{-1} K^{-2}).[366]

The most impressive TE performance achieved to date in mOSC/CNT composites was for samples prepared with the high charge mobility semiconductor 2,7-diphenyl[1]-benzothieno[3,2-*b*][1]benzothiophene (DPh-BTBT).[364] Even in the undoped DPh-BTBT/SWCNT composites, the TE power factor was quite impressive (>160 μW m^{-1} K^{-2}), but the authors also explored the impact that the p-type dopant chemistry and the doping process had on the TE performance. For both 7,7,8,8-tetracyanoquinodimethane (TCNQ) and 2,3,5,6-tetrafluoro-7,7,8,8-tetracyanoquinodimethane (F_4TCNQ), solution phase doping, by direct mixing of the dopant into the DPh-BTBT/SWCNT casting solution, resulted in a near-universal drop of the TE power factor irrespective of the doping concentration. In contrast, vapor deposition of thin TCNQ or F_4TCNQ films (<40 nm) onto a preformed DPh-BTBT/SWCNT composite enhanced the TE power factor to (>200 μW m^{-1} K^{-2}), with the 40 nm thick vapor deposited TCNQ sample reaching an optimum value of ca. 280 μW m^{-1} K^{-2}.[364]

4.2.5.3. Blended Nanocomposites of Polymers and Graphitic Nanocarbons. Much like their polymer-carbon nanotube counterparts, blended composites of polymers and two-dimensional (2D) graphitic nanocarbons have seen significant improvement in their TE performance over the past decade, with many of the notable achievements highlighted in a recent review by Nadihalli et al.[367] Although a number of polymer matrices have been explored, including polythiophenes and polypyrroles,[382−386] the most significant advances have been achieved with PANI and PEDOT:PSS.

Early studies of nanocomposites of conducting/conjugated polymers and graphitic nanocarbons focused on blends of PANI with graphite or graphene nanosheets, where the TE power factor and zT measured at room temperature were low (<10 μW m^{-1} K^{-2} and <0.001, respectively).[387−389] Improvements in the TE power factor (14 μW m^{-1} K^{-2}) were obtained for composites prepared by cold pressing powders of mechanically mixed PANI and graphene nanoplatelets (GNPs) at 10 tons for 3 min.[390] More recently, drop-cast films prepared following solution-phase ultrasonic mixing of CSA-doped PANI and GNPs achieved TE power factors exceeding 15 μW m^{-1} K^{-2}, due primarily to an enhanced electrical conductivity.[391] The authors demonstrated that disruption of the electronic structure of the sp^2-hybridized hexagonal carbon lattice, through the incorporation of oxygenic functional groups, weakened the interaction with the PANI chains and reduced the electrical conductivity and TE power factor. Motivated by this observation, Wang et al. polymerized aniline in situ on the surface of CVD-grown GNPs, which were subsequently dispersed and doped in a solution of CSA in *m*-cresol before drop-casting to form films that exhibited enhanced Seebeck coefficients (ca. 26 μV K^{-1}) and TE power factors (ca. 55 μW m^{-1} K^{-2}).[392] To date, the most impressive TE performance was achieved for spin-cast films of CSA-doped PANI and thermally reduced GO nanoplatelets prepared by solution-phase ultrasonic mixing, reaching TE power factors exceeding ca. 210 μW m^{-1} K^{-2}.[393] An interesting alternative approach was recently demonstrated by Hsieh et al., who demonstrated TE power factors exceeding ca. 80 μW m^{-1} K^{-2} for a three-dimensional

https://doi.org/10.1021/acs.chemrev.1c00218
Chem. Rev. XXXX, XXX, XXX−XXX

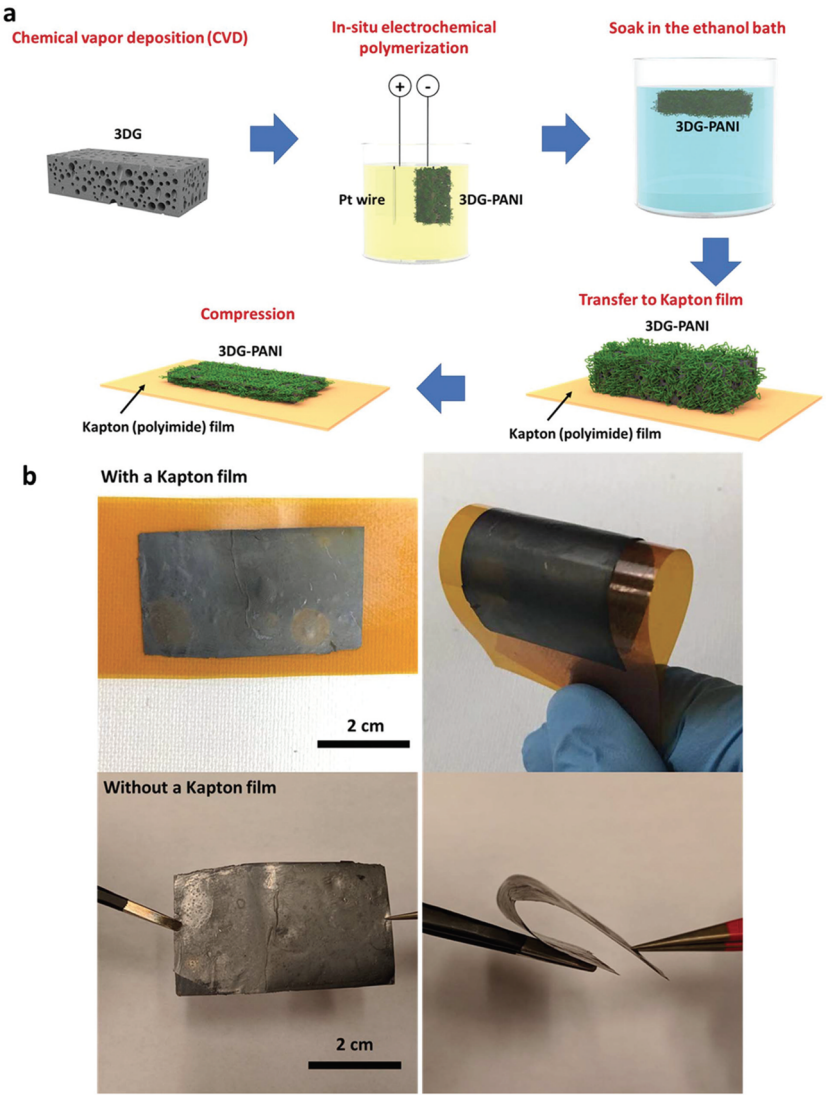

Figure 45. (a) Schematic illustration showing the template synthesis of a 3D graphene−PANI composite. (b) Digital photographs of the 3D graphene−PANI composite containing 80 wt % PANI supported by a Kapton (polyimide) film (upper images) and as a free-standing flexible sample (lower images). Reproduced with permission from ref 394. Copyright 2019 The Royal Society of Chemistry.

(3D) graphene matrix infiltrated with PANI via in situ polymerization of aniline in the porous 3D graphene matrix (Figure 45a).[394] One advantage of this approach is that the 3D graphene matrix, produced via CVD synthesis of graphene in a polymer-bound nickel powder catalyst template, can be cast into various form factors, including onto a supporting substrate or as free-standing films (Figure 45b). This versatility could enable fabrication of TE composites that can be tailored for the waste heat source.

Similar to PANI-based nanocomposites, early composites based on PEDOT and graphitic nanocarbons exhibited relatively low room-temperature power factor and zT (<15 μW m^{-1} K^{-2} and <0.02, respectively). Motivated by previous demonstrations that >35 wt % CNT loadings were typically required to improve the electrical conductivity in PEDOT:PSS-CNT composites, Kim et al. prepared composites with low loadings (<3 wt %) of reduced graphene sheets, which afforded an increase in both the carrier concentration and mobility relative to the pristine PEDOT:PSS sample.[395] The increased carrier concentration resulted in a decrease of the Seebeck coefficient by a factor of ca. 3, but this was more than offset by a >20 times enhancement in the electrical conductivity, enabling TE power factors of ca. 11 μW m^{-1} K^{-2}. Surprisingly, the thermal conductivity of the composites was actually reduced by the inclusion of graphene, which the authors attributed to a reduction in the phonon (lattice) thermal conductivity due to the low graphene loading and phonon scattering at the interfaces between the polymer matrix and graphene fillers. Several subsequent studies demonstrated that similarly low loadings (<5 wt %) of graphene or reduced-GO improved both the electrical condu and TE power factor (exceeding >25 μW m^{-1} K^{-2}) of the pristine PEDOT:PSS but had little impact on the magnitude of the Seebeck coefficient.[396−398] For samples prepared by in situ polymerization of EDOT in an ultrasonically mixed aqueous PSS-graphene dispersion, a peak TE power factor of ca. 45 μW m^{-1} K^{-2} was achieved for the composite with 3 wt % graphene.[396] Recently, flexible p-type TEGs with 5 legs were fabricated from vacuum-filtered PEDOT:PSS-graphene dispersions (Figure 46), exhibiting reasonable TE open-circuit voltages of ca. 4 mV for a temperature difference of 56 K (corresponding to a Seebeck coefficient of ca. 14 μV K^{-1}) and

https://doi.org/10.1021/acs.chemrev.1c00218
Chem. Rev. XXXX, XXX, XXX−XXX

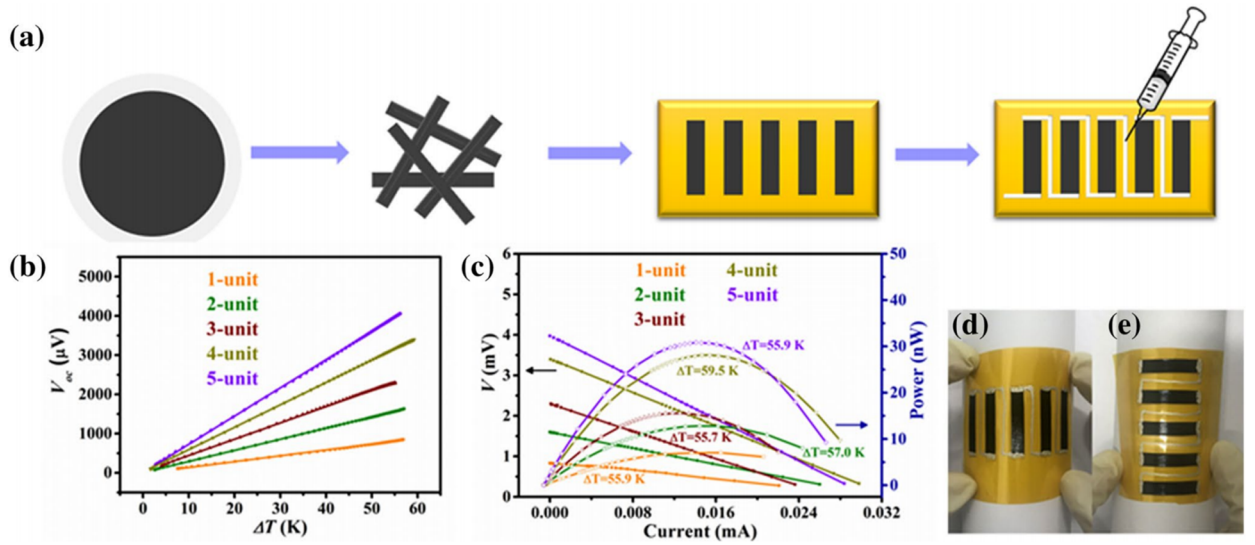

Figure 46. (a) Schematic illustration showing preparation of a flexible p-type TEG from vacuum-filtered PEDOT:PSS-graphene composite. (b) Temperature-dependent open-circuit voltage generated by the TEGs and (c) Output voltage and power as a function of current for the prepared TEGs as a function of the number of p-type legs. (d,e) Digital photos illustrating the TEG flexibility. Reproduced with permission from ref 398. Copyright 2019 Springer Science+Business Media, LLC.

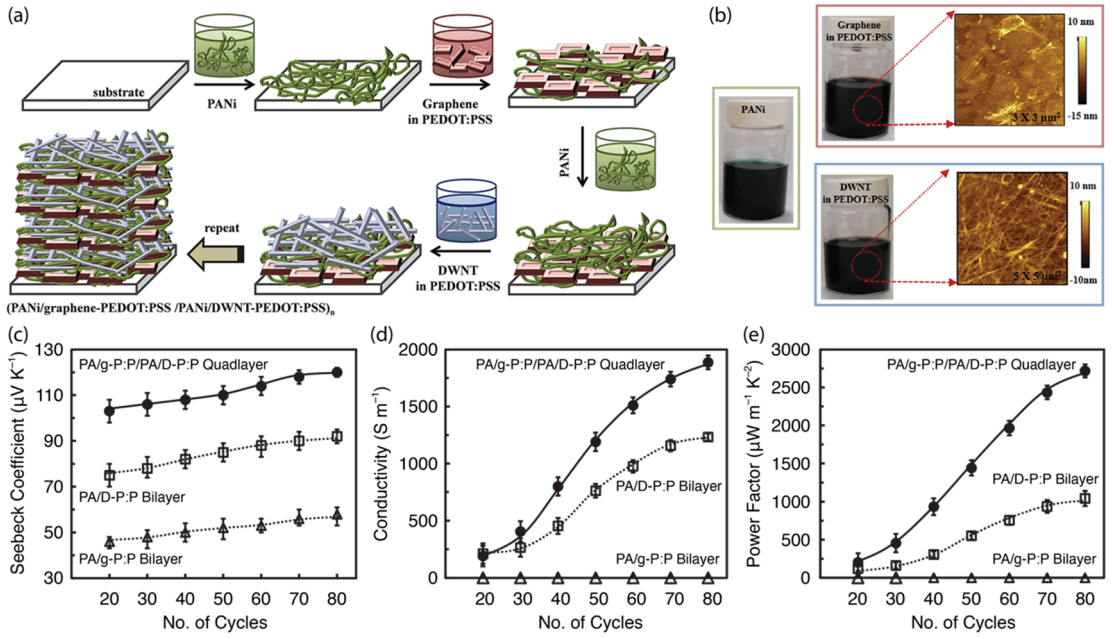

Figure 47. (a) Schematic representation of the layer-by-layer self-assembly procedure and (b) images of aqueous suspensions of PANI, graphene (stabilized by PEDOT:PSS), and DWCNT (stabilized by PEDOT:PSS). AFM topographical images of the corresponding suspensions cast onto silicon wafers are shown next to graphene and DWNT suspensions. The corresponding thermoelectric performance of the multilayer PCNs: (a) Seebeck coefficient, (d) electrical conductivity, and (e) thermoelectric power factor. Adapted with permission from ref 335. Copyright 2015 Wiley-VCH.

less than 3% reduction in device resistance the after 100 bending cycles.[398]

Several other nanocarbon fillers have been explored for PEDOT-based composites, including fullerene-decorated reduced GO[399] and graphene quantum dots (GQDs).[400] In the former study, noncovalent attachment of a heavily fluorinated C_{60} fullerene ($C_{60}F_{36}$) to the surface of reduced GO and subsequent loading (<3 wt %) into PEDOT:PSS led to an enhanced TE power factor relative to both the pristine PEDOT:PSS sample and PEDOT:PSS-rGO composite.[399] The enhanced performance was primarily associated with an improved Seebeck coefficient, which the authors attributed to carrier filtering of low-energy carriers by the Schottky barrier at the interface between the PEDOT:PSS and rGO-$C_{60}F_{36}$ fillers. In the latter study, although the baseline TE performance of the pristine PEDOT:PSS sample was low compared to most previously reported values, the inclusion of GQDs prepared via chemical cutting of GO resulted in an enhancement of the electrical conductivity, Seebeck coefficient, and TE power factor.[400]

Inspired by the demonstration that replacement of the PSS polyanion with the molecular toluenesulfonate, or tosylate

https://doi.org/10.1021/acs.chemrev.1c00218
Chem. Rev. XXXX, XXX, XXX−XXX

(Tos), anion can lead to huge enhancements in the TE performance of PEDOT,[401] Maity et al. explored the TE properties of composites prepared via polymerization of EDOT in the presence of Tos and graphene.[402] Despite the rather high content of graphene (>10 wt %), the composites exhibited large Seebeck coefficients (>130 μV K^{-1}) and reasonable electrical conductivities (>500 S m^{-1}), resulting in a peak TE power factor of ca. 25 μW m^{-1} K^{-2} for 25 wt % graphene loading.

4.2.5.4. Multilayer Nanocomposites. Layer-by-layer (LbL) assembly, through sequential exposure of a substrate to solutions containing complementarily functionalized materials, is a simple and versatile method for creating conformal multifunctional films, particularly for composites with a large number of constituent components. The LbL approach has been used to explore the thermoelectric performance of hierarchical assemblies generated from (i) polycation/polyanion multilayers,[403] (ii) CNTs sequentially wrapped by polycation/polyanion layers,[404] and (iii) ligand-exchanged $Cu_{2-x}Se$ nanocrystal arrays.[405]

While there has been significant progress in the TE performance of blended nanocomposites with different nanocarbon inclusions, the best-performing systems remain the multilayered nanocomposites prepared by LbL deposition of the various constituents, which can address some of the difficulties associated with the creation of uniform, high-performance bulk composites. Cho et al. provided the first example of multilayered polymer carbon nanocomposites (PCNs) fabricated from PANI, graphene, and DWCNTs using the LbL approach.[406] This study demonstrated that PCNs comprised of PANI/DWCNT bilayers or PANI/graphene/PANI/DWCNT quadlayers both exhibited increasing electrical conductivity and Seebeck with the number of deposition cycles, up to an optimum around 40 cycles. The PANI/DWCNT bilayers exhibited TE power factors >750 μW m^{-1} K^{-2}, more than a factor of 4 larger than those for previously published blended PANI/CNT composites. However, the PANI/graphene/PANI/DWCNT quadlayers exhibited impressive Seebeck coefficients (ca. 130 μV K^{-1}) and TE power factors exceeding 1800 μW m^{-1} K^{-2}, which approached those for state-of-the-art inorganic telluride semiconductors. The authors attributed the impressive transport properties to the good electrical transport of the graphene and DWCNT network and the large Seebeck coefficients to carrier energy filtering at the ubiquitous nanoscale interfaces within the composite, both enabled by the deposition of thin (few nm) layers during each step in the LbL process.[406]

Through the stabilization of the graphene and DWCNT suspensions with PEDOT:PSS (Figure 47a), Cho et al. were able to induce almost a factor of 2 enhancement in the electrical conductivity (ca. 190 000 S m^{-1}) with smaller than a 10% decrease in the Seebeck coefficient compared to the non-PEDOT:PSS sample (Figure 47c,d).[335] These observations were attributed primarily to an enhanced charge-carrier mobility in the PEDOT:PSS stabilized composites, reaching ca. 19 cm^2 V^{-1} s^{-1}, for similar charge-carrier densities. The use of PEDOT:PSS also appeared to allow for the fabrication of thicker PCNs (80 cycles) with continued improvement in the performance.[335] The PEDOT:PSS stabilized 80 quadlayer PCN achieved a peak TE power factor exceeding 2700 μW m^{-1} K^{-2} (Figure 47e), which represents one of the highest performing all-organic thin-film TE materials to date.

In an effort to produce the n-type PCNs, required to build an all-PCN thermoelectric generator, Cho et al. employed the same LbL approach, this time stabilizing the DWCNTs and graphene with the n-type polymers polyethyleneimine (PEI) and polyvinylpyrrolidone (PVP), respectively.[334] The DWCNT-PEI/graphene-PVP bilayer PCNs exhibit n-type transport behavior with electrical conductivities of ca. 30 000 S m^{-1} and Seebeck coefficients of ca. −80 μV K^{-1}. However, the magnitude of the Seebeck coefficient appears to be constrained by the large electron concentration, which limits the TE performance ($PF \sim$ 190 μW m^{-1} K^{-2}) and potentially also reduces the charge-carrier mobility. These observations point to (i) improved PCN nanomorphology and (ii) carefully controlled electron density as strategies to improve the TE performance of n-type multilayered PCNs. Interestingly, the PCN nanomorphology appears to provide some resistance to the loss of n-type TE performance via compensation of the n-type dopants by oxygen, attributed to the tortuosity for gas diffusion offered by the exfoliated graphene layers.[334]

While the performance of the p-type multilayer composites with PEDOT:PSS-stabilized graphene and DWCNTs has not been surpassed, the LbL fabrication approach has been used to demonstrate impressive p-type and n-type behavior in multilayer composites containing reduced graphene oxide (rGO).[337,407] For the p-type composite, which is comprised of multiple bilayers formed from PANI and DWCNTs stabilized by graphene oxide (GO), the composite initially yielded reasonable performance, with a TE power factor of ca. 135 μW m^{-1} K^{-2}.[337] However, reduction of GO by L-ascorbic acid enhances both the electrical conductivity and Seebeck coefficient, resulting in an order of magnitude improvement in the TE power factor to ca. 1250 μW m^{-1} K^{-2}. Consistent with the observations for n-type multilayer composites based on DWCNTs and graphene, the n-type multilayer composites based on PEI-stabilized DWCNTs and GO underperform their p-type counterparts.[407] However, thermal reduction of the composite, at 150 °C for 30 min, to yield rGO results in a similar enhancement of the TE performance to the p-type rGO composite, resulting in a power factor of ca. 400 μW m^{-1} K^{-2}. These observations for both the p-type and n-type composites are attributed to a reduction in the number of sp^3 hybridized carbon atoms in the graphene oxide layer through removal of some of the surface oxide species, as determined from Raman and X-ray photoelectron spectroscopy measurements, and a corresponding increase in the charge-carrier mobility.[337,407]

In the last couple of years, poly(diallyldimethylammonium chloride) (PDDA) has been explored as an alternative to PANI in multilayer PCNs in composites with PEDOT:PSS stabilized graphene and/or DWCNTs.[408,409] Improved TE performance in these composites could be induced by thermal treatment at temperatures above 300 °C[408] or solution-phase predoping of the PEDOT:PSS with potassium bromide (KBr).[409] In both cases, an enhancement in the TE performance was attributed to removal of insulating PSS (as determined by X-ray photoelectron spectroscopy of the sulfur 2p peaks) from the multilayer composite, with an improved charge-carrier density and electrical conductivity but little deterioration in the Seebeck coefficient. In their first study, Stevens et al. showed that the thermal treatment of a PDDA/graphene-PEDOT:PSS/PDDA/DWCNT-PEDOT:PSS quadlayer PCN induced degradation of the PDDA and PSS components, resulting in an increase in the electrical conductivity that improved the peak TE power factor by an order of magnitude to ca. 170 μW m^{-1} K^{-2}.[408] Subsequently, Stevens et al. fabricated a PDDA/DWCNT-PEDOT:PSS bilayer PCN where KBr doping of the PEDOT:PSS eliminated the need for the thermal treatment.[409]

https://doi.org/10.1021/acs.chemrev.1c00218
Chem. Rev. XXXX, XXX, XXX−XXX

The KBr doping approach yielded increased film thickness for the same number of LbL deposition cycles and composites that exhibited an impressive peak TE power factor of ca. 625 μW m^{-1} K^{-2}.

The excellent TE performance and relative ease of fabrication for the multilayer all-organic TE composites prepared by LbL fabrication processes mark them out as a one of the most promising candidates for incorporation into commercially viable flexible TEGs. Further advances in this area will require the fabrication and optimization of TEGs, where both the n-type and p-type materials that have been demonstrated, as well as a more fundamental understanding of the underlying physical mechanisms behind the impressive TE performance introduced by the nanoscale interfaces and transport pathways in these multilayer composite materials.

A transparent, flexible hybrid conductive film, prepared by spin-coating a PEDOT:PSS film onto a graphene film prepared by rapid thermal chemical vapor deposition (RTCVD), recently demonstrated exceptional electrical conductivity (>100 000 S m^{-1}) and TE power factors exceeding 55 μW m^{-1} K^{-2}.[410] This hybrid exhibited >85% transmittance across the visible spectrum, and the TE properties of the flexible films on PET substrates were robust to repeated bending cycles (<15% increase in the sheet resistance and negligible change in the Seebeck coefficient).

4.2.5.5. Hybrid Nanocarbon–Inorganic Composites. Inorganic chalcogenides, including elemental Te and compound chalcogenide semiconductors, represent one of the most well-studied and highest-performing TE material classes.[411,412] However, the approach to reduce the thermal conductivity of the inorganic chalcogenides, via micro- and nanostructuring, often limits the electrical conductivity, requiring a carefully tuned balance between optimization of the two transport processes for peak TE performance.[411] Nanostructured carbon networks, and particularly carbon nanotube networks, have great potential for serving as high surface area conductive scaffolds (vide supra) in a number of technologies, including photo- and electrocatalytic architectures, fuel cell electrodes, batteries, and photovoltaics.[207,219] The introduction of nanoscale inclusions into inorganic TE materials has also been suggested as a method to yield interfaces that facilitate carrier energy filtering and phonon scattering. These interfaces may facilitate decoupling of the Seebeck coefficient, electrical conductivity, and thermal conductivity, allowing for enhancement of the TE performance,[413] although a recent study advocates for more thorough experimental and theoretical treatment of composites, including explicit consideration of the interfaces present in inhomogeneous materials.[338] These predictions have inspired the incorporation of nanocarbon scaffolds for hybrid nanocarbon–inorganic TE composites, while the questions that remain to be answered provide motivation for rigorous fundamental studies to better understand the role interfaces play in the TE properties of nanocomposite systems.

The majority carrier type in these hybrid nanocarbon–metal chalcogenide nanocomposites is typically dependent on the nature of the chalcogenide semiconductor, with bismuth[414−417] and silver[418] chalcogenides being n-type and antimony,[419−423] lead,[424] and tin[425−427] chalcogenides p-type.

The bulk of research in the past decade has focused on mechanically mixed and fabricated composites of bismuth- and antimony-based chalcogenides and FWCNTs or MWCNTs,[414−417,419,421] with examples of bismuth-antimony telluride composites achieving a material zT of >1.0.[419,421] Several studies have demonstrated that the incorporation of small quantities of MWCNT "nanoinclusions" (<0.25 wt %) in $Bi_2(Te_{0.9}Se_{0.1})_3$[414] or $(Bi_{0.2}Sb_{0.8})_2Te_3$[419,421] (see Figure 48) can

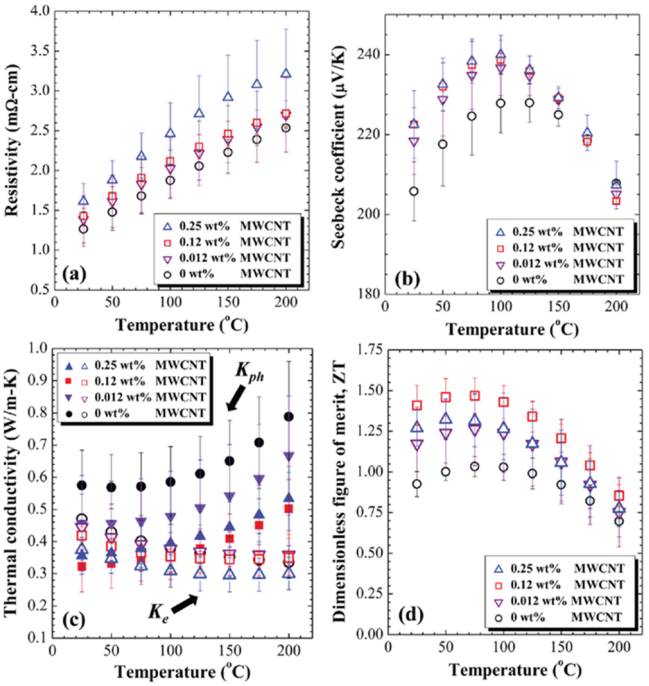

Figure 48. Thermoelectric performance of p-type $(Bi_{0.2}Sb_{0.8})_2Te_3$ nanocomposites. (a) Electrical resistivity, (b) Seebeck coefficient, (c) electronic and phonon thermal conductivity, and (d) dimensionless figure of merit, ZT. Small loadings of MWCNTs result in a slight decrease in the electrical conductivity, which is compensated for by a significant enhancement of the Seebeck coefficient and reduction of the phonon thermal conductivity, resulting in a 50% increase in the ZT. Reproduced with permission from ref 419. Copyright 2014 Elsevier Ltd.

reduce the thermal conductivity to less that 1 W m^{-1} K^{-1} at room temperature due to a phonon mismatch between the two components and a concomitant reduction in the phonon thermal conductivity. The introduction of interfaces in nanocomposite appears to have little to no impact on the electrical conductivity and induces either an enhancement or only a small decrease in the Seebeck coefficient, resulting in peak zT values that approach or exceed 1.0 (Figure 48).[419,421] Similar observations have been made recently for mechanically mixed composites of graphite and $(Bi_{0.25}Sb_{0.75})_2Te_3$, where a graphite loading of <0.2 wt % resulted in a zT > 1.0 at room temperature.[422] In contrast, other studies have suggested that the incorporation of MWCNTs into nanocomposites of $Bi_2(Te_{0.8}Se_{0.2})_3$ have a dramatic deleterious effect on the TE transport properties and performance,[416] suggested to arise from (i) the reduced grain size of the $Bi_2(Te_{0.8}Se_{0.2})_3$ grains, (ii) a reduction in the number of tellurium vacancies, and (iii) apparent n-type donor effects due to the MWCNTs.

Several chemical approaches have also been explored for the generation of CNT/bismuth chalcogenide nanocomposites. A solvothermal approach to the growth of Bi_2Te_3 on the MWCNT surface, via nucleation at MWCNT surface oxygen functional groups generated prior to the reaction with $Bi(CH_3COO)_3$ and $TeCl_4$, generated "nanopowders" that were subsequently ball-milled and subjected to spark plasma sintering to form the bulk nanocomposite.[428] The resulting nanocomposites exhibited

https://doi.org/10.1021/acs.chemrev.1c00218
Chem. Rev. XXXX, XXX, XXX−XXX

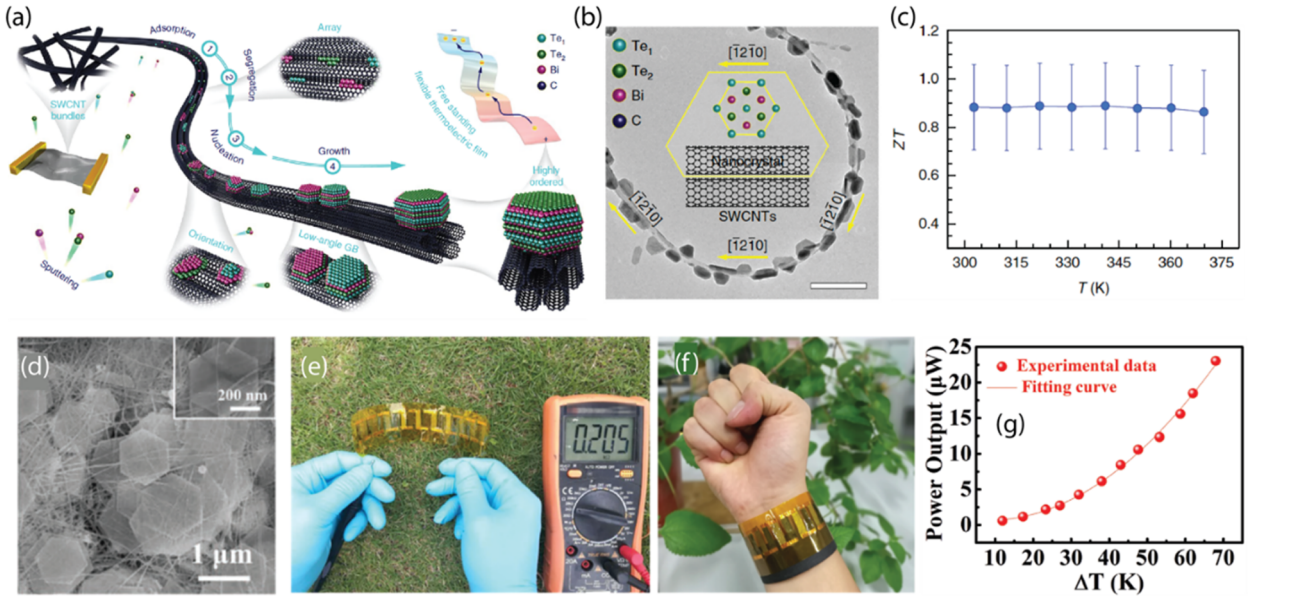

Figure 49. (a) Schematic illustration of the fabrication of a free-standing Bi_2Te_3/SWCNT hybrid thermoelectric material. (b) Bright-field TEM image of Bi_2Te_3 nanocrystals anchored on a SWCNT bundle. Inset is a schematic of the Bi_2Te_3-SWCNT orientation alignment. (c) zT for 600 nm thick Bi_2Te_3/SWCNT hybrid thermoelectric. (a−c) Reproduced with permission from ref 431. Copyright 2019 Springer Nature. (d) FESEM image of the surface of a Sb_2Te_3/SWCNT hybrid film after annealing. (e−f) Photos of a flexible TE generator formed from 10 p/n legs where p-type legs are Sb_2Te_3/SWCNT films and n-type legs are Bi_2Te_3/RGO films. (g) Power output of the TE generator as a function of temperature difference ΔT. (d−g) reprinted with permission from ref 423. Copyright 2019 Wiley.

more than an order of magnitude enhancement in the carrier mobility, but with almost 2 orders of magnitude decrease in carrier density that led to a significantly enhanced Seebeck coefficient (ca. 35% increase). This increase in the thermopower, coupled with a ca. 40% reduction in the thermal conductivity to ca. 0.65 W m^{-1} K^{-1}, gave an enhanced zT of ca. 0.5 at room temperature and ca. 0.85 at 473 K.[428] More recently, composites have been prepared via vacuum filtration of a ca. 50:50 mix of SWCNTs and DWCNTs and pregrown Bi_2Te_3 nanowires (prepared by a NW templating process, involving reaction of Te NWs with a Bi precursor solution).[429] The as-prepared nanocomposites exhibited rather low Seebeck coefficients and electrical conductivities, but a thermal annealing process (300 °C for two hours in flowing argon at ambient conditions) resulted in enhanced charge-carrier transport and a factor of 2 enhancement in the Seebeck coefficient, yielding peak TE power factors of. ca. 225 μW m^{-1} K^{-2} for composites with <2 vol % CNTs.[429]

There have also been a number of recent studies focused on SWCNT:Bi_2Te_3 nanocomposites. One of the earliest reports found that the majority carrier was dependent on the SWCNT loading, with n-type transport for compositions with <1 wt % SWCNT and p-type transport for higher loadings.[430] For a SWCNT loading of 0.5 wt %, there was a slight reduction in the thermal conductivity and a significantly enhanced Seebeck coefficient, yielding a ca. 25% improvement in the zT close to room temperature.[430] More recently, Jin et al. demonstrated the growth of layered Bi_2Te_3 on a SWCNT scaffold by magnetron sputtering (Figure 49a).[431] Crystallographic alignment between the $Bi_2Te_3\langle\bar{1}2\bar{1}0\rangle$ axis, and the SWCNT bundle axis leads to a highly ordered Bi_2Te_3 nanocrystals on the SWCNT bundles (Figure 49b). The authors suggest that high in-plane electrical conductivity is favored by two factors. First, amorphous material is not observed between Bi_2Te_3 nanocrystals or between Bi_2Te_3 and the SWCNT bundles, suggesting very clean interfaces and minimized carrier scattering. Second, crystallographic Bi_2Te_3 orientation on the bundle axis, leading to (000l) texturing, capitalizes upon high in-plane conductivity of the anisotropic Bi_2Te_3. The resulting hybrid composite achieves PF values in the range of ca. 1600−1100 μW m^{-1} K^{-2} in the range of 300−473 K. A low in-plane thermal conductivity of ca. 0.26 W m^{-1} K^{-1}, one of the lowest reported to date for this type of hybrid composite, results in a room temperature zT of 0.89 (Figure 49c). This low in-plane k arises primarily from a reduction in the lattice contribution and is attributed to (i) phonon mismatch between Bi_2Te_3 and the SWCNT scaffold, (ii) a high number of multiscale defects in the hybrid material, and (iii) interface roughness on the length scale of the primary Bi_2Te_3 phonons.

This hybrid organic−inorganic TE material appears to have good potential for flexible TE devices, with exceptional flexibility and resilience to bending[431] and promising power conversion factors.[432] The resistance of the hybrid material changed negligibly down to a bend radius of 5 mm and was also unaffected after 100 bending cycles at a bend radius of 10 mm. In contrast, the resistance of a Bi_2Te_3 film on a polyimide substrate doubled upon bending at a 5 mm radius and increased by 400% after 100 cycles at 10 mm bend radius.[431]

Wu et al. recently prepared thin-film TE composites from SWCNTs and Sb_2Te_3 by a solution-based filtration process (Figure 49d).[423] They obtained an optimal p-type PF of ca. 55 μW m^{-1} K^{-2} for a SWCNT loading of 16%. These p-type SWCNT/Sb_2Te_3 showed good performance stability with respect to repeated bending and could be combined with n-type composites containing Bi_2Te_3 and reduced graphene oxide (rGO) to form TE generators (Figure 49e,f). Flexible and wearable generators formed from 10 legs of p/n couples provided a power output of ca. 25 μW for a temperature difference of 70 K (Figure 49g).[423]

One early example of CNT composites with inorganic materials was the fabrication of n-type CNT/Ag_2Te hybrid

https://doi.org/10.1021/acs.chemrev.1c00218
Chem. Rev. XXXX, XXX, XXX−XXX

buckypapers reported by Yan et al.[418] Well-dispersed CNTs were added to silver precursor solution, followed by the injection of TOP-Te solution to form a hybrid of Ag_2Te nanoparticles bound to the surface of the CNT bundles.[418] The CNT/Ag_2Te nanocomposite with a loading of ca. 5 wt % CNTs exhibited a *PF* of >200 $\mu W\ m^{-1}\ K^{-2}$ close to room temperature and 579 $\mu W\ m^{-1}\ K^{-2}$ at 525 K, both superior to the pure CNT and Ag_2Te samples. Combined with a slightly lower thermal conductivity of ~0.7 $W\ m^{-1}\ K^{-1}$, a high zT value of 0.44 at 525 K was estimated for n-type CNT/Ag_2Te hybrid buckypaper with a weight ratio of 1:17.

MWCNTs have also been explored as conductive fillers in TE composites with tellurium nanorods synthesized from a Te precursor solution via a polyvinylpyrrolidone-assisted solution-phase process.[433,434] Although the MWCNTs result in a decrease of the Seebeck coefficient of the composite, low loadings (<2 wt %) enhance the electrical conductivity and suppress the lattice thermal conductivity, presumably due to phonon scattering at the interface between the two components, resulting in an enhanced TE power factor a peak zT for the composite with 2 wt % MWCNT. Composites with chemically synthesized Te nanorods outperform those prepared from ball-milled Te beads, primarily due to the improved electrical conductivity and reduced thermal conductivity.[434]

Several studies have begun exploring the incorporation of graphene into composites with inorganic TE materials. Composites of Bi_2Te_3 with 4−5 nm thick sheets of graphene oxide (GO) showed slight improvement of zT, relative to the Bi_2Te_3 material alone.[435] The peak zT for composites reached ca. 0.4 for Bi_2Te_3 NWs composited with 2 wt % GO, compared to zT = 0.3 for the Bi_2Te_3 NWs on their own. $Bi_{0.5}Sb_{1.5}Te_3$ composites with 0.1 vol % expanded graphene showed a 45% improvement to zT, relative to the neat $Bi_{0.5}Sb_{1.5}Te_3$ material, with peak zT values in the range of 1.13−1.24 for the composites.[436] Ding et al. fabricated flexible TEGs out of rGO sheets and Bi_2Te_3 nanoplates.[437] Six-element TEGs with 1% mass ratio of rGO produced ~1.72 μW at a ΔT of 20 K and retained its performance over 1000 bending cycles.

Zong et al. noted that few-layer rGO sheets increased the grain boundary (GB) thermal resistivity by a factor of 3−5 (relative to GBs without graphene) in skutterudite thermoelectric composites.[438] This modification led to peak zT values of 1.5 for n-type $Yb_yCo_4Sb_{12}$ and 1.06 for p-type $Ce_yFe_3CoSb_{12}$, allowing the authors to produce 4−8% efficient 16-leg TE modules using n- and p-type skutterudite/graphene composites.

Bhardwaj et al. prepared ball-milled composites of p-type Mg_3Sb_2 and $Mg_3Sb_{1.8}Bi_{0.2}$ with varying ratios of few-layer graphene nanosheets (GNS), where the GNS were derived from thermally expanded graphite.[439] Champion zT values were obtained for ca. 1.25 wt % loading of GNS into each composite, with zT = 0.71 at 773 K for Mg_3Sb_2/GNS and zT = 1.35 at 773 K for $Mg_3Sb_{1.8}Bi_{0.2}$/GNS (Figure 50a). The improvements of ca. 170% and 125%, relative to the uncomposited Mg_3Sb_2 and $Mg_3Sb_{1.8}Bi_{0.2}$ materials, respectively, derived from an increase in conductivity (due to an increase in both carrier concentration and mobility). The Seebeck coefficient decreased with GNS addition, as expected for the increase in carrier concentration, and the thermal conductivity increased.

Lin et al. recently explored the potential energy filtering role of graphene nanoplatelets (GNP) at the grain boundaries of n-type Te-doped Mg_3Sb_2 (Figure 50b,c).[338] In this study, the GNPs were produced by a surfactant exfoliation process[440] and composites were fabricated by sintering and annealing. Nano-

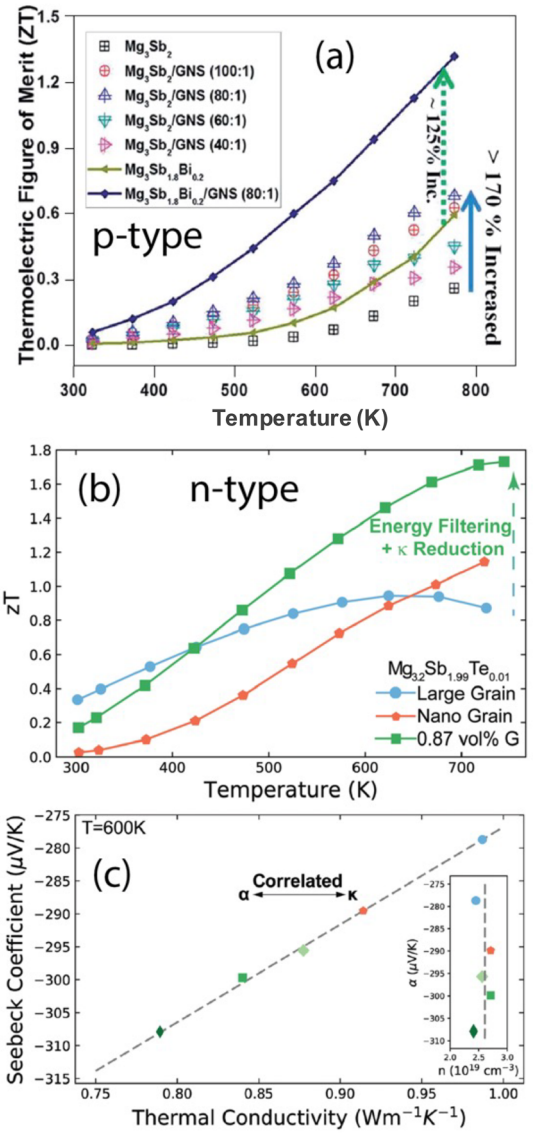

Figure 50. (a) Temperature-dependent zT of p-type Mg_3Sb_2/GNS composites with varying mass ratios and for $Mg_3Sb_{1.8}Bi_{0.2}$/GNS composites with mass ratio of 80:1. Reproduced with permission from ref 439. Copyright 2015 Royal Society of Chemistry. (b) Temperature-dependent zT of n-type $Mg_{3.2}Sb_{1.99}Te_{0.01}$, either prepared with large (ca. 13 μm) or small (ca. 0.6) grains and $Mg_{3.2}Sb_{1.99}Te_{0.01}$/GNP composite with ca. 1 μm grains. (c) Linear correlation between Seebeck coefficient and thermal conductivity in $Mg_{3.2}Sb_{1.99}Te_{0.01}$ and $Mg_{3.2}Sb_{1.99}Te_{0.01}$/GNP composites, demonstrating that the Seebeck coefficient scales with thermal conductivity and not carrier concentration (inset). (b,c) Reproduced with permission from ref 338. Copyright 2020 Royal Society of Chemistry.

structuring and the inclusion of GNPs lead to a 40% increase in zT, up to 1.73 near 773 K (Figure 50b). The authors note that the inclusion of the GNPs leads to an increase of the materials' Seebeck coefficients without a change in the carrier concentration (Figure 50c inset), a classic effect that is theoretically expected for energy filtering but rarely experimentally observed. They introduce a new two-phase (grain + grain boundary) heterogeneous transport model to analyze their finding, with an important outcome of the model being the introduction of an interfacial Seebeck coefficient term. This term arises from the large temperature drop associated with the grain boundary

https://doi.org/10.1021/acs.chemrev.1c00218
Chem. Rev. XXXX, XXX, XXX−XXX

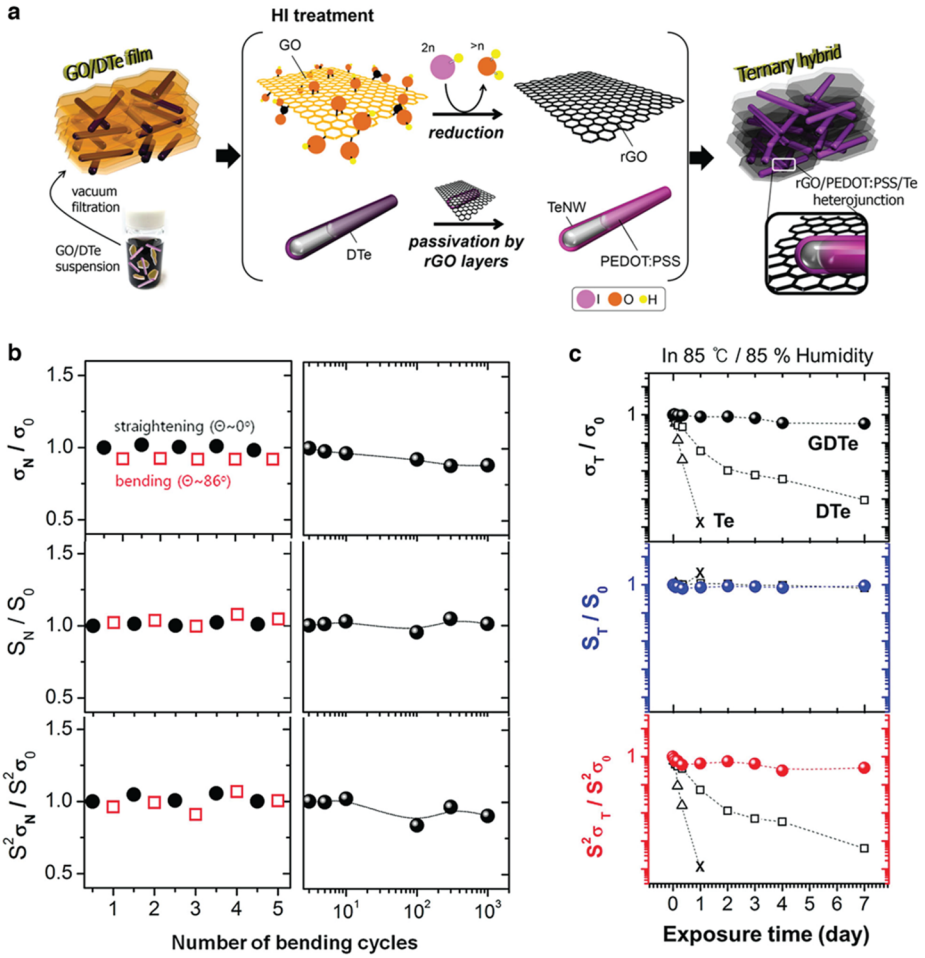

Figure 51. Hybrid GDTe thermoelectric papers: (a) Schematic illustration of the preparation of the ternary hybrid TE papers from reduced GO and PEDOT:PSS-coated Te NWs. (b) Impact of the number of bending cycles on the electrical conductivity (top), thermopower (middle), and TE power factor (bottom) of a $G_{0.1}DTe_{0.9}$ paper, illustrating only small negative impacts on the TE performance up to 1000 bending cycles. (c) Improved stability of the electrical conductivity (top), thermopower (middle), and TE power factor (bottom) for the $G_{0.1}DTe_{0.9}$ paper relative to the Te NWs and PEDOT:PSS-coated Te NWs. Reproduced with permission from ref 261. Copyright 2016 Wiley-VCH.

thermal resistance, which in turn creates a large associated grain boundary voltage. Thus, the authors posit that the key to realizing the large energy filtering effect is by maximizing the temperature drop across the grain boundary region and is thus anticorrelated with thermal conductivity (Figure 50c). They conclude that GNP and associated 2D materials can play such a role in materials with charged grain boundaries and grain size dependent transport properties.

4.2.5.6. Multinary Nanocomposites. In an effort to exploit the prevalent interfaces formed in multinary nanocomposites, which may enhance carrier filtering effect and introduce phonon scattering due to material mismatch, several studies have explored composites formed with either two different nanocarbon fillers,[441] two different nanoscale inorganic fillers,[442−444] or some combination of the two filler types.[426,427,445−447]

In one of the first examples, Kim et al. prepared a three-component nanocomposite made via vacuum filtration of a dispersion of inorganic Te nanowires coated with conducting polymer PEDOT:PSS combined with reduced-GO (Figure 51a).[261] The free-standing and flexible composite possessed a power factor of ca. 140 $\mu W\ m^{-1}\ K^{-2}$ at 300 K, allowing fabrication of flexible devices that were robust to repeated bending cycles and retained the majority of their TE performance even after stressing at 85 °C and 85% humidity for 7 days (Figure 51b,c).

Recently, Erden et al. demonstrated ternary composites prepared from anatase TiO_2 nanocrystals with PANI-coated amine-functionalized CNTs that exhibited impressive room temperature TE power factors exceeding of 100 $\mu W\ m^{-1}\ K^{-2}$.[446] The addition of the TiO_2 nanocrystals caused a significant decrease in the electrical conductivity due to a reduction in both the carrier mobility and concentration which led to an increase in the Seebeck coefficient and an optimum TE power factor for 30 wt % TiO_2.

Multinary TE composites have also been demonstrated for tin chalcogenide nanosheets combined with carbon nanotubes and conducting polymers.[426,427] The addition of a small loading of MWCNTs (<1.0 wt %) to a nanocomposite of PVDF and PANI-coated $SnSe_{0.8}S_{0.2}$ nanosheets resulted in an enhanced electrical conductivity and a room temperature TE power factor of ca. 260 $\mu W\ m^{-1}\ K^{-2}$, which increased to ca. 300 $\mu W\ m^{-1}\ K^{-2}$ at 400 K.[426] More recently, Liu et al. fabricated flexible, free-standing TE composites by vacuum filtration of dispersions of SWCNTs, PEDOT:PSS, and SnSe nanosheets that were prepared via chemical intercalation and exfoliation.[427] The TE properties of these composites were optimized for a SWCNT loading of 60 wt %, reaching ca. 160 $\mu W\ m^{-1}\ K^{-2}$ at room

https://doi.org/10.1021/acs.chemrev.1c00218
Chem. Rev. XXXX, XXX, XXX−XXX

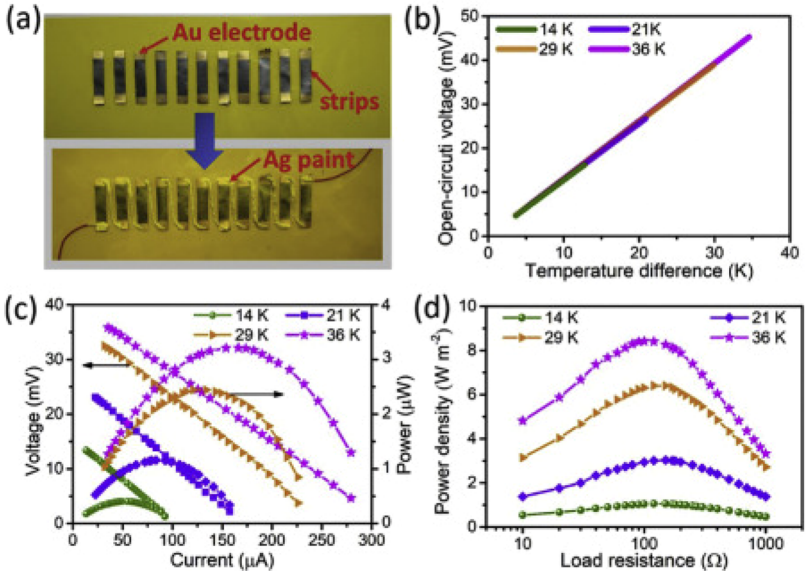

Figure 52. (a) Photograph of the 11-leg TEG before and after series connection using silver paint. (b) Open-circuit voltage of the TEG as a function of temperature difference. (c) Output voltage and power versus current for different temperature differences. (d) The power density of the device as a function of load resistance. Reproduced with permission from ref 444. Copyright 2020 Elsevier Ltd.

temperature, mainly due to an enhancement in the Seebeck coefficient.

In the past few years, metal halide perovskites have received some attention as potential TE materials,[448] partly because their "soft" crystal structure should lead to exceptionally low thermal conductivity, although their typically low electrical conductivity and issues associated with the chemical and compositional stability need to be overcome. Kishan et al. recently demonstrated PANI-methylammonium lead iodide (MAPI)-MWCNTs TE composites, where the PANI and MWCNTs appeared to synergistically enhance the electrical conductivity and Seebeck coefficient, resulting in a peak TE power factor of ca. 10 μW m^{-1} K^{-2}.[447]

Over the last several years, several studies have explored ternary composites of PEDOT:PSS and PVP with two different nanoscale inorganic fillers, with those based on silver chalcogenides exhibiting particularly impressive performance.[443,444] In all cases, alloy metal chalcogenide nanowires (NWs) were prepared by chemical alloying of polymer-coated chalcogen NWs. Chemical conversion of polymer-coated Te NWs was achieved via reaction with either copper chloride or silver nitrate to form Cu_7Te_4 or Ag_2Te NWs, respectively. For ternary composites prepared from a mixture of PEDOT:PSS-coated Te NWs and PEDOT:PSS-coated Cu_7Te_4 NWs, the peak TE power factor exceeded ca. 60 μW m^{-1} K^{-2} for >90 wt % PEDOT:PSS-coated Te NWs content.[442] The performance of a PVP/Ag nanoparticle/Ag_2Te NW ternary composite, prepared via vacuum filtration and subsequent heat treatment, delivered even more impressive performance, with a room temperature TE power factor of ca. 215 μW m^{-1} K^{-2} and ca. 370 μW m^{-1} K^{-2} at 393 K.[443] In 2020, Lu et al. demonstrated exceptional TE performance for an n-type PEDOT:PSS/Ag_2Se NW/CuAgSe NW composite, with a room temperature TE power factor of ca. 1600 μW m^{-1} K^{-2} and an estimated zT of as much as 1.[444] Flexible TEGs comprising 11 n-type legs were fabricated from the PEDOT:PSS/Ag_2Se NW/CuAgSe NW composite (Figure 52), and power densities of >6 W m^{-2} were achieved for a temperature difference of ca. 30 K (Figure 52d).

4.3. Ionic Thermoelectric Materials

Thus far, this review has presented results concerning voltage generation through the thermal diffusion of electronic charge carriers. However, *ionic charge carriers* can also drift under an external thermal gradient, the so-called Soret effect. This effect is particularly pronounced at high humidity due to faster ion transport in liquid/electrolyte media. Contrary to the electronic Seebeck effect, the thermodiffused ions remain confined in the film instead of being extracted by the electrodes, making these materials more suitable for capacitor-like applications instead of for continuous power generation. For a more in-depth explanation of the role of humidity, we refer the reader to a recently published review by Sohn et al.[449]

In 2015, Wang et al. reported an ionic Seebeck effect in the mixed ion-electron conducting polymer PEDOT:PSS.[450] It was found that the Seebeck coefficient of PEDOT:PSS increased from 10 μV K^{-1} to 215 μV K^{-1} with increasing ambient humidity from 10 to 80% RH, accompanied by a dramatic enhancement in the ionic conductivity. The resulting instantaneous power factor could then be increased by 4 orders of magnitude, but the fact that the thermogenerated current dropped with time indicated that the ionic contribution was not constant. Later, Ail et al. studied the mechanism underlying this phenomenon and observed that the thermodiffusion of protons in PEDOT:PSS, at high humidity, promoted an internal electrochemical reaction within the mixed ion-electron conductor film.[451] The time dependence of the open-circuit voltage $V_{oc}(t)$, after applying a thermal gradient, showed a peak that corresponded to the ionic Seebeck contribution, which then decreased until reaching a constant value at equilibrium; this behavior was ascribed to the electronic Seebeck effect. Therefore, the ionic Seebeck effect in mixed polymer conductors could not be used to produce much extra power in a TE module because its character vanishes with time. Instead, the ionic Seebeck effect was used to independently sense the humidity and temperature gradient with a three-parameter sensor (pressure, humidity, temperature) made of the polymer aerogel,[452] which exploits the ion thermodiffusion in high humidity environment to expand the sensing capability of

https://doi.org/10.1021/acs.chemrev.1c00218
Chem. Rev. XXXX, XXX, XXX−XXX

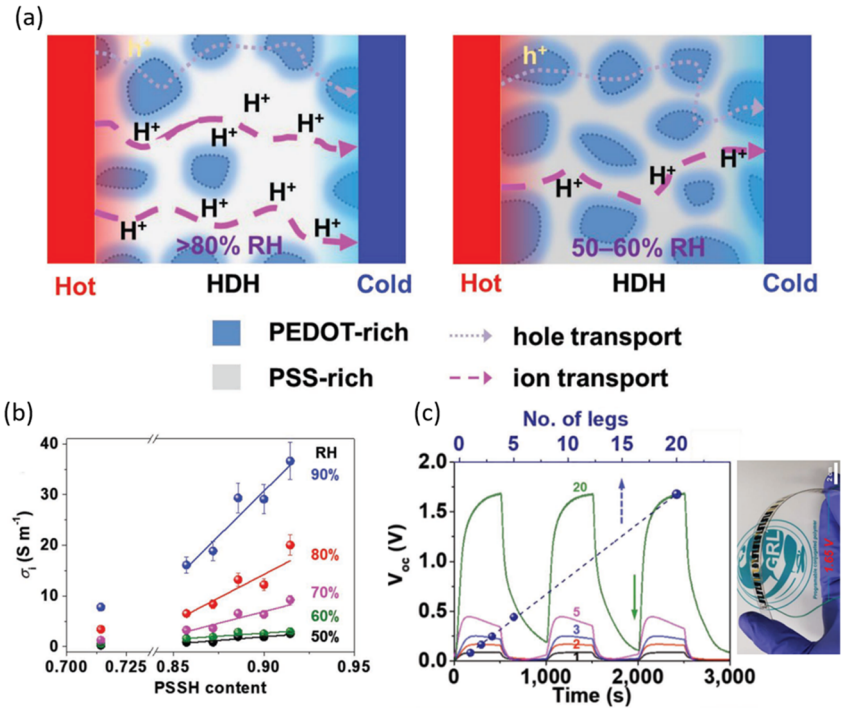

Figure 53. (a) Sketch of charge transport (ions and electrons) inside the PEDOT:PSS films at high (left) and low (right) humidity levels. (b) Ionic conductivity as a function of PSSH content and for different RH values (from 50% to 90%). (c) Voltage output vs time for different TE modules having different number of thermocouples, with the 20-leg device photo on the right. Reproduced with permission from ref 456. Copyright 2019 Wiley.

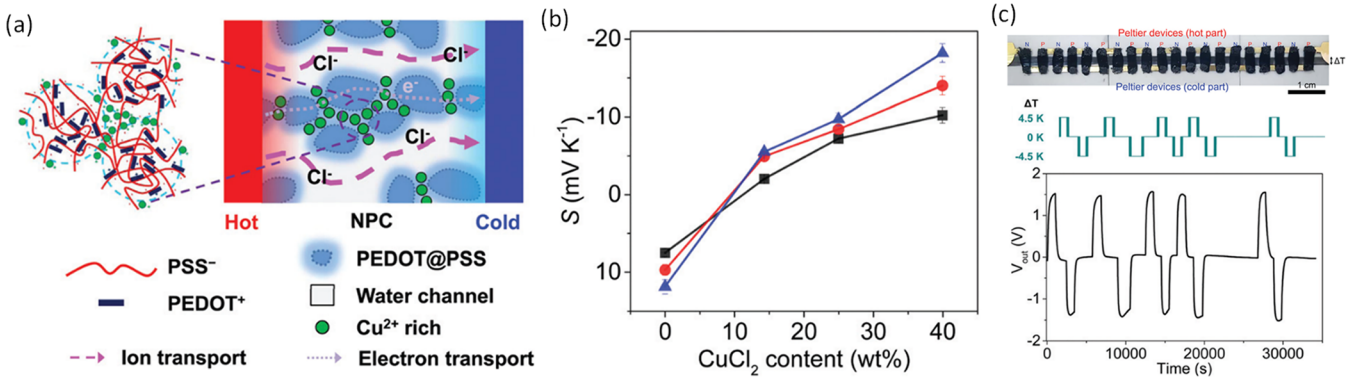

Figure 54. (a) Schematic ion transport and morphology of PEDOT:PSS $CuCl_2$ films. (b) Seebeck coefficient vs $CuCl_2$ content (wt %) for 60% (black), 70% (red), and 80% (blue) of relative humidity. (c) Picture of the thermionic generator together with voltage output and temperature difference over time. Reproduced with permission from ref 457. Copyright 2019 Royal Society of Chemistry.

previously published results.[453,454] Other examples of temperature sensors based on the thermodiffusion of ions were presented by Zhao et al., using PEO-NaOH electrolyte to modulate the current of an electrolyte-gated organic transistor (with P3HT as the active material), enhancing the device sensitivity to small temperature variations.[455] The high Seebeck values connected to ion transport in polymers represented interesting results and offered a new path toward the development of a new generation of thermal harvesters.

The first example of a stable thermionic effect in PEDOT:PSS films was reported in 2016, with the addition of polystyrene sulfonic acid (PSSH), showing an ionic conductivity of 9 S m^{-1} and an ionic Seebeck coefficient of 7.9 mV K^{-1} at 70% humidity.[66] Later on, Wang et al. studied the effect of humidity on the ionic mobility and ionic Seebeck coefficient of polystyrene sulfonate sodium (PSS^-Na^+), in which PSSNa served as a polyanionic membrane because the negative charges (sulfonate) were attached covalently to the polymer chain and effectively immobile, while the cations were the only mobile species. When the humidity was increased from 50% to 100%, the ionic Seebeck coefficient increased from 0.26 mV K^{-1} to 4 mV K^{-1}.[64] In 2018, Kim et al. expanded these results by reporting a mixed polymer film of PEDOT:PSS doped with PSSH, using a PEDOT:PSS formulation with higher PSS content (1:6) and PSSH possessing a similar molecular weight (M_w) to that of the PSS. In this case, the Seebeck coefficient reached 16 mV K^{-1} and remained constant over time, with a conductivity of 29 S m^{-1} observed at 90% relative humidity.[456] The addition of PSSH acted as a proton dopant by creating PSS-rich domains, where H^+ ions could move freely under high humidity conditions (Figure 53a,b). Finally, they demonstrated that the high thermionic properties remained constant under ambient conditions by using a hydrogel bilayer architecture for the thermoelectric generator to maintain high humidity levels,

https://doi.org/10.1021/acs.chemrev.1c00218
Chem. Rev. XXXX, XXX, XXX−XXX

thus allowing the exploitation of the maximum harvesting capacity of such material.[290]

In 2019, the same group reported the conversion of thermionic properties of PEDOT:PSS from p- to n-type when in the presence of copper chloride ($CuCl_2$) salts.[457] Through metal binding with the PSS domains, a Cl^- channel could be observed inside the film, leading to an S of ~ -18 mV K^{-1} and a PF of $\sim$1.7 mW m^{-1} K^{-2} at 80% RH (Figure 54a,b). In addition, they integrated their p- and n-type thermionic materials in a generator composed of 10 thermocouples, achieving 1.55 V at an external temperature difference of 4.5 K and with an RH of 80% (Figure 54c).

However, the above method was not the only route followed to increase the time response of the ionic contribution, thus harvesting constant power. Chang et al. added Ag cations (using Ag-based salts) in Nafion (Ag-Nafion) and polystyrene-sulfonate (Ag-PSS),[458] which, coupled with Ag electrodes, enabled a thermogalvanic effect, producing an additional constant thermogenerated current on top of the nonconstant ionic Seebeck effect over time. Figure 55b shows the values of the Seebeck coefficient corresponding to two different blends: a positive Seebeck coefficient of approximately 5 mV K^{-1} for the 100% Ag^+/SO_3^- molar ratio in PSS and a maximum negative S of -1.5 mV K^{-1} for silver nitrate ($AgNO_3$) in Nafion. Regarding the ion conductivity (Figure 55b), a maximum was instead obtained for low Ag^+ concentrations (33%), corresponding to 2.7 mS cm^{-1} for Ag-PSS and 4.3 mS cm^{-1} for Ag-Nafion. Because the ionic conductivity of Nafion is extremely humidity dependent due to water-assisted ion transport, Chang et al. investigated the effects of humidity on the conductivity and Seebeck coefficient of these materials (Figure 55d,e). The Ag-Nafion ionic conductivity increased exponentially by more than 3 orders of magnitude, while the Seebeck coefficient switched from being positive to negative and reached a plateau at -2 mV K^{-1} for RH >50%. On the other hand, for Ag-PSS, S decreased but remained positive up to a value of 1 mV K^{-1}. Finally, they constructed a flexible device (Figure 55f) with six thermionic legs connected by silver paste, showing a maximum of 7 mV at a ΔT = 4 K and an RH of 50%.

Another important feature of these materials, apart from the Seebeck coefficient and electrical/thermal conductivity, is the stability of such properties after mechanical stress; indeed, brittle materials are not compatible for use in flexible and conformable electronics. Therefore, the development of composites can offer an effective way to combine the properties of different components in a single material to further broaden their applications in flexible and wearable electronics. Jiao et al. recently prepared robust and flexible ionic thermoelectric paper by a simple and cost-effective method.[459] In contrast to the extremely brittle pure polystyrene sulfonate sodium (PSSNa) film, the nanofibrillated cellulose (NFC)-PSSNa composite paper (Figure 56a) exhibited a tensile strength of 16.6 ± 1.5 MPa and a Young's modulus of 0.9 ± 0.1 GPa. Remarkably, the NFC-PSSNa paper retained high ionic thermoelectric properties (Figure 56c), with an overall figure-of-merit of 0.025 at 100 RH % and room temperature, which was slightly higher than that of pure PSSNa.

While polyelectrolytes display a large ionic Seebeck coefficient in humid environments, the drawback of using water to enable ionic thermodiffusion is that water evaporates, thus, there is a small temperature window for operation. Instead, polymer electrolytes have also been investigated for their ionic thermoelectric properties. Zhao et al. showed a low molecular

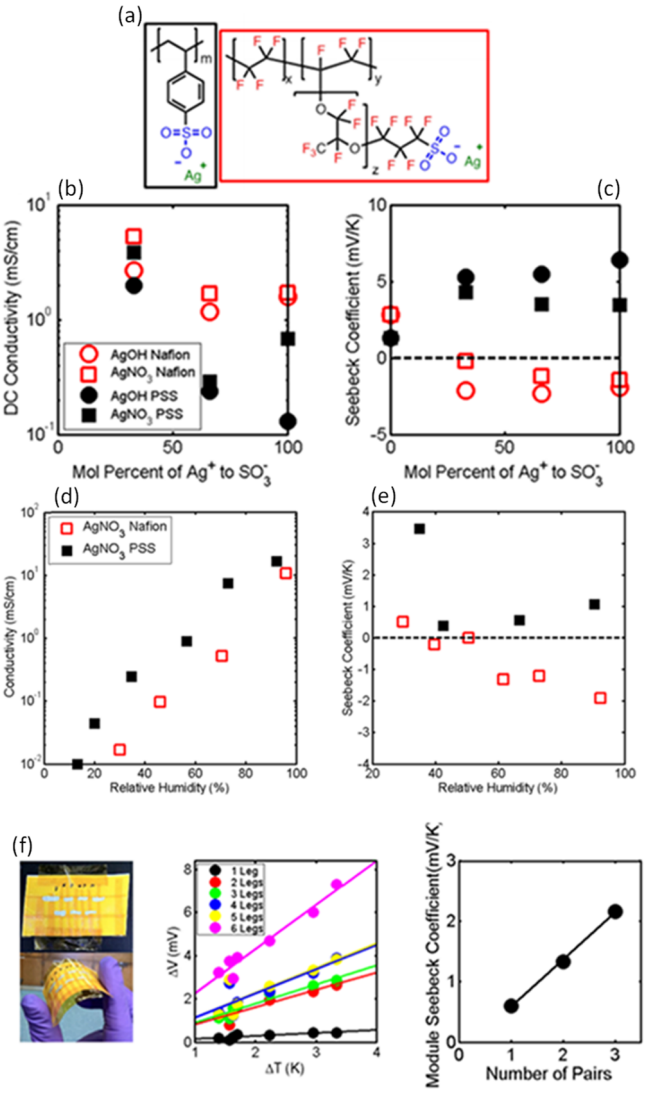

Figure 55. (a) Chemical structures of Ag-PSS (black box) and AgNafion (red box). (b) Ionic conductivity and (c) Seebeck coefficient of PSS and Nafion with the addition of different molar ratios of Ag salts. (d) Ionic conductivity and (e) Seebeck coefficient of Ag-PSS and Ag-Nafion with increasing RH values. (f) Picture (left) and voltage output (middle) of a flexible p−n device as a function of different external temperature differences, and the module thermopower (right) as a function of the number of pairs of p−n components. Reproduced with permission from ref 458. Copyright 2016 American Chemical Society.

weight polyethylene glycol (PEG) with NaOH possessing a positive Seebeck coefficient of 10 mV K^{-1}.[24] Recently, Li et al. impregnated porous aligned cellulose fibers with PEG-NaOH and reported an even higher Seebeck coefficient reaching 24 mV K^{-1}.[460] It was also found that poly(vinylidene fluoride-*co*-hexafluoropropylene) (PVDF-HFP) blended with the ionic liquid 1-ethyl-3-methylimidazolium ([EMIM]) bis(trifluoromethylsulfonyl)imide ([TFSI]) (Figure 56d) had a negative Seebeck coefficient of -4 mV K^{-1} (Figure 56e), while the addition of low molecular weight PEG switched the sign of the Seebeck coefficient to +12 mV K^{-1}, which enabled the authors to screen print the first ionic thermopile on a flexible polymide substrate (Figure 56e,f).[461]

The impressive values of S linked to ionic charge carries are unfortunately counterbalanced by the low charge conductivity, usually in the order of mS cm^{-1}, which severely limits the power

https://doi.org/10.1021/acs.chemrev.1c00218
Chem. Rev. XXXX, XXX, XXX−XXX

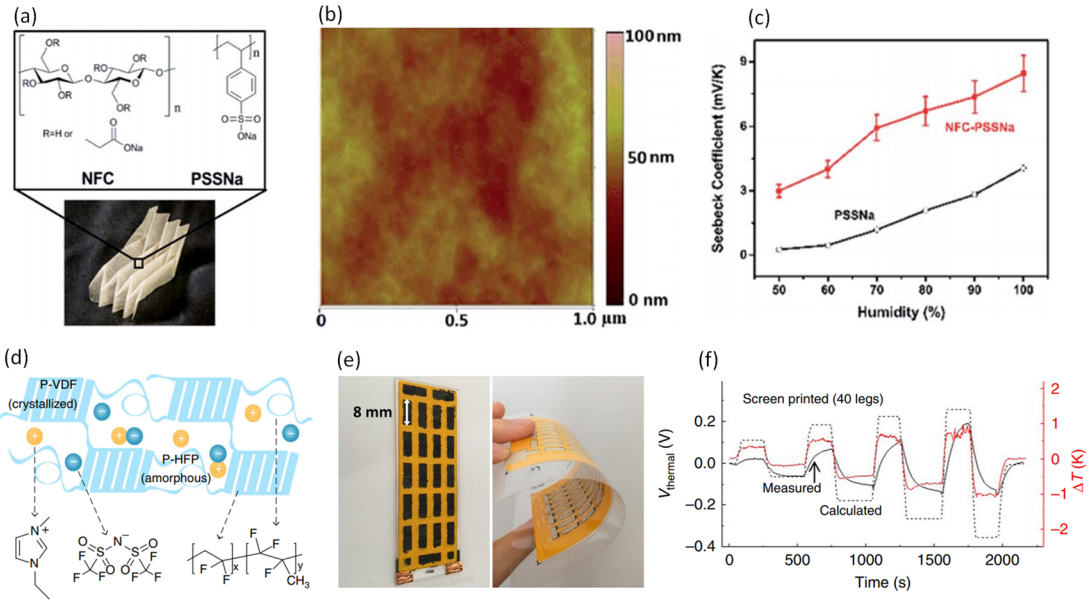

Figure 56. (a) Photo and structure of the NFC-PSSNa composite films. (b) AFM images of the NFC-PSSNa film. (c) Seebeck coefficient of NFC-PSSNa at various humidity levels and a comparison with pure PSSNa. (a–c) Reproduced with permission from ref 459. Copyright 2017 The Royal Society of Chemistry. (d) Composition of [EMIM][TFSI]/PVDFHFP polymer gels. Organic thermionic generator printed on a flexible substrate (e) and the voltage output for small temperature differences (f). (d–f) Reproduced with permission from ref 461. Copyright 2019 Nature.

that can be extracted. Recently, Jiang et al. tried to circumvent this issue by proposing a mixed ion-electron n-type organic conductor with a highly crystalline and reduced perylene bisimide.[462] This material presented a $S > 3$ mV K^{-1} due to the presence of quasi-frozen ionic charges, while the charge transport is mediated by electrons yielding a conductivity as high as 0.18 S cm^{-1}, an impressive value for an n-type organic semiconductor. The efficient combination of ion-electron transport allowed to yield a *PF* as high as 165 μW m^{-1} K^{-2} and a $zT = 0.23$ at room temperature. Note that the high *PF* values were calculated using *S* (generated by the thermodiffusion of ion) and the electronic component of σ. While this approach might look unusual because of the mixed ion-electron contribution, the authors reported stable power output in a condition of matched resistance, compatible with the conductivity of electronic charge carriers. At the same time, the thermal voltage was generated by ionic contribution, as verified by the authors. Therefore, because *PF* is a parameter that indicates the capability of a material to generate continuous power output thermally, we believe this approach to be suitable to calculate *PF*.

4.4. Materials for Thermogalvanic Cells (TGCs)

4.4.1. Redox Couples. Another thermodiffusion phenomenon is the thermogalvanic effect. Here, the Seebeck coefficient is proportional to the entropy change of the redox reaction. This reaction has an entropic contribution from the redox molecule itself but also from the solvation shell, which is sensitive to the interactions between the redox molecule and the solvent. Redox couples considered for TGC applications are comprised of inorganic, organic, and radioactive redox couples in aqueous or nonaqueous electrolytes, and they display either positive or negative values of the Seebeck coefficient. Regarding aqueous electrolytes, the highest values of S_{redox} have been reported as −1.4 to −1.5 mV K^{-1} for $Fe(CN)_6^{3-}/Fe(CN)_6^{4-}$,[54,62,463] 0.5–0.7 mV K^{-1} for Fe^{3+}/Fe^{2+},[464,465] 0.55 mV K^{-1} for I_3^-/I^-,[466] 1.87 mV K^{-1} for Np^{4+}/Np^{3+}, and −1.53 mV K^{-1} for Pu^{4+}/Pu^{3+}. In nonaqueous electrolytes, the largest Seebeck coefficient recorded is for cobalt(II/III) tris(bipyridyl) (−2.19 mV K^{-1}).

Among redox-active electrolytes, ferro/ferrocyanide [$Fe(CN)_6^{3-}/Fe(CN)_6^{4-}$] has been extensively studied for TGCs due to its high solubility and stability in water, its high exchange current density, and relatively high Seebeck coefficient of 1.4 mV K^{-1}. However, the Seebeck coefficient of ferro/ferrocyanide also depends weakly on the concentration of the redox couple, with maximum values as high as 1.72 mV K^{-1} reported for 5 mM solutions.[467] Unfortunately, power generation is too small at these low concentrations. Studies have shown that the Seebeck coefficient remains constant for redox couple concentrations above 0.1 M and a concentration of up to 0.4 M can be used for stable TGC applications.[467] A high concentration (0.9 M) of ferro/ferricyanide in aqueous solution can be reached by replacing the conventional $K_4Fe(CN)_6/K_3Fe(CN)_6$ with $(NH_4)_4Fe(CN)_6/K_3Fe(CN)_6$.[468] While the Seebeck coefficients are not significantly modified (1.43 mV K^{-1}), the increase in concentration from 0.4 to 0.9 M is accompanied by a 66% enhancement in the ionic conductivity and a minor decrease in the thermal conductivity of the electrolyte. The combination of these effects results in a 50% improvement in the generated power.

Chaotropic agents, molecules that disrupt the hydrogen bonding network of water, can have a significant impact on the entropy (and thus thermopower) of thermogalvanic reactions. Duan et al. introduced strong chaotropic cations (guanidinium) and highly soluble amide derivatives (urea) into aqueous [$Fe(CN)_6^{3-}/Fe(CN)_6^{4-}$] electrolytes to significantly boost the thermopowers from 1.4 to 4.2 mV K^{-1}.[469] [$Fe(CN)_6^{3-}/Fe(CN)_6^{4-}$] are categorized as chaotropic anions in the Hofmeister series and can bond with chaotropic cations based on chaotrope–chaotrope ion specificity.[470] Therefore, strong chaotropic cations can be expected to rearrange the solvation shells of the redox couple and change the entropy of the redox reaction, thereby affecting the Seebeck coefficient. By introducing guanidinium chloride (GdmCl) into the ferro/

https://doi.org/10.1021/acs.chemrev.1c00218
Chem. Rev. XXXX, XXX, XXX−XXX

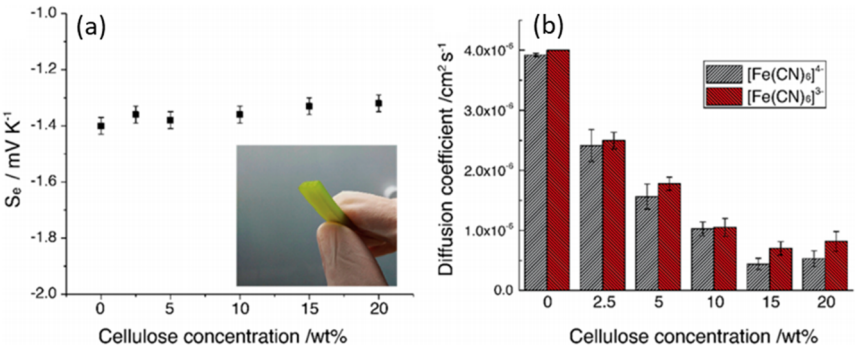

Figure 57. (a) Seebeck coefficients of the solidified electrolytes and aqueous solution. (b) Diffusion coefficients of $[Fe(CN)6]^{4-}$ and $[Fe(CN)6]^{3-}$ in the solid electrolytes and the solution at 22 °C. Reproduced with permission from ref 476. Copyright 2016 American Chemical Society.

ferricyanide aqueous electrolyte, the Seebeck coefficient increased up to 2.7 mV K^{-1}. Urea is known to strongly impact the hydrogen-bonding network and hydration shell of ions in water.[469] An extremely high Seebeck coefficient value of ∼4.2 mV K^{-1} is achieved when adding urea (24 M) and GdmCl (2.6 M) simultaneously.

Recently, a few groups have demonstrated TGC applications of ferro/ferricyanide in a mixture of aqueous/nonaqueous solvents. When ferro/ferricyanide is used in a mixture of an organic solvent, such as methanol or DMSO, with water, it shows a significant improvement in the Seebeck coefficient (2.9 mV K^{-1}).[471] However, the solubility is affected, and the ionic conductivity decreases from approximately 180 mS cm^{-1} to 50 mS cm^{-1}. Overall, there is a positive effect of the mixing of solvent, with an area power density of 0.64 mW m^{-2} K^{-2} for the TGC, which is higher than the 0.35 mW m^{-2} K^{-2} with an aqueous electrolyte at a ΔT of 4.1 °C.

The iron(II)/(III) system is yet another well-known redox couple for thermogalvanic applications and was tested at the early stage of thermogalvanic research. Iron(II)/(III) systems have not been investigated in detail due to their low Seebeck coefficient (0.54 mV K^{-1}) at high ionic concentrations compared to the $[Fe(CN)_6^{3-}/Fe(CN)_6^{4-}]$ system. However, while high Seebeck values of 1.8 mV K^{-1} have been reported for aqueous iron (II)/(III) systems at very low ionic concentrations, above 0.2 M these values decrease rapidly. A high-power TGC requires more concentrated redox molecules. Among the studied iron(II)/(III) systems, aqueous chlorides and sulfate systems have been studied the most. Indeed, regarding aqueous iron(II/III) chloride systems, Burrows reported a Seebeck value of +0.6 mV K^{-1} for aqueous $FeCl_2/FeCl_3$ in the presence of HCl.[472] On the other hand, with regard to iron(II/III) sulfate systems, Al Maimani et al. reported Seebeck values in the range of +0.24 to +0.40 mV K^{-1} at different concentrations (1.4 M Fe(II)/Fe(III) to 0.0014 M Fe(II)/Fe(III), respectively), which could be further increased to +0.54 mV K^{-1} with the addition of H_2SO_4,[473] clearly showing the influence of electrolyte pH on the Seebeck coefficient of the iron(II)/(III) systems.

This dependence was further proven by Buckingham et al., who reported a Seebeck coefficient of +1.46 mV K^{-1} for acidified iron(II/III) trifluoromethanesulfonate at ΔT = 20 K.[474] In this report, they studied four aqueous Fe(II)/Fe(III) salt systems that were based on 0.2 M ammonium iron sulfate, iron sulfate, iron trifluoromethanesulfonate, and iron nitrate, and the Seebeck coefficient varied from +0.13, +0.29, +1.35, and +1.34 mV K^{-1}, respectively. The value of the Seebeck coefficient was further enhanced in the presence of 1 M conjugate acid, reaching values of +0.84, +0.90, +1.46, and +1.38 mV K^{-1} for acidified ammonium iron sulfate, iron sulfate, iron trifluoromethanesulfonate, and iron nitrate, respectively. The addition of 1 M conjugate acid to the systems resulted in significant increases in the Seebeck coefficients of both $Fe[SO_4]^-$ and $[NH_4]FeSO_4$ based systems, while only slightly increasing the Seebeck coefficients of the $FeNO_3$ and $FeCF_3SO_3$ systems. In this report, this observation was rationalized in terms of acid−base equilibrium and ion pairing.

Because of the liquid nature of the electrolytes, the application of TGCs in flexible and wearable devices is limited, mainly due to the potential leakage of the electrolyte. Recently, there have been a few attempts to fabricate TGCs using ferro/ferrocyanide redox couples in polymer gels to eliminate electrolyte leakage and to support the development of flexible TGCs.[23,475] Jin et al. reported a ferric/ferrocyanide redox couple within a cellulose matrix.[476] Figure 57 displays the effect of the addition of cellulose on the Seebeck coefficient and the diffusion coefficient of the redox couples in gel. The introduction of 5% cellulose in the electrolyte barely affected the Seebeck coefficient (−1.38 mV K^{-1}, Figure 57a) but provided decent mechanical properties and a maximum power output of 14 mW m^{-2} (compared to 18 mW m^{-2} without cellulose). Thus, modules of TGCs based on legs composed of two types of gel redox electrolytes with positive and negative Seebeck coefficients were envisioned to power wearable electronics.[23] Poly(vinyl alcohol) (PVA) was used as the polymer gel matrix, yielding Seebeck coefficients as high as 1.02 mV K^{-1} and −1.21 mV K^{-1} when used in combination with ferric/ferrous chloride and ferro/ferricyanide, respectively.

The second most studied redox couple in thermogalvanics is iodide/triiodide. Its Seebeck coefficient depends on the nature of the solvent (aqueous/organic), the concentration of the electrolyte, and the presence of additives. As an additive, Zhou et al. proposed the addition of α-cyclodextrin in an aqueous iodide/triiodide redox electrolyte and reported a maximum Seebeck coefficient of 2 mV K^{-1}.[477] The proposed hypothesis was that α-cyclodextrin encapsulated triiodide ions and affected their solvation entropy. Abraham et al. studied the thermogalvanic properties of the iodide/triiodide redox couple in various ionic liquids.[478] Typically, when switching from water to ionic liquids, the Seebeck coefficient decreased. The main advantage of ionic liquids compared to aqueous electrolytes was that a larger temperature gradient could be utilized in thermogalvanic cells with temperatures at the hot side reaching 400 °C. Interestingly, changing the anionic component of the ionic liquid, e.g., from 1-butyl-3-methylimidazolium tetrafluoroborate to 1-butyl-3-methylimidazolium iodide, led to a change in the sign of the Seebeck coefficient.[466,477,479] TGCs based on

https://doi.org/10.1021/acs.chemrev.1c00218
Chem. Rev. XXXX, XXX, XXX−XXX

iodide/triiodide in ionic liquids could reach a power output of 29 mW m^{-2} when the hot side was at 150 °C.[480]

A cobalt redox couple is promising for TGC applications, as it displays a relatively high Seebeck coefficient in nonaqueous electrolytes compared to iodide/triiodide.[55,478,481,482] The first demonstration of cobalt redox couple-based TGCs made use of a $Co^{2+/3+}(bpy)_3(NTf_2)_{2/3}$ couple in combination with a series of ionic liquids and 3-methoxypropionitrile (MPN).[478] These electrolytes showed high Seebeck coefficients ranging from 1.5 to 2.2 mV K^{-1} in the temperature range of 20−140 °C. The highest Seebeck coefficient value of 2.19 mV K^{-1} was obtained with the 0.01 M $Co^{2+/3+}(bpy)_3(NTf_2)_{2/3}$ couple in MPN and 1.88 mV K^{-1} with the ionic liquid ([C2mim][eFAP]). These values of the cobalt redox couple were attributed to the additional electronic entropy component of the total entropy change.[483] The power output of TGCs reached 522 mW m^{-2} for the 0.1 M $Co^{2+/3+}$ $(bpy)_3(NTf_2)_{2/3}$ redox couple in MPN and 880 mW m^{-2} at ΔT = 70 °C with an electrolyte composition of 3:1 (v/v) MPN-[C2mim][$B(CN)_4$].[478]

Regarding the development of solid or quasi-solid-state electrolytes, Taheri et al. reported gelation of an organic solvent-based electrolyte system containing a cobalt bipyridyl redox couple for application in thermogalvanic cells.[484] Polyvinylidene difluoride (PVDF) and PVDF-HFP were used for gelation of the liquid electrolyte (Figure 58a,b), which was consistent with a cobalt bipyridyl redox couple dissolved in 3-methoxypropionitrile (MPN). Cobalt bipyridyl redox couples

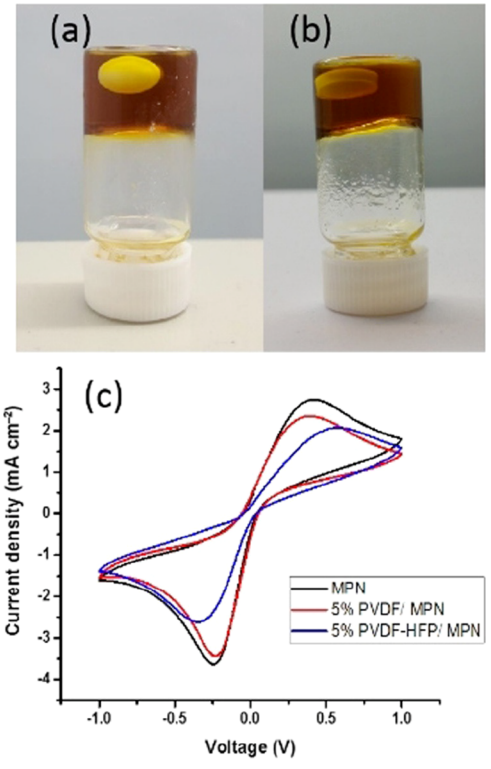

Figure 58. Quasi-solid-state electrolytes containing 0.05 M $[Co(bpy)_3]^{2+/3+}[NTf_2]_{2/3}$ in MPN gelled with (a) 5 wt% PVDF and (b) 5 wt% PVDF-HFP. (c) Electrochemical behavior of the redox electrolytes before and after gelation measured using a three-electrode cell equipped with a platinum working electrode and two platinum wires as the counter and pseudoreference electrodes at a scan rate of 50 mV s^{-1}. Reproduced with permission from ref 484. Copyright 2018 European Chemical Society.

are known to display high Seebeck coefficients; thus, the use of cobalt redox couples in a quasi-solid-state electrolyte could allow access to higher Seebeck coefficients. Interestingly, the addition of PVDF or PVDF-HFP to the cobalt bipyridyl redox electrolyte did not significantly affect the Seebeck coefficient. Indeed, the presence of solvent interactions with redox molecules affected the Seebeck coefficient because of changes in the entropy and free energy.[483,485,486] In this report, the absence of any strong interaction between the polymer chains and redox molecules resulted in a negligible effect on the entropy change in the redox reaction, thus not affecting the Seebeck coefficient.[484] The diffusivity of the redox couple in the gel electrolyte was the key to TGC operation, and in this report, the study on the effect of gelation, investigated using chronoamperometry, revealed that gelation did not cause a significant decrease in the diffusion coefficient (Table 3). Furthermore, this observation was

Table 3. Effects of the Gelation of the Electrolyte on the Seebeck Coefficient (S) and Diffusion Coefficient (D) at 25 °C

		D ($10^6 cm^2 s^{-1}$)	
electrolyte	S (mV K^{-1})	$Co(bpy)_3^{2+}$	$Co(bpy)_3^{3+}$
MPN	1.81 ± 0.03	5.00 ± 0.39	4.90 ± 0.27
5 wt % PVDF-MPN	1.80 ± 0.02	4.63 ± 0.13	4.21 ± 0.09
5 wt % PVDF-HFP-MPN	1.84 ± 0.01	4.48 ± 0.15	3.55 ± 0.25

supported by cyclic voltammetry (Figure 58c), which showed that the redox couple in the gelled electrolytes maintained quasi-reversible electrochemical behavior.

Maximum power densities of 6 and 4.5 mW m^{-2} have been obtained for PVDF and PVDF-HFP gel electrolytes, respectively, compared to 48 mW m^{-2} for a liquid MPN-based electrolyte at the same temperature difference. The decrease in thermogalvanic cell power with the gel electrolyte is mainly due to the limited convection in the device, which decreases mass transport. A free-standing cellulose-based electrolyte, prepared by immersing a cellulose membrane (Figure 59) in a liquid electrolyte, was also reported for use in thermogalvanic cells.[487]

Three different redox systems were studied: $[Co(bpy)_3]Cl_{2/3}$ in water, $[Co(bpy)_3][NTf2]_{2/3}$ in MPN, and $K_{3/4}Fe(CN)_6$ in water. The Seebeck coefficient of the water-soluble cobalt redox couple decreased by one-third (1/3) compared to that of the cobalt redox couple in the organic electrolyte. The Seebeck coefficient of the three different redox systems was not significantly affected in the free-standing cellulose electrolytes; however, the diffusion coefficient decreased by ∼20% and ∼50% for the $K_{3/4}Fe(CN)_6$ and $[Co(bpy)_3]$ redox systems, respectively (see Table 4). As a result, the performance of the thermocells decreased after solidification, but the performance was improved by increasing the redox couple concentration. The highest power densities of 168 and 24 mW m^{-2} were produced using cellulose/0.4 M aqueous $K_{3/4}Fe(CN)_6^{3/4-}$ or cellulose/0.1 M $[Co(bpy)_3][NTf_2]_{2/3}$ in MPN, respectively (Table 4).

Al-Masri et al. studied the influence of the nature of the redox couple on the Seebeck coefficient and further investigated the diffusion coefficient and charge transfer resistance of different redox couples.[488] In their paper, they chose four different cobalt complexes containing the ligands 2-(1*H*-pyrazol-1-yl)pyridine ($Co^{2+/3+}(py\text{-}pz)_3$), 2-(1*H*-pyrazol-1-yl)-4-*tert*-butylpyridine ($Co^{2+/3+}(bupy\text{-}pz)_3$), 2,6-di(1*H*-pyrazol-1-yl)pyridine ($Co^{2+/3+}(pz\text{-}py\text{-}pz)_2$), and 1,10-phenanthroline ($Co^{2+/3+}(phen)_3$) in a 3:1 dimethyl sulfoxide:1-ethyl-3-methyl-

https://doi.org/10.1021/acs.chemrev.1c00218
Chem. Rev. XXXX, XXX, XXX−XXX

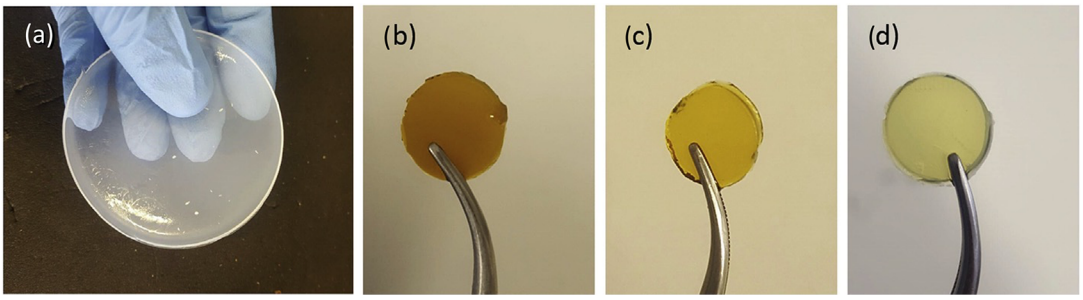

Figure 59. Cellulose-based quasi-solid-state electrolytes: (a) before immersion in an electrolyte (containing water without a redox couple) and after immersion in (b) 0.05 M $[Co(bpy)_3]Cl_{2/3}$ in water, (c) 0.05 M $[Co(bpy)_3][NTf_2]_{2/3}$ in MPN, and (d) 0.05 M $K_{3/4}Fe(CN)_6$ in water. Reproduced with permission from ref 487. Copyright 2019 Elsevier Ltd.

Table 4. Effect of the Solidification of the Electrolyte on the Seebeck Coefficient and Diffusion Coefficient of $[Co(bpy)_3]^{2+/3+}$ and $[Fe(CN)_6]^{3-/4-}$ Ions

			diffusion coefficient at 25 °C ($D \times 10^6$ cm^2 s^{-1})	
electrolyte	Seebeck coefficient (mV K^{-1})	CV peak-to-peak potential separation (mV)	$[Co(bpy)3]^{2+}$ or $[Fe(CN)_6]^{4-}$	$[Co(bpy)3]^{3+}$ or $[Fe(CN)_6]^{3-}$
0.05 M $[Co(bpy)_3]Cl^{2/3}$ in water	1.21 ± 0.08	159	3.18 ± 0.08	5.90 ± 0.07
cellulose/0.05 M $[Co(bpy)_3]Cl^{2/3}$ in water	1.15 ± 0.06	114	1.86 ± 0.10	2.95 ± 0.20
0.05 M $[Co(bpy)_3][NTf_2]^{2/3}$ in MPN	1.81 ± 0.03	380	5.00 ± 0.39	54.90 ± 0.27
cellulose/0.05 M $[Co(bpy)_3][NTf_2]^{2/3}$ in MPN	1.83 ± 0.01	254	3.65 ± 0.04	3.43 ± 0.21
0.05 M $K_{3/4}Fe(CN)_6$ in water	−1.55 ± 0.04	153	10.51 ± 0.31	10.32 ± 0.13
cellulose/0.05 M $K_{3/4}Fe(CN)_6$ in water	−1.44 ± 0.03	142	8.52 ± 0.02	8.89 ± 0.08

Table 5. Seebeck Coefficients (S) of the Redox Couples Measured in 3:1 DMSO:$[C_2mim][eFAP]$ or 3:1 PC:$[C_2mim][eFAP]$ at 0.1 M, Plus the Calculated Radius of Each Complex

redox couple	solvent mixture	S (mV K^{-1}) ± 0.02	Co^{2+} complex radius ± 0.03 (Å)
$Co^{2+/3+}(py\text{-}pz)_3$	3:1 DMSO:$[C_2mim][eFAP]$	2.36	5.76
$Co^{2+/3+}(bupy\text{-}pz)_3$	3:1 DMSO:$[C_2mim][eFAP]$	2.23	6.73
$Co^{2+/3+}(pz\text{-}py\text{-}pz)_3$	3:1 PC:$[C_2mim][eFAP]$	1.78	6.31
$Co^{2+/3+}(phen)_3$	3:1 DMSO:$[C_2mim][eFAP]$	1.70	6.10
$Co^{2+/3+}(bpy)_3$	3:1 DMSO:$[C_2mim][eFAP]$	2.00	5.75
$Co^{2+/3+}(bpy)_3$	3:1 PC:$[C_2mim][eFAP]$	1.84	5.75

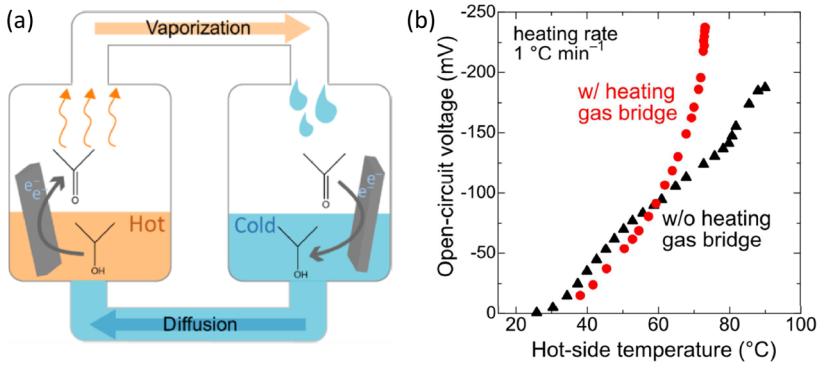

Figure 60. (a) Schematic of an acetone−2-propanol thermocell. (b) Open-circuit voltage (V_{oc}) between the hot-side electrode and cold-side electrode in the acetone−2-propanol thermocell. The cold-side temperature was maintained at 20−23 °C. The heating of the gas bridge allows acetone vapor to transfer from the hot side to the cold side and increases the V_{oc}. Without heating the gas bridge, acetone vapor condenses at the neck of the hot-side cell and continues to reflux inside. Average heating rate = 1 °C/min. Reproduced with permission from ref 489. Copyright 2018 American Chemical Society.

imidazolium tris(pentafluoroethyl) trifluorophosphate mixture. The highest Seebeck coefficient was measured for $Co^{2+/3+}(py\text{-}pz)_3$ (2.36 mV K^{-1}), which was related to a combination of its small radius, bidenticity, and lower degree of aromaticity compared to the other listed ligands in Table 5.

Recently, Zhou et al. were the first to demonstrate a TGC based on the redox couple of acetone and 2-propanol, reporting the highest Seebeck coefficient of −9.9 mV K^{-1} when the hot side was above the boiling point of acetone.[489] However, in the temperature range (20−60 °C) below the boiling point of

https://doi.org/10.1021/acs.chemrev.1c00218
Chem. Rev. XXXX, XXX, XXX−XXX

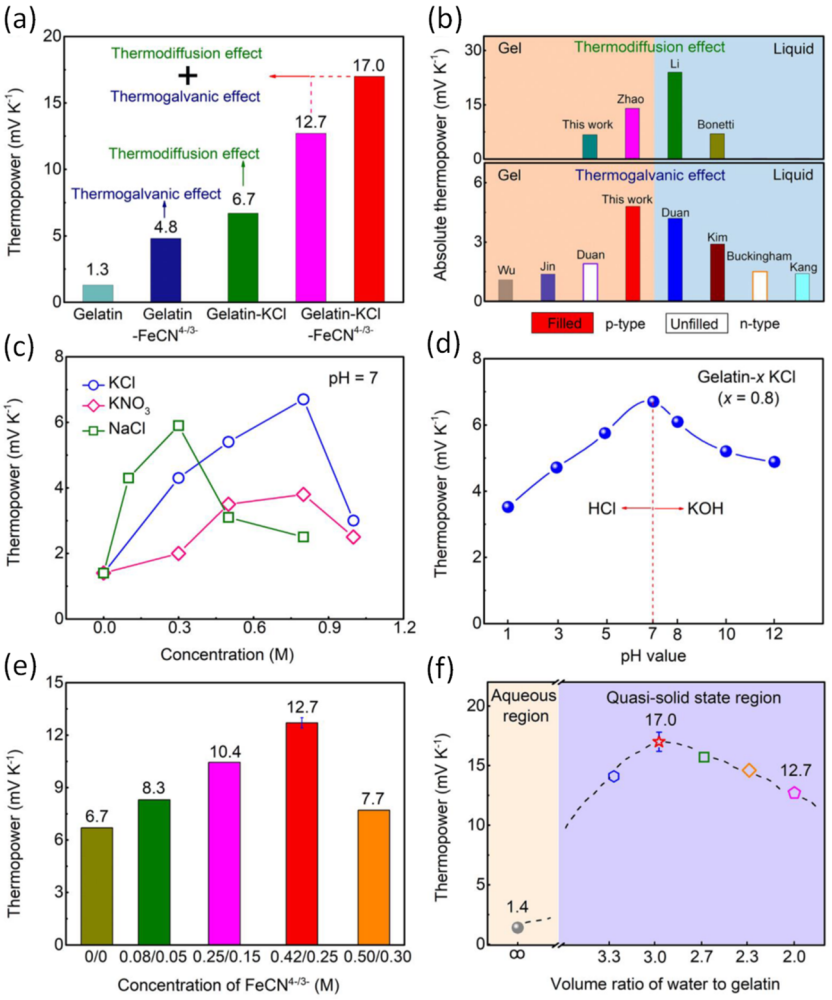

Figure 61. (a) Comparison of the thermopower among the as-fabricated i-TE materials of gelatin-x KCl-m/n $FeCN^{4-/3-}$ (x and m/n are the KCl and $K_4Fe(CN)_6/K_3Fe(CN)_6$ molar concentrations, respectively) in this work as gelatin (x = 0 M, m/n = 0 M), gelatin-$FeCN^{4-/3-}$ (x = 0 M, m/n = 0.42/0.25 M), gelatin-KCl (x = 0.8 M, m/n = 0 M), and gelatin-KCl-$FeCN^{4-/3-}$ (x = 0.8 M, m/n = 0.42/0.25 M, volume ratio of water to gelatin r_v = 2.0 and 3.0). (b) Absolute thermopower of the i-TE materials containing the thermodiffusion effect or the thermogalvanic effect. The filled and unfilled columns represent p-type and n-type thermopower, respectively. (c) Thermopower of the i-TE materials of gelatin-x KCl, gelatin-x KNO_3, and gelatin-x NaCl at varying concentrations of KCl, KNO_3, and NaCl. (d) Thermopower of the i-TE materials of gelatin-x KCl, at various pH values tuned by HCl and KOH. (e) Thermopower of the i-TE materials of gelatin-x KCl-m/n $FeCN^{4-/3-}$ at x = 0.8 M. (f) Thermopower dependence of the volume ratio of water to gelatin for gelatin-0.8 M KCl-0.42/0.25 M $FeCN^{4-/3-}$. r_v = 2.0 was maintained in (c−e). Reproduced with permission from ref 491. Copyright 2020 American Association for the Advancement of Science.

acetone, the reported Seebeck coefficient was −3.4 mV K^{-1}. Above 60 °C, the Seebeck coefficient increased by a factor of 3 and reached its highest reported value due to the phase change of acetone from the liquid to the gas state. In addition, heating of the gas bridge that connected the hot-side and cold-side cells promoted an increase in the Seebeck coefficient due to the increase in the mass transfer of acetone vapor (see Figure 60). In that report, a Pt−Sn catalyst electrodeposited on a Pt substrate was used as the electrode for two reasons: (1) the reduction of acetone to 2-propanol on platinum catalysts had not yet been reported[489] and (2) the oxidation of isopropanol on a Pt−Sn catalyst was usually conducted in strongly acidic solutions. However, when acetone was heated under strongly acidic conditions, self-condensation readily occurred to produce phorone and acetone-derived polymers.[490]

Han et al. recently demonstrated a giant positive Seebeck coefficient in ionic gelatin-based thermoelectric materials in which they synergistically combined the thermodiffusion of ions (KCl, NaCl, KNO_3) and the thermogalvanic effect of the ferro cyanide redox couple, as shown in Figure 61.[491] A high Seebeck coefficient of 12.7 mV K^{-1} was obtained for a flexible, quasi-solid-state, ionic thermoelectric material of gelatin-x KCl-m/n $Fe(CN)^{4-/3-}$ (x = 0.8 M and m/n = 0.42/0.25), where x and m/n are the molar concentrations of KCl and $K_4Fe(CN)_6/K_3Fe(CN)_6$, respectively. Finally, they further increased the Seebeck coefficient from 12.7 to 17 mV K^{-1} by optimizing the volume ratio of water to gelatin.

4.4.2. Electrode Materials. Platinum electrodes have been studied for TGC applications due to their absence of an oxide layer and their high electrochemical activity.[492−494] However, the wide application of TGCs with platinum electrodes is limited simply due to the cost of the material, which promotes investigating alternative electrode materials. Metal-free materials, such as carbon and conducting polymers, have recently emerged as efficient electrode materials for TGCs.[62,463,495,496] Among carbon-based materials, carbon nanostructures, such as carbon fibers, CNTs, graphite, and graphene, have displayed higher performance than platinum electrodes because of their

https://doi.org/10.1021/acs.chemrev.1c00218
Chem. Rev. XXXX, XXX, XXX−XXX

Table 6. Performance of TGCs with Different Combinations of Electrodes and Electrolytes

electrode	electrolyte	S (mV K^{-1})	ΔT (K)	P_{max} (W m^{-2})	η	η_c
Pt	0.26 M $Fe(CN)_6^{3-}/Fe(CN)_6^{4-}$ 0.8 M KC	−1.50	20		0.031	0.500
MWCNT buckypaper	0.4 M $Fe(CN)_6^{3-}/Fe(CN)_6^{4-}$	−1.40	60	1.800		1.400
SWCNT	0.2 M $Fe(CN)_6^{3-}/Fe(CN)_6^{4-}$		20			
Pt	0.4 M I^-/I^{3-} in [C2mim][BF4]	0.23	70	0.029		
Pt	0.1 M $Co^{2+/3+}(bpy)_3(NTf2)_{2/3}$	2.19	70	0.499		
CNT/RGO composites	0.4 M $Fe(CN)_6^{3-}/Fe(CN)_6^{4-}$	−1.40	31	1.850	0.218	2.630
Pt Black	0.1 M $Con(bpy)_3(NTf2)_n$ in [C2mim][B(CN)4]	1.80	70	0.240		
CNT/carbon fabric	0.4 M $Fe(CN)_6^{3-}/Fe(CN)_6^{4-}$	−1.40	31	0.460		
Pt	30 mM [Fc]/[I^{3-}]	0.81	50	2.4×10^{-7}		
Pt/CNT	0.4 M $Fe(CN)_6^{3-}/Fe(CN)_6^{4-}$	−1.43	51	6.600	0.560	3.950
Pt	0.4 M $Fe(CN)_6^{3-}/Fe(CN)_6^{4-}$/5% cellulose	−1.38	15	0.014		
Pt	0.1 M $Co^{2+/3+}$tris(bipyridyl)/MPN−[C2mim][B(CN)4]	2.01	70	0.880		
Pt	4 mM α-CD-2,5 mM I3-/10 mM I- in 200 mM KCl	1.90	34			
Pt	0.4 M $Fe(CN)_6^{3-}/Fe(CN)_6^{4-}$/methanol	−2.90	4.1	0.011	0.003	0.024
PEDOT-Tos	0.4 M $Fe(CN)_6^{3-}/Fe(CN)_6^{4-}$	−1.43	30	0.417	0.024	0.260
activated carbon cloth	0.9 M $Fe(CN)_6^{3-}/Fe(CN)_6^{4-}$	−1.50	84	12.000	0.065	0.300
Au/Cr	0.1 M $Fe(CN)_6^{3-}/Fe(CN)_6^{4}$ and 0.1 M Fe^{3+}/Fe^{2+}	−1.21 and 1.02	10	90×10^{-9}		
PEDOT-PSS	0.4 M $Fe(CN)_6^{3-}/Fe(CN)_6^{4-}$	−1.43	30	0.410	0.023	0.256

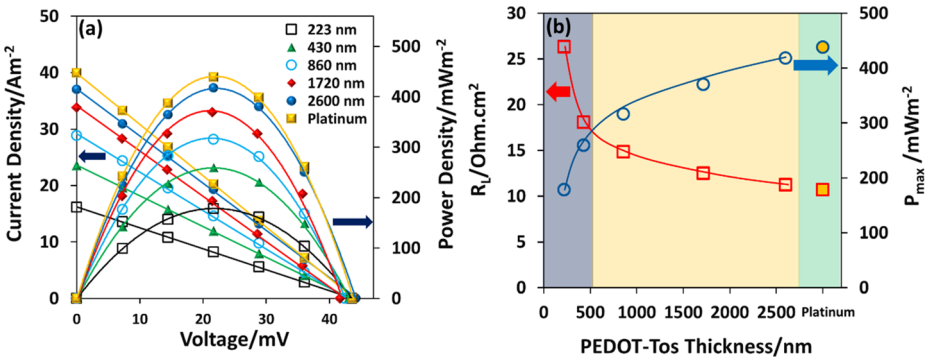

Figure 62. Performance of thermogalvanic cells with various PEDOT-Tos and platinum thicknesses. (a) Power output and current density (normalized with the geometric surface area) as a function of the device voltage. (b) Comparison of the maximum power for a cell with platinum electrode to cells with PEDOT-Tos electrodes of different thicknesses. Reproduced with permission from ref 496. Copyright 2017 Royal Society of Chemistry.

high surface area.[61,62,468,497,498] A wide range of manufacturing techniques are available to fabricate different varieties of high surface area carbon materials. Most of the recent research on carbon-based electrode TGCs has focused on composite carbon materials, such as nanostructures and graphene. In addition, there are some demonstrations with additives and doping on carbon materials that show promising performance.[54,499]

The first demonstration of TGCs comprised of CNT-based electrodes was reported in 2010.[61] Well-ordered MWCNTs, prepared by chemical vapor deposition with acetylene as the carbon source, were used as the electrodes of a TGC composed of $[Fe(CN)_6]^{4-}$ and $[Fe(CN)_6]^{3-}$ as the redox couple, and this TGC showed an efficiency as high as 1.4% of the Carnot efficiency, which was 3 times that of the equivalent platinum-based TGC measured under the same conditions.

Romano et al. enhanced the electrode porosity by fabricating a composite of CNTs and reduced graphene oxide.[62] On the one hand, the porous nature of these materials provided a larger active surface area in comparison to flat electrodes, allowing for a higher exchange current density. On the other hand, the accessibility of the redox couples in these tortuous electrodes could limit the transport of the reaction product, thus limiting the TGC power output as well. They optimized the composite electrode by varying the composition of the two materials. It was found that the electrode comprised of 90% SWCNTs and 10% rGO had the best performance, with a power output as high as 337 mW m^{-2} (ΔT = 30 K). The power output could be enhanced by increasing the electrode thickness, reaching up to 460 mW m^{-2} with 4.5 μm thick electrodes or even 1800 mW m^{-2} for electrodes consisting of 10 stacked layers (45 μm) at the same ΔT, with an efficiency as high as 2.6% of the Carnot efficiency.

Table 6 summarizes the performance of some TGCs based on a typical combination of electrodes and electrolytes. The highest power output achieved so far for a TGC is 12 W m^{-2} (ΔT = 84 K) by using an activated carbon cloth electrode and an aqueous ferro/ferricyanide electrolyte.[468] A high power density could be achieved by using an electrolyte-filled thermal separator and by using the highly soluble redox electrolyte $(NH_4)_4Fe(CN)_6/(NH_4)_3Fe(CN)_6$ at a concentration of 0.9 M. This strategy increased the ionic conductivity by 66% and reduced the thermal conductivity by 5.7%, thereby improving the thermogalvanic power efficiency.

Another type of low-cost electrode without an insulating oxide on the surface is a conducting polymer. Abraham et al. considered a coating of conducting polymer on a metal electrode for use in TGCs.[55] To avoid any electron transfer with the metal electrode and to reveal the true potential of polymer electrodes

https://doi.org/10.1021/acs.chemrev.1c00218
Chem. Rev. XXXX, XXX, XXX−XXX

alone, a highly conducting polymer electrode made of PEDOT-Tos (conductivity ~1000 S cm^{-1}) was used.[75,500−503] Thin films of the PEDOT-Tos electrodes were fabricated on glass by chemical polymerization, and the performance of the TGCs was studied by using a 0.4 M $K_4Fe(CN)_6/K_3Fe(CN)_6$ redox electrolyte. As shown in Figure 62a, the maximum power generation of the TGC with a 223 nm thick electrode reached 178 mW m^{-2} (ΔT = 30 K), which was only three times lower than that of flat platinum electrodes (438 mW m^{-2}) under the same conditions. Increasing the thickness of the PEDOT-Tos electrodes led to the same power as that of flat Pt electrodes (Figure 62b). The same authors further investigated the interplay between the electrical conductivity of the polymer electrode and the rate of electron transfer with ferro/ferricyanide, as well as its impact on the performance of the TGCs.[504] PEDOT-PSS (PH1000) was modified with various amounts of DMSO (up to 6 wt %) to tune its morphology by inducing the demixing of excess insulating PSS, which resulted in an increase in conductivity by more than 3 orders of magnitude (Figure 63a). The rate of electron transfer from the

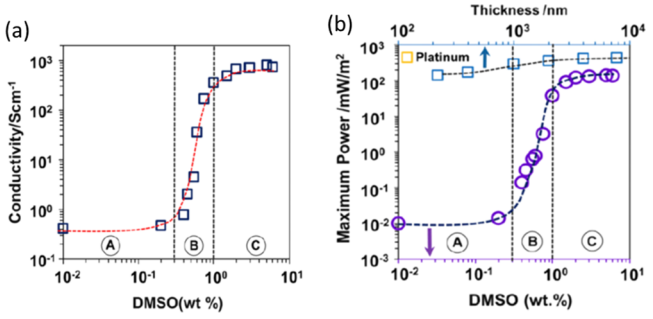

Figure 63. (a) Conductivity of PEDOT:PSS-DMSO electrodes (the dashed red line demonstrates the trend in the electrical conductivity with respect to the DMSO wt %). (b) Maximum power output of the TGC as a function of the DMSO ratio and the maximum power output of TGC as a function of the different thicknesses of PEDOT:PSS-5% DMSO. The dashed black lines are guides for the eyes to show the trend in those graphs. All measurements are taken at a ΔT of 30 °C. Reproduced with permission from ref 504. Copyright 2018 National Academy of Sciences.

PEDOT:PSS electrode to the ferro/ferricyanide couple was related to the percolation transport of the polymer electrode. The power produced by the TGC increased by 4 orders of magnitude after changing the morphology and electrical conductivity of the PEDOT electrode (Figure 63b).

PEDOT:PSS films represent an attractive alternative to platinum electrodes. Recently, Wang et al. demonstrated a PEDOT:PSS-based thermo-electrochemical cell using ferricyanide/ferrocyanide as the electrolyte. This device delivered a maximum power output of 300 μW, with a 1 Ω loading at a temperature difference of 30 K; additionally, this device powered an array of light-emitting diodes and Bluetooth humidity/temperature sensors for wireless communication.[505] Furthermore, they investigated the electrochemical properties of insoluble redox couples such as Prussian blue (PB) analogue compounds by hybridizing them with PEDOT:PSS via ball milling, drop-casting on a polystyrene mold, and heating at 70 °C for 24 h. In this work, they combined nickel ferrocyanide (NiHFC) with Fe^{2+}/Fe^{3+} using a cation separator (Figure 64a) and PB with $K_3Fe(CN)_6/K_4Fe(CN)_6$ using an anion separator (Figure 64b). This electrochemical cell generated a maximum power of 4 μW over a temperature range of 5−60 °C.

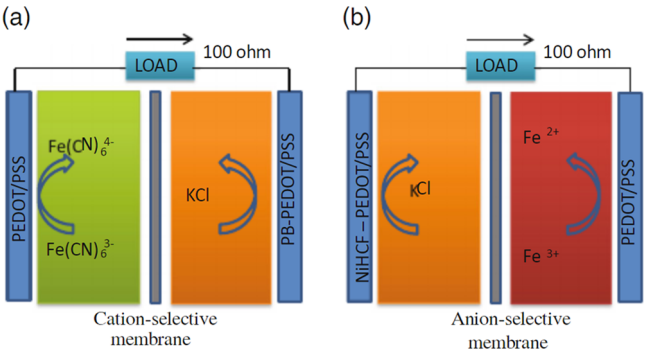

Figure 64. Schematic of the charge-free TREC system combining (a) PB-PEDOT:PSS with $Fe(CN)_6^{3-/4-}$ and (b) NiHCF-PEDOT:PSS with $Fe^{2+/3+}$. Reproduced with permission from ref 505. Copyright 2020 Wiley.

Li et al. demonstrated highly efficient cylindrical TGCs, working in a wide operation window of cold temperatures down to −40 °C.[506] In parallel, they developed a eutectic electrolyte composed of formamide and water, which exhibited high ionic conductivities (between 10 and 100 mS cm^{-1} in the temperature range of −40 to 90 °C, as shown in Figure 65a), and an electrode material based on an anisotropic porous graphene aerogel, which had aligned sheets and pores (Figure 65b) and demonstrated high ionic conductivity. These two materials were then employed to create a device composed of 15 thermocells capable of delivering 2 V and 350 μW at an external ΔT = 106 K (Figure 65c,d).

Recently, Ding et al. reported a hybrid photothermal generator consisting of a pyroelectric generator and a TGC for multiple situations, namely structured/unstructured, static/dynamic, and day/night waste heat harnessing for continuous operation.[507] In this device, CNT-based nanocomposites served as: (1) broadband solar absorbers, (2) good thermally/electrically conductive electrodes, and (3) electrodes with a high electrochemical specific surface area. The high photothermal properties and electrical conductivity of the carbon nanotube/cellulose nanocrystal nanocomposite, together with the heat localization effect, resulted from the sponge-confined electrolyte; thus, the simultaneously high thermogalvanic and pyroelectric performances were achieved with maximum outputs of 1.86 and 0.9 mW m^{-2}, respectively (Figure 66). In addition, a scaled-up hybrid photothermal generator was successfully tested on both land and water surfaces under natural sunlight, and the feasibility of nighttime operation was verified.

Shin et al. demonstrated a hybrid photovoltaic thermogalvanic cell module (PV/T) by integrating a TGC directly into the back of a solar panel (Figure 67), exploring the feasibility of the module for practical implementation.[508] Here, a fabricated thermogalvanic cell consisting of an electrolyte with a ferric/ferrous redox couple ($[Fe(CN)_6]^{4-}$ and $[Fe(CN)_6]^{3-}$) and SWCNT electrodes was integrated directly into the back of a commercial solar panel array. The TGC in the fabricated PV/T hybrid system performed both as a cooling system and produced additional power output by converting the thermal energy absorbed by the solar panel into useful electrical energy. Under illumination with air mass (AM) of 1.5 G, using a solar simulator,

https://doi.org/10.1021/acs.chemrev.1c00218
Chem. Rev. XXXX, XXX, XXX−XXX

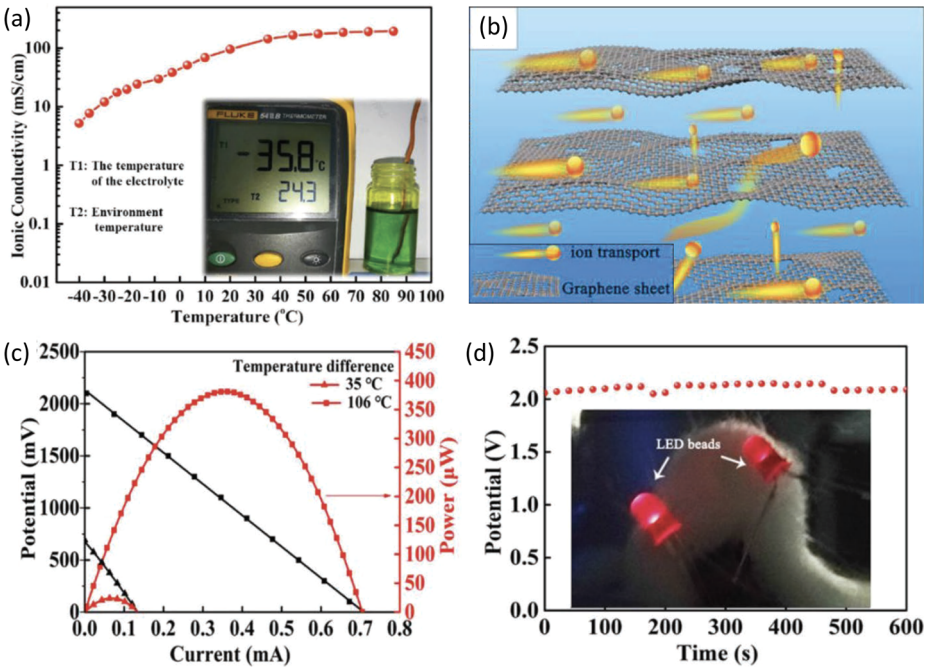

Figure 65. (a) Conductivity of the 0.4 M electrolyte at different temperatures. The inset is a photo measurement of the electrolyte temperature with a thermocouple. (b) Illustration showing the ionic transport model in the ordered porous graphene channels. (c) Plots of the output voltage and power versus the current of the 15-cylinder device for different temperature differences. (d) Output voltage versus time obtained from $\Delta T = 106$ °C. The inset in (d) is the photo of LED beads powered by the device. Reproduced with permission from ref 506. Copyright 2019 Wiley.

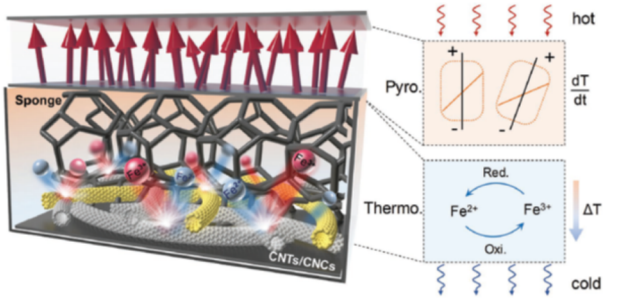

Figure 66. Schematic of the hybrid photothermal generator. The mechanism of the photothermal pyroelectric generator (Pyro) and thermocell (Thermo) are depicted in the upper and lower figures on the right, respectively. Reproduced with permission from ref 507. Copyright 2019 Wiley.

the conversion efficiency of the solar cell improved from 13.2% to 15% by cooling the solar cell from 61 to 34 °C due to the thermogalvanic cell and the additional harvested power of 3.53 μW cm^{-2}.

Kim et al. combined n-type Fe-TECs with p-type FeCN-TECs in series to produce output powers sufficient for large-scale applications.[509] They fabricated a TEC module consisting of 32 pairs of Fe-TEC ClO_4[0.5 M $Fe(ClO_4)_2/Fe(ClO_4)_3$] and FeCN-TEC-NH_4 [0.9 M $K_3Fe(CN)_6/(NH_4)_4Fe(CN)_6$] (Figure 68c). The TEC module generated a V_{oc} of 2.05 V and an I_{sc} of 0.2 A m^{-2}, respectively, at a ΔT of 25 °C, which powered a commercial light-emitting diode (Figure 68d).

Duan et al.[469] demonstrated potential applications of their optimized systems (previously discussed) for harvesting low-grade thermal energy and fabricated a prototype module containing 50 urea/guanidine chloride (UGdmCl) units (1 cm^2 area, 0.5 cm thickness) connected by Cu wires in series (Figure 69). This device generated a voltage of 3.4 V and a current of 1.2 mA at an applied $\Delta T = 18$ °C and directly powered an LED array. Furthermore, the module could harvest heat from the human body, and a stable voltage of more than 0.3 V was generated by a small temperature difference of approximately 1.3 K, as shown in Figure 69d. In addition, this module could harvest waste heat in a cold environment.

An array of series-connected n-type and p-type TGCs that provided an output voltage of 2 V were fabricated by Zhang et al.[468] Figure 70b–d describes this TGC array, which consists of a $K_3Fe(CN)_6/(NH_4)_4Fe(CN)_6$ couple for the p-type element and a $FeSO_4/Fe_2(SO4)_3$ couple for the n-type element. The low voltage of the iron sulfate TGC limited the maximum output current for the array. A TGC array containing 28 alternating, series-connected half-cells is shown in Figure 70c,d, where the cross-sectional areas of both legs are the same. The voltage generated by the 28 half-cells was ~27 mV K^{-1} (1.93 mV K^{-1} × 14 cells), and four identical TGC arrays were connected in series to obtain an open-circuit voltage of 2.18 V for a ΔT of 21 °C. This TGC output was used to charge commercial capacitors with capacitances of 47 to 1000 μF to 2 V during times ranging from 1 to 20 min.

Yang et al. fabricated a wearable TGC system to harvest low-grade body heat.[23] The system consisted of two types of thermogalvanic gel electrolytes with positive and negative thermo-electrochemical Seebeck coefficients, corresponding to the n-type and p-type elements of a conventional thermoelectric generator, respectively. Poly(vinyl alcohol) (PVA) was used as the gel solution, with ferric/ferrous chloride or potassium ferricyanide/ferrocyanide couples to obtain the thermogalvanic gel electrolytes exhibiting positive and negative thermo-electrochemical Seebeck coefficients. These gel electrolytes exhibited both moderate thermoelectric performance and good mechanical properties. The integrated wearable device contained 59 n-type and 59 p-type TGC gel units (a height of 1 mm and a diameter of 3 mm), with bridging Au/Cr interconnections

https://doi.org/10.1021/acs.chemrev.1c00218
Chem. Rev. XXXX, XXX, XXX−XXX

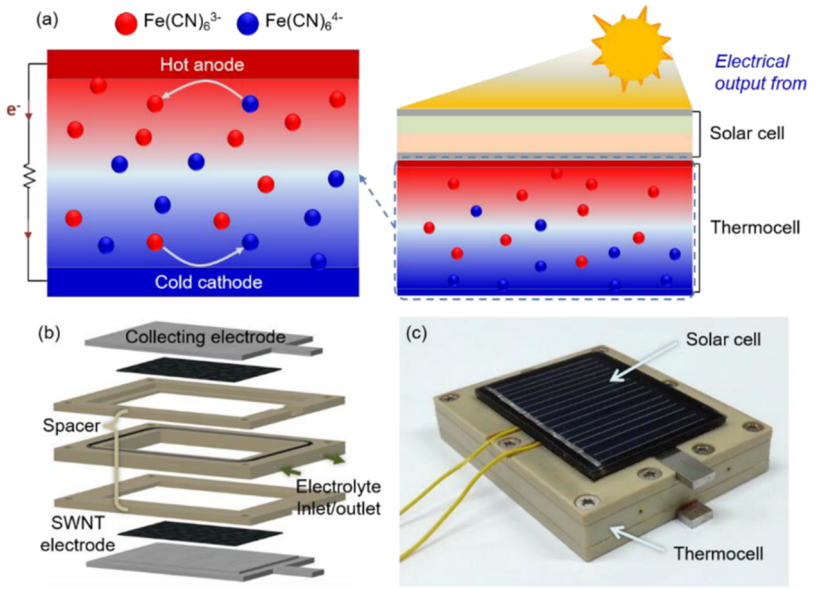

Figure 67. Fabrication and operation of the hybrid PV/T module: (a) schematic of the hybrid PV/T module and thermocell operation, (b) cell components and their assembly in a thermocell, and (c) optical image of the fabricated PV/T module. Reproduced with permission from ref 508. Copyright 2020 Multidisciplinary Digital Publishing Institute.

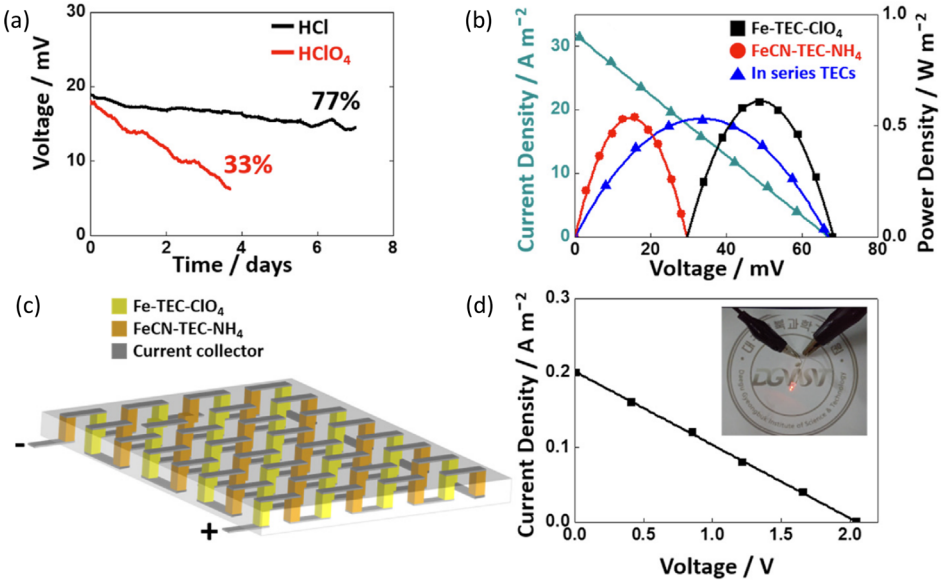

Figure 68. (a) Long-term performance of Fe-TEC-ClO_4 using 0.1 M HCl or 0.1 M $HClO_4$ for T_{cold} and T_{hot} of 25 and 50 °C, respectively. (b) Thermoelectrochemical performances of Fe-TEC-ClO_4, FeCN-TEC-NH_4, and TECs connected in series for T_{cold} and T_{hot} of 25 and 50 °C, respectively. (c) Schematic diagram of the series module and the (d) current vs voltage of the series module containing 64 units. The inset in (d) is an image of LED powered by the series module. Reproduced with permission from ref 509. Copyright 2020 Elsevier Ltd.

on a flexible PI substrate, as illustrated in Figure 71; this device could generate a maximum output power of approximately 0.3 mW by utilizing body heat (Figure 71).

Finally, because of the thermocell voltage's direct dependence on the electrode's surface temperature, the lack of thermal contact resistance between the specimen and TGC makes the thermal response of thermogalvanic cells fast (<300 μs).[510] The fast response to thermal variation, combined with the high sensitivity linked to the high values of S, makes such devices an attractive solution for sensing applications.

5. CONCLUSIONS AND OUTLOOKS

Solid-state inorganic semiconductors currently dominate research on thermal-to-electrical energy conversion due to their high performances and efficiencies. In this case, the concept of electron-crystal/phonon-glass behavior has been the driving force for developing new materials. However, despite the impressive results that have been obtained, this technology has been limited to niche applications such as space (e.g., powering satellites) and scientific instrumentation (e.g., cooling detectors) due to the high costs of materials and processing. In the last 20 years, carbon-based semiconductors have been scrutinized as potential thermoelectric materials for low-temperature energy harvesting because of the high abundance of their atomic

https://doi.org/10.1021/acs.chemrev.1c00218
Chem. Rev. XXXX, XXX, XXX−XXX

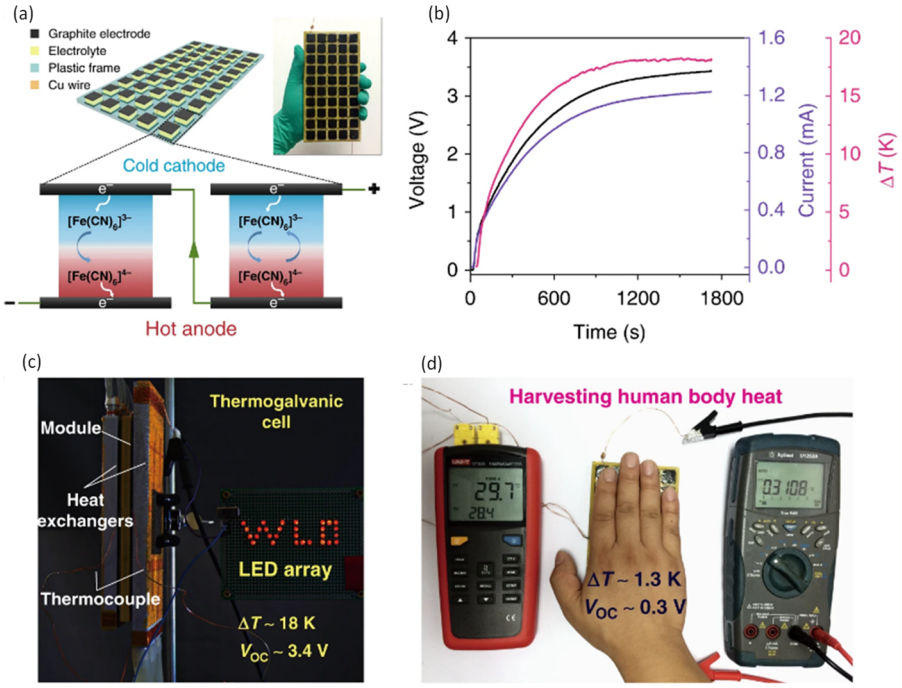

Figure 69. Demonstration of low-grade heat harvesting by a prototype module. (a) Schematic of the structure and a photograph of the module. (b) Voltage and current curves of the module corresponding to the applied temperature difference. (c) Image of the module directly powering an LED array containing 29 red LEDs. The module was sandwiched by two aluminum heat exchangers with water as the heat transfer fluid. The temperatures of the cold and hot water were controlled at approximately 278 and 333 K, respectively. Because of inevitable thermal conduction in the module and thermal contact resistance between the module and heat exchangers, the ΔT of 18 K shown by the module at the steady state was smaller than the nominal temperature difference between the two heat exchangers. (d) Harvesting heat energy from the human body. The module was placed on a steel platform as a heat sink with a temperature of approximately 298 K and then covered by one hand. After several minutes, a stable temperature difference of 1.3 K was observed, which induced an output of approximately 0.3 V by the module. The temperature and voltage were measured by a thermocouple (left) and multimeter (right), respectively. Reproduced with permission from ref 469. Copyright 2018 Nature.

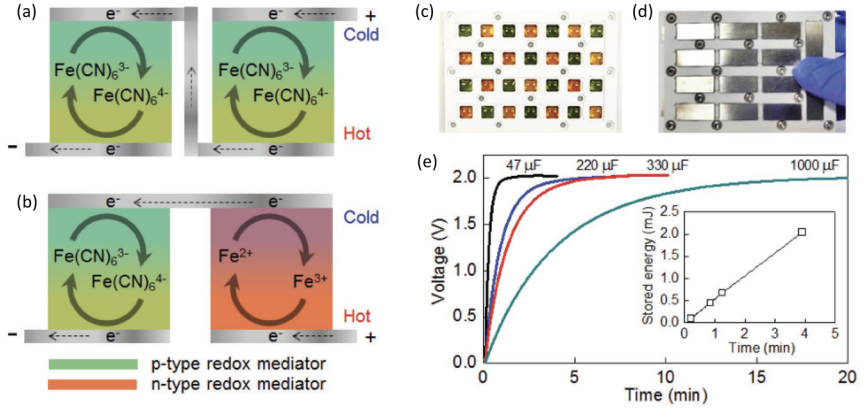

Figure 70. Enhanced output voltage using interconnected thermocell modules. (a) Illustration of two series-connected p-type half-cells that both use aqueous $Fe(CN)_6^{4-}/Fe(CN)_6^{3-}$ as the redox mediator. (b) Illustration of a p-type half-cell (using aqueous $Fe(CN)_6^{4-}/Fe(CN)_6^{3-}$ as the redox mediator) and an n-type half-cell (using aqueous Fe^{2+}/Fe^{3+} as the redox mediator) that are connected in series. (c) Photograph of alternating n-type and p-type mediators for a thermocell array with 14 n−p cells. (d) Photograph of the sealed thermocell array for the redox couple array in (c), showing the top plate that completes the electrical connections. (e) Voltage−time curves of different capacitors when charged by four series-connected thermocell arrays. Reproduced with permission from ref 468. Copyright 2017 Wiley.

elements. Other advantages are linked to their low-costs and large-area (low T) processing, using printing techniques. Furthermore, their intrinsically lower thermal conductivity represents a significant advantage in harvesting energy from small temperature differences.

These materials can be divided into two main classes: carbon nanostructures (e.g., carbon nanotubes and graphene) and organic polymers/small molecules. Semiconducting single-walled carbon nanotubes can be separated from their metallic counterparts, using scalable solution processes through specific complexation with specific polymers. While the thermal conductivity is large along single nanostructures, in thin films composed of a network of these elements, the thermal conductance is significantly reduced by phonon scattering at interfaces, thus making them viable candidates for thermoelectric applications. Their Seebeck coefficients can be

https://doi.org/10.1021/acs.chemrev.1c00218
Chem. Rev. XXXX, XXX, XXX−XXX

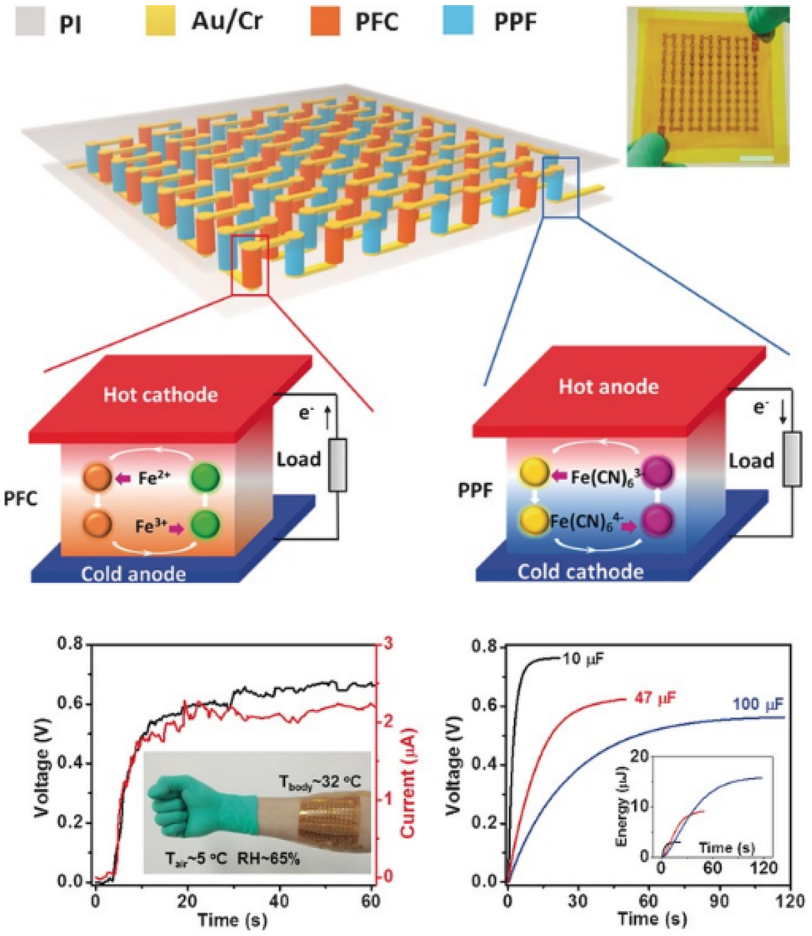

Figure 71. (top) Schematic and image of the integrated gel-based thermocell. Both the PFC and PPF gels are sandwiched between two flexible substrates (polyimide, PI). With alternating top and bottom interconnections, the PFC and PPF gels are connected in series. (bottom) Applications of the wearable thermocell. (left) Voltage and current generated by the thermocell from body heat. The inset shows a photograph of the wearable thermocell on a forearm. (right) Voltage−time curves of different capacitors charged by the thermocell utilizing human body heat. The inset shows the energy stored in the capacitors, which is also the electrical energy harvested from body heat. Reproduced with the permission from ref 23. Copyright 2016 Wiley.

controlled by tuning their structure (e.g., the nanotube diameter) and doping level. One unique feature is that they can be reduced by chemical means to display a stable negative Seebeck coefficient in air and a power factor higher than many n-doped conducting polymers. Conducting polymers are stable in air in their oxidized form (p-doped) and reach impressive values of power factor and zT (e.g., 0.52 for PEDOT:PSS), much higher than that of their n-doped counterparts. The power factor of conducting polymers can be controlled not only through their doping level but also by tuning their morphology at various scales because it affects the electronic properties and transport regime of the charge carriers.

For both classes of materials, emerging processing techniques enable the fabrication of thick layers necessary to utilize large thermal gradients in a traditional vertical thermoelectric module. Unfortunately, stable high thermoelectric performance is challenging to achieve with thick layers. Thus, technical solutions have been proposed to overcome this problem, for example, employing new geometries based on printing lateral thermocouples on flexible and foldable substrates. However, even with this strategy, thick layers will be beneficial, and such a structure prevents the actual integration of thermocouples in a monolithic device.

Recently, the blending of high *PF* inorganic nanostructures with conducting polymers, CNTs, and graphene matrices has shown promising results, representing an innovative way to process these novel materials. However, the thermoelectric properties of the individual parts of the composite are not additive, and they typically lead to decreased thermoelectric performance because the nanocomposites cannot have higher performance than the individual parts unless quantum effects dominate. In this regard, one of the challenges is to avoid the percolation of one phase of the composite because the phase with the highest conductivity will then govern most of the thermoelectric properties of the composite. In addition, the transport of charge carriers across both phases is typically made difficult by the presence of a potential barrier at the interface, which can stem from an oxide layer on the inorganic filler or equilibration of the Fermi levels of the two phases.

A less explored area of research on thermoelectricity is that of the thermodiffusion of matter. The thermodiffusion of ions in electrolytes yields large ionic Seebeck coefficients, in the range of tens of mV K^{-1}, opening new avenues for energy storage, ultrasensitive heat sensors, and thermoelectronics. Unfortunately, ionic thermoelectric energy storage devices are restricted to discontinuous heat sources or need to be coupled with a supercapacitor to work as energy harvesters.

https://doi.org/10.1021/acs.chemrev.1c00218
Chem. Rev. XXXX, XXX, XXX−XXX

Another type of thermoelectric effect is based on the entropy of electron transfer during an electrochemical reaction, which leads to thermogalvanic cells. Despite the low efficiency (only a tiny fraction of the Carnot efficiency), several breakthroughs have motivated research on these energy conversion devices, e.g., redox couples with high Seebeck coefficients, high surface area electrodes, and heat transport control in electrolytes and complementary p-/n- thermoelectric modules. The use of gel electrolytes is attractive because thermogalvanic cells can be flexible and stretchable or elastic. These properties will open a new unique research path compared to solid-state thermoelectric materials for powering low-power electronics from body heat. While the solvent's chaotropic effect around charged species is mainly understood for aqueous electrolytes in biochemistry, these mechanisms are less understood for other media. Therefore, through studies on thermogalvanic cell optimization, new knowledge will be acquired for various other organic, ionic liquid, and polymer gel electrolytes.

In conclusion, carbon-based materials represent a novel path in the field of thermoelectricity and allow for the development of a new generation of energy harvesters and sensors. This new generation of thermoelectric devices will be available for some niche applications and everyday life scenarios, from the IoT to wearable and biomedical devices. In this regard, it is of paramount importance to evaluate material toxicity when placed in contact with biological media (tissues, cells, skin, and others). Some materials, such as PEDOT:PSS, have already proven to be biocompatible.[511] However, for many other materials presented in this review, not enough data are currently available. The use of robust, biocompatible, and nondegradable capping/protection layers (e.g., PDMS or parylene) could represent a solution to material toxicity and enable the integration of TE devices with biological tissues. In addition, the inherent flexibility of additive manufacturing techniques has led to the development of new geometries and devices that can adapt to many kinds of irregular flexible and soft substrates (e.g., plastic or cloth) while still maintaining most of the thermoelectric properties. Because of this, organic materials represent the best choice for inexpensive low-power, room-temperature TE devices. Unfortunately, the development of scalable devices and fabrication processes has lagged far behind materials development and is mainly limited to simple demonstrators. As new carbon-based thermoelectric materials continue to be discovered and the material performance continues to improve, additional focus will need to be directed toward the integration of these materials into functional devices. This will require consideration of the various materials interfaces and the device/system architectures to successfully translate lab-scale demonstrators into commercially relevant products. Recently, however, more and more examples of integrated, printed, and woven devices have been presented in the literature, showing the possibility of commercializing OTEG in a not-so-far future.

AUTHOR INFORMATION

Corresponding Authors

Simone Fabiano − *Department of Science and Technology, Linköping University, SE-60174 Norrköping, Sweden;* orcid.org/0000-0001-7016-6514; Email: simone.fabiano@liu.se

Jeffrey L. Blackburn − *National Renewable Energy Laboratory, Golden, Colorado 80401, United States;* orcid.org/0000-0002-9237-5891; Email: jeffrey.blackburn@nrel.gov

Xavier Crispin − *Department of Science and Technology, Linköping University, SE-60174 Norrköping, Sweden;* orcid.org/0000-0001-8845-6296; Email: xavier.crispin@liu.se

Authors

Matteo Massetti − *Department of Science and Technology, Linköping University, SE-60174 Norrköping, Sweden*

Fei Jiao − *Department of Science and Technology, Linköping University, SE-60174 Norrköping, Sweden; Tianjin Key Laboratory of Molecular Optoelectronic Sciences, Department of Chemistry, School of Sciences, Tianjin University & Collaborative Innovation Center of Chemical Science and Engineering, Tianjin 300072, China;* orcid.org/0000-0002-9801-6283

Andrew J. Ferguson − *National Renewable Energy Laboratory, Golden, Colorado 80401, United States*

Dan Zhao − *Department of Science and Technology, Linköping University, SE-60174 Norrköping, Sweden*

Kosala Wijeratne − *Department of Science and Technology, Linköping University, SE-60174 Norrköping, Sweden*

Alois Würger − *Laboratoire Ondes et Matière d'Aquitaine, Université de Bordeaux, F-33405 Talence Cedex, France*

Complete contact information is available at: https://pubs.acs.org/10.1021/acs.chemrev.1c00218

Author Contributions

M.M. and F.J. contributed equally. The manuscript was written through contributions of all authors. All authors have given approval to the final version of the manuscript.

Notes

The authors declare the following competing financial interest(s): S.F. is the founder and Chief Scientific Officer of n-Ink AB.

Biographies

Matteo Massetti obtained his Ph.D. in Physics in 2019 at "Politecnico di Milano" (Italy) with a thesis on the study of the thermoelectric properties of organic semiconductors and on the development of printed integrated thermoelectric generators. He then joined Prof. Fabiano's group at the Laboratory of Organic Electronics (Linkoping University, Sweden) as a postdoc, where he is currently working on neuromorphic devices and continuing his activity in the field of printed electronics with a focus on organic electrochemical transistors, thermoelectric/thermoionic generators.

Fei Jiao is an associate professor at the School of Science in Tianjin University. He received his B.S. degree in Chemical Engineering and Technology from Jilin University in 2009 and Ph.D. degree in Organic Chemistry from the Institute of Chemistry, Chinese Academy of Sciences (ICCAS) in 2014, under the supervision of Prof. Daoben Zhu. From 2014 to 2018, he worked as a postdoctoral researcher in Prof. Xavier Crispin's group in the Laboratory of Organic Electronics in Linköping University, and currently his research interests focus on organic composites for thermoelectrics and field-effect transistors.

Andrew Ferguson received his Ph.D. in Physical Chemistry from Imperial College, United Kingdom. Following a postdoctoral appointment at the National Renewable Energy Laboratory (NREL), he became a senior scientist and then group manager in NREL's Chemistry & Nanoscience Center. His primary research interests focus on light−matter interactions and developing an understanding of exciton, carrier, and heat transport in organic, inorganic, and nanoscale material

https://doi.org/10.1021/acs.chemrev.1c00218
Chem. Rev. XXXX, XXX, XXX−XXX

systems. He is also working on the integration of these materials into novel energy harvesting and conversion technologies.

Dan Zhao is an Assistant professor at the Laboratory of Organic Electronics (LOE) at Linköping University. She received her B.S. from the Chemistry Department in Nankai University in 2008. After finishing her Ph.D. in Renmin University in China, she joined LOE to continue postdoctoral research in 2013. Her research interest includes ionic thermoelectrics and electrolyte-based and dielectric materials.

Kosala Wijeratne received his Ph.D. in Applied Physics from the Linköping University, Sweden, in 2018. After that, he joined the Research Institute of Sweden as a development engineer. He is currently an Electrochemical Engineer at Battery Materials, Johnson Matthey, United Kingdom. His primary research interests focus on lithium-ion batteries.

Alois Würger is Professor in the Condensed Matter Theory Group of LOMA, at the Université de Bordeaux. He received his Ph.D. from the University of Erlangen, and his venia legendi from University Heidelberg and was a Research Associate at the Institut Laue-Langevin in Grenoble, where he worked on low-temperature physics and quantum dissipation. His present research interests include non-equilibrium complex fluids, colloidal thermophoresis, nanofluidics, and thermoelectric effects.

Jeff Blackburn received his Ph.D in Chemistry from the University of Colorado, Boulder, in 2004 and performed his postdoctoral studies at the National Renewable Energy Laboratory (NREL). He is currently a senior scientist, group manager, and Distinguished Member of the Research Staff at NREL. His research interests include the fundamental understanding of optical and electrical properties and processes in low-dimensional materials (SWCNTs, graphene, two-dimensional semiconductors, and hybrid organic/inorganic semiconductors) and the integration of these materials into sustainable energy technologies.

Xavier Crispin is a Professor in the Laboratory of Organic Electronics (LOE) at Linköping University, Sweden. In 2000, He obtained his Ph.D. in the University of Mons (Belgium) and developed his own research group at Linköping University as an ERC fellow. He was awarded the Tage Erlander and Göran Gustafsson prizes by the Swedish Academy of Science for his work on organic thermoelectrics. His research interest is the use of organic materials in energy devices: batteries, thermoelectrics, and fuel cells/electrolysers.

Simone Fabiano received his Ph.D. in Physical Chemistry from the University of Palermo (Italy) in 2012. From 2010 to 2012, he worked as a visiting researcher in the Zernike Institute for Advanced Materials at the University of Groningen (The Netherlands). He then carried out postdoctoral research at Linköping University (Sweden) in 2012 and Northwestern University (USA) in 2016. Since 2018, he is an Associate Professor at the Department of Science and Technology at Linköping University, guiding the Organic Nanoelectronics Group. He is a Docent in Applied Physics and founder and Chief Scientific Officer of n-Ink AB, a company developing n-type conductive inks. His research interests include developing organic (electronic and mixed ionic-electronic) conductors and integrating them into printed electronics and novel energy technologies.

ACKNOWLEDGMENTS

We authors at Linköping University thank the Knut and Alice Wallenberg foundation, the Swedish Research Council (2016-03979 and 2020-03243), ÅForsk (18-313 and 19-310), Olle Engkvists Stiftelse (204-0256), the European Commission through the Marie Sklodowska-Curie project HORATES (GA-955837), and the Swedish Government Strategic Research Area in Materials Science on Functional Materials at Linköping University (faculty grant SFO-Mat-LiU 2009-00971). This work was authored in part by the National Renewable Energy Laboratory, operated by Alliance for Sustainable Energy, LLC, for the U.S. Department of Energy (DOE) under contract no. DE-AC36-08GO28308. The views expressed in the article do not necessarily represent the views of the DOE or the U.S. Government.

REFERENCES

(1) *Data and Statistics*; International Energy Agency, 2021; https://www.iea.org/data-and-statistics?country=WORLD&fuel=Energy%20supply&indicator=TPESbySource (accessed 2021-06-30).
(2) *Renewable Energy*; Center for Climate and Energy Solutions, 2021; https://www.c2es.org/content/renewable-energy (accessed 2021-06-30).
(3) Chen, H. J.; Goswami, D. Y.; Stefanakos, E. K. A review of thermodynamic cycles and working fluids for the conversion of low-grade heat. *Renewable Sustainable Energy Rev.* **2010**, *14*, 3059.
(4) Pathak, S.; Shukla, S. A Review on the Performance of Organic Rankine Cycle with Different Heat Sources and Absorption Chillers. *Distrib. Gener. Altern. Energy J.* **2018**, *33*, 6.
(5) Poudel, B.; Hao, Q.; Ma, Y.; Lan, Y. C.; Minnich, A.; Yu, B.; Yan, X. A.; Wang, D. Z.; Muto, A.; Vashaee, D.; et al. High-thermoelectric performance of nanostructured bismuth antimony telluride bulk alloys. *Science* **2008**, *320*, 634.
(6) Kraemer, D.; Poudel, B.; Feng, H. P.; Caylor, J. C.; Yu, B.; Yan, X.; Ma, Y.; Wang, X. W.; Wang, D. Z.; Muto, A.; et al. High-performance flat-panel solar thermoelectric generators with high thermal concentration. *Nat. Mater.* **2011**, *10*, 532.
(7) Beretta, D.; Neophytou, N.; Hodges, J. M.; Kanatzidis, M. G.; Narducci, D.; Martin- Gonzalez, M.; Beekman, M.; Balke, B.; Cerretti, G.; Tremel, W.; et al. Thermoelectrics: From history, a window to the future. *Mater. Sci. Eng., R* **2019**, *138*, 100501.
(8) Vining, C. B. An inconvenient truth about thermoelectrics. *Nat. Mater.* **2009**, *8*, 83.
(9) Avery, A. D.; Zhou, B. H.; Lee, J.; Lee, E. S.; Miller, E. M.; Ihly, R.; Wesenberg, D.; Mistry, K. S.; Guillot, S. L.; Zink, B. L.; et al. Tailored semiconducting carbon nanotube networks with enhanced thermoelectric properties. *Nat. Energy* **2016**, *1*, 16033.
(10) Bubnova, O.; Khan, Z. U.; Malti, A.; Braun, S.; Fahlman, M.; Berggren, M.; Crispin, X. Optimization of the thermoelectric figure of merit in the conducting polymer poly(3,4-ethylenedioxythiophene). *Nat. Mater.* **2011**, *10*, 429.
(11) Yao, Q.; Chen, L. D.; Zhang, W. Q.; Liufu, S. C.; Chen, X. H. Enhanced Thermoelectric Performance of Single-Walled Carbon Nanotubes/Polyaniline Hybrid Nanocomposites. *ACS Nano* **2010**, *4*, 2445.
(12) Sher, I.; Levinzon-Sher, D.; Sher, E. Miniaturization limitations of HCCI internal combustion engines. *Appl. Therm. Eng.* **2009**, *29*, 400.
(13) Bottner, H.; Nurnus, J.; Gavrikov, A.; Kuhner, G.; Jagle, M.; Kunzel, C.; Eberhard, D.; Plescher, G.; Schubert, A.; Schlereth, K. H. New thermoelectric components using microsystem technologies. *J. Microelectromech. Syst.* **2004**, *13*, 414.
(14) Kim, Y. J.; Gu, H. M.; Kim, C. S.; Choi, H.; Lee, G.; Kim, S.; Yi, K. K.; Lee, S. G.; Cho, B. J. High-performance self-powered wireless sensor node driven by a flexible thermoelectric generator. *Energy* **2018**, *162*, 526.
(15) vom Boegel, G.; Meyer, F.; Kemmerling, M. Wireless Sensor System for Industrial Applications Powered by Thermoelectric Generator. In *Smart SysTech 2014, European Conference on Smart Objects, Systems and Technologies*, 2014; p 1.
(16) Yang, Y.; Wei, X. J.; Liu, J. Suitability of a thermoelectric power generator for implantable medical electronic devices. *J. Phys. D: Appl. Phys.* **2007**, *40*, 5790.
(17) Weber, J.; Potje-Kamloth, K.; Haase, F.; Detemple, P.; Völklein, F.; Doll, T. Coin-size coiled-up polymer foil thermoelectric power generator for wearable electronics. *Sens. Actuators, A* **2006**, *132*, 325.

https://doi.org/10.1021/acs.chemrev.1c00218
Chem. Rev. XXXX, XXX, XXX−XXX

(18) Kim, S. J.; We, J. H.; Cho, B. J. A wearable thermoelectric generator fabricated on a glass fabric. *Energy Environ. Sci.* **2014**, *7*, 1959.
(19) Jo, S. E.; Kim, M. K.; Kim, M. S.; Kim, Y. J. Flexible thermoelectric generator for human body heat energy harvesting. *Electron. Lett.* **2012**, *48*, 1015.
(20) Zhang, F. J.; Zang, Y. P.; Huang, D. Z.; Di, C. A.; Zhu, D. B. Flexible and self-powered temperature-pressure dual-parameter sensors using microstructure-frame-supported organic thermoelectric materials. *Nat. Commun.* **2015**, *6*, 8356.
(21) Wu, W.; Du, Z.; Cui, J.; Shi, Z.; Deng, Y. Thermoelectric Generator Used in Fire-Alarm Temperature Sensing. *J. Electron. Mater.* **2015**, *44*, 1851.
(22) Shi, Y.; Wang, Y.; Deng, Y.; Gao, H.; Lin, Z.; Zhu, W.; Ye, H. A novel self-powered wireless temperature sensor based on thermoelectric generators. *Energy Convers. Manage.* **2014**, *80*, 110.
(23) Yang, P.; Liu, K.; Chen, Q.; Mo, X.; Zhou, Y.; Li, S.; Feng, G.; Zhou, J. Wearable Thermocells Based on Gel Electrolytes for the Utilization of Body Heat. *Angew. Chem., Int. Ed.* **2016**, *55*, 12050.
(24) Zhao, D.; Wang, H.; Khan, Z. U.; Chen, J.; Gabrielsson, R.; Jonsson, M. P.; Berggren, M.; Crispin, X. Ionic thermoelectric supercapacitors. *Energy Environ. Sci.* **2016**, *9*, 1450.
(25) Wood, C. Materials for thermoelectric energy conversion. *Rep. Prog. Phys.* **1988**, *51*, 459.
(26) De Groot, S. R.; Mazur, P. *Non-equilibrium Thermodynamics*; Dover Publication Inc: NewYork, 1953.
(27) Simpkins, P. G.; Greenberg-Kosinski, S.; MacChesney, J. B. Thermophoresis: the mass transfer mechanism in modified chemical vapor deposition. *J. Appl. Phys.* **1979**, *50*, 5676.
(28) Stejskal, J.; Trchova, M.; Ananieva, I. A.; Janca, J.; Prokes, J.; Fedorova, S.; Sapurina, I. Poly(aniline-co-pyrrole): powders, films, and colloids. Thermophoretic mobility of colloidal particles. *Synth. Met.* **2004**, *146*, 29.
(29) Thamdrup, L. H.; Larsen, N. B.; Kristensen, A. Light-Induced Local Heating for Thermophoretic Manipulation of DNA in Polymer Micro- and Nanochannels. *Nano Lett.* **2010**, *10*, 826.
(30) Chapman, S.; Cowling, T. G. *The Mathematical Theory of Non-uniform Gases: An Account of the Kinetic Theory of Viscosity, Thermal Conduction and Diffusion in Gases*, 3rd ed.; Cambridge University Press, 1970.
(31) Wurger, A. Thermal non-equilibrium transport in colloids. *Rep. Prog. Phys.* **2010**, *73*, 126601.
(32) Ashcroft, N. W.; Mermin, N. D. *Solid State Physics*; Academic Press: New York, 1976.
(33) Goupil, C.; Seifert, W.; Zabrocki, K.; Müller, E.; Snyder, G. J. Thermodynamics of Thermoelectric Phenomena and Applications. *Entropy* **2011**, *13*, 1481.
(34) Zhu, T.; Liu, Y.; Fu, C.; Heremans, J. P.; Snyder, J. G.; Zhao, X. Compromise and Synergy in High-Efficiency Thermoelectric Materials. *Adv. Mater.* **2017**, *29*, 1605884.
(35) He, J.; Tritt, T. M. Advances in thermoelectric materials research: Looking back and moving forward. *Science* **2017**, *357*, eaak9997.
(36) Lu, N. D.; Li, L.; Liu, M. A review of carrier thermoelectric-transport theory in organic semiconductors. *Phys. Chem. Chem. Phys.* **2016**, *18*, 19503.
(37) Assael, M. J.; Goodwin, A. R.; Vesovic, V.; Wakeham, W. A. *Experimental Thermodynamics, Volume IX: Advances in Transport Properties of Fluids*; Royal Society of Chemistry, 2014.
(38) Agar, J. N.; Mou, C. Y.; Lin, J. L. Single-Ion Heat of Transport in Electrolyte-Solutions-a Hydrodynamic Theory. *J. Phys. Chem.* **1989**, *93*, 2079.
(39) Wurger, A. Transport in charged colloids driven by thermoelectricity. *Phys. Rev. Lett.* **2008**, *101*, 108302.
(40) Vigolo, D.; Buzzaccaro, S.; Piazza, R. Thermophoresis and Thermoelectricity in Surfactant Solutions. *Langmuir* **2010**, *26*, 7792.
(41) Eslahian, K. A.; Majee, A.; Maskos, M.; Wurger, A. Specific salt effects on thermophoresis of charged colloids. *Soft Matter* **2014**, *10*, 1931.
(42) Majee, A.; Würger, A. Thermocharge of a hot spot in an electrolyte solution. *Soft Matter* **2013**, *9*, 2145.
(43) Di Lecce, S.; Albrecht, T.; Bresme, F. The role of ion-water interactions in determining the Soret coefficient of LiCl aqueous solutions. *Phys. Chem. Chem. Phys.* **2017**, *19*, 9575.
(44) Di Lecce, S.; Bresme, F. Thermal Polarization of Water Influences the Thermoelectric Response of Aqueous Solutions. *J. Phys. Chem. B* **2018**, *122*, 1662.
(45) Würger, A. Thermopower of ionic conductors and ionic capacitors. *Phys. Rev. Res.* **2020**, *2*, No. 042030(R).
(46) Heikes, R. R.; Ure, R. W. *Thermoelectricity: Science and Engineering*; Interscience Publishers, University of Michigan, 1961.
(47) Liu, L.; Sun, Y.; Li, W.; Zhang, J.; Huang, X.; Chen, Z.; Sun, Y.; Di, C.; Xu, W.; Zhu, D. Flexible unipolar thermoelectric devices based on patterned poly[Kx(Ni-ethylenetetrathiolate)] thin films. *Mater. Chem. Front.* **2017**, *1*, 2111.
(48) Zheng, C.; Xiang, L.; Jin, W.; Shen, H.; Zhao, W.; Zhang, F.; Di, C.-A.; Zhu, D. A Flexible Self-Powered Sensing Element with Integrated Organic Thermoelectric Generator. *Adv. Mater. Technol.* **2019**, *4*, 1900247.
(49) Bubnova, O.; Crispin, X. Towards polymer-based organic thermoelectric generators. *Energy Environ. Sci.* **2012**, *5*, 9345.
(50) Sun, T.; Zhou, B.; Zheng, Q.; Wang, L.; Jiang, W.; Snyder, G. J. Stretchable fabric generates electric power from woven thermoelectric fibers. *Nat. Commun.* **2020**, *11*, 572.
(51) Chen, A.; Madan, D.; Wright, P. K.; Evans, J. W. Dispenser-printed planar thick-film thermoelectric energy generators. *J. Micromech. Microeng.* **2011**, *21*, 104006.
(52) Wijeratne, K. Conducting Polymer Electrodes for Thermogalvanic Cells. Doctoral dissertation. Linköping University Electronic Press: Linköping, Sweden, 2018.
(53) Mua, Y.; Quickenden, T. Power conversion efficiency, electrode separation, and overpotential in the ferricyanide/ferrocyanide thermogalvanic cell. *J. Electrochem. Soc.* **1996**, *143*, 2558.
(54) Salazar, P. F.; Kumar, S.; Cola, B. A. Nitrogen-and boron-doped carbon nanotube electrodes in a thermo-electrochemical cell. *J. Electrochem. Soc.* **2012**, *159*, B483.
(55) Abraham, T. J.; Tachikawa, N.; MacFarlane, D. R.; Pringle, J. M. Investigation of the kinetic and mass transport limitations in thermoelectrochemical cells with different electrode materials. *Phys. Chem. Chem. Phys.* **2014**, *16*, 2527.
(56) Dupont, M. F.; MacFarlane, D. R.; Pringle, J. M. Thermo-electrochemical cells for waste heat harvesting - progress and perspectives. *Chem. Commun.* **2017**, *53*, 6288.
(57) Romano, M. S.; Razal, J. M.; Antiohos, D.; Wallace, G.; Chen, J. Nano-Carbon Electrodes for Thermal Energy Harvesting. *J. Nanosci. Nanotechnol.* **2015**, *15*, 1.
(58) Romano, M. S.; Gambhir, S.; Razal, J. M.; Gestos, A.; Wallace, G. G.; Chen, J. Novel carbon materials for thermal energy harvesting. *J. Therm. Anal. Calorim.* **2012**, *109*, 1229.
(59) Quickenden, T.; Mua, Y. A review of power generation in aqueous thermogalvanic cells. *J. Electrochem. Soc.* **1995**, *142*, 3985.
(60) Quickenden, T.; Mua, Y. The power conversion efficiencies of a thermogalvanic cell operated in three different orientations. *J. Electrochem. Soc.* **1995**, *142*, 3652.
(61) Hu, R.; Cola, B. A.; Haram, N.; Barisci, J. N.; Lee, S.; Stoughton, S.; Wallace, G.; Too, C.; Thomas, M.; Gestos, A.; et al. Harvesting Waste Thermal Energy Using a Carbon-Nanotube-Based Thermo-Electrochemical Cell. *Nano Lett.* **2010**, *10*, 838.
(62) Romano, M. S.; Li, N.; Antiohos, D.; Razal, J. M.; Nattestad, A.; Beirne, S.; Fang, S.; Chen, Y.; Jalili, R.; Wallace, G. G.; et al. Carbon nanotube-reduced graphene oxide composites for thermal energy harvesting applications. *Adv. Mater.* **2013**, *25*, 6602.
(63) Im, H.; Kim, T.; Song, H.; Choi, J.; Park, J. S.; Ovalle-Robles, R.; Yang, H. D.; Kihm, K. D.; Baughman, R. H.; Lee, H. H.; et al. High-efficiency electrochemical thermal energy harvester using carbon nanotube aerogel sheet electrodes. *Nat. Commun.* **2016**, *7*, 10600.
(64) Wang, H.; Zhao, D.; Khan, Z. U.; Puzinas, S.; Jonsson, M. P.; Berggren, M.; Crispin, X. Ionic Thermoelectric Figure of Merit for Charging of Supercapacitors. *Adv. Electron. Mater.* **2017**, *3*, 1700013.

https://doi.org/10.1021/acs.chemrev.1c00218
Chem. Rev. XXXX, XXX, XXX−XXX

(65) Bonetti, M.; Nakamae, S.; Huang, B. T.; Salez, T. J.; Wiertel-Gasquet, C.; Roger, M. Thermoelectric energy recovery at ionic-liquid/electrode interface. *J. Chem. Phys.* **2015**, *142*, 244708.
(66) Kim, S. L.; Lin, H. T.; Yu, C. Thermally Chargeable Solid-State Supercapacitor. *Adv. Energy Mater.* **2016**, *6*, 1600546.
(67) Zhao, D.; Fabiano, S.; Berggren, M.; Crispin, X. Ionic thermoelectric gating organic transistors. *Nat. Commun.* **2017**, *8*, 14214.
(68) Lim, H.; Shi, Y.; Wang, M.; Qiao, Y. Effects of work function on thermal sensitivity of electrode potential. *Appl. Phys. Lett.* **2015**, *106*, 223901.
(69) Lim, H.; Lu, W. Y.; Chen, X.; Qiao, Y. Effects of ion concentration on thermally-chargeable double-layer supercapacitors. *Nanotechnology* **2013**, *24*, 465401.
(70) Lim, H.; Lu, W. Y.; Qiao, Y. Dependence on cation size of thermally induced capacitive effect of a nanoporous carbon. *Appl. Phys. Lett.* **2012**, *101*, 063902.
(71) Fujii, S.; Suzuki, Y.; Kawamata, J.; Tsunashima, R. Large in-plane/out-of-plane anisotropic conduction in PEDOT-based hybrid films: lamellar assemblies structured by mono-layered nanosheets. *J. Mater. Chem. C* **2015**, *3*, 7153.
(72) Lee, J. A.; Aliev, A. E.; Bykova, J. S.; de Andrade, M. J.; Kim, D.; Sim, H. J.; Lepro, X.; Zakhidov, A. A.; Lee, J. B.; Spinks, G. M.; et al. Woven-Yarn Thermoelectric Textiles. *Adv. Mater.* **2016**, *28*, 5038.
(73) Rojas, J. P.; Singh, D.; Inayat, S. B.; Sevilla, G. A. T.; Fahad, H. M.; Hussain, M. M. Micro and Nano-Engineering Enabled New Generation of Thermoelectric Generator Devices and Applications. *ECS J. Solid State Sci. Technol.* **2017**, *6*, N3036.
(74) Park, Y. W. Structure and Morphology-Relation to Thermopower Properties of Conductive Polymers. *Synth. Met.* **1991**, *45*, 173.
(75) Bubnova, O.; Khan, Z. U.; Wang, H.; Braun, S.; Evans, D. R.; Fabretto, M.; Hojati-Talemi, P.; Dagnelund, D.; Arlin, J. B.; Geerts, Y. H.; et al. Semi-metallic polymers. *Nat. Mater.* **2014**, *13*, 190.
(76) Park, T.; Park, C.; Kim, B.; Shin, H.; Kim, E. Flexible PEDOT electrodes with large thermoelectric power factors to generate electricity by the touch of fingertips. *Energy Environ. Sci.* **2013**, *6*, 788.
(77) Culebras, M.; Gomez, C. M.; Cantarero, A. Enhanced thermoelectric performance of PEDOT with different counter-ions optimized by chemical reduction. *J. Mater. Chem. A* **2014**, *2*, 10109.
(78) Kim, B.; Shin, H.; Park, T.; Lim, H.; Kim, E. NIR-Sensitive Poly(3,4-ethylenedioxyselenophene) Derivatives for Transparent Photo-Thermo-Electric Converters. *Adv. Mater.* **2013**, *25*, 5483.
(79) Kim, G. H.; Shao, L.; Zhang, K.; Pipe, K. P. Engineered doping of organic semiconductors for enhanced thermoelectric efficiency. *Nat. Mater.* **2013**, *12*, 719.
(80) Lee, S. H.; Park, H.; Kim, S.; Son, W.; Cheong, I. W.; Kim, J. H. Transparent and flexible organic semiconductor nanofilms with enhanced thermoelectric efficiency. *J. Mater. Chem. A* **2014**, *2*, 7288.
(81) See, K. C.; Feser, J. P.; Chen, C. E.; Majumdar, A.; Urban, J. J.; Segalman, R. A. Water-Processable Polymer-Nanocrystal Hybrids for Thermoelectrics. *Nano Lett.* **2010**, *10*, 4664.
(82) Villalva, D. R.; Haque, M. A.; Nugraha, M. I.; Baran, D. Enhanced Thermoelectric Performance and Lifetime in Acid-Doped PEDOT:PSS Films Via Work Function Modification. *ACS Appl. Energy Mater.* **2020**, *3*, 9126.
(83) Wang, L.; Zhang, Z.; Liu, Y.; Wang, B.; Fang, L.; Qiu, J.; Zhang, K.; Wang, S. Exceptional thermoelectric properties of flexible organic-inorganic hybrids with monodispersed and periodic nanophase. *Nat. Commun.* **2018**, *9*, 3817.
(84) Qu, S. Y.; Yao, Q.; Wang, L. M.; Chen, Z. H.; Xu, K. Q.; Zeng, H. R.; Shi, W.; Zhang, T. S.; Uher, C.; Chen, L. D. Highly anisotropic P3HT films with enhanced thermoelectric performance via organic small molecule epitaxy. *NPG Asia Mater.* **2016**, *8*, No. e292.
(85) Untilova, V.; Hynynen, J.; Hofmann, A. I.; Scheunemann, D.; Zhang, Y.; Barlow, S.; Kemerink, M.; Marder, S. R.; Biniek, L.; Müller, C.; et al. High Thermoelectric Power Factor of Poly(3-hexylthiophene) through In-Plane Alignment and Doping with a Molybdenum Dithiolene Complex. *Macromolecules* **2020**, *53*, 6314.
(86) Hiroshige, Y.; Ookawa, M.; Toshima, N. Thermoelectric figure-of-merit of iodine-doped copolymer of phenylenevinylene with dialkoxyphenylenevinylene. *Synth. Met.* **2007**, *157*, 467.
(87) Kiyota, Y.; Kadoya, T.; Yamamoto, K.; Iijima, K.; Higashino, T.; Kawamoto, T.; Takimiya, K.; Mori, T. Benzothienobenzothiophene-Based Molecular Conductors: High Conductivity, Large Thermoelectric Power Factor, and One-Dimensional Instability. *J. Am. Chem. Soc.* **2016**, *138*, 3920.
(88) Patel, S. N.; Glaudell, A. M.; Peterson, K. A.; Thomas, E. M.; O'Hara, K. A.; Lim, E.; Chabinyc, M. L. Morphology controls the thermoelectric power factor of a doped semiconducting polymer. *Sci. Adv.* **2017**, *3*, No. e1700434.
(89) Vijayakumar, V.; Zhong, Y.; Untilova, V.; Bahri, M.; Herrmann, L.; Biniek, L.; Leclerc, N.; Brinkmann, M. Bringing Conducting Polymers to High Order: Toward Conductivities beyond 105 S cm-1 and Thermoelectric Power Factors of 2 mW m-1 K-2. *Adv. Energy Mater.* **2019**, *9*, 1900266.
(90) Wang, Y.; Zhang, S. M.; Deng, Y. Flexible low-grade energy utilization devices based on high-performance thermoelectric polyaniline/tellurium nanorod hybrid films. *J. Mater. Chem. A* **2016**, *4*, 3554.
(91) Li, H.; Song, J.; Xiao, J.; Wu, L.; Katz, H. E.; Chen, L. Synergistically Improved Molecular Doping and Carrier Mobility by Copolymerization of Donor-Acceptor and Donor-Donor Building Blocks for Thermoelectric Application. *Adv. Funct. Mater.* **2020**, *30*, 2004378.
(92) Sun, Y. M.; Sheng, P.; Di, C. A.; Jiao, F.; Xu, W.; Qiu, D.; Zhu, D. B. Organic Thermoelectric Materials and Devices Based on p- and n-Type Poly(metal 1,1,2,2-ethenetetrathiolate)s. *Adv. Mater.* **2012**, *24*, 932.
(93) Sun, Y. H.; Qiu, L.; Tang, L. P.; Geng, H.; Wang, H. F.; Zhang, F. J.; Huang, D. Z.; Xu, W.; Yue, P.; Guan, Y. S.; et al. Flexible n-Type High-Performance Thermoelectric Thin Films of Poly(nickel-ethylenetetrathiolate) Prepared by an Electrochemical Method. *Adv. Mater.* **2016**, *28*, 3351.
(94) Chen, Y. N.; He, M. H.; Liu, B.; Bazan, G. C.; Zhou, J.; Liang, Z. Q. Bendable n-Type Metallic Nanocomposites with Large Thermoelectric Power Factor. *Adv. Mater.* **2017**, *29*, 1604752.
(95) Liu, J.; van der Zee, B.; Alessandri, R.; Sami, S.; Dong, J.; Nugraha, M. I.; Barker, A. J.; Rousseva, S.; Qiu, L.; Qiu, X.; et al. N-type organic thermoelectrics: demonstration of ZT > 0.3. *Nat. Commun.* **2020**, *11*, 5694.
(96) Lu, Y.; Yu, Z.-D.; Liu, Y.; Ding, Y.-F.; Yang, C.-Y.; Yao, Z.-F.; Wang, Z.-Y.; You, H.-Y.; Cheng, X.-F.; Tang, B.; et al. The Critical Role of Dopant Cations in Electrical Conductivity and Thermoelectric Performance of n-Doped Polymers. *J. Am. Chem. Soc.* **2020**, *142*, 15340.
(97) Yang, C.-Y.; Ding, Y.-F.; Huang, D.; Wang, J.; Yao, Z.-F.; Huang, C.-X.; Lu, Y.; Un, H.-I.; Zhuang, F.-D.; Dou, J.-H.; et al. A thermally activated and highly miscible dopant for n-type organic thermoelectrics. *Nat. Commun.* **2020**, *11*, 3292.
(98) Huang, D. Z.; Wang, C.; Zou, Y.; Shen, X. X.; Zang, Y. P.; Shen, H. G.; Gao, X. K.; Yi, Y. P.; Xu, W.; Di, C. A.; et al. Bismuth Interfacial Doping of Organic Small Molecules for High Performance n-type Thermoelectric Materials. *Angew. Chem., Int. Ed.* **2016**, *55*, 10672.
(99) Huang, D.; Yao, H.; Cui, Y.; Zou, Y.; Zhang, F.; Wang, C.; Shen, H.; Jin, W.; Zhu, J.; Diao, Y.; et al. Conjugated-Backbone Effect of Organic Small Molecules for n-Type Thermoelectric Materials with ZT over 0.2. *J. Am. Chem. Soc.* **2017**, *139*, 13013.
(100) McCullough, R. D. The chemistry of conducting polythiophenes. *Adv. Mater.* **1998**, *10*, 93.
(101) Groenendaal, B. L.; Jonas, F.; Freitag, D.; Pielartzik, H.; Reynolds, J. R. Poly(3,4-ethylenedioxythiophene) and its derivatives: Past, present, and future. *Adv. Mater.* **2000**, *12*, 481.
(102) Zaumseil, J.; Sirringhaus, H. Electron and ambipolar transport in organic field-effect transistors. *Chem. Rev.* **2007**, *107*, 1296.
(103) Wu, W. P.; Liu, Y. Q.; Zhu, D. B. pi-Conjugated molecules with fused rings for organic field-effect transistors: design, synthesis and applications. *Chem. Soc. Rev.* **2010**, *39*, 1489.
(104) Sekitani, T.; Nakajima, H.; Maeda, H.; Fukushima, T.; Aida, T.; Hata, K.; Someya, T. Stretchable active-matrix organic light-emitting

https://doi.org/10.1021/acs.chemrev.1c00218
Chem. Rev. XXXX, XXX, XXX−XXX

diode display using printable elastic conductors. *Nat. Mater.* **2009**, *8*, 494.
(105) Gunes, S.; Neugebauer, H.; Sariciftci, N. S. Conjugated polymer-based organic solar cells. *Chem. Rev.* **2007**, *107*, 1324.
(106) Dong, H. L.; Wang, C. L.; Hu, W. P. High performance organic semiconductors for field-effect transistors. *Chem. Commun.* **2010**, *46*, 5211.
(107) Su, W. P.; Schrieffer, J. R.; Heeger, A. J. Soliton excitations in polyacetylene. *Phys. Rev. B: Condens. Matter Mater. Phys.* **1980**, *22*, 2099.
(108) Shirakawa, H.; Louis, E. J.; MacDiarmid, A. G.; Chiang, C. K.; Heeger, A. J. Synthesis of electrically conducting organic polymers: halogen derivatives of polyacetylene, (CH). *J. Chem. Soc., Chem. Commun.* **1977**, *1977*, 578.
(109) Chiang, C. K.; Fincher, C. R.; Park, Y. W.; Heeger, A. J.; Shirakawa, H.; Louis, E. J.; Gau, S. C.; MacDiarmid, A. G. Electrical Conductivity in Doped Polyacetylene. *Phys. Rev. Lett.* **1977**, *39*, 1098.
(110) Diaz, A. F.; Castillo, J. I.; Logan, J. A.; Lee, W.-Y. Electrochemistry of conducting polypyrrole films. *J. Electroanal. Chem. Interfacial Electrochem.* **1981**, *129*, 115.
(111) MacDiarmid, A. G.; Epstein, A. J. Polyanilines: a novel class of conducting polymers. *Faraday Discuss. Chem. Soc.* **1989**, *88*, 317.
(112) Sirringhaus, H.; Brown, P. J.; Friend, R. H.; Nielsen, M. M.; Bechgaard, K.; Langeveld-Voss, B. M. W.; Spiering, A. J. H.; Janssen, R. A. J.; Meijer, E. W.; Herwig, P.; et al. Two-dimensional charge transport in self-organized, high-mobility conjugated polymers. *Nature* **1999**, *401*, 685.
(113) Noriega, R.; Rivnay, J.; Vandewal, K.; Koch, F. P. V.; Stingelin, N.; Smith, P.; Toney, M. F.; Salleo, A. A general relationship between disorder, aggregation and charge transport in conjugated polymers. *Nat. Mater.* **2013**, *12*, 1038.
(114) Park, Y. W.; Heeger, A. J.; Druy, M. A.; Macdiarmid, A. G. Electrical Transport in Doped Polyacetylene. *J. Chem. Phys.* **1980**, *73*, 946.
(115) Park, Y. W.; Yoon, C. O.; Lee, C. H.; Shirakawa, H.; Suezaki, Y.; Akagi, K. Conductivity and Thermoelectric-Power of the Newly Processed Polyacetylene. *Synth. Met.* **1989**, *28*, D27.
(116) Kaneko, H.; Ishiguro, T.; Takahashi, A.; Tsukamoto, J. Magnetoresistance and Thermoelectric-Power Studies of Metal-Nonmetal Transition in Iodine-Doped Polyacetylene. *Synth. Met.* **1993**, *57*, 4900.
(117) Bubnova, O.; Berggren, M.; Crispin, X. Tuning the Thermoelectric Properties of Conducting Polymers in an Electrochemical Transistor. *J. Am. Chem. Soc.* **2012**, *134*, 16456.
(118) Shi, W.; Zhao, T. Q.; Xi, J. Y.; Wang, D.; Shuai, Z. G. Unravelling Doping Effects on PEDOT at the Molecular Level: From Geometry to Thermoelectric Transport Properties. *J. Am. Chem. Soc.* **2015**, *137*, 12929.
(119) Yue, R. R.; Xu, J. K. Poly(3,4-ethylenedioxythiophene) as promising organic thermoelectric materials: A mini-review. *Synth. Met.* **2012**, *162*, 912.
(120) Shi, H.; Liu, C. C.; Jiang, Q. L.; Xu, J. K. Effective Approaches to Improve the Electrical Conductivity of PEDOT:PSS: A Review. *Adv. Electron. Mater.* **2015**, *1*, 1500017.
(121) Sun, K.; Zhang, S. P.; Li, P. C.; Xia, Y. J.; Zhang, X.; Du, D. H.; Isikgor, F. H.; Ouyang, J. Y. Review on application of PEDOTs and PEDOT: PSS in energy conversion and storage devices. *J. Mater. Sci.: Mater. Electron.* **2015**, *26*, 4438.
(122) Wei, Q. S.; Mukaida, M.; Kirihara, K.; Naitoh, Y.; Ishida, T. Recent Progress on PEDOT-Based Thermoelectric Materials. *Materials* **2015**, *8*, 732.
(123) Li, Y. Y.; Du, Y.; Dou, Y. C.; Cai, K. F.; Xu, J. Y. PEDOT-based thermoelectric nanocomposites - A mini-review. *Synth. Met.* **2017**, *226*, 119.
(124) Scheunemann, D.; Vijayakumar, V.; Zeng, H.; Durand, P.; Leclerc, N.; Brinkmann, M.; Kemerink, M. Rubbing and Drawing: Generic Ways to Improve the Thermoelectric Power Factor of Organic Semiconductors? *Adv. Electron. Mater.* **2020**, *6*, 2000218.
(125) Lim, E.; Glaudell, A. M.; Miller, R.; Chabinyc, M. L. The Role of Ordering on the Thermoelectric Properties of Blends of Regioregular and Regiorandom Poly(3-hexylthiophene). *Adv. Electron. Mater.* **2019**, *5*, 1800915.
(126) Hynynen, J.; Kiefer, D.; Müller, C. Influence of crystallinity on the thermoelectric power factor of P3HT vapour-doped with F4TCNQ. *RSC Adv.* **2018**, *8*, 1593.
(127) Vijayakumar, V.; Durand, P.; Zeng, H.; Untilova, V.; Herrmann, L.; Algayer, P.; Leclerc, N.; Brinkmann, M. Influence of dopant size and doping method on the structure and thermoelectric properties of PBTTT films doped with F6TCNNQ and F4TCNQ. *J. Mater. Chem. C* **2020**, *8*, 16470.
(128) Patel, S. N.; Glaudell, A. M.; Peterson, K. A.; Thomas, E. M.; O'Hara, K. A.; Lim, E.; Chabinyc, M. L. Morphology controls the thermoelectric power factor of a doped semiconducting polymer. *Sci. Adv.* **2017**, *3*, No. e1700434.
(129) Wang, L. M.; Yao, Q.; Xiao, J. X.; Zeng, K. Y.; Shi, W.; Qu, S. Y.; Chen, L. D. Enhanced Thermoelectric Properties of Polyaniline Nanofilms Induced by Self-Assembled Supramolecules. *Chem. - Asian J.* **2016**, *11*, 1955.
(130) Kee, S.; Haque, M. A.; Corzo, D.; Alshareef, H. N.; Baran, D. Self-Healing and Stretchable 3D-Printed Organic Thermoelectrics. *Adv. Funct. Mater.* **2019**, *29*, 1905426.
(131) Kee, S.; Kim, H.; Paleti, S. H. K.; El Labban, A.; Neophytou, M.; Emwas, A.-H.; Alshareef, H. N.; Baran, D. Highly Stretchable and Air-Stable PEDOT:PSS/Ionic Liquid Composites for Efficient Organic Thermoelectrics. *Chem. Mater.* **2019**, *31*, 3519.
(132) Kim, N.; Lienemann, S.; Petsagkourakis, I.; Alemu Mengistie, D.; Kee, S.; Ederth, T.; Gueskine, V.; Leclère, P.; Lazzaroni, R.; Crispin, X.; Tybrandt, K. Elastic conducting polymer composites in thermoelectric modules. *Nat. Commun.* **2020**, *11*, 1424.
(133) Sun, Y. M.; Wei, Z. M.; Xu, W.; Zhu, D. B. A three-in-one improvement in thermoelectric properties of polyaniline brought by nanostructures. *Synth. Met.* **2010**, *160*, 2371.
(134) Wu, J. S.; Sun, Y. M.; Pei, W. B.; Huang, L.; Xu, W.; Zhang, Q. C. Polypyrrole nanotube film for flexible thermoelectric application. *Synth. Met.* **2014**, *196*, 173.
(135) Lee, H. J.; Anoop, G.; Lee, H. J.; Kim, C.; Park, J. W.; Choi, J.; Kim, H.; Kim, Y. J.; Lee, E.; Lee, S. G.; et al. Enhanced thermoelectric performance of PEDOT: PSS/PANI-CSA polymer multilayer structures. *Energy Environ. Sci.* **2016**, *9*, 2806.
(136) Lu, G. H.; Bu, L. J.; Li, S. J.; Yang, X. N. Bulk Interpenetration Network of Thermoelectric Polymer in Insulating Supporting Matrix. *Adv. Mater.* **2014**, *26*, 2359.
(137) Kim, Y.; Lund, A.; Noh, H.; Hofmann, A. I.; Craighero, M.; Darabi, S.; Zokaei, S.; Park, J. I.; Yoon, M.-H.; Müller, C. Robust PEDOT:PSS Wet-Spun Fibers for Thermoelectric Textiles. *Macromol. Mater. Eng.* **2020**, *305*, 1900749.
(138) Lund, A.; Tian, Y.; Darabi, S.; Müller, C. A polymer-based textile thermoelectric generator for wearable energy harvesting. *J. Power Sources* **2020**, *480*, 228836.
(139) Coates, N. E.; Yee, S. K.; McCulloch, B.; See, K. C.; Majumdar, A.; Segalman, R. A.; Urban, J. J. Effect of Interfacial Properties on Polymer-Nanocrystal Thermoelectric Transport. *Adv. Mater.* **2013**, *25*, 1629.
(140) Zaia, E. W.; Sahu, A.; Zhou, P.; Gordon, M. P.; Forster, J. D.; Aloni, S.; Liu, Y. S.; Guo, J. H.; Urban, J. J. Carrier Scattering at Alloy Nanointerfaces Enhances Power Factor in PEDOT:PSS Hybrid Thermoelectrics. *Nano Lett.* **2016**, *16*, 3352.
(141) Zhang, B.; Sun, J.; Katz, H. E.; Fang, F.; Opila, R. L. Promising Thermoelectric Properties of Commercial PEDOT:PSS Materials and Their Bi2Te3 Powder Composites. *ACS Appl. Mater. Interfaces* **2010**, *2*, 3170.
(142) He, M.; Ge, J.; Lin, Z. Q.; Feng, X. H.; Wang, X. W.; Lu, H. B.; Yang, Y. L.; Qiu, F. Thermopower enhancement in conducting polymer nanocomposites via carrier energy scattering at the organic-inorganic semiconductor interface. *Energy Environ. Sci.* **2012**, *5*, 8351.
(143) Levesque, I.; Bertrand, P. O.; Blouin, N.; Leclerc, M.; Zecchin, S.; Zotti, G.; Ratcliffe, C. I.; Klug, D. D.; Gao, X.; Gao, F. M.; et al.

https://doi.org/10.1021/acs.chemrev.1c00218
Chem. Rev. XXXX, XXX, XXX−XXX

Synthesis and thermoelectric properties of polycarbazole, polyindolocarbazole, and polydiindolocarbazole derivatives. *Chem. Mater.* **2007**, *19*, 2128.
(144) Aich, R. B.; Blouin, N.; Bouchard, A.; Leclerc, M. Electrical and Thermoelectric Properties of Poly(2,7-Carbazole) Derivatives. *Chem. Mater.* **2009**, *21*, 751.
(145) Murase, I.; Ohnishi, T.; Noguchi, T.; Hirooka, M. Alkoxy-substituent effect of poly (p-phenylene vinylene) conductivity. *Polym. Comm.* **1985**, *26*, 362.
(146) Hiroshige, Y.; Ookawa, M.; Toshima, N. High thermoelectric performance of poly(2,5-dimethoxyphenylenevinylene) and its derivatives. *Synth. Met.* **2006**, *156*, 1341.
(147) Li, H.; Liu, F.; Wang, X.; Gu, C.; Wang, P.; Fu, H. Diketopyrrolopyrrole-Thiophene-Benzothiadiazole Random Copolymers: An Effective Strategy To Adjust Thin-Film Crystallinity for Transistor and Photovoltaic Properties. *Macromolecules* **2013**, *46*, 9211.
(148) Scholes, D. T.; Yee, P. Y.; McKeown, G. R.; Li, S.; Kang, H.; Lindemuth, J. R.; Xia, X.; King, S. C.; Seferos, D. S.; Tolbert, S. H.; et al. Designing Conjugated Polymers for Molecular Doping: The Roles of Crystallinity, Swelling, and Conductivity in Sequentially-Doped Selenophene-Based Copolymers. *Chem. Mater.* **2019**, *31*, 73.
(149) Zuo, G. Z.; Liu, X. J.; Fahlman, M.; Kemerink, M. High Seebeck Coefficient in Mixtures of Conjugated Polymers. *Adv. Funct. Mater.* **2018**, *28*, 1703280.
(150) Mahan, G.; Sofo, J. The best thermoelectric. *Proc. Natl. Acad. Sci. U. S. A.* **1996**, *93*, 7436.
(151) Sun, J.; Yeh, M. L.; Jung, B. J.; Zhang, B.; Feser, J.; Majumdar, A.; Katz, H. E. Simultaneous Increase in Seebeck Coefficient and Conductivity in a Doped Poly(alkylthiophene) Blend with Defined Density of States. *Macromolecules* **2010**, *43*, 2897.
(152) Li, H.; Plunkett, E.; Cai, Z.; Qiu, B.; Wei, T.; Chen, H.; Thon, S. M.; Reich, D. H.; Chen, L.; Katz, H. E. Dopant-Dependent Increase in Seebeck Coefficient and Electrical Conductivity in Blended Polymers with Offset Carrier Energies. *Adv. Electron. Mater.* **2019**, *5*, 1800618.
(153) Zuo, G.; Abdalla, H.; Kemerink, M. Conjugated Polymer Blends for Organic Thermoelectrics. *Adv. Electron. Mater.* **2019**, *5*, 1800821.
(154) Kim, J.-Y.; Kim, J.-T.; Kwon, M.-H.; Han, D.-K.; Kwon, S.-J. ATR-infrared spectroscopic study of n-doped polyacetylene films. *Macromol. Res.* **2007**, *15*, 5.
(155) Hua, M. Y.; Hwang, G. W.; Chuang, Y. H.; Chen, S. A.; Tsai, R. Y. Soluble n-doped polyaniline: Synthesis and characterization. *Macromolecules* **2000**, *33*, 6235.
(156) Schlitz, R. A.; Brunetti, F. G.; Glaudell, A. M.; Miller, P. L.; Brady, M. A.; Takacs, C. J.; Hawker, C. J.; Chabinyc, M. L. Solubility-Limited Extrinsic n-Type Doping of a High Electron Mobility Polymer for Thermoelectric Applications. *Adv. Mater.* **2014**, *26*, 2825.
(157) Wei, P.; Oh, J. H.; Dong, G. F.; Bao, Z. N. Use of a 1H-Benzoimidazole Derivative as an n-Type Dopant and To Enable Air-Stable Solution-Processed n-Channel Organic Thin-Film Transistors. *J. Am. Chem. Soc.* **2010**, *132*, 8852.
(158) Kiefer, D.; Giovannitti, A.; Sun, H. D.; Biskup, T.; Hofmann, A.; Koopmans, M.; Cendra, C.; Weber, S.; Koster, L. J. A.; Olsson, E.; et al. Enhanced n-Doping Efficiency of a Naphthalenediimide-Based Copolymer through Polar Side Chains for Organic Thermoelectrics. *ACS Energy Lett.* **2018**, *3*, 278.
(159) Liu, J.; Qiu, L.; Alessandri, R.; Qiu, X. K.; Portale, G.; Dong, J. J.; Talsma, W.; Ye, G.; Sengrian, A. A.; Souza, P. C. T.; et al. Enhancing Molecular n-Type Doping of Donor-Acceptor Copolymers by Tailoring Side Chains. *Adv. Mater.* **2018**, *30*, 1704630.
(160) Wang, S. H.; Sun, H. D.; Ail, U.; Vagin, M.; Persson, P. O. A.; Andreasen, J. W.; Thiel, W.; Berggren, M.; Crispin, X.; Fazzi, D.; et al. Thermoelectric Properties of Solution-Processed n-Doped Ladder-Type Conducting Polymers. *Adv. Mater.* **2016**, *28*, 10764.
(161) Wang, S.; Ruoko, T.-P.; Wang, G.; Riera-Galindo, S.; Hultmark, S.; Puttisong, Y.; Moro, F.; Yan, H.; Chen, W. M.; Berggren, M.; et al. Sequential Doping of Ladder-Type Conjugated Polymers for Thermally Stable n-Type Organic Conductors. *ACS Appl. Mater. Interfaces* **2020**, *12*, 53003.
(162) Nava, D.; Shin, Y.; Massetti, M.; Jiao, X. C.; Biskup, T.; Jagadeesh, M. S.; Calloni, A.; Duo, L.; Lanzani, G.; McNeill, C. R.; et al. Drastic Improvement of Air Stability in an n-Type Doped Naphthalene-Diimide Polymer by Thionation. *ACS Appl. Energy Mater.* **2018**, *1*, 4626.
(163) Zhan, X.; Facchetti, A.; Barlow, S.; Marks, T. J.; Ratner, M. A.; Wasielewski, M. R.; Marder, S. R. Rylene and Related Diimides for Organic Electronics. *Adv. Mater.* **2011**, *23*, 268.
(164) Shin, Y.; Massetti, M.; Komber, H.; Biskup, T.; Nava, D.; Lanzani, G.; Caironi, M.; Sommer, M. Improving Miscibility of a Naphthalene Diimide-Bithiophene Copolymer with n-Type Dopants through the Incorporation of "Kinked" Monomers. *Adv. Electron. Mater.* **2018**, *4*, 1700581.
(165) Naab, B. D.; Gu, X. D.; Kurosawa, T.; To, J. W. F.; Salleo, A.; Bao, Z. A. Role of Polymer Structure on the Conductivity of N-Doped Polymers. *Adv. Electron. Mater.* **2016**, *2*, 1600004.
(166) Shi, K.; Zhang, F. J.; Di, C. A.; Yan, T. W.; Zou, Y.; Zhou, X.; Zhu, D. B.; Wang, J. Y.; Pei, J. Toward High Performance n-Type Thermoelectric Materials by Rational Modification of BDPPV Backbones. *J. Am. Chem. Soc.* **2015**, *137*, 6979.
(167) Zhao, X.; Madan, D.; Cheng, Y.; Zhou, J.; Li, H.; Thon, S. M.; Bragg, A. E.; DeCoster, M. E.; Hopkins, P. E.; Katz, H. E. High Conductivity and Electron-Transfer Validation in an n-Type Fluoride-Anion-Doped Polymer for Thermoelectrics in Air. *Adv. Mater.* **2017**, *29*, 1606928.
(168) Han, J.; Fan, H.; Zhang, Q.; Hu, Q.; Russell, T. P.; Katz, H. E. Dichlorinated Dithienylethene-Based Copolymers for Air-Stable n-Type Conductivity and Thermoelectricity. *Adv. Funct. Mater.* **2021**, *31*, 2005901.
(169) Yang, C.-Y.; Stoeckel, M.-A.; Ruoko, T.-P.; Wu, H.-Y.; Liu, X.; Kolhe, N. B.; Wu, Z.; Puttisong, Y.; Musumeci, C.; Massetti, M.; et al. A high-conductivity n-type polymeric ink for printed electronics. *Nat. Commun.* **2021**, *12*, 2354.
(170) Jiao, F.; Di, C.-A.; Sun, Y.; Sheng, P.; Xu, W.; Zhu, D. Inkjet-printed flexible organic thin-film thermoelectric devices based on p- and n-type poly(metal 1,1,2,2-ethenetetrathiolate)s/polymer composites through ball-milling. *Philos. Trans. R. Soc., A* **2014**, *372*, 20130008.
(171) Menon, A. K.; Wolfe, R. M. W.; Marder, S. R.; Reynolds, J. R.; Yee, S. K. Systematic Power Factor Enhancement in n-Type NiETT/PVDF Composite Films. *Adv. Funct. Mater.* **2018**, *28*, 1801620.
(172) Wolfe, R. M. W.; Menon, A. K.; Fletcher, T. R.; Marder, S. R.; Reynolds, J. R.; Yee, S. K. Simultaneous Enhancement in Electrical Conductivity and Thermopower of n-Type NiETT/PVDF Composite Films by Annealing. *Adv. Funct. Mater.* **2018**, *28*, 1803275.
(173) Saglio, B.; Mura, M.; Massetti, M.; Scuratti, F.; Beretta, D.; Jiao, X.; McNeill, C. R.; Sommer, M.; Famulari, A.; Lanzani, G.; et al. N-Alkyl substituted 1H-benzimidazoles as improved n-type dopants for a naphthalene-diimide based copolymer. *J. Mater. Chem. A* **2018**, *6*, 15294.
(174) Chen, J. M.; Wang, D.; Shuai, Z. G. First-Principles Predictions of Thermoelectric Figure of Merit for Organic Materials: Deformation Potential Approximation. *J. Chem. Theory Comput.* **2012**, *8*, 3338.
(175) Kwak, J. F.; Chaikin, P. M.; Russel, A. A.; Garito, A. F.; Heeger, A. J. Anisotropic Thermoelectric-Power of TTF-TCNQ. *Solid State Commun.* **1975**, *16*, 729.
(176) Zhang, Q.; Sun, Y. M.; Xu, W.; Zhu, D. B. Organic Thermoelectric Materials: Emerging Green Energy Materials Converting Heat to Electricity Directly and Efficiently. *Adv. Mater.* **2014**, *26*, 6829.
(177) Itahara, H.; Maesato, M.; Asahi, R.; Yamochi, H.; Saito, G. Thermoelectric Properties of Organic Charge-Transfer Compounds. *J. Electron. Mater.* **2009**, *38*, 1171.
(178) Oyama, M.; Wei, Q. S.; Mukaida, M.; Kawanishi, Y.; Ishida, T. Electrical conduction and thermoelectric properties of tetrathiafulvalene-tetracyanoquinodimethane cast films prepared with N,N-dimethylacetamide. *Synth. Met.* **2017**, *230*, 12.
(179) Sato, R.; Kiyota, Y.; Kadoya, T.; Kawamoto, T.; Mori, T. Thermoelectric power of oriented thin-film organic conductors. *RSC Adv.* **2016**, *6*, 41040.

https://doi.org/10.1021/acs.chemrev.1c00218
Chem. Rev. XXXX, XXX, XXX−XXX

(180) Pudzs, K.; Vembris, A.; Rutkis, M.; Woodward, S. Thin Film Organic Thermoelectric Generator Based on Tetrathiotetracene. *Adv. Electron. Mater.* **2017**, *3*, 1600429.
(181) Sun, Y. M.; Xu, W.; Di, C. A.; Zhu, D. B. Metal-organic complexes-towards promising organic thermoelectric materials. *Synth. Met.* **2017**, *225*, 22.
(182) Rincon-Garcia, L.; Ismael, A. K.; Evangeli, C.; Grace, I.; Rubio-Bollinger, G.; Porfyrakis, K.; Agrait, N.; Lambert, C. J. Molecular design and control of fullerene-based bi-thermoelectric materials. *Nat. Mater.* **2016**, *15*, 289.
(183) Kojima, H.; Abe, R.; Ito, M.; Tomatsu, Y.; Fujiwara, F.; Matsubara, R.; Yoshimoto, N.; Nakamura, M. Giant Seebeck effect in pure fullerene thin films. *Appl. Phys. Express* **2015**, *8*, 121301.
(184) Park, E. B.; Shim, J. W.; Choi, H. J.; Park, Y. W. Anomalous Thermoelectric-Power of the Alkali-Metal Doped and the Pyrolyzed Fullerene. *Synth. Met.* **1993**, *56*, 3258.
(185) Tang, J. K.; Chepko, C.; Wang, W. D.; Wang, X. J.; Zhao, G. L. Crossover Behavior of Variable Range Hopping in Bi-Doped C-60. *J. Supercond. Novel Magn.* **2010**, *23*, 873.
(186) Barbot, A.; Di Bin, C.; Lucas, B.; Ratier, B.; Aldissi, M. N-type doping and thermoelectric properties of co-sublimed cesium-carbonate-doped fullerene. *J. Mater. Sci.* **2013**, *48*, 2785.
(187) Almutlaq, N.; Al-Galiby, Q.; Bailey, S.; Lambert, C. J. Identification of a positive-Seebeck-coefficient exohedral fullerene. *Nanoscale* **2016**, *8*, 13597.
(188) Hayashi, K.; Shinano, T.; Miyazaki, Y.; Kajitani, T. Fabrication of iodine-doped pentacene thin films for organic thermoelectric devices. *J. Appl. Phys.* **2011**, *109*, 023712.
(189) Liu, J.; Qiu, L.; Portale, G.; Koopmans, M.; Ten Brink, G.; Hummelen, J. C.; Koster, L. J. A. N-Type Organic Thermoelectrics: Improved Power Factor by Tailoring Host-Dopant Miscibility. *Adv. Mater.* **2017**, *29*, 1701641.
(190) Massetti, M.; Bonfadini, S.; Nava, D.; Butti, M.; Criante, L.; Lanzani, G.; Qiu, L.; Hummelen, J. C.; Liu, J.; Koster, L. J. A.; et al. Fully direct written organic micro-thermoelectric generators embedded in a plastic foil. *Nano Energy* **2020**, *75*, 104983.
(191) Russ, B.; Robb, M. J.; Brunetti, F. G.; Miller, P. L.; Perry, E. E.; Patel, S. N.; Ho, V.; Chang, W. B.; Urban, J. J.; Chabinyc, M. L.; et al. Power Factor Enhancement in Solution-Processed Organic n-Type Thermoelectrics Through Molecular Design. *Adv. Mater.* **2014**, *26*, 3473.
(192) Zuo, G. Z.; Li, Z. J.; Wang, E. G.; Kemerink, M. High Seebeck Coefficient and Power Factor in n-Type Organic Thermoelectrics. *Adv. Electron. Mater.* **2018**, *4*, 1700501.
(193) Russ, B.; Glaudell, A.; Urban, J. J.; Chabinyc, M. L.; Segalman, R. A. Organic thermoelectric materials for energy harvesting and temperature control. *Nat. Rev. Mater.* **2016**, *1*, 16050.
(194) Ushirokita, H.; Tada, H. In-plane Thermal Conductivity Measurement of Conjugated Polymer Films by Membrane-based AC Calorimetry. *Chem. Lett.* **2016**, *45*, 735.
(195) Choy, C. L.; Wong, Y. W.; Yang, G. W.; Kanamoto, T. Elastic modulus and thermal conductivity of ultradrawn polyethylene. *J. Polym. Sci., Part B: Polym. Phys.* **1999**, *37*, 3359.
(196) Shen, S.; Henry, A.; Tong, J.; Zheng, R.; Chen, G. Polyethylene nanofibres with very high thermal conductivities. *Nat. Nanotechnol.* **2010**, *5*, 251.
(197) Singh, V.; Bougher, T. L.; Weathers, A.; Cai, Y.; Bi, K.; Pettes, M. T.; McMenamin, S. A.; Lv, W.; Resler, D. P.; Gattuso, T. R.; et al. High thermal conductivity of chain-oriented amorphous polythiophene. *Nat. Nanotechnol.* **2014**, *9*, 384.
(198) Zhang, T.; Wu, X.; Luo, T. Polymer Nanofibers with Outstanding Thermal Conductivity and Thermal Stability: Fundamental Linkage between Molecular Characteristics and Macroscopic Thermal Properties. *J. Phys. Chem. C* **2014**, *118*, 21148.
(199) Liu, J.; Wang, X.; Li, D.; Coates, N. E.; Segalman, R. A.; Cahill, D. G. Thermal Conductivity and Elastic Constants of PEDOT:PSS with High Electrical Conductivity. *Macromolecules* **2015**, *48*, 585.
(200) Weathers, A.; Khan, Z. U.; Brooke, R.; Evans, D.; Pettes, M. T.; Andreasen, J. W.; Crispin, X.; Shi, L. Significant Electronic Thermal Transport in the Conducting Polymer Poly(3,4-ethylenedioxythiophene). *Adv. Mater.* **2015**, *27*, 2101.
(201) Scheunemann, D.; Kemerink, M. Non-Wiedemann-Franz behavior of the thermal conductivity of organic semiconductors. *Phys. Rev. B: Condens. Matter Mater. Phys.* **2020**, *101*, 075206.
(202) Zapata-Arteaga, O.; Perevedentsev, A.; Marina, S.; Martin, J.; Reparaz, J. S.; Campoy-Quiles, M. Reduction of the Lattice Thermal Conductivity of Polymer Semiconductors by Molecular Doping. *ACS Energy Lett.* **2020**, *5*, 2972.
(203) Patel, S. N.; Chabinyc, M. L. Anisotropies and the thermoelectric properties of semiconducting polymers. *J. Appl. Polym. Sci.* **2017**, *134*, 44403.
(204) Kommandur, S.; Yee, S. K. An empirical model to predict temperature-dependent thermal conductivity of amorphous polymers. *J. Polym. Sci., Part B: Polym. Phys.* **2017**, *55*, 1160.
(205) Paulsen, B. D.; Fabiano, S.; Rivnay, J. Mixed Ionic-Electronic Transport in Polymers. *Annu. Rev. Mater. Res.* **2021**, *51*, 73.
(206) Peterson, K. A.; Thomas, E. M.; Chabinyc, M. L. Thermoelectric Properties of Semiconducting Polymers. *Annu. Rev. Mater. Res.* **2020**, *50*, 551.
(207) Dai, L. M.; Chang, D. W.; Baek, J. B.; Lu, W. Carbon Nanomaterials for Advanced Energy Conversion and Storage. *Small* **2012**, *8*, 1130.
(208) Blackburn, J. L.; Ferguson, A. J.; Cho, C.; Grunlan, J. C. Carbon-Nanotube-Based Thermoelectric Materials and Devices. *Adv. Mater.* **2018**, *30*, 1704386.
(209) Iijima, S. Helical microtubules of graphitic carbon. *Nature* **1991**, *354*, 56.
(210) Wilder, J. W. G.; Venema, L. C.; Rinzler, A. G.; Smalley, R. E.; Dekker, C. Electronic structure of atomically resolved carbon nanotubes. *Nature* **1998**, *391*, 59.
(211) Prasek, J.; Drbohlavova, J.; Chomoucka, J.; Hubalek, J.; Jasek, O.; Adam, V.; Kizek, R. Methods for carbon nanotubes synthesis—review. *J. Mater. Chem.* **2011**, *21*, 15872.
(212) Janas, D. Towards monochiral carbon nanotubes: a review of progress in the sorting of single-walled carbon nanotubes. *Mater. Chem. Front.* **2018**, *2*, 36.
(213) Weisman, R. B.; Bachilo, S. M. Dependence of Optical Transition Energies on Structure for Single-Walled Carbon Nanotubes in Aqueous Suspension: An Empirical Kataura Plot. *Nano Lett.* **2003**, *3*, 1235.
(214) Dukovic, G.; Wang, F.; Song, D.; Sfeir, M. Y.; Heinz, T. F.; Brus, L. E. Structural Dependence of Excitonic Optical Transitions and Band-Gap Energies in Carbon Nanotubes. *Nano Lett.* **2005**, *5*, 2314.
(215) Bergin, S. D.; Sun, Z.; Rickard, D.; Streich, P. V.; Hamilton, J. P.; Coleman, J. N. Multicomponent Solubility Parameters for Single-Walled Carbon Nanotube-Solvent Mixtures. *ACS Nano* **2009**, *3*, 2340.
(216) Arnold, M. S.; Green, A. A.; Hulvat, J. F.; Stupp, S. I.; Hersam, M. C. Sorting carbon nanotubes by electronic structure using density differentiation. *Nat. Nanotechnol.* **2006**, *1*, 60.
(217) Tu, X.; Manohar, S.; Jagota, A.; Zheng, M. DNA sequence motifs for structure-specific recognition and separation of carbon nanotubes. *Nature* **2009**, *460*, 250.
(218) Wang, H.; Bao, Z. Conjugated polymer sorting of semiconducting carbon nanotubes and their electronic applications. *Nano Today* **2015**, *10*, 737.
(219) Hirotani, J.; Ohno, Y. Carbon Nanotube Thin Films for High-Performance Flexible Electronics Applications. *Top. Curr. Chem.* **2019**, *377*, 3.
(220) Ghosh, S.; Bachilo, S. M.; Weisman, R. B. Advanced sorting of single-walled carbon nanotubes by nonlinear density-gradient ultracentrifugation. *Nat. Nanotechnol.* **2010**, *5*, 443.
(221) Liu, H.; Nishide, D.; Tanaka, T.; Kataura, H. Large-scale single-chirality separation of single-wall carbon nanotubes by simple gel chromatography. *Nat. Commun.* **2011**, *2*, 309.
(222) Fagan, J. A.; Khripin, C. Y.; Silvera Batista, C. A.; Simpson, J. R.; Hároz, E. H.; Hight Walker, A. R.; Zheng, M. Isolation of Specific Small-Diameter Single-Wall Carbon Nanotube Species via Aqueous Two-Phase Extraction. *Adv. Mater.* **2014**, *26*, 2800.

https://doi.org/10.1021/acs.chemrev.1c00218
Chem. Rev. XXXX, XXX, XXX−XXX

(223) Fagan, J. A.; Hároz, E. H.; Ihly, R.; Gui, H.; Blackburn, J. L.; Simpson, J. R.; Lam, S.; Hight Walker, A. R.; Doorn, S. K.; Zheng, M. Isolation of > 1 nm Diameter Single-Wall Carbon Nanotube Species Using Aqueous Two-Phase Extraction. *ACS Nano* **2015**, *9*, 5377.
(224) Nish, A.; Hwang, J.-Y.; Doig, J.; Nicholas, R. J. Highly selective dispersion of single-walled carbon nanotubes using aromatic polymers. *Nat. Nanotechnol.* **2007**, *2*, 640.
(225) Mistry, K. S.; Larsen, B. A.; Blackburn, J. L. High-Yield Dispersions of Large-Diameter Semiconducting Single-Walled Carbon Nanotubes with Tunable Narrow Chirality Distributions. *ACS Nano* **2013**, *7*, 2231.
(226) Tenent, R. C.; Barnes, T. M.; Bergeson, J. D.; Ferguson, A. J.; To, B.; Gedvilas, L. M.; Heben, M. J.; Blackburn, J. L. Ultrasmooth, Large-Area, High-Uniformity, Conductive Transparent Single-Walled-Carbon-Nanotube Films for Photovoltaics Produced by Ultrasonic Spraying. *Adv. Mater.* **2009**, *21*, 3210.
(227) Graf, A.; Zakharko, Y.; Schießl, S. P.; Backes, C.; Pfohl, M.; Flavel, B. S.; Zaumseil, J. Large scale, selective dispersion of long single-walled carbon nanotubes with high photoluminescence quantum yield by shear force mixing. *Carbon* **2016**, *105*, 593.
(228) An, C. J.; Kang, Y. H.; Lee, A. Y.; Jang, K.-S.; Jeong, Y.; Cho, S. Y. Foldable Thermoelectric Materials: Improvement of the Thermoelectric Performance of Directly Spun CNT Webs by Individual Control of Electrical and Thermal Conductivity. *ACS Appl. Mater. Interfaces* **2016**, *8*, 22142.
(229) Zhou, W.; Fan, Q.; Zhang, Q.; Cai, L.; Li, K.; Gu, X.; Yang, F.; Zhang, N.; Wang, Y.; Liu, H.; et al. High-performance and compact-designed flexible thermoelectric modules enabled by a reticulate carbon nanotube architecture. *Nat. Commun.* **2017**, *8*, 14886.
(230) Choi, J.; Jung, Y.; Yang, S. J.; Oh, J. Y.; Oh, J.; Jo, K.; Son, J. G.; Moon, S. E.; Park, C. R.; Kim, H. Flexible and Robust Thermoelectric Generators Based on All-Carbon Nanotube Yarn without Metal Electrodes. *ACS Nano* **2017**, *11*, 7608.
(231) An, C. J.; Kang, Y. H.; Song, H.; Jeong, Y.; Cho, S. Y. Highly Integrated and Flexible Thermoelectric Module Fabricated by Brush-Cast Doping of a Highly Aligned Carbon Nanotube Web. *ACS Appl. Energy Mater.* **2019**, *2*, 1093.
(232) Hung, N. T.; Nugraha, A. R.; Hasdeo, E. H.; Dresselhaus, M. S.; Saito, R. Diameter dependence of thermoelectric power of semiconducting carbon nanotubes. *Phys. Rev. B: Condens. Matter Mater. Phys.* **2015**, *92*, 165426.
(233) Hayashi, D.; Nakai, Y.; Kyakuno, H.; Yamamoto, T.; Miyata, Y.; Yanagi, K.; Maniwa, Y. Improvement of thermoelectric performance of single-wall carbon nanotubes by heavy doping: Effect of one-dimensional band multiplicity. *Appl. Phys. Express* **2016**, *9*, 125103.
(234) Kim, S. M.; Jang, J. H.; Kim, K. K.; Park, H. K.; Bae, J. J.; Yu, W. J.; Lee, I. H.; Kim, G.; Loc, D. D.; Kim, U. J.; et al. Reduction-Controlled Viologen in Bisolvent as an Environmentally Stable n-Type Dopant for Carbon Nanotubes. *J. Am. Chem. Soc.* **2009**, *131*, 327.
(235) Mistry, K. S.; Larsen, B. A.; Bergeson, J. D.; Barnes, T. M.; Teeter, G.; Engtrakul, C.; Blackburn, J. L. n-Type Transparent Conducting Films of Small Molecule and Polymer Amine Doped Single-Walled Carbon Nanotubes. *ACS Nano* **2011**, *5*, 3714.
(236) Nonoguchi, Y.; Ohashi, K.; Kanazawa, R.; Ashiba, K.; Hata, K.; Nakagawa, T.; Adachi, C.; Tanase, T.; Kawai, T. Systematic Conversion of Single Walled Carbon Nanotubes into n-type Thermoelectric Materials by Molecular Dopants. *Sci. Rep.* **2013**, *3*, 3344.
(237) Nonoguchi, Y.; Nakano, M.; Murayama, T.; Hagino, H.; Hama, S.; Miyazaki, K.; Matsubara, R.; Nakamura, M.; Kawai, T. Simple Salt-Coordinated n-Type Nanocarbon Materials Stable in Air. *Adv. Funct. Mater.* **2016**, *26*, 3021.
(238) Li, L.-J.; Khlobystov, A. N.; Wiltshire, J. G.; Briggs, G. A. D.; Nicholas, R. J. Diameter-selective encapsulation of metallocenes in single-walled carbon nanotubes. *Nat. Mater.* **2005**, *4*, 481.
(239) Sauer, M.; Shiozawa, H.; Ayala, P.; Ruiz-Soria, G.; Kataura, H.; Yanagi, K.; Krause, S.; Pichler, T. In situ filling of metallic single-walled carbon nanotubes with ferrocene molecules. *Phys. Status Solidi B* **2012**, *249*, 2408.
(240) Sauer, M.; Shiozawa, H.; Ayala, P.; Ruiz-Soria, G.; Liu, X.; Chernov, A.; Krause, S.; Yanagi, K.; Kataura, H.; Pichler, T. Internal charge transfer in metallicity sorted ferrocene filled carbon nanotube hybrids. *Carbon* **2013**, *59*, 237.
(241) Fukumaru, T.; Fujigaya, T.; Nakashima, N. Development of n-type cobaltocene-encapsulated carbon nanotubes with remarkable thermoelectric property. *Sci. Rep.* **2015**, *5*, 7951.
(242) Kharlamova, M. V.; Kramberger, C.; Domanov, O.; Mittelberger, A.; Saito, T.; Yanagi, K.; Pichler, T.; Eder, D. Comparison of Doping Levels of Single-Walled Carbon Nanotubes Synthesized by Arc-Discharge and Chemical Vapor Deposition Methods by Encapsulated Silver Chloride. *Phys. Status Solidi B* **2018**, *255*, 1800178.
(243) Shimotani, H.; Tsuda, S.; Yuan, H.; Yomogida, Y.; Moriya, R.; Takenobu, T.; Yanagi, K.; Iwasa, Y. Continuous Band-Filling Control and One-Dimensional Transport in Metallic and Semiconducting Carbon Nanotube Tangled Films. *Adv. Funct. Mater.* **2014**, *24*, 3305.
(244) Yanagi, K.; Kanda, S.; Oshima, Y.; Kitamura, Y.; Kawai, H.; Yamamoto, T.; Takenobu, T.; Nakai, Y.; Maniwa, Y. Tuning of the Thermoelectric Properties of One-Dimensional Material Networks by Electric Double Layer Techniques Using Ionic Liquids. *Nano Lett.* **2014**, *14*, 6437.
(245) Shimizu, S.; Iizuka, T.; Kanahashi, K.; Pu, J.; Yanagi, K.; Takenobu, T.; Iwasa, Y. Thermoelectric Detection of Multi-Subband Density of States in Semiconducting and Metallic Single-Walled Carbon Nanotubes. *Small* **2016**, *12*, 3388.
(246) Fukuhara, K.; Ichinose, Y.; Nishidome, H.; Yomogida, Y.; Katsutani, F.; Komatsu, N.; Gao, W.; Kono, J.; Yanagi, K. Isotropic Seebeck coefficient of aligned single-wall carbon nanotube films. *Appl. Phys. Lett.* **2018**, *113*, 243105.
(247) Gao, W.; Komatsu, N.; Taylor, L. W.; Naik, G. V.; Yanagi, K.; Pasquali, M.; Kono, J. Macroscopically aligned carbon nanotubes for flexible and high-temperature electronics, optoelectronics, and thermoelectrics. *J. Phys. D: Appl. Phys.* **2020**, *53*, 063001.
(248) Ichinose, Y.; Yoshida, A.; Horiuchi, K.; Fukuhara, K.; Komatsu, N.; Gao, W.; Yomogida, Y.; Matsubara, M.; Yamamoto, T.; Kono, J.; et al. Solving the Thermoelectric Trade-Off Problem with Metallic Carbon Nanotubes. *Nano Lett.* **2019**, *19*, 7370.
(249) Blackburn, J. L.; Ferguson, A. J.; Reid, O. G. In *Handbook of Carbon Nanomaterials*; World Scientific, 2017; Vols. *9/10*.
(250) Hertel, T. In *Handbook of Carbon Nanomaterials*; World Scientific, 2017; Vols. *9/10*.
(251) Eckstein, K. H.; Oberndorfer, F.; Achsnich, M. M.; Schöppler, F.; Hertel, T. Quantifying Doping Levels in Carbon Nanotubes by Optical Spectroscopy. *J. Phys. Chem. C* **2019**, *123*, 30001.
(252) MacLeod, B. A.; Stanton, N. J.; Gould, I. E.; Wesenberg, D.; Ihly, R.; Owczarczyk, Z. R.; Hurst, K. E.; Fewox, C. S.; Folmar, C. N.; Holman Hughes, K.; et al. Large n- and p-type thermoelectric power factors from doped semiconducting single-walled carbon nanotube thin films. *Energy Environ. Sci.* **2017**, *10*, 2168.
(253) Blackburn, J. L.; Kang, S. D.; Roos, M. J.; Norton-Baker, B.; Miller, E. M.; Ferguson, A. J. Intrinsic and Extrinsically Limited Thermoelectric Transport within Semiconducting Single-Walled Carbon Nanotube Networks. *Adv. Electron. Mater.* **2019**, *5*, 1800910.
(254) Nonoguchi, Y.; Takata, A.; Goto, C.; Kitano, T.; Kawai, T. Thickness-dependent thermoelectric power factor of polymer-functionalized semiconducting carbon nanotube thin films. *Sci. Technol. Adv. Mater.* **2018**, *19*, 581.
(255) Blackburn, J. L.; Barnes, T. M.; Beard, M. C.; Kim, Y.-H.; Tenent, R. C.; McDonald, T. J.; To, B.; Coutts, T. J.; Heben, M. J. Transparent Conductive Single-Walled Carbon Nanotube Networks with Precisely Tunable Ratios of Semiconducting and Metallic Nanotubes. *ACS Nano* **2008**, *2*, 1266.
(256) Zhang, Q.; Hároz, E. H.; Jin, Z.; Ren, L.; Wang, X.; Arvidson, R. S.; Lüttge, A.; Kono, J. Plasmonic Nature of the Terahertz Conductivity Peak in Single-Wall Carbon Nanotubes. *Nano Lett.* **2013**, *13*, 5991.
(257) Graupner, R.; Abraham, J.; Vencelová, A.; Seyller, T.; Hennrich, F.; Kappes, M. M.; Hirsch, A.; Ley, L. Doping of single-walled carbon nanotube bundles by Brønsted acids. *Phys. Chem. Chem. Phys.* **2003**, *5*, 5472.

https://doi.org/10.1021/acs.chemrev.1c00218
Chem. Rev. XXXX, XXX, XXX−XXX

(258) Zhao, Y.; Wei, J.; Vajtai, R.; Ajayan, P. M.; Barrera, E. V. Iodine doped carbon nanotube cables exceeding specific electrical conductivity of metals. *Sci. Rep.* **2011**, *1*, 83.
(259) Grigorian, L.; Sumanasekera, G. U.; Loper, A. L.; Fang, S.; Allen, J. L.; Eklund, P. C. Transport properties of alkali-metal-doped single-wall carbon nanotubes. *Phys. Rev. B: Condens. Matter Mater. Phys.* **1998**, *58*, R4195.
(260) Dettlaff-Weglikowska, U.; Skákalová, V.; Graupner, R.; Jhang, S. H.; Kim, B. H.; Lee, H. J.; Ley, L.; Park, Y. W.; Berber, S.; Tománek, D.; et al. Effect of SOCl2 Treatment on Electrical and Mechanical Properties of Single-Wall Carbon Nanotube Networks. *J. Am. Chem. Soc.* **2005**, *127*, 5125.
(261) Choi, J.; Lee, J. Y.; Lee, S. S.; Park, C. R.; Kim, H. High-Performance Thermoelectric Paper Based on Double Carrier-Filtering Processes at Nanowire Heterojunctions. *Adv. Energy Mater.* **2016**, *6*, 1502181.
(262) Lee, M.-H.; Kang, Y. H.; Kim, J.; Lee, Y. K.; Cho, S. Y. Freely Shapable and 3D Porous Carbon Nanotube Foam Using Rapid Solvent Evaporation Method for Flexible Thermoelectric Power Generators. *Adv. Energy Mater.* **2019**, *9*, 1900914.
(263) Rathore, R.; Loyd, S. H.; Kochi, J. K. Isolation, Structure, and Reactivity of a Novel Chloro-Arenium Cation for Electrophilic (Transfer) Chlorinations. *J. Am. Chem. Soc.* **1994**, *116*, 8414.
(264) Rathore, R.; Kumar, A. S.; Lindeman, S. V.; Kochi, J. K. Preparation and Structures of Crystalline Aromatic Cation-Radical Salts. Triethyloxonium Hexachloroantimonate as a Novel (One-Electron) Oxidant. *J. Org. Chem.* **1998**, *63*, 5847.
(265) Norton-Baker, B.; Ihly, R.; Gould, I. E.; Avery, A. D.; Owczarczyk, Z. R.; Ferguson, A. J.; Blackburn, J. L. Polymer-Free Carbon Nanotube Thermoelectrics with Improved Charge Carrier Transport and Power Factor. *ACS Energy Lett.* **2016**, *1*, 1212.
(266) Chandra, B.; Afzali, A.; Khare, N.; El-Ashry, M. M.; Tulevski, G. S. Stable Charge-Transfer Doping of Transparent Single-Walled Carbon Nanotube Films. *Chem. Mater.* **2010**, *22*, 5179.
(267) Zhou, W. B.; Fan, Q. X.; Zhang, Q.; Cai, L.; Li, K. W.; Gu, X. G.; Yang, F.; Zhang, N.; Wang, Y. C.; Liu, H. P.; et al. High-performance and compact-designed flexible thermoelectric modules enabled by a reticulate carbon nanotube architecture. *Nat. Commun.* **2017**, *8*, 14886.
(268) Kim, S.; Mo, J.-H.; Jang, K.-S. Solution-Processed Carbon Nanotube Buckypapers for Foldable Thermoelectric Generators. *ACS Appl. Mater. Interfaces* **2019**, *11*, 35675.
(269) Choi, J.; Jung, Y.; Dun, C.; Park, K. T.; Gordon, M. P.; Haas, K.; Yuan, P.; Kim, H.; Park, C. R.; Urban, J. J. High-Performance, Wearable Thermoelectric Generator Based on a Highly Aligned Carbon Nanotube Sheet. *ACS Appl. Energy Mater.* **2020**, *3*, 1199.
(270) Zheng, Y.; Zhang, Q.; Jin, W.; Jing, Y.; Chen, X.; Han, X.; Bao, Q.; Liu, Y.; Wang, X.; Wang, S.; et al. Carbon nanotube yarn based thermoelectric textiles for harvesting thermal energy and powering electronics. *J. Mater. Chem. A* **2020**, *8*, 2984.
(271) Nakashima, Y.; Yamaguchi, R.; Toshimitsu, F.; Matsumoto, M.; Borah, A.; Staykov, A.; Islam, M. S.; Hayami, S.; Fujigaya, T. Air-Stable n-Type Single-Walled Carbon Nanotubes Doped with Benzimidazole Derivatives for Thermoelectric Conversion and Their Air-Stable Mechanism. *ACS Appl. Nano Mater.* **2019**, *2*, 4703.
(272) Nakai, Y.; Honda, K.; Yanagi, K.; Kataura, H.; Kato, T.; Yamamoto, T.; Maniwa, Y. Giant Seebeck coefficient in semiconducting single-wall carbon nanotube film. *Appl. Phys. Express* **2014**, *7*, 025103.
(273) Huang, W.; Toshimitsu, F.; Ozono, K.; Matsumoto, M.; Borah, A.; Motoishi, Y.; Park, K. H.; Jang, J. W.; Fujigaya, T. Thermoelectric properties of dispersant-free semiconducting single-walled carbon nanotubes sorted by a flavin extraction method. *Chem. Commun.* **2019**, *55*, 2636.
(274) Huang, W.; Tokunaga, E.; Nakashima, Y.; Fujigaya, T. Thermoelectric properties of sorted semiconducting single-walled carbon nanotube sheets. *Sci. Technol. Adv. Mater.* **2019**, *20*, 97.
(275) Behabtu, N.; Young, C. C.; Tsentalovich, D. E.; Kleinerman, O.; Wang, X.; Ma, A. W. K.; Bengio, E. A.; ter Waarbeek, R. F.; de Jong, J. J.; Hoogerwerf, R. E.; et al. Strong, Light, Multifunctional Fibers of Carbon Nanotubes with Ultrahigh Conductivity. *Science* **2013**, *339*, 182.
(276) Kodama, T.; Ohnishi, M.; Park, W.; Shiga, T.; Park, J.; Shimada, T.; Shinohara, H.; Shiomi, J.; Goodson, K. E. Modulation of thermal and thermoelectric transport in individual carbon nanotubes by fullerene encapsulation. *Nat. Mater.* **2017**, *16*, 892.
(277) Wesenberg, D. J.; Roos, M. J.; Avery, A. D.; Blackburn, J. L.; Ferguson, A. J.; Zink, B. L. Size- and Temperature-Dependent Suppression of Phonon Thermal Conductivity in Carbon Nanotube Thermoelectric Films. *Adv. Electron. Mater.* **2020**, *6*, 2000746.
(278) Kang, S. D.; Snyder, G. J. Charge-transport model for conducting polymers. *Nat. Mater.* **2017**, *16*, 252.
(279) Liu, Y.; Nitschke, M.; Stepien, L.; Khavrus, V.; Bezugly, V.; Cuniberti, G. Ammonia Plasma-Induced n-Type Doping of Semiconducting Carbon Nanotube Films: Thermoelectric Properties and Ambient Effects. *ACS Appl. Mater. Interfaces* **2019**, *11*, 21807.
(280) Zhao, W.; Fan, S.; Xiao, N.; Liu, D.; Tay, Y. Y.; Yu, C.; Sim, D.; Hng, H. H.; Zhang, Q.; Boey, F.; et al. Flexible carbon nanotube papers with improved thermoelectric properties. *Energy Environ. Sci.* **2012**, *5*, 5364.
(281) Nonoguchi, Y.; Tani, A.; Kitano, T.; Kawai, T. Enhanced thermoelectric properties of semiconducting carbon nanotube films by UV/ozone treatment. *J. Appl. Phys.* **2019**, *126*, 135108.
(282) Ewels, C. P.; Glerup, M. Nitrogen Doping in Carbon Nanotubes. *J. Nanosci. Nanotechnol.* **2005**, *5*, 1345.
(283) McGuire, K.; Gothard, N.; Gai, P. L.; Dresselhaus, M. S.; Sumanasekera, G.; Rao, A. M. Synthesis and Raman characterization of boron-doped single-walled carbon nanotubes. *Carbon* **2005**, *43*, 219.
(284) Blackburn, J. L.; Yan, Y.; Engtrakul, C.; Parilla, P. A.; Jones, K.; Gennett, T.; Dillon, A. C.; Heben, M. J. Synthesis and Characterization of Boron-Doped Single-Wall Carbon Nanotubes Produced by the Laser Vaporization Technique. *Chem. Mater.* **2006**, *18*, 2558.
(285) Dörling, B.; Sandoval, S.; Kankla, P.; Fuertes, A.; Tobias, G.; Campoy-Quiles, M. Exploring different doping mechanisms in thermoelectric polymer/carbon nanotube composites. *Synth. Met.* **2017**, *225*, 70.
(286) Dörling, B.; Ryan, J. D.; Craddock, J. D.; Sorrentino, A.; Basaty, A. E.; Gomez, A.; Garriga, M.; Pereiro, E.; Anthony, J. E.; Weisenberger, M. C.; et al. Photoinduced p- to n-type Switching in Thermoelectric Polymer-Carbon Nanotube Composites. *Adv. Mater.* **2016**, *28*, 2782.
(287) Chiang, W.-H.; Iihara, Y.; Li, W.-T.; Hsieh, C.-Y.; Lo, S.-C.; Goto, C.; Tani, A.; Kawai, T.; Nonoguchi, Y. Enhanced Thermoelectric Properties of Boron-Substituted Single-Walled Carbon Nanotube Films. *ACS Appl. Mater. Interfaces* **2019**, *11*, 7235.
(288) Yamaguchi, S.; Tsunekawa, I.; Komatsu, N.; Gao, W.; Shiga, T.; Kodama, T.; Kono, J.; Shiomi, J. One-directional thermal transport in densely aligned single-wall carbon nanotube films. *Appl. Phys. Lett.* **2019**, *115*, 223104.
(289) Ryu, S. W.; Hwang, J. W.; Hong, S. H. Synthesis and Characterization of Vertically Aligned Carbon Nanotube Forest for Solid State Fiber Spinning. *J. Nanosci. Nanotechnol.* **2012**, *12*, 5653.
(290) Lee, J.; Lee, D.-M.; Jung, Y.; Park, J.; Lee, H. S.; Kim, Y.-K.; Park, C. R.; Jeong, H. S.; Kim, S. M. Direct spinning and densification method for high-performance carbon nanotube fibers. *Nat. Commun.* **2019**, *10*, 2962.
(291) Abol-Fotouh, D.; Dörling, B.; Zapata-Arteaga, O.; Rodríguez-Martínez, X.; Gómez, A.; Reparaz, J. S.; Laromaine, A.; Roig, A.; Campoy-Quiles, M. Farming thermoelectric paper. *Energy Environ. Sci.* **2019**, *12*, 716.
(292) Lee, T.; Park, K. T.; Ku, B.-C.; Kim, H. Carbon nanotube fibers with enhanced longitudinal carrier mobility for high-performance all-carbon thermoelectric generators. *Nanoscale* **2019**, *11*, 16919.
(293) Ryan, J. D.; Lund, A.; Hofmann, A. I.; Kroon, R.; Sarabia-Riquelme, R.; Weisenberger, M. C.; Müller, C. All-Organic Textile Thermoelectrics with Carbon-Nanotube-Coated n-Type Yarns. *ACS Appl. Energy Mater.* **2018**, *1*, 2934.
(294) Xu, Y.; Li, Z.; Duan, W. Thermal and Thermoelectric Properties of Graphene. *Small* **2014**, *10*, 2182.

https://doi.org/10.1021/acs.chemrev.1c00218
Chem. Rev. XXXX, XXX, XXX−XXX

(295) Dollfus, P.; Hung Nguyen, V.; Saint-Martin, J. Thermoelectric effects in graphene nanostructures. *J. Phys.: Condens. Matter* **2015**, *27*, 133204.
(296) Zong, P.-A.; Liang, J.; Zhang, P.; Wan, C.; Wang, Y.; Koumoto, K. Graphene-Based Thermoelectrics. *ACS Appl. Energy Mater.* **2020**, *3*, 2224.
(297) Andrei, E. Y.; Li, G.; Du, X. Electronic properties of graphene: a perspective from scanning tunneling microscopy and magnetotransport. *Rep. Prog. Phys.* **2012**, *75*, 056501.
(298) Cai, J.; Ruffieux, P.; Jaafar, R.; Bieri, M.; Braun, T.; Blankenburg, S.; Muoth, M.; Seitsonen, A. P.; Saleh, M.; Feng, X.; et al. Atomically precise bottom-up fabrication of graphene nanoribbons. *Nature* **2010**, *466*, 470.
(299) Han, M. Y.; Özyilmaz, B.; Zhang, Y.; Kim, P. Energy Band-Gap Engineering of Graphene Nanoribbons. *Phys. Rev. Lett.* **2007**, *98*, 206805.
(300) Hernandez, Y.; Nicolosi, V.; Lotya, M.; Blighe, F. M.; Sun, Z.; De, S.; McGovern, I. T.; Holland, B.; Byrne, M.; Gun'Ko, Y. K.; et al. High-yield production of graphene by liquid-phase exfoliation of graphite. *Nat. Nanotechnol.* **2008**, *3*, 563.
(301) Dikin, D. A.; Stankovich, S.; Zimney, E. J.; Piner, R. D.; Dommett, G. H. B.; Evmenenko, G.; Nguyen, S. T.; Ruoff, R. S. Preparation and characterization of graphene oxide paper. *Nature* **2007**, *448*, 457.
(302) Balandin, A. A.; Ghosh, S.; Bao, W.; Calizo, I.; Teweldebrhan, D.; Miao, F.; Lau, C. N. Superior Thermal Conductivity of Single-Layer Graphene. *Nano Lett.* **2008**, *8*, 902.
(303) Ghosh, S.; Nika, D. L.; Pokatilov, E. P.; Balandin, A. A. Heat conduction in graphene: experimental study and theoretical interpretation. *New J. Phys.* **2009**, *11*, 095012.
(304) Chen, S.; Wu, Q.; Mishra, C.; Kang, J.; Zhang, H.; Cho, K.; Cai, W.; Balandin, A. A.; Ruoff, R. S. Thermal conductivity of isotopically modified graphene. *Nat. Mater.* **2012**, *11*, 203.
(305) Löfwander, T.; Fogelström, M. Impurity scattering and Mott's formula in graphene. *Phys. Rev. B: Condens. Matter Mater. Phys.* **2007**, *76*, 193401.
(306) Zuev, Y. M.; Chang, W.; Kim, P. Thermoelectric and Magnetothermoelectric Transport Measurements of Graphene. *Phys. Rev. Lett.* **2009**, *102*, 096807.
(307) Wei, P.; Bao, W.; Pu, Y.; Lau, C. N.; Shi, J. Anomalous Thermoelectric Transport of Dirac Particles in Graphene. *Phys. Rev. Lett.* **2009**, *102*, 166808.
(308) Seol, J. H.; Jo, I.; Moore, A. L.; Lindsay, L.; Aitken, Z. H.; Pettes, M. T.; Li, X. S.; Yao, Z.; Huang, R.; Broido, D.; et al. Two-Dimensional Phonon Transport in Supported Graphene. *Science* **2010**, *328*, 213.
(309) Kanahashi, K.; Ishihara, M.; Hasegawa, M.; Ohta, H.; Takenobu, T. Giant power factors in p- and n-type large-area graphene films on a flexible plastic substrate. *npj 2D Mater. Appl.* **2019**, *3*, 44.
(310) Ouyang, Y.; Guo, J. A theoretical study on thermoelectric properties of graphene nanoribbons. *Appl. Phys. Lett.* **2009**, *94*, 263107.
(311) Sevincli, H.; Cuniberti, G. Enhanced thermoelectric figure of merit in edge-disordered zigzag graphene nanoribbons. *Phys. Rev. B: Condens. Matter Mater. Phys.* **2010**, *81*, 113401.
(312) Chen, Y.; Jayasekera, T.; Calzolari, A.; Kim, K. W.; Buongiorno Nardelli, M. Thermoelectric properties of graphene nanoribbons, junctions and superlattices. *J. Phys.: Condens. Matter* **2010**, *22*, 372202.
(313) Kim, J. Y.; Grossman, J. C. High-Efficiency Thermoelectrics with Functionalized Graphene. *Nano Lett.* **2015**, *15*, 2830.
(314) Oh, J.; Yoo, H.; Choi, J.; Kim, J. Y.; Lee, D. S.; Kim, M. J.; Lee, J.-C.; Kim, W. N.; Grossman, J. C.; Park, J. H.; et al. Significantly reduced thermal conductivity and enhanced thermoelectric properties of single- and bi-layer graphene nanomeshes with sub-10nm neck-width. *Nano Energy* **2017**, *35*, 26.
(315) Li, Q.-Y.; Feng, T.; Okita, W.; Komori, Y.; Suzuki, H.; Kato, T.; Kaneko, T.; Ikuta, T.; Ruan, X.; Takahashi, K. Enhanced Thermoelectric Performance of As-Grown Suspended Graphene Nanoribbons. *ACS Nano* **2019**, *13*, 9182.
(316) Ma, W.; Liu, Y.; Yan, S.; Miao, T.; Shi, S.; Xu, Z.; Zhang, X.; Gao, C. Chemically doped macroscopic graphene fibers with significantly enhanced thermoelectric properties. *Nano Res.* **2018**, *11*, 741.
(317) Yi, M.; Shen, Z. A review on mechanical exfoliation for the scalable production of graphene. *J. Mater. Chem. A* **2015**, *3*, 11700.
(318) Choi, J.; Tu, N. D. K.; Lee, S.-S.; Lee, H.; Kim, J. S.; Kim, H. Controlled oxidation level of reduced graphene oxides and its effect on thermoelectric properties. *Macromol. Res.* **2014**, *22*, 1104.
(319) Wang, W.; Zhang, Q.; Li, J.; Liu, X.; Wang, L.; Zhu, J.; Luo, W.; Jiang, W. An efficient thermoelectric material: preparation of reduced graphene oxide/polyaniline hybrid composites by cryogenic grinding. *RSC Adv.* **2015**, *5*, 8988.
(320) Gao, J.; Liu, C.; Miao, L.; Wang, X.; Peng, Y.; Chen, Y. Enhanced power factor in flexible reduced graphene oxide/nanowires hybrid films for thermoelectrics. *RSC Adv.* **2016**, *6*, 31580.
(321) Li, T.; Pickel, A. D.; Yao, Y.; Chen, Y.; Zeng, Y.; Lacey, S. D.; Li, Y.; Wang, Y.; Dai, J.; Wang, Y.; et al. Thermoelectric properties and performance of flexible reduced graphene oxide films up to 3,000 K. *Nat. Energy* **2018**, *3*, 148.
(322) Novak, T. G.; Kim, J.; Kim, J.; Tiwari, A. P.; Shin, H.; Song, J. Y.; Jeon, S. Complementary n-Type and p-Type Graphene Films for High Power Factor Thermoelectric Generators. *Adv. Funct. Mater.* **2020**, *30*, 2001760.
(323) Novak, T. G.; Kim, J.; Kim, J.; Shin, H.; Tiwari, A. P.; Song, J. Y.; Jeon, S. Flexible thermoelectric films with high power factor made of non-oxidized graphene flakes. *2D Mater.* **2019**, *6*, 045019.
(324) Zengin, H.; Zhou, W.; Jin, J.; Czerw, R.; Smith, D. W., Jr; Echegoyen, L.; Carroll, D. L.; Foulger, S. H.; Ballato, J. Carbon Nanotube Doped Polyaniline. *Adv. Mater.* **2002**, *14*, 1480.
(325) Feng, W.; Bai, X. D.; Lian, Y. Q.; Liang, J.; Wang, X. G.; Yoshino, K. Well-aligned polyaniline/carbon-nanotube composite films grown by in-situ aniline polymerization. *Carbon* **2003**, *41*, 1551.
(326) Yu, C.; Kim, Y. S.; Kim, D.; Grunlan, J. C. Thermoelectric Behavior of Segregated-Network Polymer Nanocomposites. *Nano Lett.* **2008**, *8*, 4428.
(327) Kim, D.; Kim, Y.; Choi, K.; Grunlan, J. C.; Yu, C. Improved Thermoelectric Behavior of Nanotube-Filled Polymer Composites with Poly(3,4-ethylenedioxythiophene) Poly(styrenesulfonate). *ACS Nano* **2010**, *4*, 513.
(328) Meng, C. Z.; Liu, C. H.; Fan, S. S. A Promising Approach to Enhanced Thermoelectric Properties Using Carbon Nanotube Networks. *Adv. Mater.* **2010**, *22*, 535.
(329) Yao, Q.; Chen, L.; Zhang, W.; Liufu, S.; Chen, X. Enhanced Thermoelectric Performance of Single-Walled Carbon Nanotubes/Polyaniline Hybrid Nanocomposites. *ACS Nano* **2010**, *4*, 2445.
(330) Minnich, A. J.; Dresselhaus, M. S.; Ren, Z. F.; Chen, G. Bulk nanostructured thermoelectric materials: current research and future prospects. *Energy Environ. Sci.* **2009**, *2*, 466.
(331) Szczech, J. R.; Higgins, J. M.; Jin, S. Enhancement of the thermoelectric properties in nanoscale and nanostructured materials. *J. Mater. Chem.* **2011**, *21*, 4037.
(332) Blackburn, J. L.; Ferguson, A. J.; Cho, C.; Grunlan, J. C. Carbon-Nanotube-Based Thermoelectric Materials and Devices. *Adv. Mater.* **2018**, *30*, 1704386.
(333) Faleev, S. V.; Léonard, F. Theory of enhancement of thermoelectric properties of materials with nanoinclusions. *Phys. Rev. B: Condens. Matter Mater. Phys.* **2008**, *77*, 214304.
(334) Cho, C.; Culebras, M.; Wallace, K. L.; Song, Y.; Holder, K.; Hsu, J.-H.; Yu, C.; Grunlan, J. C. Stable n-type thermoelectric multilayer thin films with high power factor from carbonaceous nanofillers. *Nano Energy* **2016**, *28*, 426.
(335) Cho, C.; Wallace, K. L.; Tzeng, P.; Hsu, J. H.; Yu, C.; Grunlan, J. C. Outstanding Low Temperature Thermoelectric Power Factor from Completely Organic Thin Films Enabled by Multidimensional Conjugated Nanomaterials. *Adv. Energy Mater.* **2016**, *6*, 1502168.
(336) Zhang, K.; Wang, S.; Qiu, J.; Blackburn, J. L.; Zhang, X.; Ferguson, A. J.; Miller, E. M.; Weeks, B. L. Effect of host-mobility dependent carrier scattering on thermoelectric power factors of polymer composites. *Nano Energy* **2016**, *19*, 128.

https://doi.org/10.1021/acs.chemrev.1c00218
Chem. Rev. XXXX, XXX, XXX−XXX

(337) Cho, C.; Qin, S.; Choi, K.; Grunlan, J. C. Improved Thermoelectric Power Factor in Completely Organic Nanocomposite Enabled by l-Ascorbic Acid. *ACS Appl. Polym. Mater.* **2019**, *1*, 1942.
(338) Lin, Y.; Wood, M.; Imasato, K.; Kuo, J. J.; Lam, D.; Mortazavi, A. N.; Slade, T. J.; Hodge, S. A.; Xi, K.; Kanatzidis, M. G.; et al. Expression of interfacial Seebeck coefficient through grain boundary engineering with multi-layer graphene nanoplatelets. *Energy Environ. Sci.* **2020**, *13*, 4114.
(339) Yu, C.; Choi, K.; Yin, L.; Grunlan, J. C. Light-Weight Flexible Carbon Nanotube Based Organic Composites with Large Thermoelectric Power Factors. *ACS Nano* **2011**, *5*, 7885.
(340) Moriarty, G. P.; De, S.; King, P. J.; Khan, U.; Via, M.; King, J. A.; Coleman, J. N.; Grunlan, J. C. Thermoelectric behavior of organic thin film nanocomposites. *J. Polym. Sci., Part B: Polym. Phys.* **2013**, *51*, 119.
(341) Moriarty, G. P.; Briggs, K.; Stevens, B.; Yu, C.; Grunlan, J. C. Fully Organic Nanocomposites with High Thermoelectric Power Factors by using a Dual-Stabilizer Preparation. *Energy Technol.* **2013**, *1*, 265.
(342) Yao, Q.; Wang, Q.; Wang, L. M.; Chen, L. D. Abnormally enhanced thermoelectric transport properties of SWNT/PANI hybrid films by the strengthened PANI molecular ordering. *Energy Environ. Sci.* **2014**, *7*, 3801.
(343) Lee, W.; Hong, C. T.; Kwon, O. H.; Yoo, Y.; Kang, Y. H.; Lee, J. Y.; Cho, S. Y.; Jang, K.-S. Enhanced Thermoelectric Performance of Bar-Coated SWCNT/P3HT Thin Films. *ACS Appl. Mater. Interfaces* **2015**, *7*, 6550.
(344) Wang, H.; Yi, S.-I.; Pu, X.; Yu, C. Simultaneously Improving Electrical Conductivity and Thermopower of Polyaniline Composites by Utilizing Carbon Nanotubes as High Mobility Conduits. *ACS Appl. Mater. Interfaces* **2015**, *7*, 9589.
(345) Hong, C. T.; Lee, W.; Kang, Y. H.; Yoo, Y.; Ryu, J.; Cho, S. Y.; Jang, K.-S. Effective doping by spin-coating and enhanced thermoelectric power factors in SWCNT/P3HT hybrid films. *J. Mater. Chem. A* **2015**, *3*, 12314.
(346) Lee, W.; Kang, Y. H.; Lee, J. Y.; Jang, K.-S.; Cho, S. Y. Improving the thermoelectric power factor of CNT/PEDOT:PSS nanocomposite films by ethylene glycol treatment. *RSC Adv.* **2016**, *6*, 53339.
(347) Wang, L.; Yao, Q.; Xiao, J.; Zeng, K.; Qu, S.; Shi, W.; Wang, Q.; Chen, L. Engineered Molecular Chain Ordering in Single-Walled Carbon Nanotubes/Polyaniline Composite Films for High-Performance Organic Thermoelectric Materials. *Chem. - Asian J.* **2016**, *11*, 1804.
(348) Wang, L.; Yao, Q.; Shi, W.; Qu, S.; Chen, L. Engineering carrier scattering at the interfaces in polyaniline based nanocomposites for high thermoelectric performances. *Mater. Chem. Front.* **2017**, *1*, 741.
(349) Fan, W.; Liang, L.; Zhang, B.; Guo, C.-Y.; Chen, G. PEDOT thermoelectric composites with excellent power factors prepared by 3-phase interfacial electropolymerization and carbon nanotube chemical doping. *J. Mater. Chem. A* **2019**, *7*, 13687.
(350) Ha, J. U.; Cho, J.; Yoon, S.; Jang, M. S.; Hassan, S. Z.; Kang, M. G.; Chung, D. S. Polyvinyl alcohol covalently grafted CNT for free-standing, flexible, and high-performance thermoelectric generator film. *Nanotechnology* **2019**, *30*, 14LT01.
(351) Wang, L.; Zhang, J.; Guo, Y.; Chen, X.; Jin, X.; Yang, Q.; Zhang, K.; Wang, S.; Qiu, Y. Fabrication of core-shell structured poly(3,4-ethylenedioxythiophene)/carbon nanotube hybrids with enhanced thermoelectric power factors. *Carbon* **2019**, *148*, 290.
(352) Liu, S.; Kong, J.; Chen, H.; He, C. Interfacial Energy Barrier Tuning for Enhanced Thermoelectric Performance of PEDOT Nanowire/SWNT/PEDOT:PSS Ternary Composites. *ACS Appl. Energy Mater.* **2019**, *2*, 8843.
(353) Jung, J.; Suh, E. H.; Jeong, Y. J.; Yang, H. S.; Lee, T.; Jang, J. Efficient Debundling of Few-Walled Carbon Nanotubes by Wrapping with Donor-Acceptor Polymers for Improving Thermoelectric Properties. *ACS Appl. Mater. Interfaces* **2019**, *11*, 47330.
(354) Hata, S.; Mihara, T.; Shiraishi, M.; Yamaguchi, Y.; Du, Y.; Shiraishi, Y.; Toshima, N. Development of carbon nanotube organic thermoelectric materials using cyclodextrin polymer: control of semiconductor characteristics by the solvent effect. *Jpn. J. Appl. Phys.* **2020**, *59*, SDDD05.
(355) Li, H.; Liu, S.; Li, P.; Yuan, D.; Zhou, X.; Sun, J.; Lu, X.; He, C. Interfacial control and carrier tuning of carbon nanotube/polyaniline composites for high thermoelectric performance. *Carbon* **2018**, *136*, 292.
(356) Maity, S.; Sepay, N.; Kulsi, C.; Kool, A.; Das, S.; Banerjee, D.; Chatterjee, K. Enhancement of Thermoelectric Performance in Oligomeric PEDOT-SWCNT Nanocomposite via Band Gap Tuning. *Chemistry Select* **2018**, *3*, 8992.
(357) Tonga, M.; Wei, L.; Wilusz, E.; Korugic-Karasz, L.; Karasz, F. E.; Lahti, P. M. Solution-fabrication dependent thermoelectric behavior of iodine-doped regioregular and regiorandom P3HT/carbon nanotube composites. *Synth. Met.* **2018**, *239*, 51.
(358) Mo, J.-H.; Kim, J.-Y.; Kang, Y. H.; Cho, S. Y.; Jang, K.-S. Carbon Nanotube/Cellulose Acetate Thermoelectric Papers. *ACS Sustainable Chem. Eng.* **2018**, *6*, 15970.
(359) Wu, G.; Zhang, Z.-G.; Li, Y.; Gao, C.; Wang, X.; Chen, G. Exploring High-Performance n-Type Thermoelectric Composites Using Amino-Substituted Rylene Dimides and Carbon Nanotubes. *ACS Nano* **2017**, *11*, 5746.
(360) Gao, C.; Chen, G. In Situ Oxidation Synthesis of p-Type Composite with Narrow-Bandgap Small Organic Molecule Coating on Single-Walled Carbon Nanotube: Flexible Film and Thermoelectric Performance. *Small* **2018**, *14*, 1703453.
(361) Gao, C.; Liu, Y.; Gao, Y.; Zhou, Y.; Zhou, X.; Yin, X.; Pan, C.; Yang, C.; Wang, H.; Chen, G.; et al. High-performance n-type thermoelectric composites of acridones with tethered tertiary amines and carbon nanotubes. *J. Mater. Chem. A* **2018**, *6*, 20161.
(362) Yin, X.; Peng, Y.; Luo, J.; Zhou, X.; Gao, C.; Wang, L.; Yang, C. Tailoring the framework of organic small molecule semiconductors towards high-performance thermoelectric composites via conglutinated carbon nanotube webs. *J. Mater. Chem. A* **2018**, *6*, 8323.
(363) Liu, Y.; Dai, Q.; Zhou, Y.; Li, B.; Mao, X.; Gao, C.; Gao, Y.; Pan, C.; Jiang, Q.; Wu, Y.; et al. High-Performance N-Type Carbon Nanotube Composites: Improved Power Factor by Optimizing the Acridine Scaffold and Tailoring the Side Chains. *ACS Appl. Mater. Interfaces* **2019**, *11*, 29320.
(364) Tan, J.; Chen, Z.; Wang, D.; Qin, S.; Xiao, X.; Xie, D.; Liu, D.; Wang, L. Balancing the electrical conductivity and Seebeck coefficient by controlled interfacial doping towards high performance benzothienobenzothiophene-based organic thermoelectric materials. *J. Mater. Chem. A* **2019**, *7*, 24982.
(365) Chen, Y.; Qu, S.; Shi, W.; Yao, Q.; Chen, L. Enhanced thermoelectric properties of copper phthalocyanine/single-walled carbon nanotubes hybrids. *Carbon* **2020**, *159*, 471.
(366) Yin, X.; Zhong, F.; Chen, Z.; Gao, C.; Xie, G.; Wang, L.; Yang, C. Manipulating the doping level via host-dopant synergism towards high performance n-type thermoelectric composites. *Chem. Eng. J.* **2020**, *382*, 122817.
(367) Nandihalli, N.; Liu, C.-J.; Mori, T. Polymer based thermoelectric nanocomposite materials and devices: Fabrication and characteristics. *Nano Energy* **2020**, *78*, 105186.
(368) Yao, Q.; Wang, Q.; Wang, L.; Wang, Y.; Sun, J.; Zeng, H.; Jin, Z.; Huang, X.; Chen, L. The synergic regulation of conductivity and Seebeck coefficient in pure polyaniline by chemically changing the ordered degree of molecular chains. *J. Mater. Chem. A* **2014**, *2*, 2634.
(369) Wu, R.; Yuan, H.; Liu, C.; Lan, J.-L.; Yang, X.; Lin, Y.-H. Flexible PANI/SWCNT thermoelectric films with ultrahigh electrical conductivity. *RSC Adv.* **2018**, *8*, 26011.
(370) Du, Y.; Shen, S. Z.; Yang, W. D.; Cai, K. F.; Casey, P. S. Preparation and characterization of multiwalled carbon nanotube/poly(3-hexylthiophene) thermoelectric composite materials. *Synth. Met.* **2012**, *162*, 375.
(371) Schuettfort, T.; Nish, A.; Nicholas, R. J. Observation of a Type II Heterojunction in a Highly Ordered Polymer-Carbon Nanotube Nanohybrid Structure. *Nano Lett.* **2009**, *9*, 3871.
(372) Schuettfort, T.; Snaith, H. J.; Nish, A.; Nicholas, R. J. Synthesis and spectroscopic characterization of solution processable highly ordered polythiophene-carbon nanotube nanohybrid structures. *Nanotechnology* **2010**, *21*, 025201.

https://doi.org/10.1021/acs.chemrev.1c00218
Chem. Rev. XXXX, XXX, XXX−XXX

(373) Ferguson, A. J.; Blackburn, J. L.; Holt, J. M.; Kopidakis, N.; Tenent, R. C.; Barnes, T. M.; Heben, M. J.; Rumbles, G. Photoinduced Energy and Charge Transfer in P3HT:SWNT Composites. *J. Phys. Chem. Lett.* **2010**, *1*, 2406.
(374) Bounioux, C.; Diaz-Chao, P.; Campoy-Quiles, M.; Martin-Gonzalez, M. S.; Goni, A. R.; Yerushalmi-Rozen, R.; Muller, C. Thermoelectric composites of poly(3-hexylthiophene) and carbon nanotubes with a large power factor. *Energy Environ. Sci.* **2013**, *6*, 918.
(375) Lee, W.; Hong, C. T.; Kwon, O. H.; Yoo, Y.; Kang, Y. H.; Lee, J. Y.; Cho, S. Y.; Jang, K. S. Enhanced thermoelectric performance of bar-coated SWCNT/P3HT thin films. *ACS Appl. Mater. Interfaces* **2015**, *7*, 6550.
(376) Hong, C. T.; Kang, Y. H.; Ryu, J.; Cho, S. Y.; Jang, K.-S. Spray-printed CNT/P3HT organic thermoelectric films and power generators. *J. Mater. Chem. A* **2015**, *3*, 21428.
(377) Huang, D.; Wang, C.; Zou, Y.; Shen, X.; Zang, Y.; Shen, H.; Gao, X.; Yi, Y.; Xu, W.; Di, C.-A.; et al. Bismuth Interfacial Doping of Organic Small Molecules for High Performance n-type Thermoelectric Materials. *Angew. Chem., Int. Ed.* **2016**, *55*, 10672.
(378) Huang, D.; Yao, H.; Cui, Y.; Zou, Y.; Zhang, F.; Wang, C.; Shen, H.; Jin, W.; Zhu, J.; Diao, Y.; et al. Conjugated-Backbone Effect of Organic Small Molecules for n-Type Thermoelectric Materials with ZT over 0.2. *J. Am. Chem. Soc.* **2017**, *139*, 13013.
(379) Yuan, D.; Huang, D.; Zhang, C.; Zou, Y.; Di, C.-A.; Zhu, X.; Zhu, D. Efficient Solution-Processed n-Type Small-Molecule Thermoelectric Materials Achieved by Precisely Regulating Energy Level of Organic Dopants. *ACS Appl. Mater. Interfaces* **2017**, *9*, 28795.
(380) Jhulki, S.; Moorthy, J. N. Small molecular hole-transporting materials (HTMs) in organic light-emitting diodes (OLEDs): structural diversity and classification. *J. Mater. Chem. C* **2018**, *6*, 8280.
(381) Shahnawaz; Sudheendran Swayamprabha, S.; Nagar, M. R.; Yadav, R. A. K.; Gull, S.; Dubey, D. K.; Jou, J.-H. Hole-transporting materials for organic light-emitting diodes: an overview. *J. Mater. Chem. C* **2019**, *7*, 7144.
(382) Du, Y.; Cai, K. F.; Shen, S. Z.; Casey, P. S. Preparation and characterization of graphene nanosheets/poly(3-hexylthiophene) thermoelectric composite materials. *Synth. Met.* **2012**, *162*, 2102.
(383) Han, S.; Zhai, W.; Chen, G.; Wang, X. Morphology and thermoelectric properties of graphene nanosheets enwrapped with polypyrrole. *RSC Adv.* **2014**, *4*, 29281.
(384) Wang, L.; Liu, F.; Jin, C.; Zhang, T.; Yin, Q. Preparation of polypyrrole/graphene nanosheets composites with enhanced thermoelectric properties. *RSC Adv.* **2014**, *4*, 46187.
(385) Zhang, Z.; Chen, G.; Wang, H.; Zhai, W. Enhanced thermoelectric property by the construction of a nanocomposite 3D interconnected architecture consisting of graphene nanolayers sandwiched by polypyrrole nanowires. *J. Mater. Chem. C* **2015**, *3*, 1649.
(386) Xin, S.; Yang, N.; Gao, F.; Zhao, J.; Li, L.; Teng, C. Free-standing and flexible polypyrrole nanotube/reduced graphene oxide hybrid film with promising thermoelectric performance. *Mater. Chem. Phys.* **2018**, *212*, 440.
(387) Wang, L.; Wang, D.; Zhu, G.; Li, J.; Pan, F. Thermoelectric properties of conducting polyaniline/graphite composites. *Mater. Lett.* **2011**, *65*, 1086.
(388) Du, Y.; Shen, S. Z.; Yang, W.; Donelson, R.; Cai, K.; Casey, P. S. Simultaneous increase in conductivity and Seebeck coefficient in a polyaniline/graphene nanosheets thermoelectric nanocomposite. *Synth. Met.* **2012**, *161*, 2688.
(389) Xiang, J.; Drzal, L. T. Templated growth of polyaniline on exfoliated graphene nanoplatelets (GNP) and its thermoelectric properties. *Polymer* **2012**, *53*, 4202.
(390) Abad, B.; Alda, I.; Díaz-Chao, P.; Kawakami, H.; Almarza, A.; Amantia, D.; Gutierrez, D.; Aubouy, L.; Martín-González, M. Improved power factor of polyaniline nanocomposites with exfoliated graphene nanoplatelets (GNPs). *J. Mater. Chem. A* **2013**, *1*, 10450.
(391) Wang, L.; Yao, Q.; Bi, H.; Huang, F.; Wang, Q.; Chen, L. Large thermoelectric power factor in polyaniline/graphene nanocomposite films prepared by solution-assistant dispersing method. *J. Mater. Chem. A* **2014**, *2*, 11107.
(392) Wang, L.; Yao, Q.; Bi, H.; Huang, F.; Wang, Q.; Chen, L. PANI/graphene nanocomposite films with high thermoelectric properties by enhanced molecular ordering. *J. Mater. Chem. A* **2015**, *3*, 7086.
(393) Ube, T.; Koyanagi, J.; Kosaki, T.; Fujimoto, K.; Yokozeki, T.; Ishiguro, T.; Nishio, K. Fabrication of well-isolated graphene and evaluation of thermoelectric performance of polyaniline-graphene composite film. *J. Mater. Sci.* **2019**, *54*, 3904.
(394) Hsieh, Y.-Y.; Zhang, Y.; Zhang, L.; Fang, Y.; Kanakaraaj, S. N.; Bahk, J.-H.; Shanov, V. High thermoelectric power-factor composites based on flexible three-dimensional graphene and polyaniline. *Nanoscale* **2019**, *11*, 6552.
(395) Kim, G. H.; Hwang, D. H.; Woo, S. I. Thermoelectric properties of nanocomposite thin films prepared with poly(3,4-ethylenedioxythiophene) poly(styrenesulfonate) and graphene. *Phys. Chem. Chem. Phys.* **2012**, *14*, 3530.
(396) Yoo, D.; Kim, J.; Kim, J. H. Direct synthesis of highly conductive poly(3,4-ethylenedioxythiophene):poly(4-styrenesulfonate) (PEDOT:PSS)/graphene composites and their applications in energy harvesting systems. *Nano Res.* **2014**, *7*, 717.
(397) Li, F.; Cai, K.; Shen, S.; Chen, S. Preparation and thermoelectric properties of reduced graphene oxide/PEDOT:PSS composite films. *Synth. Met.* **2014**, *197*, 58.
(398) Liu, X.; Du, Y.; Meng, Q.; Shen, S. Z.; Xu, J. Flexible thermoelectric power generators fabricated using graphene/PEDOT:PSS nanocomposite films. *J. Mater. Sci.: Mater. Electron.* **2019**, *30*, 20369.
(399) Zhang, K.; Wang, S.; Zhang, X.; Zhang, Y.; Cui, Y.; Qiu, J. Thermoelectric performance of p-type nanohybrids filled polymer composites. *Nano Energy* **2015**, *13*, 327.
(400) Du, F.-P.; Cao, N.-N.; Zhang, Y.-F.; Fu, P.; Wu, Y.-G.; Lin, Z.-D.; Shi, R.; Amini, A.; Cheng, C. PEDOT:PSS/graphene quantum dots films with enhanced thermoelectric properties via strong interfacial interaction and phase separation. *Sci. Rep.* **2018**, *8*, 6441.
(401) Bubnova, O.; Khan, Z. U.; Malti, A.; Braun, S.; Fahlman, M.; Berggren, M.; Crispin, X. Optimization of the thermoelectric figure of merit in the conducting polymer poly(3,4-ethylenedioxythiophene). *Nat. Mater.* **2011**, *10*, 429.
(402) Maity, S.; Kulsi, C.; Banerjee, S.; Das, S.; Chatterjee, K. Dependence of thermoelectric power and electrical conductivity on structural order of PEDOT-Tos-graphene nanocomposite via charge carrier mobility. *Mater. Res. Express* **2019**, *6*, 105095.
(403) Paloheimo, J.; Laakso, K.; Isotalo, H.; Stubb, H. Conductivity, thermoelectric power and field-effect mobility in self-assembled films of polyanilines and oligoanilines. *Synth. Met.* **1995**, *68*, 249.
(404) Rivadulla, F.; Mateo-Mateo, C.; Correa-Duarte, M. A. Layer-by-layer polymer coating of carbon nanotubes: tuning of electrical conductivity in random networks. *J. Am. Chem. Soc.* **2010**, *132*, 3751.
(405) Lynch, J.; Kotiuga, M.; Doan-Nguyen, V. V. T.; Queen, W. L.; Forster, J. D.; Schlitz, R. A.; Murray, C. B.; Neaton, J. B.; Chabinyc, M. L.; Urban, J. J. Ligand Coupling Symmetry Correlates with Thermopower Enhancement in Small-Molecule/Nanocrystal Hybrid Materials. *ACS Nano* **2014**, *8*, 10528.
(406) Cho, C.; Stevens, B.; Hsu, J.-H.; Bureau, R.; Hagen, D. A.; Regev, O.; Yu, C.; Grunlan, J. C. Completely Organic Multilayer Thin Film with Thermoelectric Power Factor Rivaling Inorganic Tellurides. *Adv. Mater.* **2015**, *27*, 2996.
(407) Cho, C.; Bittner, N.; Choi, W.; Hsu, J.-H.; Yu, C.; Grunlan, J. C. Thermally Enhanced n-Type Thermoelectric Behavior in Completely Organic Graphene Oxide-Based Thin Films. *Adv. Electron. Mater.* **2019**, *5*, 1800465.
(408) Stevens, D. L.; Parra, A.; Grunlan, J. C. Thermoelectric Performance Improvement of Polymer Nanocomposites by Selective Thermal Degradation. *ACS Appl. Energy Mater.* **2019**, *2*, 5975.
(409) Stevens, D. L.; Gamage, G. A.; Ren, Z.; Grunlan, J. C. Salt doping to improve thermoelectric power factor of organic nanocomposite thin films. *RSC Adv.* **2020**, *10*, 11800.
(410) Park, C.; Yoo, D.; Im, S.; Kim, S.; Cho, W.; Ryu, J.; Kim, J. H. Large-scalable RTCVD Graphene/PEDOT:PSS hybrid conductive

https://doi.org/10.1021/acs.chemrev.1c00218
Chem. Rev. XXXX, XXX, XXX−XXX

film for application in transparent and flexible thermoelectric nanogenerators. *RSC Adv.* **2017**, *7*, 25237.
(411) Snyder, G. J.; Toberer, E. S. Complex thermoelectric materials. *Nat. Mater.* **2008**, *7*, 105.
(412) Yu, Y.; Cagnoni, M.; Cojocaru-Mirédin, O.; Wuttig, M. Chalcogenide Thermoelectrics Empowered by an Unconventional Bonding Mechanism. *Adv. Funct. Mater.* **2020**, *30*, 1904862.
(413) Thiagarajan, S. J.; Wang, W.; Yang, R. In *Annual Review of Nano Research*; World Scientific, 2009; Vol. 3.
(414) Park, D.-H.; Kim, M.-Y.; Oh, T.-S. Thermoelectric energy-conversion characteristics of n-type Bi2(Te,Se)3 nanocomposites processed with carbon nanotube dispersion. *Curr. Appl Phys.* **2011**, *11*, S41.
(415) Bark, H.; Kim, J.-S.; Kim, H.; Yim, J.-H.; Lee, H. Effect of multiwalled carbon nanotubes on the thermoelectric properties of a bismuth telluride matrix. *Curr. Appl Phys.* **2013**, *13*, S111.
(416) Lognoné, Q.; Gascoin, F. On the effect of carbon nanotubes on the thermoelectric properties of n-Bi2Te2.4Se0.6 made by mechanical alloying. *J. Alloys Compd.* **2015**, *635*, 107.
(417) Trawiński, B.; Bochentyn, B.; Gostkowska, N.; Łapiński, M.; Miruszewski, T.; Kusz, B. Structure and thermoelectric properties of bismuth telluride—Carbon composites. *Mater. Res. Bull.* **2018**, *99*, 10.
(418) Zhao, W.; Tan, H. T.; Tan, L. P.; Fan, S.; Hng, H. H.; Boey, Y. C. F.; Beloborodov, I.; Yan, Q. n-Type Carbon Nanotubes/Silver Telluride Nanohybrid Buckypaper with a High-Thermoelectric Figure of Merit. *ACS Appl. Mater. Interfaces* **2014**, *6*, 4940.
(419) Yeo, Y. H.; Oh, T. S. Thermoelectric properties of p-type (Bi,Sb)2Te3 nanocomposites dispersed with multiwall carbon nanotubes. *Mater. Res. Bull.* **2014**, *58*, 54.
(420) Nandihalli, N.; Gorsse, S.; Kleinke, H. Effects of additions of carbon nanotubes on the thermoelectric properties of Ni0.05-Mo3Sb5.4Te1.6. *J. Solid State Chem.* **2015**, *226*, 164.
(421) Zhang, Y.; Jia, X.; Sun, H.; Sun, B.; Liu, B.; Liu, H.; Kong, L.; Ma, H. Enhanced thermoelectric performance of nanostructured CNTs/BiSbTe bulk composite from rapid pressure-quenching induced multi-scale microstructure. *J. Materiomics* **2016**, *2*, 316.
(422) Hu, W.; Zhou, H.; Mu, X.; He, D.; Ji, P.; Hou, W.; Wei, P.; Zhu, W.; Nie, X.; Zhao, W. Preparation and Thermoelectric Properties of Graphite/Bi0.5Sb1.5Te3 Composites. *J. Electron. Mater.* **2018**, *47*, 3344.
(423) Wu, B.; Guo, Y.; Hou, C.; Zhang, Q.; Li, Y.; Wang, H. High-Performance Flexible Thermoelectric Devices Based on All-Inorganic Hybrid Films for Harvesting Low-Grade Heat. *Adv. Funct. Mater.* **2019**, *29*, 1900304.
(424) Khasimsaheb, B.; Singh, N. K.; Bathula, S.; Gahtori, B.; Haranath, D.; Neeleshwar, S. The effect of carbon nanotubes (CNT) on thermoelectric properties of lead telluride (PbTe) nanocubes. *Curr. Appl Phys.* **2017**, *17*, 306.
(425) Chu, F.; Zhang, Q.; Zhou, Z.; Hou, D.; Wang, L.; Jiang, W. Enhanced thermoelectric and mechanical properties of Na-doped polycrystalline SnSe thermoelectric materials via CNTs dispersion. *J. Alloys Compd.* **2018**, *741*, 756.
(426) Ju, H.; Park, D.; Kim, J. Solution-processable flexible thermoelectric composite films based on conductive polymer/SnSe0.8S0.2 nanosheets/carbon nanotubes for wearable electronic applications. *J. Mater. Chem. A* **2018**, *6*, 5627.
(427) Liu, X.; Du, Y.; Meng, Q.; Dou, Y.; Jin, M.; Xu, J.; Shen, S. Z. Free-Standing Single-Walled Carbon Nanotube/SnSe Nanosheet/Poly(3,4-Ethylenedioxythiophene):Poly(4-Styrenesulfonate) Nanocomposite Films for Flexible Thermoelectric Power Generators. *Adv. Eng. Mater.* **2020**, *22*, 2000605.
(428) Kim, K. T.; Choi, S. Y.; Shin, E. H.; Moon, K. S.; Koo, H. Y.; Lee, G.-G.; Ha, G. H. The influence of CNTs on the thermoelectric properties of a CNT/Bi2Te3 composite. *Carbon* **2013**, *52*, 541.
(429) An, H.; Karas, D.; Kim, B.-W.; Trabia, S.; Moon, J. Flexible n-type thermoelectric composite films with enhanced performance through interface engineering and post-treatment. *Nanotechnology* **2018**, *29*, 275403.
(430) Zhang, Y.; Wang, X. L.; Yeoh, W. K.; Zheng, R. K.; Zhang, C. Electrical and thermoelectric properties of single-wall carbon nanotube doped Bi2Te3. *Appl. Phys. Lett.* **2012**, *101*, 031909.
(431) Jin, Q.; Jiang, S.; Zhao, Y.; Wang, D.; Qiu, J.; Tang, D.-M.; Tan, J.; Sun, D.-M.; Hou, P.-X.; Chen, X.-Q.; et al. Flexible layer-structured Bi2Te3 thermoelectric on a carbon nanotube scaffold. *Nat. Mater.* **2019**, *18*, 62.
(432) Li, Y.; Qiao, J.; Zhao, Y.; Lan, Q.; Mao, P.; Qiu, J.; Tai, K.; Liu, C.; Cheng, H. A flexible thermoelectric device based on a Bi2Te3-carbon nanotube hybrid. *J. Mater. Sci. Technol.* **2020**, *58*, 80.
(433) Park, D.; Ju, H.; Oh, T.; Kim, J. A p-type multi-wall carbon nanotube/Te nanorod composite with enhanced thermoelectric performance. *RSC Adv.* **2018**, *8*, 8739.
(434) Park, D.; Ju, H.; Kim, J. Preparation and thermoelectric properties of two types of nanostructured tellurium with multi-walled carbon nanotubes. *J. Alloys Compd.* **2018**, *748*, 305.
(435) Ju, H.; Kim, J. Preparation and structure dependent thermoelectric properties of nanostructured bulk bismuth telluride with graphene. *J. Alloys Compd.* **2016**, *664*, 639.
(436) Suh, D.; Lee, S.; Mun, H.; Park, S.-H.; Lee, K. H.; Wng Kim, S.; Choi, J.-Y.; Baik, S. Enhanced thermoelectric performance of Bi0.5Sb1.5Te3-expanded graphene composites by simultaneous modulation of electronic and thermal carrier transport. *Nano Energy* **2015**, *13*, 67.
(437) Ding, D.; Sun, F.; Xia, F.; Tang, Z. A high-performance and flexible thermoelectric generator based on the solution-processed composites of reduced graphene oxide nanosheets and bismuth telluride nanoplates. *Nanoscale Adv.* **2020**, *2*, 3244.
(438) Zong, P.-A.; Hanus, R.; Dylla, M.; Tang, Y.; Liao, J.; Zhang, Q.; Snyder, G. J.; Chen, L. Skutterudite with graphene-modified grain-boundary complexion enhances zT enabling high-efficiency thermoelectric device. *Energy Environ. Sci.* **2017**, *10*, 183.
(439) Bhardwaj, A.; Shukla, A. K.; Dhakate, S. R.; Misra, D. K. Graphene boosts thermoelectric performance of a Zintl phase compound. *RSC Adv.* **2015**, *5*, 11058.
(440) Lin, Y.; Jin, J.; Kusmartsevab, O.; Song, M. Preparation of Pristine Graphene Sheets and Large-Area/Ultrathin Graphene Films for High Conducting and Transparent Applications. *J. Phys. Chem. C* **2013**, *117*, 17237.
(441) Li, X.; Liang, L.; Yang, M.; Chen, G.; Guo, C.-Y. Poly(3,4-ethylenedioxythiophene)/graphene/carbon nanotube ternary composites with improved thermoelectric performance. *Org. Electron.* **2016**, *38*, 200.
(442) Lu, Y.; Qiu, Y.; Jiang, Q.; Cai, K.; Du, Y.; Song, H.; Gao, M.; Huang, C.; He, J.; Hu, D. Preparation and Characterization of Te/Poly(3,4-ethylenedioxythiophene):Poly(styrenesulfonate)/Cu7Te4 Ternary Composite Films for Flexible Thermoelectric Power Generator. *ACS Appl. Mater. Interfaces* **2018**, *10*, 42310.
(443) Meng, Q.; Qiu, Y.; Cai, K.; Ding, Y.; Wang, M.; Pu, H.; Yao, Q.; Chen, L.; He, J. High Performance and Flexible Polyvinylpyrrolidone/Ag/Ag2Te Ternary Composite Film for Thermoelectric Power Generator. *ACS Appl. Mater. Interfaces* **2019**, *11*, 33254.
(444) Lu, Y.; Qiu, Y.; Cai, K.; Li, X.; Gao, M.; Jiang, C.; He, J. Ultrahigh performance PEDOT/Ag2Se/CuAgSe composite film for wearable thermoelectric power generators. *Mater. Today Phys.* **2020**, *14*, 100223.
(445) Choi, J.; Lee, J. Y.; Lee, S.-S.; Park, C. R.; Kim, H. High-Performance Thermoelectric Paper Based on Double Carrier-Filtering Processes at Nanowire Heterojunctions. *Adv. Energy Mater.* **2016**, *6*, 1502181.
(446) Erden, F.; Li, H.; Wang, X.; Wang, F.; He, C. High-performance thermoelectric materials based on ternary TiO2/CNT/PANI composites. *Phys. Chem. Chem. Phys.* **2018**, *20*, 9411.
(447) Kishan, K. Y.; Bisht, N.; Hiragond, C.; Dey, A.; Khanna, P. K.; More, P. V. Room temperature thermoelectric performance of Methyl Ammonium Lead Iodide Perovskite and their MWCNT-PANI composites. *Mater. Today Chem.* **2020**, *17*, 100275.

https://doi.org/10.1021/acs.chemrev.1c00218
Chem. Rev. XXXX, XXX, XXX−XXX

(448) Haque, M. A.; Kee, S.; Villalva, D. R.; Ong, W.-L.; Baran, D. Halide Perovskites: Thermal Transport and Prospects for Thermoelectricity. *Adv. Sci.* **2020**, *7*, 1903389.
(449) Sohn, A.; Yu, C. Ionic Transport Properties and Their Empirical Correlations for Thermal-to-Electrical Energy Conversion. *Mater. Today Phys.* **2021**, *19*, 100433.
(450) Wang, H.; Ail, U.; Gabrielsson, R.; Berggren, M.; Crispin, X. Ionic Seebeck Effect in Conducting Polymers. *Adv. Energy Mater.* **2015**, *5*, 1500044.
(451) Ail, U.; Jafari, M. J.; Wang, H.; Ederth, T.; Berggren, M.; Crispin, X. Thermoelectric Properties of Polymeric Mixed Conductors. *Adv. Funct. Mater.* **2016**, *26*, 6288.
(452) Han, S.; Jiao, F.; Khan, Z. U.; Edberg, J.; Fabiano, S.; Crispin, X. Thermoelectric Polymer Aerogels for Pressure-Temperature Sensing Applications. *Adv. Funct. Mater.* **2017**, *27*, 1703549.
(453) Zhang, F.; Zang, Y.; Huang, D.; Di, C.-A.; Zhu, D. Flexible and self-powered temperature-pressure dual-parameter sensors using microstructure-frame-supported organic thermoelectric materials. *Nat. Commun.* **2015**, *6*, 8356.
(454) Liu, K.; Zhou, Y.; Yuan, F.; Mo, X.; Yang, P.; Chen, Q.; Li, J.; Ding, T.; Zhou, J. Self-Powered Multimodal Temperature and Force Sensor Based-On a Liquid Droplet. *Angew. Chem., Int. Ed.* **2016**, *55*, 15864.
(455) Zhao, D.; Fabiano, S.; Berggren, M.; Crispin, X. Ionic thermoelectric gating organic transistors. *Nat. Commun.* **2017**, *8*, 14214.
(456) Kim, B.; Na, J.; Lim, H.; Kim, Y.; Kim, J.; Kim, E. Robust High Thermoelectric Harvesting Under a Self-Humidifying Bilayer of Metal Organic Framework and Hydrogel Layer. *Adv. Funct. Mater.* **2019**, *29*, 1807549.
(457) Kim, B.; Hwang, J. U.; Kim, E. Chloride transport in conductive polymer films for an n-type thermoelectric platform †. *Energy Environ. Sci.* **2020**, *13*, 859.
(458) Chang, W. B.; Evans, C. M.; Popere, B. C.; Russ, B. M.; Liu, J.; Newman, J.; Segalman, R. A. Harvesting Waste Heat in Unipolar Ion Conducting Polymers. *ACS Macro Lett.* **2016**, *5*, 94.
(459) Jiao, F.; Naderi, A.; Zhao, D.; Schlueter, J.; Shahi, M.; Sundstrom, J.; Granberg, H.; Edberg, J.; Ail, U.; Brill, J.; et al. Ionic thermoelectric paper. *J. Mater. Chem. A* **2017**, *5*, 16883.
(460) Li, T.; Zhang, X.; Lacey, S. D.; Mi, R.; Zhao, X.; Jiang, F.; Song, J.; Liu, Z.; Chen, G.; Dai, J.; et al. Cellulose ionic conductors with high differential thermal voltage for low-grade heat harvesting. *Nat. Mater.* **2019**, *18*, 608.
(461) Zhao, D.; Martinelli, A.; Willfahrt, A.; Fischer, T.; Bernin, D.; Khan, Z. U.; Shahi, M.; Brill, J.; Jonsson, M. P.; Fabiano, S.; Crispin, X. Polymer gels with tunable ionic Seebeck coefficient for ultra-sensitive printed thermopiles. *Nat. Commun.* **2019**, *10*, 1093.
(462) Jiang, Q.; Sun, H.; Zhao, D.; Zhang, F.; Hu, D.; Jiao, F.; Qin, L.; Linseis, V.; Fabiano, S.; Crispin, X.; et al. High Thermoelectric Performance in n-Type Perylene Bisimide Induced by the Soret Effect. *Adv. Mater.* **2020**, *32*, 2002752.
(463) Yang, H. D.; Tufa, L. T.; Bae, K. M.; Kang, T. J. A tubing shaped, flexible thermal energy harvester based on a carbon nanotube sheet electrode. *Carbon* **2015**, *86*, 118.
(464) Ikeshoji, T. Thermoelectric Conversion by Thin-Layer Thermogalvanic Cells with Soluble Redox Couples. *Bull. Chem. Soc. Jpn.* **1987**, *60*, 1505.
(465) Ikeshoji, T.; Goncalves, R. S. Thermogalvanic cells with aqueous redox couples and temperature differences larger than 100 K. *J. Appl. Electrochem.* **1993**, *23*, 516.
(466) Abraham, T. J.; MacFarlane, D. R.; Pringle, J. M. Seebeck coefficients in ionic liquids -prospects for thermo-electrochemical cells. *Chem. Commun.* **2011**, *47*, 6260.
(467) Kang, T. J.; Fang, S.; Kozlov, M. E.; Haines, C. S.; Li, N.; Kim, Y. H.; Chen, Y.; Baughman, R. H. Electrical Power From Nanotube and Graphene Electrochemical Thermal Energy Harvesters. *Adv. Funct. Mater.* **2012**, *22*, 477.
(468) Zhang, L.; Kim, T.; Li, N.; Kang, T. J.; Chen, J.; Pringle, J. M.; Zhang, M.; Kazim, A. H.; Fang, S.; Haines, C.; et al. High Power Density Electrochemical Thermocells for Inexpensively Harvesting Low-Grade Thermal Energy. *Adv. Mater.* **2017**, *29*, 1605652.
(469) Duan, J. J.; Feng, G.; Yu, B. Y.; Li, J.; Chen, M.; Yang, P. H.; Feng, J. M.; Liu, K.; Zhou, J. Aqueous thermogalvanic cells with a high Seebeck coefficient for low-grade heat harvest. *Nat. Commun.* **2018**, *9*, 5146.
(470) Marcus, Y. Effect of Ions on the Structure of Water: Structure Making and Breaking. *Chem. Rev.* **2009**, *109*, 1346.
(471) Kim, T.; Lee, J. S.; Lee, G.; Yoon, H.; Yoon, J.; Kang, T. J.; Kim, Y. H. High thermopower of ferri/ferrocyanide redox couple in organic-water solutions. *Nano Energy* **2017**, *31*, 160.
(472) Burrows, B. Discharge Behavior of Redox Thermogalvanic Cells. *J. Electrochem. Soc.* **1976**, *123*, 154.
(473) Al Maimani, M.; Black, J. J.; Aldous, L. Achieving pseudo-'n-type p-type' in-series and parallel liquid thermoelectrics using all-iron thermoelectrochemical cells with opposite Seebeck coefficients. *Electrochem. Commun.* **2016**, *72*, 181.
(474) Buckingham, M. A.; Marken, F.; Aldous, L. The thermo-electrochemistry of the aqueous iron(ii)/iron(iii) redox couple: significance of the anion and pH in thermogalvanic thermal-to-electrical energy conversion. *Sustainable Energy Fuels* **2018**, *2*, 2717.
(475) Wu, J.; Black, J. J.; Aldous, L. Thermoelectrochemistry using conventional and novel gelled electrolytes in heat-to-current thermocells. *Electrochim. Acta* **2017**, *225*, 482.
(476) Jin, L.; Greene, G. W.; MacFarlane, D. R.; Pringle, J. M. Redox-Active Quasi-Solid-State Electrolytes for Thermal Energy Harvesting. *ACS Energy Lett.* **2016**, *1*, 654.
(477) Zhou, H.; Yamada, T.; Kimizuka, N. Supramolecular Thermo-Electrochemical Cells: Enhanced Thermoelectric Performance by Host-Guest Complexation and Salt-Induced Crystallization. *J. Am. Chem. Soc.* **2016**, *138*, 10502.
(478) Abraham, T. J.; MacFarlane, D. R.; Pringle, J. M. High Seebeck coefficient redox ionic liquid electrolytes for thermal energy harvesting. *Energy Environ. Sci.* **2013**, *6*, 2639.
(479) Uhl, S.; Laux, E.; Journot, T.; Jeandupeux, L.; Charmet, J.; Keppner, H. Development of Flexible Micro-Thermo-electrochemical Generators Based on Ionic Liquids. *J. Electron. Mater.* **2014**, *43*, 3758.
(480) Abraham, T. J.; MacFarlane, D. R.; Baughman, R. H.; Jin, L.; Li, N.; Pringle, J. M. Towards ionic liquid-based thermoelectrochemical cells for the harvesting of thermal energy. *Electrochim. Acta* **2013**, *113*, 87.
(481) He, J.; Al-Masri, D.; MacFarlane, D. R.; Pringle, J. M. Temperature dependence of the electrode potential of a cobalt-based redox couple in ionic liquid electrolytes for thermal energy harvesting. *Faraday Discuss.* **2016**, *190*, 205.
(482) Jiao, N.; Abraham, T. J.; MacFarlane, D. R.; Pringle, J. M. Ionic Liquid Electrolytes for Thermal Energy Harvesting Using a Cobalt Redox Couple. *J. Electrochem. Soc.* **2014**, *161*, D3061.
(483) Yee, E. L.; Cave, R. J.; Guyer, K. L.; Tyma, P. D.; Weaver, M. J. A survey of ligand effects upon the reaction entropies of some transition metal redox couples. *J. Am. Chem. Soc.* **1979**, *101*, 1131.
(484) Taheri, A.; MacFarlane, D. R.; Pozo-Gonzalo, C.; Pringle, J. M. Quasi-solid-State Electrolytes for Low-Grade Thermal Energy Harvesting using a Cobalt Redox Couple. *ChemSusChem* **2018**, *11*, 2788.
(485) Sahami, S.; Weaver, M. J. Entropic and enthalpic contributions to the solvent dependence of the thermodynamics of transition-metal redox couples: Part I. Couples containing aromatic ligands. *J. Electroanal. Chem. Interfacial Electrochem.* **1981**, *122*, 155.
(486) Sahami, S.; Weaver, M. J. Solvent effects on the kinetics of simple electrochemical reactions: Part I. Comparison of the behavior of Co(III)/(II) trisethylenediamine and ammine couples with the predictions of dielectric conitnuum theory. *J. Electroanal. Chem. Interfacial Electrochem.* **1981**, *124*, 35.
(487) Taheri, A.; MacFarlane, D. R.; Pozo-Gonzalo, C.; Pringle, J. M. Application of a water-soluble cobalt redox couple in free-standing cellulose films for thermal energy harvesting. *Electrochim. Acta* **2019**, *297*, 669.
(488) Al-Masri, D.; Dupont, M.; Yunis, R.; MacFarlane, D. R.; Pringle, J. M. The electrochemistry and performance of cobalt-based redox

https://doi.org/10.1021/acs.chemrev.1c00218
Chem. Rev. XXXX, XXX, XXX−XXX

couples for thermoelectrochemical cells. *Electrochim. Acta* **2018**, *269*, 714.
(489) Zhou, H.; Liu, P. High Seebeck Coefficient Electrochemical Thermocells for Efficient Waste Heat Recovery. *ACS Appl. Energy Mater.* **2018**, *1*, 1424.
(490) Cataldo, F. Synthesis of ketonic resins from self-polymerization of acetone, 1. Action of protic and lewis acids on acetone. *Angew. Makromol. Chem.* **1996**, *236*, 1.
(491) Han, C.-G.; Qian, X.; Li, Q.; Deng, B.; Zhu, Y.; Han, Z.; Zhang, W.; Wang, W.; Feng, S.-P.; Chen, G.; et al. Giant thermopower of ionic gelatin near room temperature. *Science* **2020**, *368*, 1091.
(492) Burrows, B. Discharge Behavior of Redox Thermogalvanic Cells. *J. Electrochem. Soc.* **1976**, *123*, 154.
(493) Quickenden, T. I.; Mua, Y. The Power Conversion Efficiencies of a Thermogalvanic Cell Operated in Three Different Orientations. *J. Electrochem. Soc.* **1995**, *142*, 3652.
(494) Mua, Y.; Quickenden, T. I. Power Conversion Efficiency, Electrode Separation, and Overpotential in the Ferricyanide/Ferrocyanide Thermogalvanic Cell. *J. Electrochem. Soc.* **1996**, *143*, 2558.
(495) Holubowitch, N. E.; Landon, J.; Lippert, C. A.; Craddock, J. D.; Weisenberger, M. C.; Liu, K. Spray-Coated Multiwalled Carbon Nanotube Composite Electrodes for Thermal Energy Scavenging Electrochemical Cells. *ACS Appl. Mater. Interfaces* **2016**, *8*, 22159.
(496) Wijeratne, K.; Vagin, M.; Brooke, R.; Crispin, X. Poly(3,4-ethylenedioxythiophene)-tosylate (PEDOT-Tos) electrodes in thermogalvanic cells. *J. Mater. Chem. A* **2017**, *5*, 19619.
(497) Maeda, Y.; Kitamura, H.; Itoh, E.; Inagaki, M. A new carbon fiber and nitric acid cell with a temperature difference between electrodes. *Synth. Met.* **1983**, *7*, 211.
(498) Endo, M.; Yamagishi, Y.; Inagaki, M. Thermocell with graphite fiber-bromine intercalation compounds. *Synth. Met.* **1983**, *7*, 203.
(499) Qian, W.; Li, M.; Chen, L.; Zhang, J.; Dong, C. Improving thermo-electrochemical cell performance by constructing Ag-MgO-CNTs nanocomposite electrodes. *RSC Adv.* **2015**, *5*, 97982.
(500) Cottis, P. P.; Evans, D.; Fabretto, M.; Pering, S.; Murphy, P.; Hojati-Talemi, P. Metal-free oxygen reduction electrodes based on thin PEDOT films with high electrocatalytic activity. *RSC Adv.* **2014**, *4*, 9819.
(501) Levermore, P. A.; Chen, L.; Wang, X.; Das, R.; Bradley, D. D. C. Fabrication of Highly Conductive Poly(3,4-ethylenedioxythiophene) Films by Vapor Phase Polymerization and Their Application in Efficient Organic Light-Emitting Diodes. *Adv. Mater.* **2007**, *19*, 2379.
(502) Khan, Z. U.; Bubnova, O.; Jafari, M. J.; Brooke, R.; Liu, X.; Gabrielsson, R.; Ederth, T.; Evans, D. R.; Andreasen, J. W.; Fahlman, M.; et al. Acido-basic control of the thermoelectric properties of poly(3,4-ethylenedioxythiophene)tosylate (PEDOT-Tos) thin films. *J. Mater. Chem. C* **2015**, *3*, 10616.
(503) Mitraka, E.; Jafari, M. J.; Vagin, M.; Liu, X.; Fahlman, M.; Ederth, T.; Berggren, M.; Jonsson, M. P.; Crispin, X. Oxygen-induced doping on reduced PEDOT. *J. Mater. Chem. A* **2017**, *5*, 4404.
(504) Wijeratne, K.; Ail, U.; Brooke, R.; Vagin, M.; Liu, X.; Fahlman, M.; Crispin, X. Bulk electronic transport impacts on electron transfer at conducting polymer electrode-electrolyte interfaces. *Proc. Natl. Acad. Sci. U. S. A.* **2018**, *115*, 11899.
(505) Wang, Y.; Mukaida, M.; Kirihara, K.; Lyu, L.; Wei, Q. Poly(3,4-Ethylene Dioxythiophene)/Poly(Styrene Sulfonate) Electrodes in Electrochemical Cells for Harvesting Waste Heat. *Energy Technol.* **2020**, *8*, 1900998.
(506) Li, G.; Dong, D.; Hong, G.; Yan, L.; Zhang, X.; Song, W. High-Efficiency Cryo-Thermocells Assembled with Anisotropic Holey Graphene Aerogel Electrodes and a Eutectic Redox Electrolyte. *Adv. Mater.* **2019**, *31*, 1901403.
(507) Ding, T.; Zhu, L.; Wang, X.-Q.; Chan, K. H.; Lu, X.; Cheng, Y.; Ho, G. W. Hybrid Photothermal Pyroelectric and Thermogalvanic Generator for Multisituation Low Grade Heat Harvesting. *Adv. Energy Mater.* **2018**, *8*, 1802397.
(508) Shin, G.; Jeon, J. G.; Kim, J. H.; Lee, J. H.; Kim, H. J.; Lee, J.; Kang, K. M.; Kang, T. J. Thermocells for hybrid photovoltaic/thermal systems. *Molecules* **2020**, *25*, 1928.
(509) Kim, K.; Hwang, S.; Lee, H. Unravelling ionic speciation and hydration structure of Fe(III/II) redox couples for thermoelectrochemical cells. *Electrochim. Acta* **2020**, *335*, 135651.
(510) Schönig, M.; Schuster, R. Sensitive and fast measurement of surface temperature with a thermogalvanic cell. *Appl. Phys. Lett.* **2020**, *116*, 091601.
(511) He, H.; Zhang, L.; Guan, X.; Cheng, H.; Liu, X.; Yu, S.; Wei, J.; Ouyang, J. A.-O. Biocompatible Conductive Polymers with High Conductivity and High Stretchability. *ACS Appl. Mater. Interfaces* **2019**, *11*, 26185.

https://doi.org/10.1021/acs.chemrev.1c00218
Chem. Rev. XXXX, XXX, XXX−XXX